UNIVERSITÉ D'ORLÉANS

ÉCOLE DOCTORALE : Énergie - Matériaux - Sciences de la Terre et de l'Univers
Institut des Sciences de la Terre d'Orléans (ISTO)

THÈSE présentée par :

Walid OKAYBI

soutenue le : **09 juillet 2026**

pour obtenir le grade de : **Docteur de l'Université d'Orléans**

Discipline / Spécialité : **Sciences de l'univers**

Colloidal Clogging in Porous Media: A Microfluidic Investigation of Dynamics, Mechanisms, and Control

THÈSE dirigée par :

M. Cyprien Soulaine	Chargé de recherche CNRS, ISTO
Mme Sophie Roman	Associate Professor, Université d'Orléans

RAPPORTEURS :

M. Hugues Bodiguel	Professeur des universités, Grenoble INP
M. Manouk Abkarian	Directeur de recherche CNRS, CBS

JURY :

M. Lionel Mercury	Professeur des universités, Université d'Orléans, **Président du jury**
M. Hugues Bodiguel	Professeur des universités, Grenoble INP
M. Manouk Abkarian	Directeur de recherche CNRS, CBS
Mme Eleonora Secchi	Chargée de recherche, ETH Zurich
M. Alban Sauret	Associate Professor, University of Maryland
Mme Maša Prodanović	Professeure des universités, UT Austin
M. Cyprien Soulaine	Chargé de recherche CNRS, ISTO

To my wife, Sara,
who has stood by me during this challenging journey.
Your love and support gave me the strength to keep moving forward.

To my family, whom I love with all my heart.
I am deeply grateful for the person you helped me become.
Without you and without your belief in me, none of this would have been possible.

Acknowledgments

I would like to express my sincere gratitude to my PhD advisors, Cyprien Soulaine and Sophie Roman, for welcoming me into their group, first as a Master 2 intern, an experience that ultimately paved the way for this PhD. Their guidance, trust, continuous support, and the countless brainstorming sessions and discussions we shared helped shape both this work and the way I approach research. Thank you for encouraging me to think independently, pursue new ideas, and grow into an independent researcher.

I am also grateful to everyone at the Institute of Earth Sciences of Orléans (ISTO) who contributed, directly or indirectly, to making these years run smoothly. I would especially like to thank the administrative and technical staff for their help, availability, and support with the many practical aspects that accompany a PhD, and for always being there when assistance was needed. I am grateful to have carried out this work in such a collaborative and supportive research environment, with access to the facilities and resources that were essential to this project. In particular, the experiments were conducted at Nanoμlab, a nano-microfluidics laboratory in Orléans, France, which is part of the ECCSEL consortium and the StoRIES project (STorage Research Infrastructure Eco-System), which aims to strengthen European research infrastructure capacities and services to address the challenges of the European Green Deal. This work also benefited from the support of the LAAS-CNRS micro- and nanotechnologies platform, a member of the French national Renatech network.

Special thanks are due to the French National Centre for Scientific Research (CNRS) and the European Research Council (ERC) for funding my PhD through the ERC COCONUT grant (101043288), awarded to Cyprien Soulaine. This support also gave me the opportunity to participate in several national and international conferences and summer schools, as well as to visit Princeton University, where I had valuable discussions with researchers and gained insight into a different academic and research environment.

Like any PhD, this journey came with its share of scientific challenges: unanswered questions, experiments that did not work, uncertainty, moments of doubt, and periods when progress felt painfully slow. These challenges were made even more difficult by the events unfolding in my home country during these years. The worry for my family and for what was happening there often made it difficult to stay focused and added another emotional weight to an already demanding journey. During those periods, I was very fortunate to be surrounded by people who showed me genuine kindness and understanding. I am especially grateful to Cyprien and Sophie, who were always supportive when things became difficult, and to my colleagues at ISTO, whose kindness meant more to me than they may realize.

Finally, I warmly thank all my friends at ISTO for their friendship and support, and for the many good moments we shared throughout these years. Beyond the science and the work, the conversations, laughter, coffee breaks, and everyday moments brought much-needed lightness to this journey. Their presence made the difficult days easier and the good days even better. I will remember these years not only for the research and how much I grew as a scientist, but also for the people with whom I shared this journey.

Résumé étendu:

Colmatage colloïdal en milieux poreux : dynamiques, mécanismes et contrôle. Implications pour l'injectivité dans les systèmes souterrains

Systèmes souterrains : contamination et injection de fluides

Le sous-sol est une ressource essentielle pour l'approvisionnement en eau souterraine et les applications énergétiques. Plus de 95% de l'eau douce disponible, hors glaciers et calottes glaciaires, est stockée sous terre sous forme d'eaux souterraines, ce qui la rend indispensable aux écosystèmes et à l'approvisionnement en eau potable [Morris et al., 2003]. Les systèmes d'eaux souterraines sont exposés à une large gamme de contaminants issus des activités humaines, notamment des contaminants chimiques tels que les hydrocarbures et autres substances non miscibles, ainsi que des contaminants particulaires transportés en suspension. Parmi ceux-ci, les microplastiques sont devenus une préoccupation majeure en raison de leur persistance et de leur capacité à transporter d'autres contaminants. Outre son rôle de ressource en eau, le sous-sol est de plus en plus exploité pour la production d'énergie géothermique et le stockage souterrain d'énergie thermique, où l'injection et la circulation de fluides à travers des milieux poreux sont nécessaires pour garantir un fonctionnement durable [Kaminskaite et al., 2022]. Dans ces systèmes, les différences de température ou de composition chimique entre le fluide injecté et la nappe phréatique native peuvent perturber l'équilibre physico-chimique de la formation et modifier les processus de transport et de rétention au sein des pores. La compréhension de ces processus est donc essentielle, tant pour prédire la migration et la rétention des contaminants et des matières en suspension dans les eaux souterraines que pour évaluer le comportement à long terme des systèmes souterrains, où ils peuvent, à terme, contribuer à une diminution de l'injectivité et au colmatage.

Difficultés opérationnelles : diminution de l'injectivité et colmatage

Un défi opérationnel majeur des systèmes souterrains réside dans la diminution progressive de l'injectivité [Song et al., 2020], définie comme la capacité d'une formation à accepter et à transmettre les fluides injectés au fil du temps, notamment lorsque l'injection continue de fluides est nécessaire pour une exploitation à long terme. Cette diminution d'injectivité est généralement associée à des phénomènes de colmatage au sein des pores du milieu poreux. Ces phénomènes peuvent résulter de différents mécanismes, tels que des réactions chimiques conduisant à la précipitation, l'activité biologique et l'accumulation de particules en suspension, comme illustré sur la figure A. L'importance relative de ces mécanismes dépend des conditions physico-chimiques du système et des propriétés du fluide injecté et du milieu poreux. Parmi ces mécanismes, le colmatage induit par les particules joue un rôle central dans de nombreuses situations : les particules en suspension transportées par l'écoulement peuvent être retenues dans les rétrécissements des pores, s'accumuler et se réorganiser, entraînant une réduction de la perméabilité et une redistribution de l'écoulement. Ces processus modifient progressivement la structure des pores et impactent le comportement hydraulique global du système. Cette thèse accorde une attention particulière au colmatage induit par les particules afin d'identifier les mécanismes régissant la rétention des particules et de comprendre comment ils affectent l'écoulement et la perméabilité dans les milieux poreux.

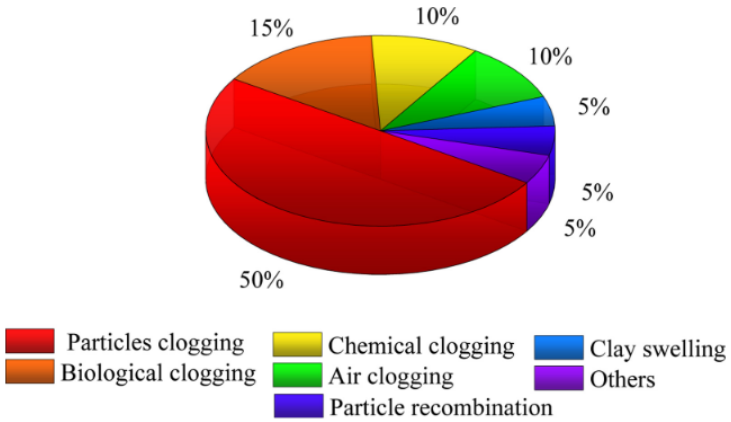

Figure A: Contribution relative des différents mécanismes de colmatage [Song et al., 2020].

À l'échelle des pores, le colmatage particulaire peut résulter de différents mécanismes, notamment le tamisage, le pontage et le dépôt ou l'agrégation progressive (Fig. B) [Dressaire and Sauret, 2017b]. Le tamisage se produit lorsque les particules sont trop grosses pour franchir un rétrécissement, tandis que le pontage résulte de l'arrivée collective de plusieurs particules qui forment une arche au-dessus du rétrécissement du pore lorsque le flux converge. En revanche, le colmatage progressif est classiquement décrit comme résultant de dépôts successifs sur des sites de dépôt opposés près de l'entrée d'un rétrécissement, soit sur la surface solide, soit sur des particules précédemment déposées, réduisant progressivement la section d'écoulement disponible jusqu'à blocage. Dans les systèmes colloïdaux, ce processus est contrôlé non seulement par le transport hydrodynamique, mais aussi par les interactions à longue portée particule-surface et particule-particule, en particulier la répulsion électrostatique et l'attraction de van der Waals. En fonction des conditions hydrodynamiques et physico-chimiques, la croissance des dépôts peut toutefois se localiser et se développer à partir d'un site de dépôt préférentiel unique, donnant naissance à différentes morphologies de dépôts, comme des structures dendritiques [de Saint Vincent et al., 2016]. Dans les milieux poreux réels, ces mécanismes ne se produisent pas nécessairement de manière isolée, mais peuvent interagir à mesure que le dépôt modifie progressivement la géométrie locale et le champ d'écoulement [Chauveteau et al., 1998]. Leur développement est contrôlé par les effets combinés de la chimie des fluides, notamment la force ionique, le pH et la température [Pelley and Tufenkji, 2008, Sang et al., 2013, Gerber et al., 2019, Sadri et al., 2017, Rosenbrand et al., 2015, Yan et al., 2020], propriétés des particules telles que la taille, la concentration et la charge de surface [Litton and Olson, 1996, Bennacer et al., 2017, Alem et al., 2015], conditions hydrodynamiques, y compris le débit et le protocole d'injection [Bradford et al., 2007, Agbangla et al., 2012b, Lohaus et al., 2020, Dincau et al., 2022], et la géométrie et les propriétés de surface du milieu poreux, telles que la taille des pores, la rugosité, la connectivité, la tortuosité et l'hétérogénéité chimique [Auset and Keller, 2006, Johnson et al., 1996, Bacchin et al., 2014].

Stratégie scientifique pour l'étude du dépôt et du colmatage dans les milieux poreux

Comprendre le transport colloïdal et le colmatage dans les milieux poreux demeure complexe car cela implique des processus couplés agissant à différentes échelles spatiales, de l'échelle moléculaire et particulaire à l'échelle du pore, de la carotte et du terrain. La physique sous-jacente et la description des écoulements et du transport de particules varient selon l'échelle considérée et le degré de résolution utilisé pour représenter la structure poreuse. Dans ce travail, une attention

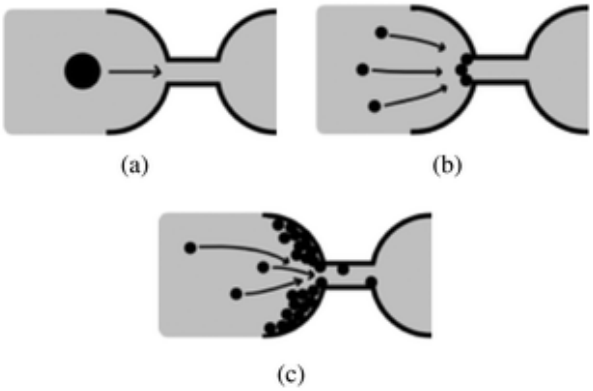

Figure B: Mécanismes d'obstruction des pores par les particules : (a) tamisage, (b) pontage et (c) obstruction progressive [Dressaire and Sauret, 2017b].

particulière est portée à l'échelle du pore, car le transport, le dépôt et le colmatage des pores par les particules se développent au sein de chaque pore et déterminent en définitive la réduction de la perméabilité à plus grande échelle. Une meilleure compréhension de ces mécanismes est donc nécessaire avant de les relier aux descriptions à plus grande échelle de l'évolution du transport et de la perméabilité.

Cependant, l'accès direct à ces mécanismes demeure limité dans les milieux poreux naturels, généralement opaques. Les approches expérimentales conventionnelles fournissent principalement des informations macroscopiques, telles que la diminution de la perméabilité ou le comportement de percée, sans permettre de comprendre comment les dépôts s'organisent au sein de l'espace poreux [Li et al., 2005, Gregory and Wishart, 1980]. Dans ce contexte, la microfluidique offre un cadre puissant pour étudier le transport de particules et le colmatage à l'échelle des pores, car elle permet la visualisation directe des trajectoires des particules, des événements de dépôt et de la dynamique de colmatage dans des conditions hydrodynamiques et physico-chimiques contrôlées [Auset and Keller, 2004]. Toutefois, la plupart des études existantes à l'échelle des pores reposent sur des géométries simplifiées ou se concentrent sur des régimes de dépôt spécifiques [Dersoir et al., 2015b, Kim et al., 2022], limitant ainsi la compréhension du colmatage dans les milieux poreux hétérogènes représentatifs des systèmes souterrains. Le présent travail utilise donc des systèmes microfluidiques poreux hétérogènes pour étudier les mécanismes à l'échelle des pores qui régissent l'accumulation de particules et la formation de structures d'obstruction, ainsi que la manière dont ces processus modifient les voies d'écoulement locales et réduisent progressivement la perméabilité et l'injectivité. Une attention particulière est portée aux dépôts dendritiques induits par agrégation dans les régimes dominés par l'adhésion, au pontage hydrodynamique dans les régimes dominés par l'hydrodynamique, et à l'effet d'un forçage d'écoulement oscillatoire dépendant du temps sur ces différents régimes de dépôt.

Approche expérimentale microfluidique

Trois modèles microfluidiques ont été utilisés pour étudier le transport et le colmatage des particules dans des conditions contrôlées à l'échelle des pores : une géométrie de collecteur monocristallin (M1) pour isoler les mécanismes de dépôt locaux autour d'un obstacle individuel, et deux micromodèles poreux tortueux hétérogènes (M2 et M3 ; Fig. C) conçus pour reproduire les principales caractéristiques géométriques des milieux poreux du sous-sol, tout en différant par la distribution de la taille des pores et des constrictions. Ces dispositifs en PDMS ont été fabriqués par lithographie molle standard à partir de matrices SU-8 et collés sur des lames de

verre [Whitesides et al., 2001]. Des expériences d'écoulement ont été réalisées avec des particules de polystyrène carboxylé de 4,5 et 6 µm en suspension dans des mélanges eau-glycérol de densité équivalente, dans des conditions hydrodynamiques et physico-chimiques contrôlées, avec et sans sel. Le transport, le dépôt et le colmatage des particules ont été suivis en temps réel par microscopie optique, tandis que les mesures de pression et de débit ont permis de quantifier la réponse hydraulique des dispositifs. L'analyse d'images a ensuite permis de reconstruire l'intégralité du domaine poreux, d'identifier les particules déposées, de suivre l'évolution de la porosité et de déterminer la distribution spatiale des dépôts lors du colmatage. Le comportement hydraulique des dispositifs en PDMS a été caractérisé au préalable afin de définir le régime de fonctionnement linéaire et d'estimer leur perméabilité apparente. De plus, des simulations à l'échelle des pores, basées sur des images microscopiques, ont été utilisées comme outil de post-traitement pour visualiser la redistribution des flux et quantifier l'influence des dépôts observés expérimentalement sur le transport local et la perméabilité [Soulaine and Tchelepi, 2016].

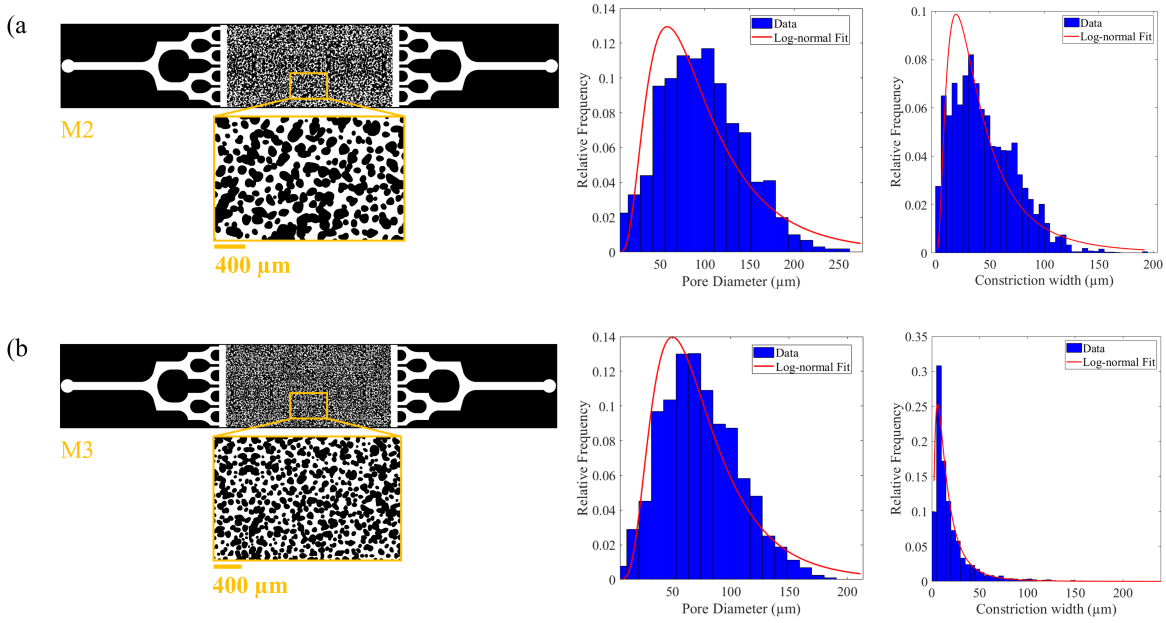

Figure C: Micromodèles microfluidiques poreux hétérogènes M2 et M3. Bien que les deux géométries aient une porosité similaire, M3 est plus resserré que M2, avec des pores plus petits et des passages plus étroits.

Obstruction induite par les dendrites dans les régimes dominés par l'adhérence

Dans des conditions d'adhérence prédominantes, nous avons étudié le dépôt par agrégation dans des milieux poreux hétérogènes et tortueux, en nous intéressant particulièrement à la formation de structures dendritiques et à leur rôle dans le colmatage. À l'aide de particules de polystyrène carboxylé de 4,5 µm en suspension dans un fluide de densité équivalente contenant 100 mM de NaCl, nous avons réalisé des expériences d'écoulement dans un domaine poreux hétérogène M2 et dans une géométrie de collecteur monocristallin M1, complétées par des simulations d'écoulement. Ces expériences révèlent un nouveau mécanisme de colmatage progressif, que nous appelons ici « colmatage dendritique », dans lequel un dépôt allongé croît à partir d'un site de dépôt préférentiel unique et comble progressivement l'espace poreux jusqu'à son obstruction (Fig. D). Contrairement à la vision classique d'une agrégation progressive à partir de sites de dépôt répartis

de part et d'autre du seuil de pore [Dressaire and Sauret, 2017b], la croissance dendritique dépend fortement du champ d'écoulement local. En combinant des expériences avec un critère d'équilibre des couples pour le détachement des particules et des champs de vitesse simulés, nous montrons que la formation de dendrites requiert une zone de stagnation conique suffisamment grande pour contenir au moins le diamètre d'une particule et une vitesse locale suffisamment faible pour permettre l'attachement entre particules. Cette condition est satisfaite à un débit modéré, où les dendrites croissent et contribuent au colmatage des pores et à une réduction plus marquée de la perméabilité, mais pas à des débits plus élevés où l'augmentation du cisaillement inhibe la croissance dendritique. Ces résultats démontrent que le dépôt dendritique peut contribuer directement au colmatage dans les milieux poreux hétérogènes et fournissent un critère à l'échelle des pores reliant les conditions d'écoulement locales à la diminution de la perméabilité induite par l'agrégation.

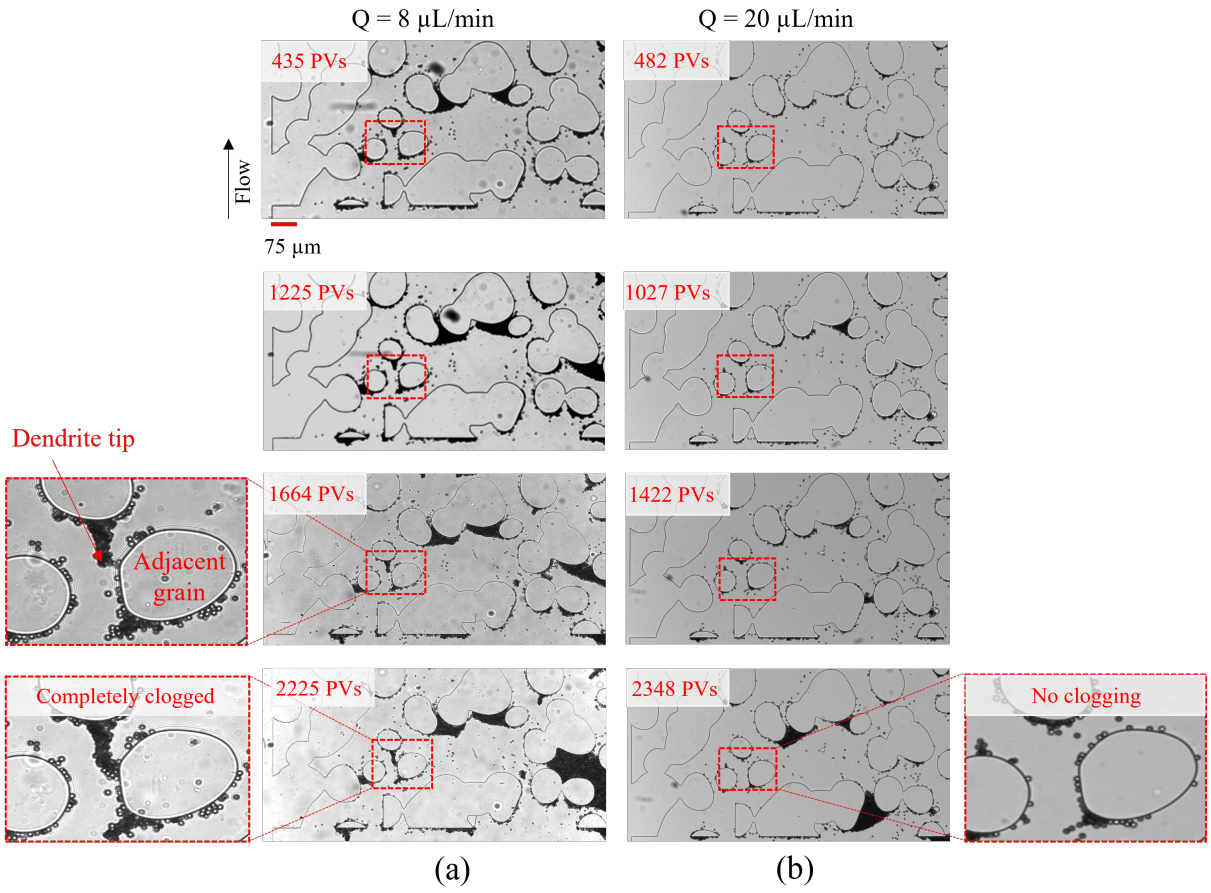

Figure D: Images microscopiques moyennes illustrant l'évolution du colmatage à 8 et 20 µL/min dans un domaine poreux hétérogène. À 8 µL/min, une dendrite croît progressivement et finit par colmater le pore, tandis qu'à 20 µL/min, aucun colmatage induit par une dendrite ne se développe dans la même région.

Colmatage induit par le pontage dans les régimes dominés par l'hydrodynamique

Dans des conditions où l'agrégation est limitée, nous avons étudié le colmatage par pontage hydrodynamique des pores dans le modèle microfluidique hétérogène et tortueux M3, choisi pour cette étude car ses pores plus petits et ses rétrécissements plus importants offrent un

confinement plus fort que M2 et favorisent ainsi le pontage. Des expériences sous pression, réalisées avec des particules de 4,5 et 6 µm dans des suspensions sans sel à densité équivalente, montrent que le colmatage induit par pontage se développe par blocage progressif des voies d'écoulement préférentielles, produisant une diminution par paliers de la perméabilité associée à la formation soudaine d'arches de particules stables au niveau des rétrécissements des pores. Les expériences montrent également que la taille des particules a l'effet le plus important sur la dynamique du colmatage, suivie par la concentration de particules, tandis que la différence de pression imposée affecte principalement l'échelle de temps de la réduction de la perméabilité (Fig. E). Pour interpréter et reproduire ces observations, un modèle de réseau de pores intégrant une loi probabiliste pour la formation des arches a été utilisé. Le modèle tient compte de la concentration particulaire, du rapport taille particule/taille du rétrécissement et de la géométrie de ce dernier, et reproduit avec une bonne concordance les tendances expérimentales de réduction de la perméabilité (Fig. E). Ces résultats montrent que le pontage hydrodynamique est un mécanisme prédominant de réduction de la perméabilité dans les conditions hydrodynamiques étudiées, et qu'une approche probabiliste du réseau de pores, étayée par des expériences à l'échelle des pores, permet de saisir son impact sur l'évolution de la perméabilité.

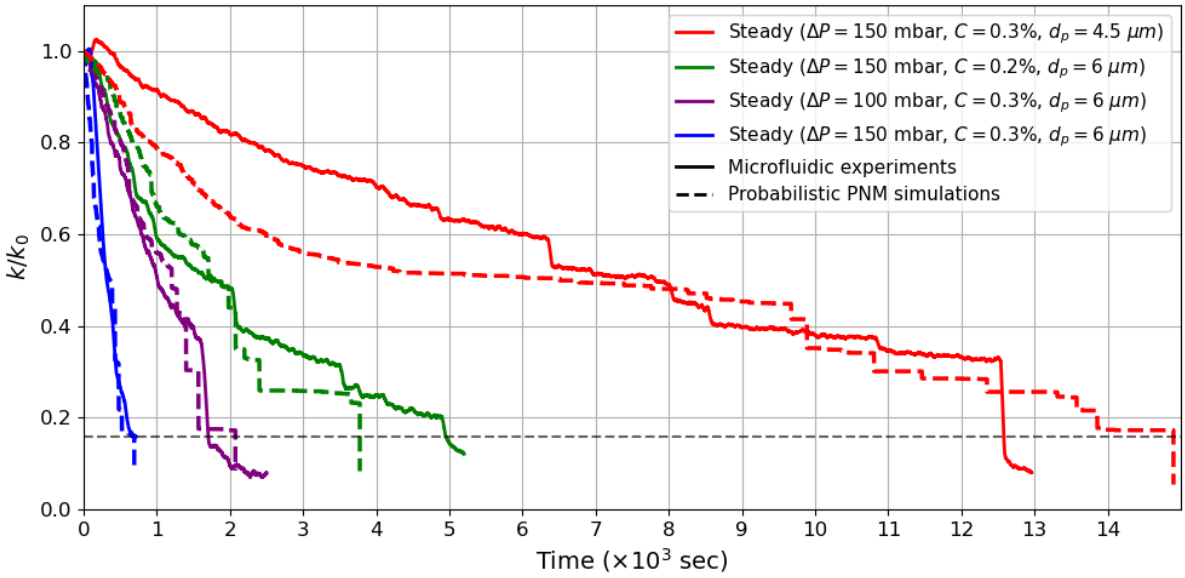

Figure E: Évolution de l'altération de la perméabilité pour les différentes conditions, obtenue par simulations PNM (ligne pointillée) et par expériences microfluidiques (ligne continue).

Effets du forçage oscillatoire sur le colmatage, dépendants du régime.

Pour examiner comment une excitation variable dans le temps modifie le colmatage dans les milieux poreux hétérogènes, nous avons comparé l'injection continue et l'injection sinusoïdale sous pression dans le modèle microfluidique hétérogène M3, sous trois conditions de salinité (100 mM, 1 mM et 0 mM NaCl) et deux fréquences d'excitation (0,01 et 0,1 Hz), chaque condition étant répétée deux fois pour évaluer la reproductibilité. Comme le montre la Figure F, la réponse dépend fortement du régime physico-chimique. Dans des conditions de salinité tamisée, où le dépôt assisté par agrégation est favorisé, l'excitation oscillatoire retarde la rupture hydraulique et augmente le volume injecté au moment du colmatage par rapport à l'injection continue Γ. Le dépôt reste orienté vers l'entrée, mais son étendue en aval augmente sous l'effet de l'excitation oscillatoire. Cet effet de fréquence est marqué à 100 mM, où une fréquence de 0,1 Hz induit une

zone de dépôt plus étendue qu'une fréquence de 0,01 Hz, et plus faible à 1 mM, où une fréquence de 0,01 Hz provoque une extension légèrement plus importante en aval. En revanche, en l'absence de sel, où la répulsion électrostatique inhibe l'agrégation et où le colmatage est principalement dû à la formation de ponts mécaniques sous confinement, la réponse en fréquence s'inverse : une excitation à basse fréquence retarde toujours le colmatage, tandis qu'une excitation à haute fréquence l'accélère. Parallèlement, les profils de dépôt finaux restent majoritairement contrôlés par l'entrée et ne présentent pas de différence qualitative nette entre les deux fréquences.

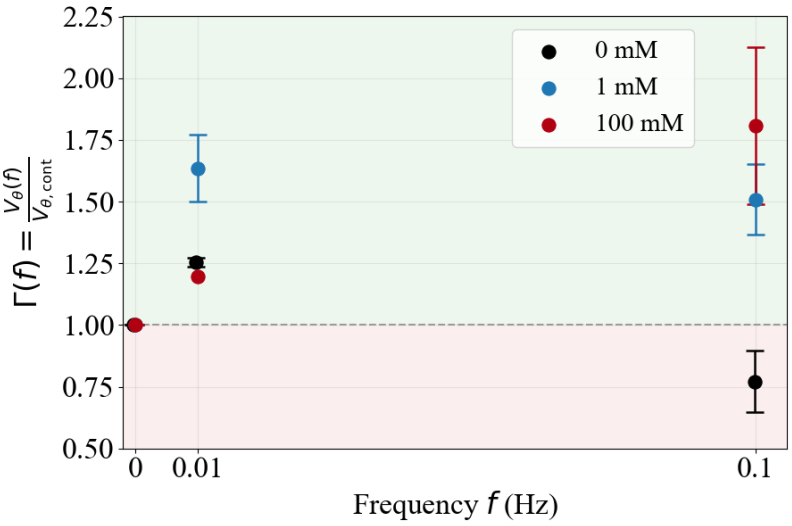

Figure F: Facteur d'atténuation $\Gamma(f) = V_\theta(f)/V_{\theta,\mathrm{cont}}$ en fonction de la fréquence d'oscillation pour 0 mM, 1 mM et 100 mM. La ligne pointillée indique $\Gamma = 1$ (injection continue) ; les zones vert clair indiquent une atténuation ($\Gamma > 1$) et les zones rouge clair indiquent une accélération ($\Gamma < 1$). Les oscillations augmentent le transport à 1 mM et 100 mM pour les deux fréquences, tandis que dans le cas de 0 mM, on observe une inversion de régime, passant d'une atténuation à $0,01$ Hz à une accélération à $0,1$ Hz. Le point de référence d'injection continue à $\Gamma = 1$ pour 100 mM est légèrement décalé horizontalement à des fins de visualisation uniquement, afin d'éviter tout chevauchement avec les points correspondants pour 0 mM et 1 mM dans les mêmes conditions de référence. Les barres d'erreur indiquent la variabilité entre les répétitions.

Conclusions et perspectives

L'objectif de cette thèse était d'améliorer la compréhension du transport colloïdal et du colmatage dans les milieux poreux en étudiant les mécanismes à l'échelle des pores qui régissent l'accumulation des particules et la formation de structures de colmatage dans les réseaux poreux hétérogènes. Plus largement, ce travail était motivé par la nécessité de mieux comprendre comment la rétention des particules modifie les voies d'écoulement locales, réduit progressivement la perméabilité et l'injectivité, et affecte finalement le comportement des systèmes souterrains liés à la contamination des eaux souterraines, à la filtration et aux applications énergétiques. Pour ce faire, la thèse s'est appuyée sur des milieux poreux microfluidiques hétérogènes permettant la visualisation directe du transport, du dépôt et du colmatage des particules dans des conditions hydrodynamiques et physico-chimiques contrôlées.

Les résultats montrent que la réduction de la perméabilité dans les milieux poreux hétérogènes peut résulter de mécanismes d'obstruction distincts, selon le régime de dépôt dominant. En

conditions où les mécanismes d'adhésion sont dominants, cette étude a démontré que le dépôt par agrégation peut produire des structures dendritiques se développant à partir d'un site de dépôt préférentiel unique et conduisant progressivement à l'obstruction des pores, ce qui constitue un nouveau mécanisme d'obstruction progressive dans les milieux poreux hétérogènes. En conditions hydrodynamiques prédominantes, les résultats indiquent que la réduction de la perméabilité est régie par le pontage hydrodynamique des pores, la taille et la concentration des particules exerçant une influence plus importante sur la dynamique d'obstruction que la différence de pression imposée. De plus, l'étude de la forçage dépendant du temps a montré que l'injection oscillatoire ne peut être considérée comme une stratégie d'atténuation universelle : en conditions contrôlées, elle retarde l'obstruction, tandis qu'en conditions répulsives, son effet devient dépendant de la fréquence et peut même accélérer le blocage à des fréquences relativement élevées.

Ces résultats soulignent que la prédiction et le contrôle du colmatage dans les milieux poreux nécessitent l'identification du mécanisme dominant à l'échelle des pores, dans les conditions physico-chimiques et hydrodynamiques pertinentes, et sa corrélation avec l'évolution de la perméabilité qui en résulte.

Au-delà des écoulements monophasiques, l'étude du rôle de la redirection d'écoulement induite par le colmatage dans les systèmes multiphasiques contenant des fluides non miscibles piégés offre une perspective prometteuse. Les expériences préliminaires diphasiques menées dans le cadre de ce travail ont montré que les micromodèles en PDMS ne conviennent pas à cet effet, car l'absorption d'huile par la matrice de PDMS empêche l'obtention de conditions stables d'huile piégée. En revanche, les micromodèles en verre constituent une base plus fiable pour de telles expériences.

L'extension de ce cadre d'étude aux micromodèles en verre hétérogènes, ainsi qu'aux suspensions polydisperses, aux particules non sphériques, aux systèmes fracturés et aux milieux poreux tridimensionnels, représenterait une avancée majeure pour une meilleure compréhension du colmatage, de la redistribution des écoulements et de leurs implications pour la gestion de l'injectivité et la mobilisation des contaminants dans des environnements souterrains réalistes.

Contents

List of figures **xiv**

List of tables **xxv**

1 Introduction **1**
1.1 The subsurface as a critical resource . . . 1
1.2 Threats to groundwater quality . . . 2
1.2.1 Chemical contaminants . . . 2
1.2.2 Physical contaminants . . . 3
1.3 Subsurface systems in the energy transition and climate change . . . 4
1.3.1 Geothermal energy . . . 5
1.3.2 Underground thermal energy storage . . . 5
1.4 Operational challenges in injection-based systems . . . 6
1.5 Open challenges . . . 7
1.6 Objectives and structure of the thesis . . . 8

2 Theoretical elements of colloidal transport in porous media **9**
2.1 Colloidal particles in porous media systems . . . 9
2.2 Notion of scales . . . 10
2.2.1 Molecular scale . . . 11
2.2.2 Particle/colloid scale . . . 11
2.2.3 Pore scale . . . 11
2.2.4 Core scale . . . 12
2.2.5 Field scale . . . 12
2.3 Governing fluid flow equations at the pore scale . . . 12
2.3.1 From the Navier–Stokes equation to the Stokes equation . . . 12
2.3.2 Flow in Hele–Shaw cells . . . 13
2.4 Particle transport mechanisms . . . 14
2.4.1 Transport regimes . . . 14
2.4.2 Dimensionless numbers governing transport . . . 14
2.5 Force balance at the particle scale . . . 15
2.5.1 Hydrodynamic forces . . . 15
2.5.2 Electrochemical forces . . . 16
2.5.3 Mechanical forces . . . 18
2.6 Macroscopic description of flow in porous media . . . 19
2.7 Continuum framework for colloidal transport and deposition . . . 19

3 State of the art: particle transport, deposition and clogging in porous media 21
3.1 Pore-scale particle deposition and clogging mechanisms . . . 21
3.1.1 Sieving . . . 22
3.1.2 Bridging . . . 22
3.1.3 Progressive clogging / Aggregation . . . 23
3.1.4 Interplay of pore-scale clogging mechanisms . . . 27
3.2 Factors influencing particle deposition and clogging in porous media . . . 28
3.2.1 Fluid chemistry . . . 28
3.2.2 Properties of suspended particles . . . 33
3.2.3 Flow rate and injection protocols . . . 36
3.2.4 Influence of porous geometry and surface properties . . . 39
3.3 Techniques to investigate particle deposition and clogging in porous media . . . 41
3.3.1 Numerical approaches . . . 42
3.3.2 Experimental approaches . . . 43
3.4 Research gaps and scientific questions . . . 45
3.5 Research strategy and thesis organization . . . 46

4 Materials and Methods 49
4.1 Design and fabrication of microfluidic porous models . . . 49
4.1.1 Geometric definition of the designed porous configurations . . . 49
4.1.2 Photolithographic fabrication of the master wafer . . . 51
4.1.3 Microfluidic devices in PDMS . . . 52
4.2 Particle suspensions: composition and key properties . . . 53
4.3 Experimental apparatus . . . 54
4.4 Image analysis . . . 55
4.4.1 Image acquisition workflow . . . 55
4.4.2 Image-based porosity evaluation . . . 56
4.4.3 Spatial distribution of particle deposition along the porous domain . . . 56
4.5 Hydraulic characterization of the microfluidic devices . . . 58
4.5.1 Identification of the linear hydraulic regime and PDMS deformation threshold 58
4.5.2 Apparent permeability estimation . . . 59
4.6 Pore-scale simulation for post-processing microfluidic results . . . 60
4.6.1 Simulation strategy: Darcy–Brinkman–Stokes approach . . . 60
4.6.2 From microfluidic images to simulation . . . 61
4.6.3 Outcomes of the simulations: Flow-field visualization and impact of clogging 61

5 Progressive colloidal clogging mechanism by dendritic build-up in porous media 63
5.1 Introduction . . . 63
5.2 Materials and Methods . . . 65
5.2.1 PDMS microfluidic devices . . . 65
5.2.2 Particle suspension . . . 66
5.2.3 Flow experiments and imaging . . . 66
5.2.4 Critical velocity for particle-surface and particle-particle detachment . . . 66
5.2.5 Post-processing using computational microfluidics . . . 69
5.3 Results and Discussion . . . 69
5.3.1 Experimental evidence of dendrite clogging . . . 69
5.3.2 Conditions for dendrite formation . . . 70
5.3.3 Impact on porous media properties . . . 74
5.4 Conclusions . . . 78

6 Permeability impairment by hydrodynamic pore bridging: Probabilistic pore-network modeling and microfluidic experiments 81
6.1 Introduction . . . 81
6.2 Materials and Methods . . . 84
6.2.1 Heterogeneous porous geometry . . . 84
6.2.2 Flow experiments and image analysis . . . 84
6.2.3 Pore-network model with probability of bridging . . . 85
6.3 Results and discussion . . . 89
6.3.1 Permeability damage of hydrodynamic pore-bridging via microfluidics . . . 89
6.3.2 Permeability impairment in PNM with probabilistic bridging law . . . 93
6.4 Conclusions . . . 95

7 From clogging mitigation to clogging acceleration: particle deposition under oscillatory flow in microfluidic porous media 97
7.1 Introduction . . . 97
7.2 Materials and Methods . . . 99
7.2.1 PDMS microfluidic devices . . . 99
7.2.2 Particle suspensions . . . 100
7.2.3 Oscillatory flow generation and monitoring . . . 100
7.2.4 Flow experiments . . . 102
7.2.5 Image acquisition and deposition analysis . . . 102
7.3 Results and Discussion . . . 103
7.3.1 Baseline clogging under continuous injection . . . 103
7.3.2 Mitigation under oscillatory forcing in screened conditions . . . 104
7.3.3 Frequency-driven regime inversion in salt-free conditions . . . 106
7.4 Conclusions . . . 111

8 Two-phase microfluidic experiments toward investigating clogging-induced mobilization of trapped oil 113
8.1 Introduction . . . 113
8.2 Materials and Methods . . . 115
8.2.1 PDMS microfluidic device geometry . . . 115
8.2.2 Surface treatment and wettability control . . . 115
8.2.3 Non-wetting fluids . . . 115
8.2.4 Flow experiments . . . 115
8.3 Results and discussion . . . 116
8.3.1 Silicone oil uptake into PDMS prevents stable trapped-oil conditions . . . 117
8.3.2 Attempted mitigation of PDMS oil uptake using alternative oils . . . 117
8.3.3 Establishing stable trapped oil conditions in hydrophilic glass EOR micromodels . . . 118
8.4 Conclusions . . . 120

9 General conclusions and perspectives 121
9.1 Conclusions . . . 121
9.2 Perspectives . . . 122

A Appendix 125
A.1 DLVO parameters and corresponding interaction profiles . . . 125
A.2 MATLAB scripts . . . 126
A.2.1 Watershed-Based pore size distribution analysis . . . 126

A.2.2 CSD (Constriction size distribution) 130
A.3 Complete mask layouts 132
A.4 Dendrite clogging at multiple locations within the porous domain 132
A.5 Movies of the experiments 132

Bibliography **136**

List of Figures

1.1 Various manmade discharges and leachates contributing to groundwater contamination [Foster et al., 2003]. 2
1.2 Chart representing the percentages of various types of chemical contaminants impacting soil and groundwater in Europe [European Environment Agency, 2009]. 3
1.3 Schematic illustrating subsurface utilization to achieve decarbonization goals for net-zero carbon dioxide emissions. Decarbonization applications include nuclear waste storage (GDF-Geological Disposal Facility); Carbon Capture and Storage (CCS); geothermal heat and energy utilization (deep Enhanced/Engineered Geothermal Systems (EGS), hydrothermal systems, and shallow (<120 m) geothermal heat pumps); Underground Thermal Energy Storage (ATES, Aquifer Thermal Energy Storage; PTES, Pit Thermal Energy Storage; BTES, Borehole Thermal Energy Storage; MTES, Mine Thermal Energy Storage); Hydrogen storage in caverns and aquifers; and Compressed Air Energy Storage in Caverns (CAESC) and Aquifers (CAESA) [Kaminskaite et al., 2022]. 4
1.4 Schematic of an enhanced geothermal system (EGS). Cold water is injected into the subsurface through an injection well, circulates through the fractured hot-rock reservoir, and is then recovered as hot water through a production well for heat exchange and power generation at the surface. The inset provides a magnified view of the porous medium near the wells, where suspended particles can be transported, retained, and accumulated, leading to physical clogging, permeability reduction, and injectivity decline. Adapted from Cong et al. [2024] and Cui et al. [2022]. . . 6
1.5 Relative contribution of different clogging mechanisms, highlighting the dominant role of particle-induced clogging compared to chemical, biological, and other clogging processes [Song et al., 2020]. 7

2.1 Size ranges of particles transported in groundwater [De Zwart, 2007] 10
2.2 (a) Scanning Electron Microscopy (SEM) and (b) Transmission Electron Microscopy (TEM) images of colloidal particles showing irregular particle shapes obtained from groundwater [Ha and Lee, 2025]. 10
2.3 Schematic representation of the different length scales in porous media, ranging from the molecular scale to the field scale. 11
2.4 Schematic representation of the electrochemical double layer at the solid-liquid interface, including the Stern layer, diffuse layer, and bulk solution (surface potential Ψ and zeta potential ζ) [Anton Paar, n.d.]. 17
2.5 Schematic illustration of a typical DLVO interaction profile combining van der Waals attraction and electrostatic double-layer repulsion. Depending on the balance between these contributions, the total interaction potential may exhibit a secondary minimum (reversible attachment) or a primary minimum after overcoming the energy barrier (irreversible attachment) [Fogouang et al., 2024]. 18

3.1 Mechanisms of pore-clogging by particles: (a) Sieving, (b) Bridging, and (c) Progressive clogging [Dressaire and Sauret, 2017b] 21

3.2 Sieving of spherical particles in cylindrical pore throats (a) and slit-shaped pore geometries (b) [Warkiani et al., 2015]. (c) Confocal image of a microsieve grid (blue) with particles larger than the pore throats (red) and particles smaller than the pore throats (green) [Brans et al., 2007a]. 22

3.3 Examples of clogging by bridging or arch formation. (a) Flow and clogging by bridging of a neutrally buoyant suspension of polymethyl methacrylate (PMMA) particles in an axisymmetric tapered glass capillary [Dressaire and Sauret, 2017b]. (b) Arch formation by 48 μm particles in a capillary tube with a 150 μm inner diameter [Sharp and Adrian, 2005]. (c) Bridging-induced clogging by 200 nm sulfate polystyrene particles (white) in track-etched membrane pores (black) of typical size around 1 μm [Ramachandran and Fogler, 1999]. 23

3.4 Progressive aggregation of particles resulting in clog formation. (a–e) The density-matched suspension of polystyrene particles ($D_p = 3$ μm) with sulfate charge groups flows through a constriction of width $W = 15.5$ μm. The images are recorded at 3, 5, 10, and 36 minutes, with a flux of 2.8×10^4 particles per minute at the onset of the experiment [Dersoir et al., 2015b]. (f–h) Schematic representation of the aggregation process, from the deposition of the first particle to the clog formation [Dressaire and Sauret, 2017b]. 24

3.5 Schematic illustration of dynamic shadowing during particle deposition onto a surface. Panel (a) shows the flow field around the collector, with the dashed axis connecting the upstream and downstream stagnation points. Panel (b) provides a side view of the highlighted region, where tangential flow and the associated shadowing effect are strongest at 90° from the upstream stagnation point. Panel (c) illustrates the shadow region that develops downstream of a deposited particle. Adapted from Ko and Elimelech [2000]. 25

3.6 Examples of multilayer deposit morphologies observed under different flow and ionic strengths. (a) Deposition patterns on a single-grain collector at different Péclet numbers. Adapted from Kusaka et al. [2010]. (b) Dendrite formation at the entrance of a microfluidic filter (top) and effect of flow direction on dendrite orientation (bottom) [Agbangla et al., 2012a]. (c) Phase diagram of deposition morphologies around an obstacle as a function of ionic strength and Péclet number [de Saint Vincent et al., 2016]. 26

3.7 A schematic representation of the torques acting on a particle of diameter d_p in the vicinity of a surface or a previously deposited particle. 27

3.8 Schematic illustration of coupled clogging mechanisms in porous media. Flowing particles (black) may deposit on grain surfaces (red), progressively reducing the available flow area within constrictions. This promotes the emergence of multiple mechanisms, including sieving (green), bridging (blue), and aggregation (yellow), which can act simultaneously and lead to pore blockage. Adapted from Chauveteau et al. [1998]. 28

3.9 (a) Schematic illustration of well impairment caused by the injection of low-quality water containing suspended particles, showing deep-bed filtration within the porous formation and external filter cake formation under radial flow. (b) Progressive transition from deep-bed filtration to external filter cake formation as deposits accumulate toward the inlet in a one-dimensional porous medium. Adapted from Tale et al. [2021]. 29

3.10 Effect of ionic strength on particle deposition and attachment in porous media. (a) Deposition rate coefficient of carboxylated polystyrene particles under saturated and unsaturated conditions as a function of NaCl concentration [Sang et al., 2013]. (b) Attachment efficiency of latex particles of different sizes as a function of ionic strength (KCl) [Pelley and Tufenkji, 2008]. 29
3.11 Effect of ionic strength on particle deposition and interaction energy. (a) Deposition patterns of 4.1 µm latex particles on glass beads at different KCl ionic strengths, with flow from right to left. (b) DLVO interaction energy profiles between latex particles and glass beads, showing a high repulsive barrier at low ionic strength (1 mM) and its disappearance at high ionic strength (100 mM). Adapted from Kuznar and Elimelech [2007a]. 30
3.12 Confocal microscopy images of latex particle deposition (red) in the pore space between glass beads (black) at the entrance of a porous medium, for different ionic strengths and times. The flow is directed upwards. Adapted from Gerber et al. [2019]. 31
3.13 Effect of ionic strength on particle deposition in a 2D microfluidic array. (a) No particle deposition after 90 min of dead-end filtration with latex suspensions in ultra-pure water ($I = 0$ mM). (b) Formation of upstream multilayer deposits (dendrites) after 90 min at high ionic strength (100 mM KCl) under identical flow conditions. Flow is directed from top to bottom, and each channel has a width of 20 µm. Adapted from Agbangla et al. [2012b]. 31
3.14 Effect of pH on surface charge, interaction energy, and particle retention in porous media. (a) Zeta potential of polystyrene particles as a function of pH. (b) Zeta potential of soda-lime glass beads as a function of pH. (c) Interaction energy profiles of polystyrene nanoparticles at different pH values, showing attractive interactions at low pH. (d) Normalized UV absorbance as a function of time for different pH conditions, illustrating stronger particle retention at low pH due to enhanced aggregation and deposition. Adapted from Sadri et al. [2017]. 32
3.15 Heating causes a decline in the permeability of the Berea sandstone sample, and this reduction is reversible when the temperature is returned to its initial value. Adapted from Rosenbrand et al. [2015]. 33
3.16 (a) Videomicroscopic images of 0.93 µm polystyrene particles captured with a 10× objective under an imposed temperature gradient of 6846.9 K/m at 0, 20, 40, and 60 min; particles are visible as black dots. (b) Evolution of the number of deposited particles per unit area with time for four different temperature gradients: 78.9, 2136.5, 5516.1, and 6846.9 K/m. Adapted from Yan et al. [2020]. 34
3.17 Effect of particle size and surface functionality on attachment efficiency in a quartz-grain column. (a) Attachment efficiency of carboxyl-functionalized particles of different sizes as a function of ionic strength, showing higher attachment for larger particles. (b) Attachment efficiency of particles with different surface functionalities as a function of ionic strength, showing that hematite particles exhibit higher attachment efficiency than larger sulfate latex particles. Adapted from Litton and Olson [1996]. 34
3.18 Effect of particle size, ionic strength, and flow velocity on the permeability recovery rate R. Larger particles are associated with lower recovery rates across the range of tested ionic strengths and flow velocities [Bennacer et al., 2017]. 35
3.19 Evolution of the normalized permeability K/K_0 as a function of injected pore volumes NV_p for increasing particle concentrations under constant flow conditions [Alem et al., 2015]. Higher concentrations result in a faster permeability decline. 35

3.20 Experimental conditions leading to clogging in a dead-end microfluidic filtration system by injecting latex particles suspended in deionized water. The diagram maps the occurrence of clogging after 90 min of injection as a function of particle volume fraction and average flow velocity. Filled diamonds indicate conditions for which clogging was observed, whereas open circles correspond to conditions where no clogging occurred [Agbangla et al., 2012b]. 36

3.21 Breakthrough curves showing the retention of 1.1 µm latex colloids in quartz sand at an ionic strength of 56 mM for grain sizes of (a) 360 µm, (b) 240 µm, and (c) 150 µm. For each grain size, higher flow rates, ranging from approximately 0.1 to 0.45 cm/min, are associated with lower particle retention. Adapted from Bradford et al. [2007]. 37

3.22 Concentration breakthrough curves showing particle retention at an ionic strength of 6 mM for flow rates of 0.1 cm/min in (a) and 0.45 cm/min in (b). The case $d_c/d_{50} = 0.008$ in (a) is comparable to the 360-Data case in (b), indicating greater particle retention at the higher flow rate. Adapted from Bradford et al. [2007]. . . 37

3.23 Dominant mechanisms observed during backwashing: (a) partial cluster breakage and (b) cluster migration toward low-drag regions. Top panels show the corresponding numerical simulation results for increasing reverse-flow intensity, while bottom panels show the microfluidic experiments for increasing reverse-flow velocity, from 0.1 μL/s to 6.7 μL/s. The scale bar represents 20 μm. Adapted from Lohaus et al. [2020]. 38

3.24 Effect of oscillatory flow on clogging mitigation in a two-dimensional microfluidic channel array, adapted from Dincau et al. [2022]. (a) Evolution of the flow rate with time for different oscillation amplitudes, showing that an amplitude of 50% of the initial pressure drop provides the most effective mitigation compared with steady flow, whereas an amplitude of 125% gives a response close to the continuous-flow case. (b) Evolution of the flow rate with time for different oscillation frequencies at a fixed amplitude of 50%, showing that 0.1 Hz yields the strongest mitigation, while 0.001 Hz remains close to the steady-flow case. 39

3.25 Effect of collector surface roughness on particle deposition and collision efficiency, adapted from Auset and Keller [2006]. Microscopic images compare particle deposition in micromodels composed of smooth collectors (a) and rough collectors (b), with hand-drawn streamlines illustrating the particle trajectories around collectors. Panel (c) shows the collision efficiency as a function of ionic strength for 3 µm and 4 µm particles flowing through smooth and rough micromodels. For both particle sizes and across the investigated ionic strengths, rough collectors exhibit higher collision efficiencies than smooth collectors, indicating enhanced particle–surface interactions in the presence of surface roughness. 40

3.26 Breakthrough curves of colloidal particles in a sand column with varying degrees of surface chemical heterogeneity. The percentage indicates the fraction of iron oxyhydroxide-coated sand grains, which provide favorable sites for particle deposition. Increasing the fraction of coated grains leads to a progressive reduction in breakthrough concentration, demonstrating enhanced particle retention due to surface charge heterogeneity [Johnson et al., 1996] 41

3.27 Effect of porous structure on particle deposition and clogging, adapted from Bacchin et al. [2014]. Images correspond to the final stage of filtration in microfluidic devices with (a) straight and disconnected channels, (b) connected channels, and (c) staggered (tortuous) channels. Increasing connectivity and tortuosity leads to more heterogeneous flow fields, promoting localized deposition, particle accumulation, and the development of internal clogging. 41

3.28 Examples of regular and irregular two-dimensional porous geometries used in microfluidic micromodels: (a) pore body–throat network [Meybodi et al., 2011], (b) regular pillar array [Grate et al., 2012], (c) cross-hatched grid [Osei-Bonsu et al., 2017], (d) irregular pattern representing a thin section of real rock [Gauteplass et al., 2015], and (e) irregular interconnected channels [Soudmand-asli et al., 2007]. Reproduced from Anbari et al. [2018]. 45

4.1 Schematic of the single-grain-collector microfluidic geometry ($M1$). A 500 µm-wide inlet channel converges to a 100 µm-wide throat containing a centered cylindrical collector (grain), followed by a diverging section returning to 500 µm. 50

4.2 Two microfluidic porous micromodels used in this study, referred to throughout the thesis as M2 and M3, and their geometric characterization. Panels (a) and (b) show the full chip layouts of M2 and M3, respectively, where black denotes the solid matrix and white the pore space. Each device consists of an inlet manifold and an outlet manifold (11.5 mm each) connected by a central porous region (12 mm), for an overall footprint of 36 mm × 6 mm. The zoomed views highlight the disordered grain packing within the porous region. The histograms on the right show the pore-diameter and constriction-width distributions obtained from the 2D image analysis, with log-normal fits shown as solid red curves. In M2, the pore-diameter distribution peaks around ~ 60 μm (mean ~ 97 μm), and the constriction widths peak near ~ 19 μm (mean ~ 45 μm). In M3, pores are overall smaller (mode ~ 50 μm; mean ~ 73 μm), and the constrictions are substantially tighter, with the distribution clearly shifted toward smaller widths (mode ~ 5 μm; mean ~ 20 μm). 52

4.3 Step-by-step schematic of the microfabrication workflow. The master wafer is produced by patterning SU-8 photoresist on a silicon wafer using standard photolithography with the predefined microfeatures. The resulting reusable negative mold is then used for soft lithography: PDMS is cast, cured, and demolded to obtain the patterned replica, which is finally bonded to a substrate (glass slide) to form the microfluidic device used in the experiments. 53

4.4 (a) Consecutive time-averaged images highlighting deposited particles (black), with pore space and solid grains appearing in varying shades of gray. (b) Reconstructed 2D view of the entire porous domain obtained by stitching the images in (a). (c) Segmented image distinguishing deposited particles (black), pore space (gray), and solid grains (white). (d) Binary image isolating deposited particles (white), used to quantify pore-space reduction and porosity evolution. 57

4.5 Grayscale pixel intensity histograms from representative images used to determine the particle detection threshold. A value of 30 (dashed line) reliably separates deposited particles from pore space and solid grains. 58

4.6 Flow-rate response to increasing imposed pressure in the PDMS microfluidic device $M3$. The flow rate scales linearly with pressure up to ~ 250 mbar (negligible PDMS deformation); beyond this onset, deviations from linearity indicate PDMS deformation. 59

4.7 Representation of the porous medium on a Cartesian grid. Blue corresponds to open pore space ($\phi = 1$ and $K^{-1} = 0$ m^{-2}), while red and white corresponds to solid grains and particle deposits respectively ($\phi = 0.01$ and $K^{-1} = 1 \times 10^{15}$ m^{-2}). 61

4.8 (a) Original binary image of the entire porous domain, with solid grains shown in white and the pore space in black. (b) Segmented binary image of deposited particles only, isolated from the experimental images and shown in white. (c) Combined binary image of the deposited particles from (b) superimposed on the initial porous structure in (a), representing the experimentally modified binary image of the porous domain. (d) Simulation result for fluid flow using the initial domain (free of particles), indicating the basic distribution of streamlines with velocities between 0 and 0.02 m/s. (e) Fluid flow simulation on the modified domain with deposited particles, showing how clogging affects fluid flow patterns, with redirection and regions of increased velocity magnitude. 62

5.1 Schematic of the microfluidic setup. A syringe pump drives the particle suspension through the microfluidic device, in which pressure sensors monitor the pressure drop (ΔP) across the porous medium. The outlet flow is collected in a vial. An inverted microscope equipped with a high-speed FASTEC camera captures real-time imaging of particle deposition and clogging dynamics. Some elements were created with BioRender.com. 68

5.2 Averaged images from experiments conducted at two flow rates, (a) 8 µL/min and (b) 20 µL/min, capturing a section of the porous domain at different pore volumes and highlighting distinct clogging mechanisms. In (a), multiple clogging regions emerge, with a particular focus on the progressive development of dendritic clogging. An initial dendrite forms after 435 PVs (highlighted in a red dotted box), extending upstream by 1225 PVs. By 1664 PVs, the dendrite tip advances further toward the adjacent grain (annotated in the magnified side image), eventually leading to complete pore clogging as the structure continues to grow, constricting the local flow pathway. In (b), multiple clogging events occur, but no dendrite formation or dendrite-induced clogging is observed in the same region, even after injecting 2348 PVs. 71

5.3 Streamlines extracted from fluid flow simulations at an 8 µL/min flow rate, showing particle deposits in black and grains in white. (a) Flow field at the beginning of the experiment, illustrating the initial streamline configuration. (b) Flow field after 2225 PVs of particle suspension injection, where dendritic structures (circled in yellow) are seen growing into the pore space. These deposits progressively distort the surrounding streamlines. The red-dotted box highlights a region where dendrite-induced clogging causes a complete redirection of particle flow, contrasting with the initial pattern in (a). Additional clogging mechanisms throughout the domain are also observed to contribute to local flow redirection. 72

5.4 (a) Images captured after 2500 PVs under 100 mM salt concentration, illustrating the different deposition patterns achieved on a single-grain collector geometry at flow rates ranging from 1 µL/min to 10 µL/min. At 1 µL/min, particles progressively build up at the upstream stagnation region of the collector surface, forming a dendrite. At 5 µL/min, a monolayer of depositions forms with no particle−particle attachment observed. At 10 µL/min, no deposits are observed at the upstream stagnation region; instead, particles decelerate in this region, roll along the collector surface, and attach at the rear stagnation region. (b) Simulated fluid velocity fields normalized by the critical velocity for particle–particle detachment (V_x^f/V_x^c(p-p)). The simulations include both the collector and an explicit monolayer of deposited particles. At 1 µL/min, the upstream stagnation region is wide enough to accommodate an additional particle, promoting multilayer buildup. As the flow rate increases, this region compresses and becomes too narrow to support further deposition, explaining the absence of dendrites at higher flow rates. 73

5.5 Fluid flow velocity profiles obtained by simulations and normalized by the critical velocity for particle-particle detachment ($V_x^f/V_x^c\,(p-p)$) at flow rates of 8 µL/min (a) and 20 µL/min (b). (a) The magnified image shows a stagnation region that accommodates approximately 1.5 particle diameters. The adjacent image overlays the experimental deposition pattern onto the normalized velocity profile, highlighting dendrite formation and build-up in the front stagnation regions. The progression of dendrite growth leading to clogging is shown in the magnified image. (b) The magnified image shows a stagnation region that accommodates only 0.5 particle diameters. The adjacent image shows the superimposition of the experimental deposition pattern on the normalized velocity profile, illustrating the absence of dendrites in the front stagnation regions within the porous domain. This emphasizes the critical role of stagnation region size in initiating dendrite growth, as the region is too small to accommodate a single particle diameter. . . 75

5.6 The normalized pressure drop ($\Delta P/\Delta P_0$) across the porous domain after injecting multiple pore volumes (PVs) is shown for two flow rates, Q = 8 µL/min and Q = 20 µL/min. In both experiments, $\Delta P/\Delta P_0$ builds up due to particle deposition and clogging, with consistently higher values at Q = 8 µL/min. During the first 800 PVs, the pressure difference rises rapidly before gradually stabilizing between 1400 PVs and 2400 PVs in both cases. 76

5.7 The permeability-porosity relationships ($K(\Phi)$) describing the experimental observations for the two flow rates Q = 8 µL/min (blue) and Q = 20 µL/min (red) are shown along with their corresponding fitting curves. These curves accurately capture the experimental trends using the Nonlinear Least Squares method with a robust bisquare weighting, achieving R-squared values of 0.995 and 0.982 for Q = 8 µL/min and Q = 20 µL/min, respectively. The data for Q = 8 µL/min clearly shows a steeper permeability decline, with an exponent $\tau = 3.75$, compared to $\tau = 1.32$ for Q = 20 µL/min. This indicates a more pronounced particle deposition and clogging effect at lower flow rates. An inset shows the same data on a log–log scale, confirming the power-law behavior through the linearity of the trend in logarithmic coordinates. 77

6.1 Schematic of the experimental setup used for flow experiments. A pressure controller drives the injection of particle suspension from a reservoir through tubing equipped with a one-way valve, which facilitates fluid switching without introducing air bubbles. The flow enters the microfluidic device mounted on an inverted microscope platform, where image sequences are recorded over time using a high-speed camera. A flow rate sensor positioned downstream continuously monitors the decline in flow rate due to pore clogging. The fluid then exits into a disposal vial. 86

6.2 Time-lapse images of the base configuration in the first section of the porous domain, showing how particle deposition progressively develops over time until the domain becomes fully clogged. The insets show a constant magnified view of a selected region highlighted by a yellow arrow, indicating a constriction where particles gradually accumulate over time until the pore is completely blocked after 660 seconds. 90

6.3 Time-lapse averaged stitched experimental images of the porous domain under different experimental conditions, with each condition distinguished by a separate color. The corresponding plot shows the normalized particle deposition fraction from the final stitched images, highlighted by dotted boxes, as a function of position along the x-direction for each experimental condition. 92

6.4 Evolution of permeability impairment over time for the different experimental conditions, each represented by a different color. The light black horizontal line indicates the 85% decline in initial permeability, while the vertical lines in corresponding colors mark the time at which each experiment reaches this threshold, indicating the onset of complete particle clogging. 93

6.5 Snapshots of pore clogging obtained by probabilistic pore-network modeling for the baseline case. The throats in red are clogged. $t_1 = 0$s, $t_2 = 50$s, $t_3 = 100$s, and $t_4 = 700$s. 94

6.6 Evolution of permeability impairment for the different conditions, each represented by a different color, obtained with PNM simulations (dashed line) and microfluidic experiments (plain line). 95

7.1 (a) Schematic of the oscillatory-flow experiments. The microfluidic device layout is shown on the left, with a magnified view of the heterogeneous porous domain highlighted below. A pressure controller applies a programmed pressure waveform at frequency f by pressurizing a sealed inlet reservoir, thereby driving flow through the microfluidic chip (pressure path in blue; flow path in green). The resulting volumetric flow rate $Q(t)$ is measured downstream using a flow sensor. The chip is mounted on an inverted microscope for real-time imaging. (b) Flow-rate preprocessing and normalization procedure. Raw flow-rate signals (light curves) are smoothed using a rolling mean (thick curves). The reference flow rate Q_0 is computed at t_0 over the initial smoothing window (50 s for continuous and 0.1 Hz; 100 s for 0.01 Hz), and the signal is normalized to obtain Q/Q_0. 101

7.2 Injectivity decline under continuous forcing at different ionic strengths. Top: Normalized flow rate Q/Q_0 versus time for 0 mM (black), 1 mM (blue), and 100 mM (red). For each salinity, two independent replicates ($n = 2$) are shown as faint lines together with their mean (thick line). The horizontal dashed line marks the clogging threshold $Q/Q_0 = \theta = 0.17$, and vertical dashed lines indicate the corresponding threshold times t_θ. Bottom: Cumulative injected volume $V(t) = \int_0^t Q(t)\,\mathrm{d}t$; markers indicate $V_\theta = V(t_\theta)$. Increasing ionic strength accelerates injectivity decline and reduces V_θ. 104

7.3 Streamwise deposition profiles at t_θ for different ionic strengths. Deposited particles are shown in black (pore space and grains in light grey). One representative stitched image is displayed for each salinity, whereas deposition profiles are obtained from two independent replicates ($n = 2$) and plotted as replicate-mean-averaged curves. Deposition is inlet-biased for all salinities, with downstream extent increasing as ionic strength decreases (0 mM > 1 mM > 100 mM). 105

7.4 Injectivity decline (a) and injected volume at the clogging threshold (V_θ) (b) for 100 mM under continuous injection (red) and oscillatory forcing at $f = 0.01$ Hz (purple) and $f = 0.1$ Hz (orange). The green-shaded region denotes the mitigation regime, where V_θ for both frequencies exceeds the continuous reference. (c) Streamwise deposition profiles for continuous and oscillatory forcing. For all forcing conditions, deposition is strongly inlet-biased and decreases downstream along the porous domain. Relative to continuous injection, sinusoidal forcing increases downstream deposition coverage. Although local profile reversals may appear near the outlet, oscillatory forcing overall increases the downstream deposition extent compared to continuous injection. 107

7.5 Injectivity decline (a) and injected volume at the clogging threshold (V_θ) (b) for 1 mM under continuous injection (blue) and oscillatory forcing at $f = 0.01$ Hz (purple) and $f = 0.1$ Hz (orange). The V_θ for the two frequencies fall in the mitigation regime, where it exceeds the continuous reference. (c) Streamwise deposition profiles under continuous and oscillatory forcing. For all conditions, deposition remains strongly inlet-biased and decreases downstream along the porous domain. Relative to continuous injection, sinusoidal forcing increases the downstream deposition coverage with a slightly higher deposition footprint at 0.01 Hz than at 0.1 Hz. 108

7.6 Mitigation factor $\Gamma(f) = V_\theta(f)/V_{\theta,\mathrm{cont}}$ versus oscillation frequency for 0 mM, 1 mM, and 100 mM. The dashed line marks $\Gamma = 1$ (continuous injection); shaded regions indicate mitigation ($\Gamma > 1$) and acceleration ($\Gamma < 1$). Oscillations enhance transport at 1 mM and 100 mM for both frequencies, whereas the 0 mM case shows a regime inversion from mitigation at 0.01 Hz to acceleration at 0.1 Hz. The continuous-injection reference point at $\Gamma = 1$ for 100 mM is slightly shifted horizontally for visualization purposes only, to avoid overlap with the corresponding points for 0 mM and 1 mM at the same reference condition. Error bars denote variability across repetitions. 109

7.7 Injectivity decline (a) and injected volume at the clogging threshold (V_θ) (b) for 0 mM under continuous injection (black) and oscillatory forcing at $f = 0.01$ Hz (purple) and $f = 0.1$ Hz (orange). The $f = 0.01$ Hz condition falls in the mitigation regime (V_θ exceeding the continuous reference), whereas $f = 0.1$ Hz falls in the clogging-acceleration regime (red-shaded region). (c) Streamwise deposition profiles under continuous and oscillatory forcing. For all conditions, deposition remains strongly inlet-biased and decreases downstream along the porous domain. No clear qualitative distinction between forcing protocols emerges, as the profiles partially overlap and intersect along several regions of the domain. 110

8.1 Schematic illustration of the mobilization of a trapped immiscible droplet (air or oil) in a porous medium in the presence of colloidal particles. (a) Colloidal particles (red) are transported by the flowing water past a trapped droplet. (b) Particle accumulation clogs a neighboring pore, increasing local flow resistance and viscous stresses. (c,d) The induced flow redistribution enhances hydrodynamic forces on the droplet, resulting in its deformation and eventual mobilization. Courtesy of Cyprien Soulaine. 114
8.2 Schematic of the flow-rate–controlled two-phase microfluidic experimental setup with differential pressure sensing. CO_2 is injected to displace residual air before introducing the wetting and non-wetting fluids. Two syringe pumps supply the fluids and are selected via a valve network upstream of the microfluidic chip. The pressure drop across the porous domain is measured using upstream and downstream pressure sensors along the main flow path. The chip is mounted on an inverted microscope for real-time imaging with a FASTEC high-speed camera, and the effluent is collected downstream in a disposal vial. 116
8.3 Real-time snapshots during waterflooding in a PDMS porous micromodel initially containing silicone oil. The images show the distribution of non-wetting fluid (light grey), dyed wetting fluid (dark grey), and grains (light grey). The dyed wetting phase invades the pore space while silicone oil progressively disappears, even though no connected pathway is available for oil to exit the field of view, consistent with oil uptake (infusion) into the PDMS matrix. Times indicate elapsed time since the start of recording. 117
8.4 Pressure difference ΔP versus injected pore volumes during waterflooding at $Q = 10$ µL/min in a PDMS porous micromodel initially containing paraffin oil. After an initial transient, ΔP decreases monotonically and approaches the reference value corresponding to the fully water-saturated micromodel (red line), indicating a progressive transition toward full wetting-phase saturation. 118
8.5 Pressure difference ΔP versus injected pore volumes during waterflooding at $Q = 5$ µL/min in a PDMS porous micromodel initially containing fluorinated oil. ΔP decreases gradually but remains above the fully water-saturated reference value (red line) and does not reach a clear plateau within the explored range, indicating that residual oil persists while the system continues to evolve. 119
8.6 Pressure difference ΔP versus injected pore volumes during waterflooding at $Q = 10$ μL/min in a glass heterogeneous EOR micromodel (Micronit) initially containing silicone oil. After an initial transient, ΔP drops abruptly due to the mobilization of trapped oil in the chip and then reaches a plateau, from nearly 180 injected pore volumes until the end of the experiment at around 2300 pore volumes. This plateau, which remains above the red line representing full wetting-phase saturation, suggests the presence of residual trapped oil in the micromodel. . . . 119
8.7 Microscopic images of a specific region in the Micronit glass microchip (EOR chip) during the waterflooding process after injecting different pore volumes. The images show the distribution of non-wetting fluid (light grey), dyed wetting fluid (dark grey), and grains (light grey). The images at 800 PVs and 1600 PVs indicate similar fluid distributions, confirming the establishment of steady trapped oil conditions. 120

A.1 DLVO profiles for particle-particle and particle-surface interactions as a function of separation distance (h) in nanometers (nm). 125
A.2 Complete mask layout containing 19 replicas of the single-grain collector design ($M1$), where the gray regions represent the solid matrix (grains) and the white regions correspond to the pore space. The overall mask diameter is 10.5 cm. . . 133

A.3 Complete mask layout showing 8 replicas of the heterogeneous tortuous porous-domain designs (4 of $M2$ and 4 of $M3$). $M2$ and $M3$ differ in their internal pore-space statistics. Gray regions correspond to the solid matrix (grains), while white regions indicate the pore space. The mask diameter is 10.5 cm. 134
A.4 Averaged experimental images at a flow rate of 8 µL/min, showing the progressive formation of a dendritic clog in a specific region of the porous domain over successive pore volumes of particle injection (PVs). 135
A.5 Averaged experimental images at a flow rate of 8 µL/min, illustrating dendritic clogging in two distinct regions of the porous domain: (a) after 2370 pore volumes (PVs) of particle injection and (b) after 2261 PVs. 135

List of Tables

3.1 Comparison of the main clogging mechanisms observed in porous media, adapted from Dressaire and Sauret [2017b]. 27
3.2 Comparison of numerical approaches for modeling particle transport and clogging in porous media. 43

4.1 Geometric and hydraulic characterization of the three microfluidic models, where K_{app} is the apparent permeability, CSD is the constriction size distribution, and PSD is the pore size distribution. 50
4.2 Properties of the particles used in the experiments. 54

5.1 Parameters for fluid properties, particle characteristics, surface properties, and force calculations in the experimental and simulation setup. The annotations p and s refer to the particle and surface collector, respectively 67
5.2 Ratios of simulated fluid velocity (V_x^f) to the critical detachment velocity for particle-collector surface attachment ($V_x^c\,(p-s)$) and particle-particle attachment ($V_x^c\,(p-p)$) at a separation distance of one particle radius, across flow rates ranging from 1 µL/min to 10 µL/min 74

6.1 Cases investigated using microfluidic experiments and pore-network modeling. . . 89

7.1 Clogging metrics at threshold ($Q/Q_0 = \theta = 0.17$) for different salinity and forcing conditions. 105

8.1 Types and properties of the non-wetting oils used in the two-phase experiments (20 °C). 115

A.1 Parameters and their corresponding values used in the DLVO interaction potential approximations. The annotations p, m, and s refer to the particle, medium, and PDMS surface. 126

Chapter 1

Introduction

This chapter provides the scientific and environmental context motivating the present work (section 1.1). We first discuss groundwater contamination and the different types of contaminants that may affect subsurface environments (section 1.2). The chapter then introduces subsurface systems used in the energy transition, including geothermal energy and underground thermal energy storage (section 1.3). Next, we discuss the operational challenges associated with fluid injection in porous formations, with particular attention to injectivity decline and clogging (section 1.5). Finally, we present the open challenges addressed in this thesis (section 1.5), followed by the objectives and the structure of the study (section 1.6).

1.1 The subsurface as a critical resource

Earth contains the largest quantities of water in the solar system, with vast areas of its surface covered by oceans, rivers, and lakes [Ryecroft et al., 2019]. Yet more than 95% of the world's available freshwater—excluding glaciers and ice caps—lies hidden beneath the Earth's surface as groundwater [Morris et al., 2003]. This underground water is crucial for sustaining baseflow to rivers and wetlands, which are vital to ecosystems, and it is estimated to supply drinking water for nearly one-third of the world's population [Li et al., 2021a]. Protecting the quality and availability of groundwater is therefore a major priority for water management authorities worldwide.

Over recent decades, reliance on groundwater resources has increased considerably due to global warming, rising evaporation rates, and growing demands from agriculture, industry, and expanding urban populations [Megdal, 2018, Omran et al., 2019]. With an increase in surface water insecurity because of climate change, groundwater has become a cornerstone for socio-economic development.

Groundwater has become a target of anthropogenic activities, and a wide range of contaminants, including oil residues, microplastics, and various inorganic compounds, have been found even in well-conserved aquifers [Lapworth et al., 2015, Li et al., 2014]. These contaminants can migrate through subsurface pathways, posing risks to ecosystems and human health.

Beyond these water-quality concerns, the subsurface has become a target of exploitation for a wide range of industrial and energy applications. Technologies such as groundwater recharge, geothermal energy production, and subsurface storage operations require the injection and circulation of fluids through porous geological formations, and their performance depends on maintaining fluid pathways within the pore space.

Understanding how substances—including suspended particles and contaminants—are transported through porous geological media is therefore essential for ensuring the long-term sustainability of subsurface resources and predicting the potential fate of contaminants.

1.2 Threats to groundwater quality

Groundwater contamination occurs when pollutants released by surface or subsurface human activities (Fig. 1.1) exceed the natural attenuation capacity of the soil [Foster et al., 2003]. As shown in Fig. 1.1, human activities generate various sources of contamination, leading to different types of contaminants such as brines, metals, chemicals, microbes, fertilizers, pharmaceutical residues, microplastics, and petroleum products. Groundwater contaminants can be broadly classified into chemical contaminants, which include dissolved species and non-aqueous phase liquids (NAPLs), physical contaminants such as suspended particles, and biological contaminants such as microorganisms. In the following, the focus is placed on chemical and physical contaminants.

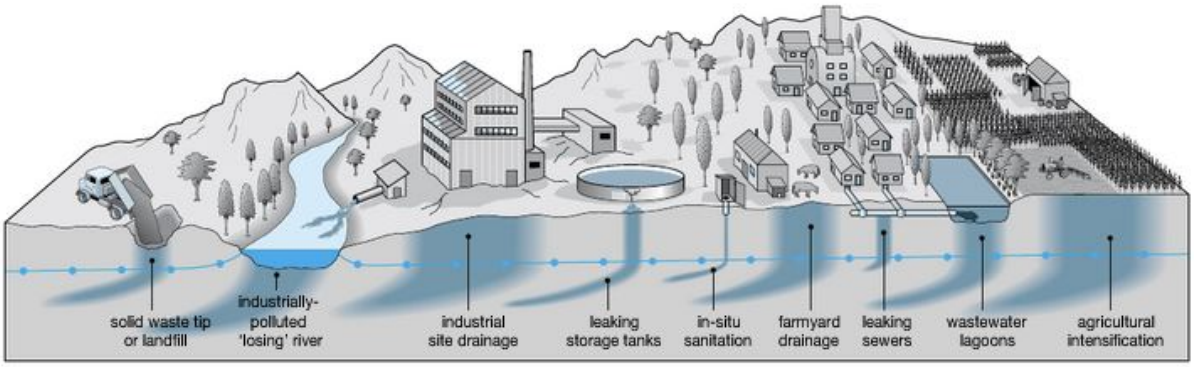

Figure 1.1: Various manmade discharges and leachates contributing to groundwater contamination [Foster et al., 2003].

1.2.1 Chemical contaminants

Chemical contaminants include substances that interact with water through dissolution or molecular dispersion. Chemical contaminants can be categorized as either inorganic or organic compounds. In the case of groundwater systems, the most frequently occurring contaminants include inorganic compounds such as heavy metals, as well as petroleum hydrocarbons, aromatic hydrocarbons, phenolic compounds, and chlorinated solvents, as depicted in Fig. 1.2. Organic contaminants are more predominant in the case of groundwater systems owing to the increasing use of these substances in different industrial processes. These include petroleum products, solvents, and different chemicals.

Many organic contaminants enter the subsurface in the form of nonaqueous phase liquids (NAPLs), which are organic liquids that are poorly soluble in water. NAPLs can be introduced into the subsurface through accidental spills, pipeline ruptures, leaking underground storage tanks, or failures in well integrity [Jackson, 2014]. Once released, these liquids migrate through the porous structure of soils and sediments under the influence of gravity, capillary forces, and pressure gradients. Over time, groundwater flowing through contaminated pores can dissolve some constituents of the NAPL phase, allowing dissolved contaminants to spread away from the source zone and form contamination plumes within aquifers. Since NAPLs can persist in the subsurface for decades, they may act as long-term sources of contamination. This persistence makes groundwater contamination particularly difficult to remediate and highlights the importance of understanding transport processes in porous media.

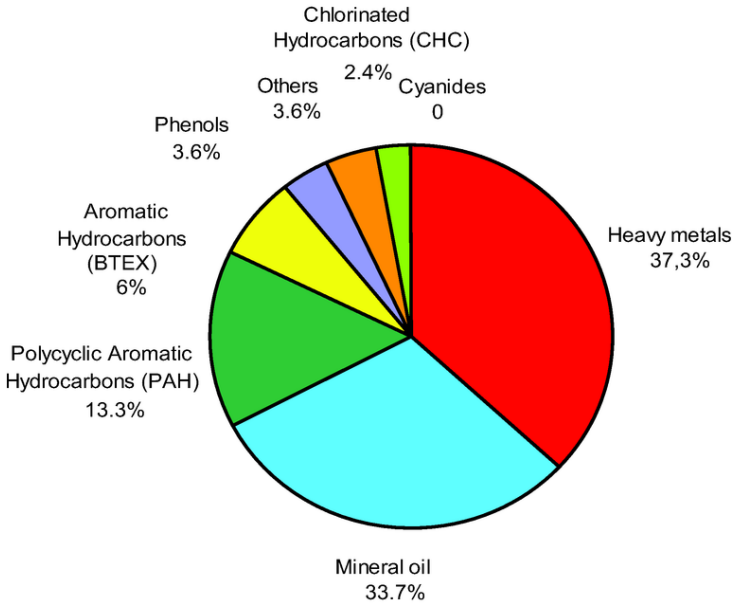

Figure 1.2: Chart representing the percentages of various types of chemical contaminants impacting soil and groundwater in Europe [European Environment Agency, 2009].

1.2.2 Physical contaminants

In addition to dissolved chemical pollutants, groundwater systems can also be affected by physical contaminants in the form of suspended particles. Unlike dissolved substances, these particles do not dissolve in water but are transported within the flowing fluid, allowing them to migrate through aquatic and subsurface environments.

Among the various types of particulate pollutants, plastic debris has emerged as a major environmental concern. Due to the widespread use of plastics since the twentieth century, large quantities of plastic waste have accumulated in natural environments, where it gradually fragments into smaller particles known as microplastics. Microplastics are generally defined as plastic particles smaller than 5 mm and can originate from industrial processes, textile fibers, cosmetic products, or the breakdown of larger plastic objects through mechanical abrasion, ultraviolet radiation, and other environmental processes [Bajt, 2021, Browne et al., 2011, Fendall and Sewell, 2009, Da Costa et al., 2018].

While most studies have focused on the presence of microplastics in oceans and surface waters, increasing evidence suggests that these particles can also reach subsurface environments. Microplastics may enter soils and groundwater through several pathways, including wastewater treatment plant effluents, the application of biosolids to agricultural soils, and leakage from septic systems or seepage tanks [Rillig, 2012, Re, 2019]. Although research on microplastics in groundwater remains limited, recent studies have reported the presence of plastic fragments and fibers in groundwater samples [Kumar and Sharma, 2021]. Beyond their direct environmental impact, microplastics are also capable of adsorbing both organic and inorganic contaminants, thereby acting as carriers that facilitate the transport of hazardous substances through aquatic systems [Połeć et al., 2018].

Understanding how such particles move within subsurface environments is therefore essential for assessing groundwater vulnerability and developing effective mitigation strategies. More broadly, the transport and retention of suspended particles within porous geological formations play a central role in determining how physical contaminants migrate through groundwater systems.

1.3 Subsurface systems in the energy transition and climate change

The subsurface has long been exploited for water and mineral resources, but in recent decades, it has also become an important component of the energy transition and climate change. Deep geological formations can provide renewable heat through geothermal systems and can also serve as large-scale storage reservoirs for carbon dioxide (CO_2) and hydrogen (H_2) (Fig. 1.3). In addition, subsurface formations can be used for thermal energy storage, where heat is injected underground and recovered later when needed. These applications rely on the injection and circulation of fluids through porous rocks, making subsurface flow processes central to both performance and long-term sustainability.

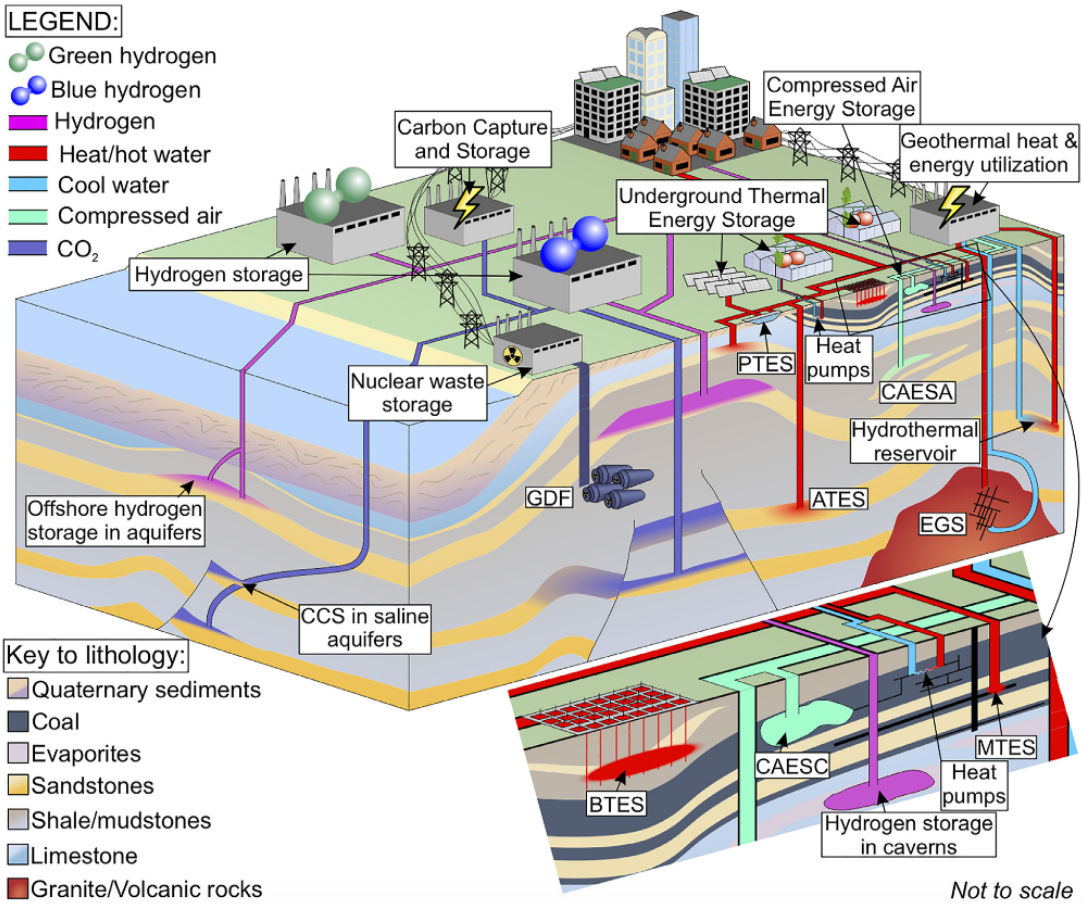

Figure 1.3: Schematic illustrating subsurface utilization to achieve decarbonization goals for net-zero carbon dioxide emissions. Decarbonization applications include nuclear waste storage (GDF-Geological Disposal Facility); Carbon Capture and Storage (CCS); geothermal heat and energy utilization (deep Enhanced/Engineered Geothermal Systems (EGS), hydrothermal systems, and shallow (<120 m) geothermal heat pumps); Underground Thermal Energy Storage (ATES, Aquifer Thermal Energy Storage; PTES, Pit Thermal Energy Storage; BTES, Borehole Thermal Energy Storage; MTES, Mine Thermal Energy Storage); Hydrogen storage in caverns and aquifers; and Compressed Air Energy Storage in Caverns (CAESC) and Aquifers (CAESA) [Kaminskaite et al., 2022].

1.3.1 Geothermal energy

A geothermal system can be described as the circulation of fluids within permeable rocks that transfer heat between a subsurface heat source and the surrounding environment. Such systems typically consist of three main components: a heat source, a permeable reservoir, and a fluid—most commonly water—that acts as the carrier of heat. The heat source may originate from magmatic intrusions or from the natural geothermal gradient of the Earth, while the reservoir provides the porous pathways through which fluids circulate and exchange heat. Heat transfer within geothermal reservoirs is largely governed by convective circulation, where heated fluids of lower density rise while cooler fluids descend, establishing a continuous flow within the system.

To harness geothermal energy, wells are drilled into the geothermal reservoir to establish hydraulic communication between the surface and the subsurface formation. In most geothermal systems, at least two wells are used: a production well that brings heated fluids to the surface and an injection well that reinjects cooled fluids back into the reservoir. This reinjection helps maintain reservoir pressure and supports long-term geothermal production. The amount of thermal energy that can be produced depends on both the temperature of the reservoir and the achievable flow rate of the circulating fluid. Outside volcanic regions, the average geothermal temperature gradient is approximately 30 °C per kilometer of depth [Goldstein et al., 2013], meaning that deeper reservoirs generally provide higher temperatures and greater energy potential.

At relatively shallow depths, groundwater temperatures typically range between about 10 °C and 20 °C, allowing geothermal heat to be used through ground-source heat pump systems for space heating and domestic hot water supply. These systems commonly operate in vertical boreholes with depths ranging from approximately 50 m to 250 m. At greater depths, where reservoir temperatures often exceed 150 °C, geothermal fluids may produce high-temperature water or steam capable of driving turbines to generate electricity in geothermal power plants [Dickson and Fanelli, 2013]. In addition to electricity generation, geothermal heat can also be used directly for various industrial processes or district heating applications.

The performance of geothermal systems, therefore, depends not only on reservoir temperature but also on the ability to maintain sufficient fluid circulation through the formation, making injectivity a key operational parameter.

1.3.2 Underground thermal energy storage

Underground thermal energy storage (UTES) uses soil, rock, or groundwater as a storage medium for heat or cold. In practice, excess thermal energy produced during warm seasons or from renewable energy sources is injected into the subsurface by circulating a heat-transfer fluid through buried pipes or wells, and is later recovered when needed through the reverse circulation of the fluid [Fleuchaus et al., 2018].

Several types of UTES systems have been designed based on different geological media used for storing energy. In borehole thermal energy storage (BTES), heat energy is stored in rock or soil using a cluster of vertical boreholes containing heat exchangers. In addition, aquifer thermal energy storage (ATES) systems use a natural medium to store heat, in which water is pumped from and reinjected into aquifers to store and recover thermal energy. Finally, cavern or pit thermal energy storage systems use a large amount of water stored in an underground pit for energy storage. In these systems, heat energy is stored in a large amount of water stored in an underground pit.

The efficiency of underground thermal energy storage systems, therefore, depends on maintaining fluid circulation within the subsurface formation during repeated injection and recovery cycles.

1.4 Operational challenges in injection-based systems

Many subsurface technologies rely on the injection and circulation of fluids through porous geological formations. A key operational challenge in such systems is maintaining sufficient injectivity, defined as the ability of the formation to accept and transmit injected fluids over time.

In groundwater remediation, pump-and-treat systems have been widely used since the 1980s to mitigate the impact of dissolved contaminants on groundwater quality [Cohen, 1994]. In these systems, contaminated groundwater is extracted through pumping wells, treated at the surface to remove pollutants, and subsequently discharged or reinjected. However, their efficiency is often limited by subsurface heterogeneities, contaminant sorption onto solid surfaces, and diffusion into low-permeability zones, which can slow remediation and leave persistent contamination [Council et al., 2005]. In addition, high operational costs and slow contaminant removal rates further limit their effectiveness [Mackay et al., 1985, McKinney and Lin, 1996]. These limitations have motivated the exploration of alternative remediation strategies, including the subsurface injection of colloidal particles to enhance contaminant degradation or mobilization.

Beyond groundwater remediation, related limitations also arise in subsurface energy systems. Despite its potential, geothermal energy accounted for only 0.34 % of global renewable power generation (including hydropower) by the end of 2024 [International Renewable Energy Agency, 2025]. Its limited deployment reflects a combination of technical, economic, and socio-political barriers. Among the most significant challenges are the high cost of drilling, the management of geothermal fluids that may contain harmful chemical species, and the progressive decline in well injectivity during operation (Fig. 1.4), all of which constrain the long-term performance of geothermal projects [Manzella et al., 2019].

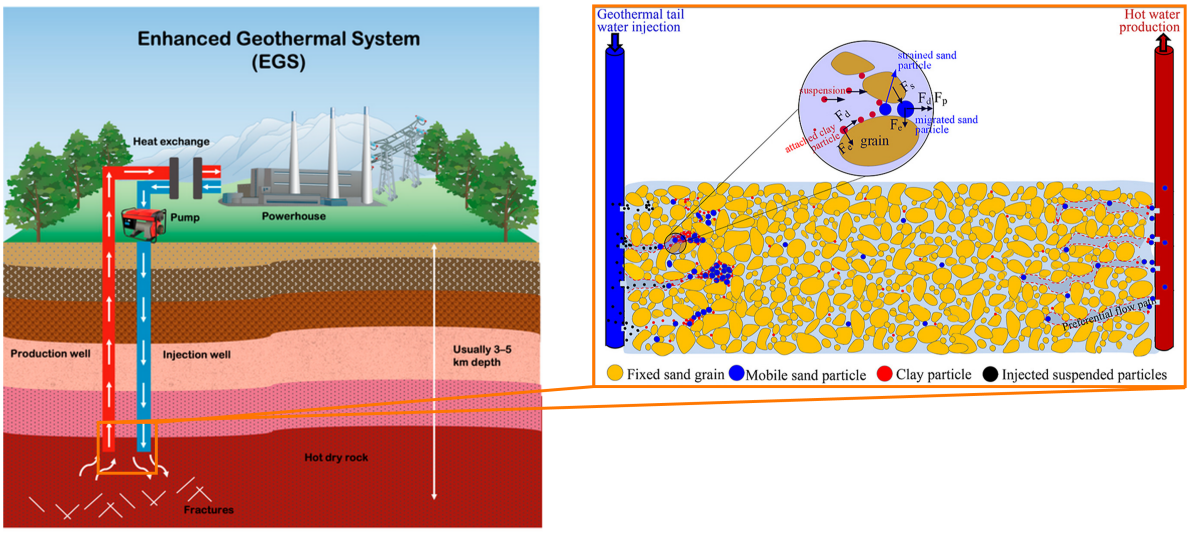

Figure 1.4: Schematic of an enhanced geothermal system (EGS). Cold water is injected into the subsurface through an injection well, circulates through the fractured hot-rock reservoir, and is then recovered as hot water through a production well for heat exchange and power generation at the surface. The inset provides a magnified view of the porous medium near the wells, where suspended particles can be transported, retained, and accumulated, leading to physical clogging, permeability reduction, and injectivity decline. Adapted from Cong et al. [2024] and Cui et al. [2022].

Injectivity impairment has long been recognized as a major operational challenge in oil and gas reservoirs [Civan, 2023] and has increasingly been reported in geothermal reservoirs

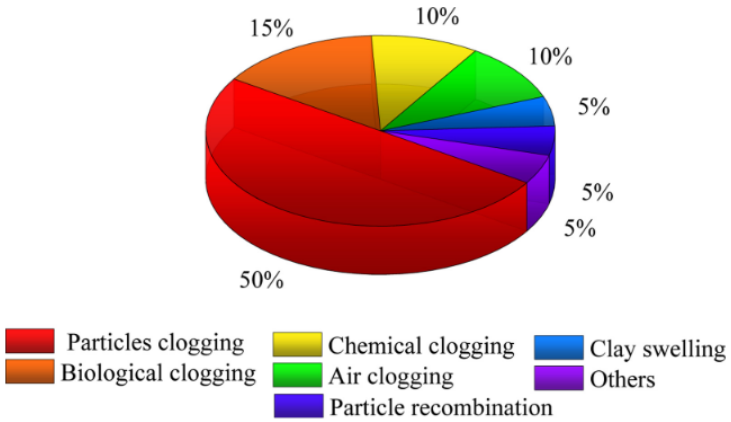

Figure 1.5: Relative contribution of different clogging mechanisms, highlighting the dominant role of particle-induced clogging compared to chemical, biological, and other clogging processes [Song et al., 2020].

and aquifer thermal energy storage systems [Martin, 2013, Schreiber et al., 2016]. In these systems, the injection of water that differs from the native groundwater in temperature or chemical composition may disturb the physico-chemical equilibrium of the reservoir and promote permeability impairment.

One of the most critical challenges associated with injectivity decline is pore clogging. Depending on the origin of the clogging substance, clogging mechanisms are commonly classified into physical, chemical, and biological processes, as illustrated in Fig. 1.5 [Song et al., 2020]. Interactions between the injected fluid, the native groundwater, and the porous medium can alter the pore structure, reduce permeability, shorten the operational lifetime of the system, and ultimately lead to severe injectivity decline [Liu et al., 2017].

Taken together, these examples highlight the importance of particle and colloidal transport in a wide range of subsurface applications. Understanding how particles move through porous media is essential for developing particle-based remediation strategies, predicting the migration of pollutants such as microplastics, and explaining clogging processes that reduce injectivity in subsurface energy systems. In this thesis, particular attention is given to *physical clogging* caused by the transport and deposition of particles (Fig. 1.5), as particle-induced clogging often represents a major contribution to clogging in such systems.

1.5 Open challenges

Understanding colloidal transport in porous media remains challenging because it involves coupled processes across multiple spatial scales and because the underlying mechanisms are difficult to observe directly in opaque porous media.

Multi-scale complexity Colloidal transport in porous media involves processes acting over several spatial scales. At the molecular scale, the behavior of fluids and solid surfaces is governed by intermolecular forces between atoms and molecules. At the pore scale, particle transport, deposition, and clogging are governed by the combined effects of flow, pore geometry, and physicochemical interactions within individual pores. At larger scales, these pore-scale processes are no longer resolved explicitly, and the porous medium is instead described through averaged properties such as porosity and permeability. Since macroscopic behavior ultimately emerges

from mechanisms occurring at smaller scales, a deeper understanding of transport and retention mechanisms at these scales is essential before averaging up to larger-scale descriptions.

Difficulties in visualizing underlying processes Natural porous media are typically opaque, which strongly limits direct observation of the processes governing colloidal transport and contaminant mobilization. Although techniques such as X-ray microtomography have provided valuable information on the spatial distribution of particles and fluids, they remain limited in resolving the detailed dynamics involved. A deeper understanding, therefore, requires experimental approaches that allow direct visualization of particle transport, deposition, and clogging processes within porous structures.

1.6 Objectives and structure of the thesis

The objective of this thesis is to improve the understanding of colloidal transport and clogging in porous media by investigating the pore-scale mechanisms that govern particle accumulation and the formation of clogging structures. Particular attention is given to how these particle retention processes modify local flow pathways and progressively reduce permeability and injectivity in porous networks.

Beyond clarifying the mechanisms responsible for clogging, this thesis also examines how clogging dynamics evolve under varying hydrodynamic and physicochemical conditions and whether these dynamics can be modulated to delay permeability loss. Building on this mechanistic understanding, the thesis finally outlines a broader perspective on the potential role of clogging-induced flow alterations in the mobilization of trapped contaminants in porous formations.

The manuscript is organized as follows. Chapter 2 introduces the theoretical framework used to describe colloidal transport and deposition in porous media. Chapter 3 presents the state of the art on the main mechanisms and parameters governing deposition and clogging, and identifies the main research gaps, scientific questions, and research strategy addressed in this work. The following chapters present the investigations conducted to address these questions, focusing on the identification of clogging mechanisms, their impact on permeability, and the role of flow conditions in modulating these processes.

Chapter 2

Theoretical elements of colloidal transport in porous media

This chapter introduces the physical framework used to describe particle-laden flows in porous media. We begin by introducing colloidal particles and their relevance in subsurface systems, along with the main properties that govern their behavior. We then present the different spatial scales involved in porous media and highlight the importance of a multiscale description to link pore-scale processes to macroscopic behavior. The governing equations of fluid flow and the associated flow regimes are then introduced, emphasizing the predominance of viscous effects under the conditions considered. Next, we describe the main mechanisms controlling particle transport, and introduce the dimensionless numbers commonly used to characterize these processes. Finally, we discuss the combined role of hydrodynamic and physicochemical interactions as particles approach solid surfaces, providing the basis for interpreting particle deposition, attachment, and detachment, as well as the resulting clogging and permeability reduction observed in the experiments. The chapter concludes with a macroscopic description of flow, linking pore-scale processes to permeability evolution in porous media.

2.1 Colloidal particles in porous media systems

Colloidal particles are ubiquitous in natural porous media, and their presence in groundwater systems is well documented across many subsurface engineering applications. Particles present in subsurface environments may originate from several mechanisms. A major source in groundwater systems is the mobilization of pre-existing colloids and fine mineral particles from the porous matrix under changing chemical or physical conditions [Ryan and Elimelech, 1996]. In addition, particles may also be generated by the physical fragmentation of host rocks in contact with groundwater [Degueldre et al., 1996]. Another important source arises when groundwater and the surrounding rock are not in chemical equilibrium, leading to mineral dissolution and subsequent precipitation until equilibrium is re-established [Stumm, 1982]. Their transport and deposition within pore networks can progressively lead to injectivity decline.

Colloidal dispersions generally refer to systems containing particles with characteristic sizes ranging from approximately 10 nm to 1 µm [McNaught et al., 1997]. At larger sizes, typically from 1 to 100 µm, the dispersed phase is more commonly described as suspended particles (Fig. 2.1) [De Zwart, 2007]. The transition between colloidal particles and suspended particles therefore lies roughly in the range of 1 to 10 µm. The dominant forces governing particle behavior depend strongly on particle size. Particles larger than about 10 µm are mainly governed by hydrodynamic forces, whereas particles smaller than about 1 µm are more strongly influenced by physicochemical interactions. The particles considered in this thesis lie within the intermediate micrometric range,

where transport and deposition result from a balance between hydrodynamic and physicochemical effects.

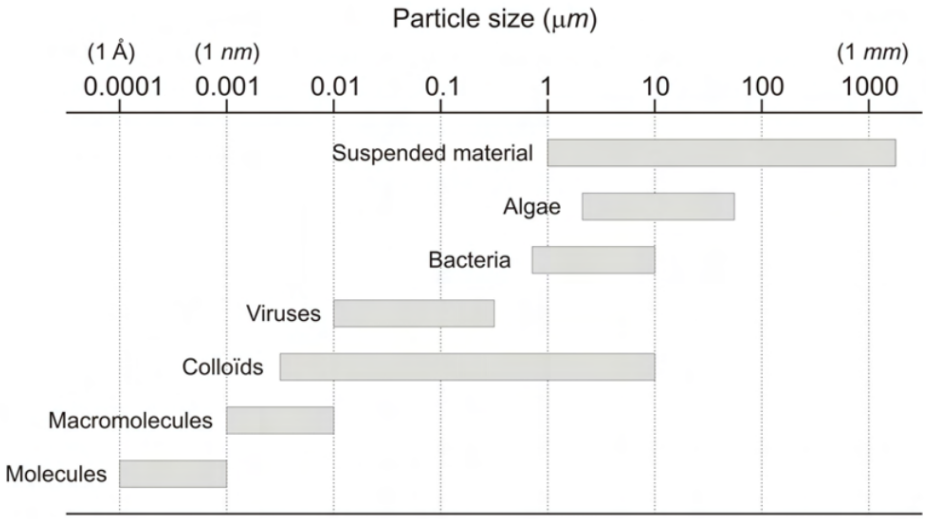

Figure 2.1: Size ranges of particles transported in groundwater [De Zwart, 2007]

In laboratory studies, artificial particles are often used as model materials to investigate particle transport in porous media under controlled conditions. These particles are commonly made of spherical polystyrene or silica, although natural particles generally exhibit more irregular shapes, as illustrated in Fig. 2.2.

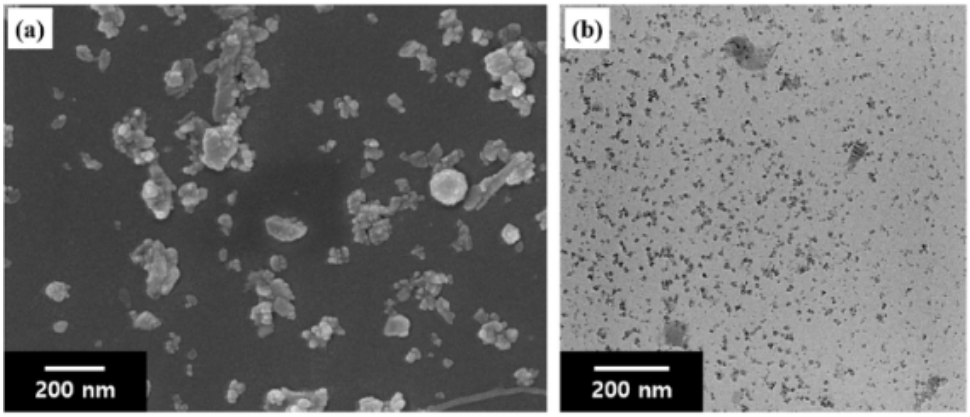

Figure 2.2: (a) Scanning Electron Microscopy (SEM) and (b) Transmission Electron Microscopy (TEM) images of colloidal particles showing irregular particle shapes obtained from groundwater [Ha and Lee, 2025].

2.2 Notion of scales

Porous media can be studied over a wide range of spatial scales, from the molecular scale to the field scale (Fig. 2.3). The governing physics and mathematical descriptions of flow and particle transport vary with the scale considered and the degree of resolution used to represent the porous structure. A conventional way to analyze these systems is to adopt a multiscale framework, in which small-scale processes are progressively averaged through homogenization or upscaling

techniques to describe larger-scale behavior. In addition to these structural scales of porous media, the transport of colloidal particles also involves the particle or colloid scale, which lies between molecular and pore scales and controls the interaction forces governing particle motion and deposition.

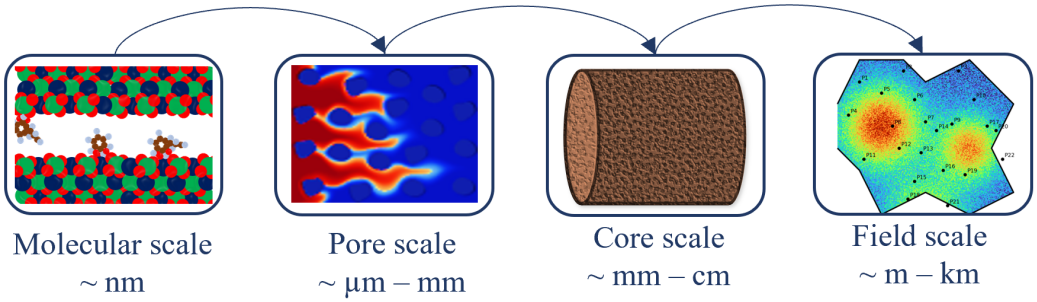

Figure 2.3: Schematic representation of the different length scales in porous media, ranging from the molecular scale to the field scale.

2.2.1 Molecular scale

The molecular scale corresponds to the scale at which individual atoms and molecules interact. Characteristic lengths at this scale typically range from fractions of a nanometer to a few nanometers. At this level, the behavior of fluids and solid surfaces is governed by intermolecular forces acting between atoms and molecules. The molecular scale is commonly investigated using molecular dynamics simulations, in which the trajectories of atoms and molecules are computed by solving Newton's equations of motion under the influence of interaction potentials.

2.2.2 Particle/colloid scale

The particle or colloid scale corresponds to the length scale of individual particles, typically ranging from a few nanometers to several micrometers. At this scale, the behavior of particles is governed by intermolecular and surface forces acting between particles, the fluid, and the solid surfaces of the porous medium.

2.2.3 Pore scale

The pore scale refers to the spatial scale at which the individual voids and solid grains forming the porous medium are explicitly resolved. Its characteristic length is set by the pore or throat size, typically ranging from micrometers to millimeters, depending on the material. At this scale, the fluid–solid boundaries are sharply defined, allowing direct investigation of the local flow field and particle trajectories within the pore space. Flow is commonly described using the Navier–Stokes equations, or reduced formulations when inertial effects are negligible. Pore-scale models explicitly resolve the void-space geometry and the resulting local flow field. So, in the absence of additional coupled processes such as poromechanical deformation or chemical reactions, the pore scale therefore provides the most relevant framework for analyzing transport and retention within porous media.

2.2.4 Core scale

At the core scale, which represents an intermediate scale between the pore scale and the field scale, the porous medium may still exhibit significant heterogeneity but is treated as an equivalent continuum rather than as an assembly of explicitly resolved pores and grains. This scale is typically associated with laboratory core samples or larger porous domains, where the pore-scale geometry is no longer resolved in detail, and the medium is instead characterized by averaged geometric and hydraulic properties, such as porosity, specific surface area, permeability, and effective transport coefficients. Fluid flow at this scale is generally governed by Darcy's law, which can be derived from volume-averaging the Navier–Stokes equations over a representative elementary volume (REV) of the porous medium. The REV must be sufficiently large to smooth out pore-scale heterogeneities while remaining small compared with the overall size of the porous domain. The core scale, therefore, provides a macroscopic description of fluid flow in porous media, emerging from the collective effects of deposition and clogging processes occurring at smaller scales. Experiments at this scale can also provide empirical data to validate models of particle transport and permeability evolution.

2.2.5 Field scale

At the field scale, the detailed pore geometry is no longer described explicitly, and the porous medium is treated as an equivalent continuum. The effects of pore structure and heterogeneity are captured through effective properties such as porosity and permeability, while flow is typically modeled using Darcy's law. This scale is mainly concerned with predicting large-scale flow behavior and evaluating system performance for engineering applications.

2.3 Governing fluid flow equations at the pore scale

Fluid flow at the pore scale plays a central role in controlling particle transport in porous media, as it determines the velocity field experienced by suspended particles. The motion of the fluid is governed by the conservation of momentum, which is described by the Navier–Stokes equations, or by reduced formulations under the small characteristic length scales and low flow velocities commonly encountered in subsurface porous media.

2.3.1 From the Navier–Stokes equation to the Stokes equation

Fluid flow through the porous medium is governed by the incompressible Navier–Stokes momentum equation,

$$\rho_f \left(\frac{\partial \mathbf{u}}{\partial t} + \mathbf{u} \cdot \nabla \mathbf{u} \right) = -\nabla P + \mu \nabla^2 \mathbf{u} + \rho_f \mathbf{g}, \tag{2.1}$$

which describes the balance between inertial forces, pressure gradients, viscous stresses, and body forces acting on the fluid. Here, ρ_f and μ are the fluid density and dynamic viscosity, $\mathbf{u}$ is the local fluid velocity field, P is the pressure, and $\mathbf{g}$ is gravity.

The relative importance of inertial and viscous effects is quantified by the Reynolds number. By comparing the order of magnitude of the inertial term $\rho_f(\mathbf{u} \cdot \nabla)\mathbf{u}$ with that of the viscous term $\mu \nabla^2 \mathbf{u}$ in the Navier–Stokes equation, one obtains

$$Re = \frac{\rho_f U \mathcal{L}}{\mu}, \tag{2.2}$$

where U and $\mathcal{L}$ are characteristic velocity and length scales of the flow.

When $Re \ll 1$, viscous forces dominate over inertia and the flow lies in the creeping-flow regime. In this limit, the Navier–Stokes equations simplify to the Stokes equation,

$$0 = -\nabla P + \mu \nabla^2 \mathbf{u} + \rho_f \mathbf{g}, \tag{2.3}$$

which describes a linear and time-reversible flow field controlled by pressure gradients and viscous dissipation. This is the typical regime encountered in microfluidic and porous-media flows at low velocities and small length scales, and it defines the hydrodynamic environment experienced by suspended colloidal particles.

In this work, two injection modes are considered: continuous injection and oscillatory injection, in which the imposed pressure varies with time. In both cases, the flow remains within the creeping-flow regime, so that the Stokes equation introduced in Eq. 2.3 remains valid. For oscillatory flow, the time dependence is not associated with fluid inertia but is instead imposed through time-dependent boundary conditions corresponding to the oscillatory pressure signal.

Under oscillatory forcing, the imposed pressure oscillation generates a time-dependent flow rate, such that the superficial velocity

$$u(t) = \frac{Q(t)}{A}, \tag{2.4}$$

varies over each cycle between low and high flow conditions. To verify that the creeping-flow assumption remains valid at all times, including at the maximum flow rate, the Reynolds number is evaluated using the peak superficial velocity and the characteristic microchannel depth H,

$$Re = \frac{\rho\, u_{\max}\, H}{\mu}. \tag{2.5}$$

For all experimental conditions investigated in this study, we find $Re < 1$, confirming that viscous forces dominate over inertial forces.

In oscillatory flows, inertia may also arise through the periodic acceleration of the fluid, even when Re is small. This unsteady effect is quantified by the Womersley number [Womersley, 1955],

$$Wo = \sqrt{\frac{\rho\, \omega\, H^2}{\mu}}, \tag{2.6}$$

where $\omega = 2\pi f$ is the angular frequency of the imposed pressure oscillation and f is the oscillation frequency. For all frequencies explored in this study, $Wo \ll 1$, indicating that the velocity profile has sufficient time to fully redevelop within each oscillation cycle and that the flow operates in a quasi-steady pulsatile regime. Consequently, any frequency-dependent effects observed in particle transport and clogging originate from particle–deposit dynamics and the evolving pore-scale flow field rather than from fluid inertia.

2.3.2 Flow in Hele–Shaw cells

In shallow microchannels, the Stokes equation can be reformulated in a depth-averaged form to account for the viscous resistance associated with the finite channel depth. Under creeping-flow conditions, the momentum equation includes an additional Hele–Shaw correction term and can be written as

$$0 = -\nabla P + \mu \nabla^2 \mathbf{u} - \mu \frac{12}{H^2} \mathbf{u} + \rho_f \mathbf{g}. \tag{2.7}$$

Here, $\mathbf{u}$ denotes the velocity field averaged over the micromodel depth. The term $-\mu \frac{12}{H^2}\mathbf{u}$ corresponds to the Hele–Shaw correction and accounts for the viscous resistance associated with confinement across the depth of the device. It relies on the assumption of a Poiseuille-like velocity profile in the out-of-plane direction. The resulting flow field, therefore, provides a depth-averaged two-dimensional description of flow in the micromodel.

2.4 Particle transport mechanisms

The transport of colloidal particles in porous media is governed primarily by two fundamental mechanisms: advection and diffusion. Advection corresponds to the transport of particles by the bulk fluid motion, while diffusion arises from random particle motion driven by concentration gradients.

These mechanisms are described by the advection–diffusion equation, which expresses the conservation of particle mass:

$$\frac{\partial C}{\partial t} + \nabla \cdot (\mathbf{u}C) = \nabla \cdot (D \nabla C)\,, \tag{2.8}$$

where $D = \frac{k_B T}{6\pi a \mu}$ is the particle diffusion coefficient, as given by the Stokes–Einstein equation, with $k_B T$ the thermal energy and a the particle radius. Here, C denotes the particle concentration field, i.e., the evolution of particle concentration in space and time, $C(\mathbf{x}, t)$. The second term on the left-hand side describes advection, whereby particles are transported by the fluid flow, while the right-hand side accounts for diffusive transport due to Brownian motion.

2.4.1 Transport regimes

The relative importance of advective and diffusive transport is determined by comparing the magnitude of each term in the previous equation, which leads to the definition of the particle Péclet number:

$$Pe = \frac{U\,\mathcal{L}}{D}, \tag{2.9}$$

which represents the ratio between advection and diffusion.

When $Pe \ll 1$, diffusion dominates, and the governing equation reduces to

$$\frac{\partial C}{\partial t} \approx \nabla \cdot (D \nabla C)\,, \tag{2.10}$$

whereas when $Pe \gg 1$, advective transport dominates, diffusion becomes negligible, and the governing equation reads

$$\frac{\partial C}{\partial t} + \nabla \cdot (\mathbf{u}C) \approx 0. \tag{2.11}$$

2.4.2 Dimensionless numbers governing transport

Additional dimensionless numbers are used to characterize particle transport. The particle Reynolds number quantifies the relative importance of inertia at the particle scale, while the Stokes number describes particle inertia relative to the characteristic flow timescale. These dimensionless groups are defined as

$$Re_p = \frac{\rho_p\, a\, U}{\mu}, \tag{2.12}$$

$$St = \frac{2a^2\, \rho_p\, U}{9\,\mu\,\mathcal{L}}. \tag{2.13}$$

In the regime considered throughout this thesis, particle transport takes place under laminar, low-Reynolds-number flow conditions ($Re_p \ll 1$), for which viscous effects dominate over inertia. In addition, the large Péclet number ($Pe \gg 1$) indicates that advection dominates over Brownian diffusion, while the small Stokes number ($St \ll 1$) shows that particles rapidly adjust to the local

fluid motion. Under these conditions, particles are transported primarily by the flow and, in the bulk of the pore space, closely follow fluid streamlines.

When particles approach solid boundaries or pore constrictions, in these near-contact regions, hydrodynamic interactions with the wall become important and can cause particle trajectories to deviate from ideal streamlines. As the separation distance decreases further, additional forces acting at the particle scale, including mechanical and electrochemical interactions, become significant and may promote particle interception and deposition. These forces are examined in the following section.

2.5 Force balance at the particle scale

Multiple forces come into play during the transport of colloids and fine particles in the subsurface, which may lead to particle deposition and clogging. These forces are briefly discussed in this section.

2.5.1 Hydrodynamic forces

Particle transport is governed by the fluid velocity, which is itself controlled by the imposed injection conditions, such as flow rate or pressure. These hydrodynamic forces can either maintain particles in suspension and promote their transport through the porous medium or contribute to their deposition. The main hydrodynamic forces considered here are:

Buoyancy and gravity

A spherical particle immersed in a static fluid is subjected to two body forces: the gravitational force, F_G, acting downward, and the buoyant force, F_B, acting upward. According to Archimedes' principle, the buoyant force is equal to the weight of the displaced fluid, whereas the gravitational force is equal to the weight of the particle:

$$\vec{F_B} = m_f \vec{g} = \frac{4}{3}\pi a^3 \rho_f \vec{g}, \tag{2.14}$$

$$\vec{F_G} = m_p \vec{g} = \frac{4}{3}\pi a^3 \rho_p \vec{g}. \tag{2.15}$$

The balance between these forces determines whether a suspended particle settles or remains neutrally buoyant. When $\rho_p \neq \rho_f$, the resulting net force leads to a sedimentation velocity. For a spherical particle in Stokes flow, the terminal settling velocity is given by

$$U_s = \frac{2}{9}\frac{(\rho_p - \rho_f)\, g\, a^2}{\mu}, \tag{2.16}$$

where g is the gravitational acceleration in m^2/s.

In our experiments, the density difference is negligible ($\Delta\rho = 0$), so sedimentation effects are avoided.

Drag force

The drag force is the resistive force that opposes the motion of a body through a liquid or a gas. In a viscous fluid, a spherical particle of radius a moving with a relative velocity U_r with respect to the surrounding fluid experiences a hydrodynamic drag force. Under Stokes flow conditions ($Re_p < 1$), this force is expressed as

$$F_D = 6\pi\mu a U_r. \tag{2.17}$$

Here, U_r denotes the relative velocity between the fluid and the particle. This expression is valid only in dilute suspensions, which corresponds to the conditions considered in our study.

2.5.2 Electrochemical forces

Once particles are brought into close proximity to solid surfaces by hydrodynamic transport, short-range colloidal interactions may further control attachment and detachment. A standard framework to describe these interactions is the DLVO theory [Derjaguin, 1941b, Verwey, 1947], which is widely used to model particle–particle and particle–wall interactions in colloidal systems. In this framework, the interaction energy arises from the combined effects of attractive van der Waals forces and repulsive electrostatic double-layer interactions.

Van der Waals potentials

Van der Waals forces are intermolecular interactions originating from fluctuations in molecular dipoles, which lead to an attractive interaction potential. The van der Waals attraction potential between two identical spherical particles with smooth surfaces [Schenkel and Kitchener, 1960] is approximated as

$$\mathcal{V}_{\mathrm{pp}}^{\mathrm{VdW}} = -\frac{Aa}{12h}, \tag{2.18}$$

where A is the Hamaker constant, which depends strongly on the properties of the interacting materials and the surrounding medium, a is the particle radius, and h is the surface-to-surface separation distance, with $h \ll a$.

For particle–surface interactions, retardation effects become important at larger separation distances. The retarded van der Waals attraction potential between a spherical particle and a planar wall surface [Hogg et al., 1966] is given by

$$\mathcal{V}_{\mathrm{ps}}^{\mathrm{VdW}} = -\frac{Aa}{6h}\left(\frac{1}{1+14h/\lambda}\right), \tag{2.19}$$

where λ is the retardation length, taken here as $\lambda = 100$ nm. This approximation is appropriate for relatively large particles (typically $a \gtrsim 1$ μm), for which retardation effects are significant at separation distances up to $a/5$ [Gregory, 1981].

Electric double-layer potentials

In polar solvents, solid surfaces often acquire an electric charge due to the dissociation of ionizable surface groups. This surface charge is compensated by a surrounding cloud of counter-ions, forming an electric double layer (EDL) that maintains overall electro-neutrality. The EDL consists of a compact Stern layer and a more diffuse Gouy–Chapman layer [Leroy and Maineult, 2018]. The Stern layer is composed of counter-ions strongly adsorbed onto the surface due to electrostatic attraction, forming a relatively immobile layer. Beyond this region, the diffuse layer contains mobile ions distributed according to a balance between electrostatic interactions and thermal motion [Grahame, 1947]. As a result, the ion concentration follows a Boltzmann distribution and gradually approaches the bulk concentration with increasing distance from the surface. The boundary between the Stern layer and the diffuse layer is associated with the onset of fluid motion and is referred to as the slipping (or shear) plane. The electrical potential at this location, relative to the bulk solution, defines the zeta potential, ζ, which is commonly used to characterize the

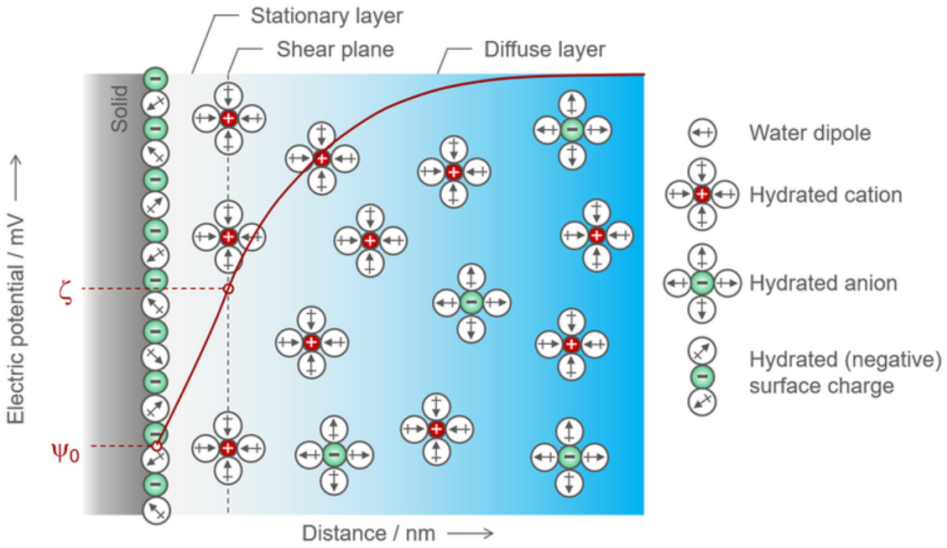

Figure 2.4: Schematic representation of the electrochemical double layer at the solid-liquid interface, including the Stern layer, diffuse layer, and bulk solution (surface potential Ψ and zeta potential ζ) [Anton Paar, n.d.].

electrostatic properties of particles and surfaces. When two charged surfaces approach each other, overlap of their electrical double layers leads to electrostatic repulsion, which plays a key role in particle stability and deposition processes.

For relatively low surface potentials ($\zeta < 25$ mV), the electrostatic repulsion energy between two identical spherical particles with equal zeta potentials [Schenkel and Kitchener, 1960, Hogg et al., 1966] is approximated as

$$\mathcal{V}_{\mathrm{pp}}^{\mathrm{EDL}} = \frac{\epsilon_0 \epsilon_r a_p \zeta_p^2}{2} \ln(1 + \exp(-\kappa h)) \,, \tag{2.20}$$

where ϵ_0 and ϵ_r are the vacuum and relative permittivities of the solvent, respectively, ϕ_p is the particle zeta potential, and κ^{-1} is the Debye length.

The Debye length is defined as

$$\kappa^{-1} = \left(\frac{\epsilon_0 \epsilon_r k_B T}{2 \times 10^{-3} N_A e^2 I_S} \right)^{1/2} , \tag{2.21}$$

where k_B is the Boltzmann constant, T the absolute temperature, N_A Avogadro's number, e the elementary charge, and I_S the ionic strength of the suspension.

For particle–surface interactions at low surface potentials ($\phi < 25$ mV), the electrostatic repulsion energy is approximated by [Hogg et al., 1966] as

$$\mathcal{V}_{\mathrm{ps}}^{\mathrm{EDL}} = \frac{\epsilon_0 \epsilon_r a}{4} (\zeta_p^2 + \zeta_s^2) \left[\frac{2\zeta_p \zeta_s}{\zeta_p^2 + \zeta_s^2} \ln\left(\frac{1 + e^{-\kappa h}}{1 - e^{-\kappa h}} \right) + \ln(1 - \exp(-2\kappa h)) \right] , \tag{2.22}$$

where ζ_s is the zeta potential of the wall surface.

Total DLVO interaction potential and adhesive force

The total DLVO interaction potential is obtained by summing the van der Waals and electrostatic double-layer contributions,

$$\mathcal{V}_{\mathrm{tot}}^{\mathrm{DLVO}} = \mathcal{V}^{\mathrm{VdW}} + \mathcal{V}^{\mathrm{EDL}}. \tag{2.23}$$

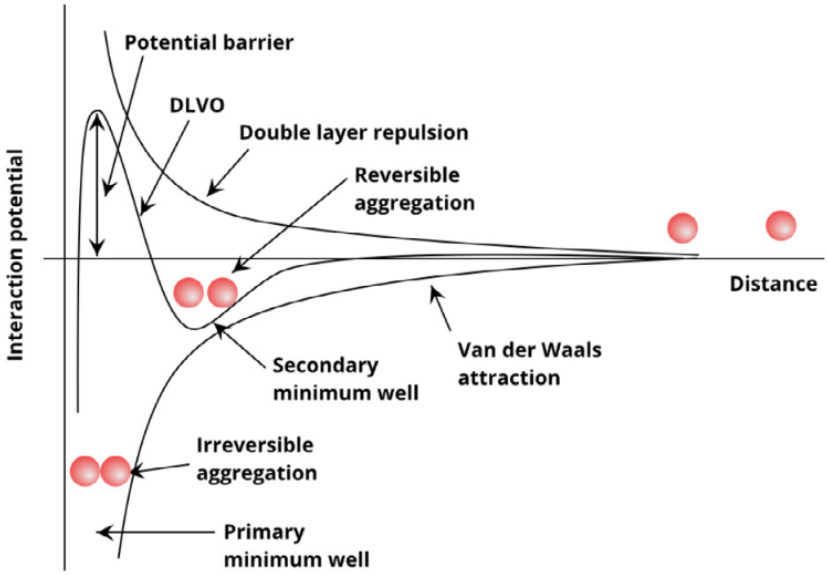

Figure 2.5: Schematic illustration of a typical DLVO interaction profile combining van der Waals attraction and electrostatic double-layer repulsion. Depending on the balance between these contributions, the total interaction potential may exhibit a secondary minimum (reversible attachment) or a primary minimum after overcoming the energy barrier (irreversible attachment) [Fogouang et al., 2024].

The balance between attractive and repulsive interactions gives rise to a total DLVO potential that may exhibit a secondary minimum at moderate separation distances, associated with reversible attachment, and a primary minimum at shorter distances once the repulsive barrier is overcome, leading to irreversible attachment (Fig. 2.5). For the physicochemical conditions considered in this work, the calculated DLVO profiles at high ionic strength (100 mM) are purely attractive, exhibiting only a primary minimum with no secondary minimum observed (Fig. A.1). The parameters used to compute these interaction potentials are reported in Table A.1 in Appendix A.

Following the Derjaguin–Langbein approximation [Israelachvili, 2011, Torkzaban et al., 2007], the adhesive force F_A is estimated from the depth of the DLVO interaction potential as

$$F_A \sim \frac{\left|\mathcal{V}_{\mathrm{tot}}^{\mathrm{DLVO}}\right|_{\mathrm{min}}}{h}, \tag{2.24}$$

where $\left|\mathcal{V}_{\mathrm{tot}}^{\mathrm{DLVO}}\right|_{\mathrm{min}}$ denotes the absolute value of the DLVO interaction minimum and h is a characteristic separation distance. We follow the approach of Torkzaban et al. [2007] and use the primary minimum evaluated at a near-contact separation distance $h = 0.2$ nm [Israelachvili, 2011] to estimate F_A. This choice provides a conservative estimate of the maximum adhesive force that must be overcome by hydrodynamic stresses to induce particle detachment. The resulting force scale is later compared with hydrodynamic forces to assess the conditions for particle deposition and detachment.

2.5.3 Mechanical forces

Mechanical forces arise when particles come into direct contact with solid surfaces or with other particles. In dilute suspensions, particle–particle interactions are generally negligible in the bulk due to the low probability of collisions, and particles can be considered to move independently

within the fluid. However, in porous media, local geometric confinement increases the likelihood of contact interactions. In particular, when particles encounter pore walls or constrictions, contact forces can become significant despite the globally dilute nature of the suspension.

At contact, normal forces prevent particle overlap, and interactions can be approximated as hard-sphere constraints, as elastic deformation of the polystyrene particles is negligible. Friction forces may also arise and contribute to the stabilization of particles once they become trapped within the pore space.

2.6 Macroscopic description of flow in porous media

At the macroscopic scale, fluid flow in porous media is commonly described by Darcy's law

$$Q = -\frac{KA}{\mu}\nabla P, \tag{2.25}$$

where Q is the volumetric flow rate, A is the cross-sectional area normal to the flow direction, and K is the effective apparent permeability of the porous domain. Darcy's law can be interpreted as an upscaled form of viscous Stokes flow, in which the detailed pore-scale velocity field is replaced by an averaged relationship between the pressure gradient and the flow rate.

Permeability is an effective property of a porous domain that describes the ease with which a fluid can flow through it. It depends not only on the porosity of the medium, but also on the geometry of the pore space and the connectivity of the flow pathways. The distribution of pores and constrictions in a porous domain is key to the transport of colloidal particles in porous media, as it may control deposition and clogging mechanisms, thereby modifying the permeability. This framework provides the basis for interpreting the evolution of permeability reduction observed in the experiments presented in this work.

While Darcy's law provides a macroscopic description of fluid flow in porous media, it does not explicitly resolve the mechanisms by which suspended particles are transported, deposited, and retained within the pore space. These processes may nevertheless affect the hydraulic response of the medium indirectly through changes in its effective permeability, which can be observed as variations in flow rate or pressure drop. A description of colloidal transport and retention, therefore, requires an additional framework at the continuum scale.

2.7 Continuum framework for colloidal transport and deposition

At the continuum scale, colloidal transport in porous media is commonly described within the framework of clean-bed filtration theory (CFT) [Iwasaki et al., 1937], particle deposition is described as a two-step process involving transport toward a collector followed by attachment at its surface. This approach is based on a probabilistic description of collisions between suspended particles and collector grains, and is particularly applicable at early times, when the collector surface remains largely available for deposition.

Under these assumptions, the evolution of particle concentration along the porous medium follows a first-order law [Iwasaki et al., 1937]:

$$\frac{\partial C}{\partial x} = -\lambda C, \tag{2.26}$$

where C is the particle concentration and λ is the filtration coefficient, which depends on both transport and attachment processes.

This formulation can be expressed in terms of the collection efficiency η, which represents the probability of particle–collector collisions and depends on flow conditions, particle size,

and collector geometry, and the attachment efficiency α, which accounts for physicochemical interactions between particles and the collector surface. The evolution of particle concentration along the porous medium is then expressed as [Yao et al., 1971]:

$$\frac{dC}{dL} = -\frac{3}{2}\frac{(1-\phi)}{d_p}\alpha\eta C, \tag{2.27}$$

where ϕ is the porosity, L is the length of the porous medium, and d_p is the particle diameter.

In this framework, η is associated with hydrodynamic transport mechanisms such as advection, diffusion, and interception, while α reflects particle–surface interactions, often described using DLVO theory.

However, in a porous medium composed of many collectors with complex and heterogeneous geometry, the collection efficiency is generally not directly predicted from these theoretical expressions. Instead, it is treated as an effective quantity and is commonly inferred from experimental measurements of concentration decay along the porous medium. Integration of the filtration equation yields:

$$\ln\left(\frac{C}{C_0}\right) = -\frac{3L}{2}\frac{(1-\phi)}{d_p}\alpha\eta, \tag{2.28}$$

which can be rearranged to obtain an apparent collection efficiency:

$$\eta_{\text{app}} = -\frac{2}{3L}\frac{d_p}{(1-\phi)}\ln\left(\frac{C}{C_0}\right). \tag{2.29}$$

This experimentally derived efficiency corresponds to an effective quantity that includes both transport and attachment processes, and therefore reflects the combined contribution of η and α. As such, it does not permit direct discrimination between the respective roles of hydrodynamic transport and physicochemical interactions.

Although clean-bed filtration theory provides a useful foundation for describing colloidal deposition in porous media, its applicability remains restricted to simplified conditions, particularly at early times and in systems where pore-scale heterogeneity, evolving deposits, and particle–particle interactions can be neglected. Because it describes deposition as a continuous and spatially averaged process, it does not resolve how particles accumulate at specific locations within the pore space.

In reality, deposition occurs at discrete points and is strongly influenced by particle properties, local pore geometry, and flow conditions. As particles accumulate, these localized deposition events progressively modify the pore structure, leading to the emergence of distinct clogging mechanisms at the pore scale. These limitations motivate a pore-scale description of deposition and clogging processes, which is examined in the next chapter.

Chapter 3

State of the art: particle transport, deposition and clogging in porous media

This chapter reviews the current state of knowledge on particle transport, deposition, and clogging in porous media. We first examine the main pore-scale clogging mechanisms reported in the literature, including sieving, bridging, and progressive clogging by aggregation, and discuss how these mechanisms may interact within porous media. Next, we review the main factors controlling particle deposition and clogging, including fluid chemistry, particle properties, hydrodynamic conditions, and the geometric and surface characteristics of the porous medium. We then present the principal numerical and experimental approaches used to investigate these processes, with particular attention to microfluidic techniques that enable direct pore-scale visualization. The chapter concludes by identifying the main research gaps that remain in the literature, formulating the scientific questions addressed in this thesis, and presenting the research strategy adopted to investigate them.

3.1 Pore-scale particle deposition and clogging mechanisms

At the pore scale, different clogging mechanisms can arise (Fig. 3.1), including direct blockage of pore throats, size-exclusion effects (sieving), bridging, and the progressive growth of particle deposits on solid surfaces [Dressaire and Sauret, 2017b]:

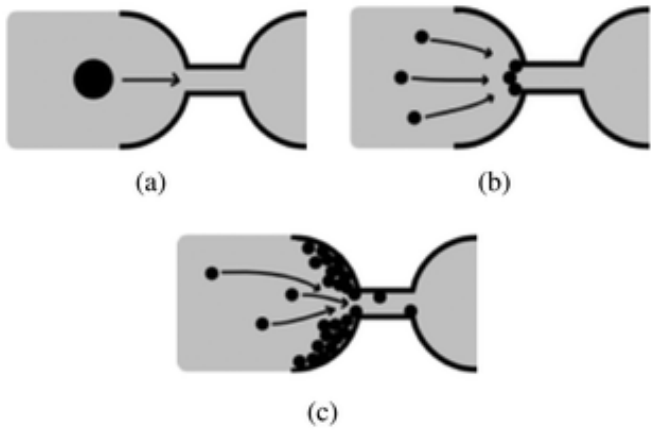

Figure 3.1: Mechanisms of pore-clogging by particles: (a) Sieving, (b) Bridging, and (c) Progressive clogging [Dressaire and Sauret, 2017b]

3.1.1 Sieving

Sieving occurs when the width of a pore or constriction (W) is smaller than or equal to the particle diameter (d_p), that is, $W \leq d_p$, under low to moderate particle volume fractions (ϕ). In this case, particles are unable to pass through the constriction and become trapped, blocking the pore space. As particle accumulation increases, the hydraulic resistance rises, leading to a reduction in flow. Warkiani et al. [2015] showed that pore geometry strongly influences the resulting permeability decline. In particular, they reported that spherical particles cover a larger fraction of the available surface in cylindrical pores than in slit-shaped pores, resulting in a stronger permeability decrease in the former case (Fig. 3.2a,b). In addition, Brans et al. [2007b] investigated the transport of binary colloidal suspensions containing particles both larger and smaller than the pore size in a cross-flow filtration system. Their results showed that the larger particles preferentially deposited at the pore centers and promoted clogging, whereas the smaller particles tended to accumulate near the pore corners, as illustrated in Fig. 3.2c.

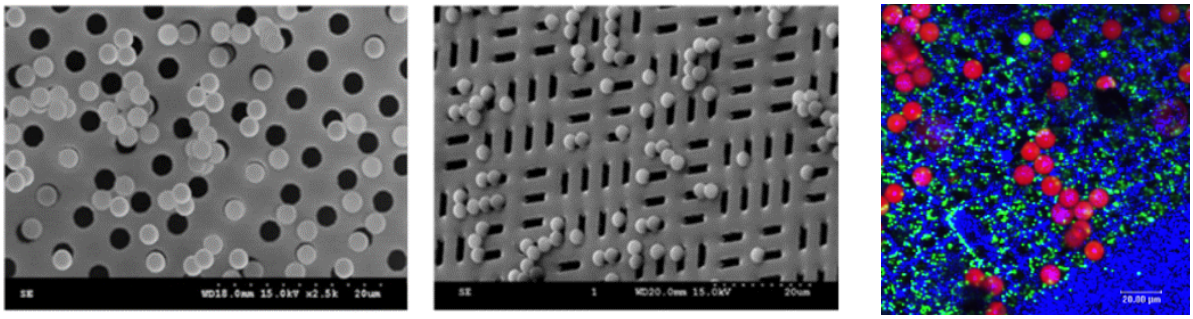

(a) (b) (c)

Figure 3.2: Sieving of spherical particles in cylindrical pore throats (a) and slit-shaped pore geometries (b) [Warkiani et al., 2015]. (c) Confocal image of a microsieve grid (blue) with particles larger than the pore throats (red) and particles smaller than the pore throats (green) [Brans et al., 2007a].

3.1.2 Bridging

Clogging by bridging, or arch formation, occurs when particles collectively span a pore throat or constriction through surface contacts, forming a stable or metastable structure that obstructs the flow. Bridging is a collective phenomenon driven by the simultaneous arrival of multiple particles at a constriction, where they organize into an arch-like structure composed of a finite number of particles that spans the pore cross-section. In contrast to sieving, this mechanism arises when the particle diameter is smaller than the constriction size, $d_p < W$, and is therefore conveniently described by the dimensionless ratio $W/d_p > 1$. Sharp and Adrian [2005] reported that flow-stopping blockages by bridging were most likely for $W/d_p \approx 2.5$–3.33.

Several experimental studies have illustrated this mechanism. For example, in a microchannel, particles driven by pressure flow can form arches due to geometric confinement and hydrodynamic effects, leading to local particle accumulation, as shown in Fig. 3.3a [Dressaire and Sauret, 2017b]. Similar bridging behavior has also been observed in capillary tubes and membrane pores, as illustrated in Fig. 3.3b,c [Sharp and Adrian, 2005, Ramachandran and Fogler, 1999].

This mechanism depends not only on geometry but also on hydrodynamic conditions and particle concentration. In dense suspensions, increasing the particle volume fraction (C) promotes frequent particle–particle interactions and enhances the probability of arch formation. However,

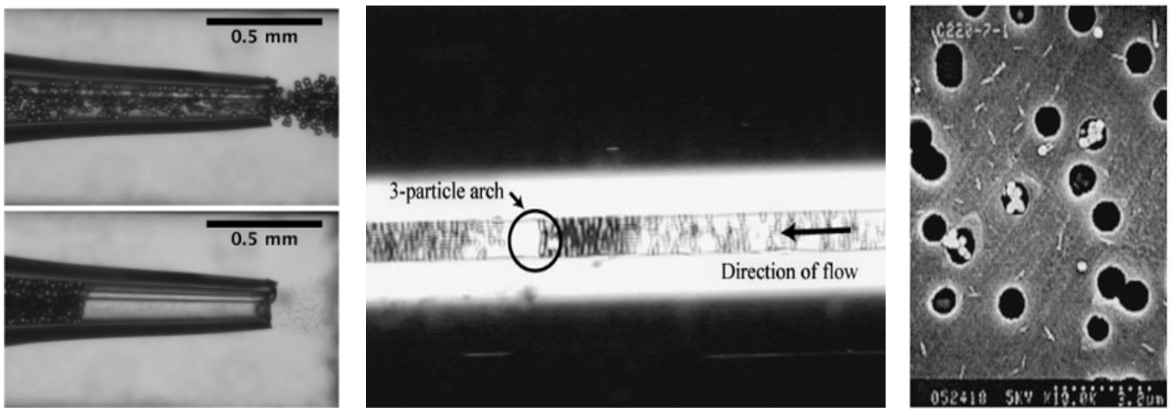

Figure 3.3: Examples of clogging by bridging or arch formation. (a) Flow and clogging by bridging of a neutrally buoyant suspension of polymethyl methacrylate (PMMA) particles in an axisymmetric tapered glass capillary [Dressaire and Sauret, 2017b]. (b) Arch formation by 48 μm particles in a capillary tube with a 150 μm inner diameter [Sharp and Adrian, 2005]. (c) Bridging-induced clogging by 200 nm sulfate polystyrene particles (white) in track-etched membrane pores (black) of typical size around 1 μm [Ramachandran and Fogler, 1999].

bridging can also occur in dilute suspensions, at concentrations lower than the jamming volume fraction C_m, where clogging results from stochastic events involving the simultaneous arrival of a limited number of particles at a constriction [Ramachandran and Fogler, 1999]. In this regime, Goldsztein and Santamarina [2004b] proposed an empirical expression for the critical number of particles, $n_{\max}$. Bridging is expected to occur when the number of particles arriving simultaneously at a circular constriction exceeds this threshold:

$$n_{\max} \propto \frac{A_c d_p}{2V_p}, \tag{3.1}$$

where A_c is the constriction area and V_p is the particle volume.

Unlike sieving, bridging does not necessarily lead to a permanent blockage. The stability of the formed arch depends on the balance between hydrodynamic forces and interparticle contacts. Flow fluctuations may destabilize and break the arch, whereas lateral confinement and shear-induced forces can contribute to its stabilization.

3.1.3 Progressive clogging / Aggregation

Particles transported by the flow can deposit and accumulate through successive deposition events, progressively reducing the cross-sectional area of a constriction until complete clogging occurs [Dersoir et al., 2015b] (Fig. 3.4a–e). In addition, colloidal particles may also form aggregates in the bulk suspension before entering the porous medium and continue to grow during filtration.

Unlike sieving and bridging, which mainly rely on hydrodynamic transport and mechanical exclusion, aggregation involves physicochemical interactions between particles, including attractive van der Waals forces and repulsive electrostatic forces. In porous media, local flow conditions in converging pores and narrow constrictions can bring particles into close proximity with the pore walls and with previously deposited particles, making these interactions significant. Progressive clogging therefore arises from the combined effects of hydrodynamic transport and particle

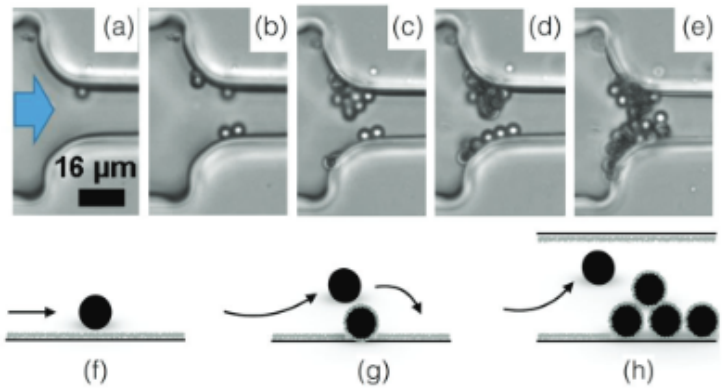

Figure 3.4: Progressive aggregation of particles resulting in clog formation. (a–e) The density-matched suspension of polystyrene particles ($D_p = 3$ μm) with sulfate charge groups flows through a constriction of width $W = 15.5$ μm. The images are recorded at 3, 5, 10, and 36 minutes, with a flux of 2.8×10^4 particles per minute at the onset of the experiment [Dersoir et al., 2015b]. (f–h) Schematic representation of the aggregation process, from the deposition of the first particle to the clog formation [Dressaire and Sauret, 2017b].

interactions, which govern both particle deposition and the subsequent growth of deposits within the pore space.

The monolayer

The growth of particle deposits starts with the attachment of individual particles onto the pore wall, forming a monolayer (Fig. 3.4f). When a particle deposits on a surface, it generates a local shadow zone in which the probability of subsequent deposition is reduced due to particle–particle repulsive interactions (Fig. 3.5) [Ko and Elimelech, 2000]. This screening region limits the available surface for further deposition and controls the maximum surface coverage.

The extent of this shadow zone is governed by the interplay between electrostatic double-layer forces and hydrodynamic transport. Increasing ionic strength compresses the electrostatic double layer, reduces the shadow zone, and allows particles to deposit closer to one another [Adamczyk et al., 1994, Johnson and Elimelech, 1995]. In addition, particle size and flow conditions influence this process: smaller particles and lower flow velocities promote higher surface coverage, whereas larger particles generate wider exclusion regions that limit deposition.

From monolayer to multilayer growth

Transition from monolayer to multilayer growth requires flowing particles to attach to previously deposited ones, as illustrated in Fig. 3.4 (panels b–d, g, and h). Describing this process remains challenging because deposited particles progressively alter both the local flow field and the interaction conditions within the constriction. Multilayer growth is therefore governed by the balance between hydrodynamic forcing and interparticle interactions. Under favorable conditions, successive particle attachment promotes aggregate growth that can progressively narrow and ultimately clog the pore [de Saint Vincent et al., 2016, Dersoir et al., 2015b]. Under unfavorable conditions, an energy barrier reduces the probability of attachment and suppresses further deposit growth [Dressaire and Sauret, 2017b]. Nevertheless, at sufficiently high flow velocities, an approaching particle may overcome this electrostatic barrier and attach to a previously deposited particle, enabling the onset of multilayer growth.

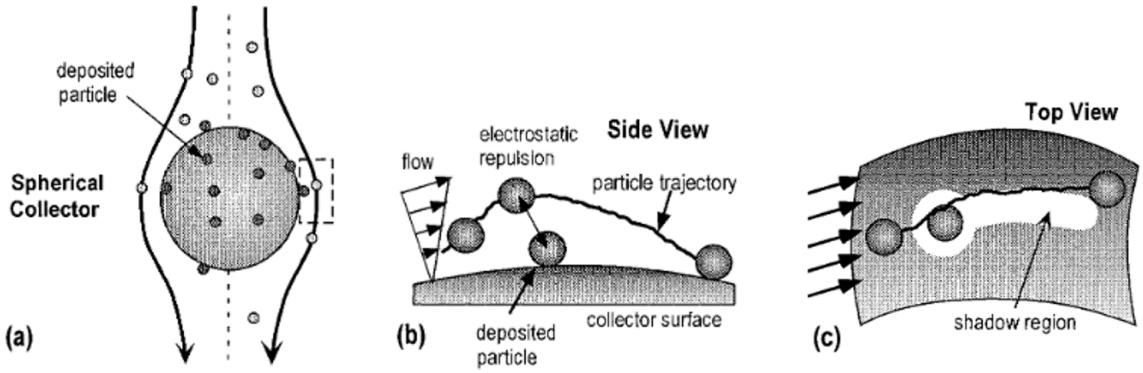

Figure 3.5: Schematic illustration of dynamic shadowing during particle deposition onto a surface. Panel (a) shows the flow field around the collector, with the dashed axis connecting the upstream and downstream stagnation points. Panel (b) provides a side view of the highlighted region, where tangential flow and the associated shadowing effect are strongest at 90° from the upstream stagnation point. Panel (c) illustrates the shadow region that develops downstream of a deposited particle. Adapted from Ko and Elimelech [2000].

As multilayer deposition develops, aggregates grow within constrictions and progressively reduce the available cross-section for flow. Progressive clogging is therefore not a single event, but the result of a sequence of deposition and growth processes controlled by the interplay between hydrodynamics and interparticle interactions.

Evolving structures of multilayer deposits

As multilayer deposition develops, particle deposits can exhibit different morphologies depending on the hydrodynamic conditions and interparticle interactions. Under screened electrostatic interactions at high salt concentrations, successive particle attachment can lead to spatially organized multilayer deposits, including dendritic structures, as illustrated in Fig. 3.6.

At low Péclet numbers, deposition occurs rather uniformly over the upstream half of the collector. As the Péclet number increases, deposition becomes increasingly localized at the front stagnation point, eventually leading to finger-like dendritic structures (Fig. 3.6a). These deposits are, however, highly sensitive to flow intensity: at sufficiently high Péclet numbers, dendrites become smaller or are eroded, and deposition shifts toward the rear stagnation region of the collector [Kusaka et al., 2010].

Similar dendritic structures were also reported at the entrance of 2D microfluidic filtration devices, where the morphology of the deposits was shown to depend on the direction of flow (Fig. 3.6b) [Agbangla et al., 2012b,a]. de Saint Vincent et al. [2016] showed that erosion promotes lateral particle detachment along the sides of the obstacle, which favors dendritic growth along the upstream centerline of the pore, whereas at higher flow velocity dendritic growth is suppressed because particle detachment at the centerline becomes too strong (Fig. 3.6c). Taken together, these studies show that dendrite formation emerges only within a limited range of physicochemical and hydrodynamic conditions, where high ionic strength promotes aggregation while flow remains strong enough to localize deposition but not so strong as to destabilize the growing structures.

Although the conditions leading to these deposit morphologies are relatively well described, their direct impact on pore clogging and permeability reduction remains insufficiently understood.

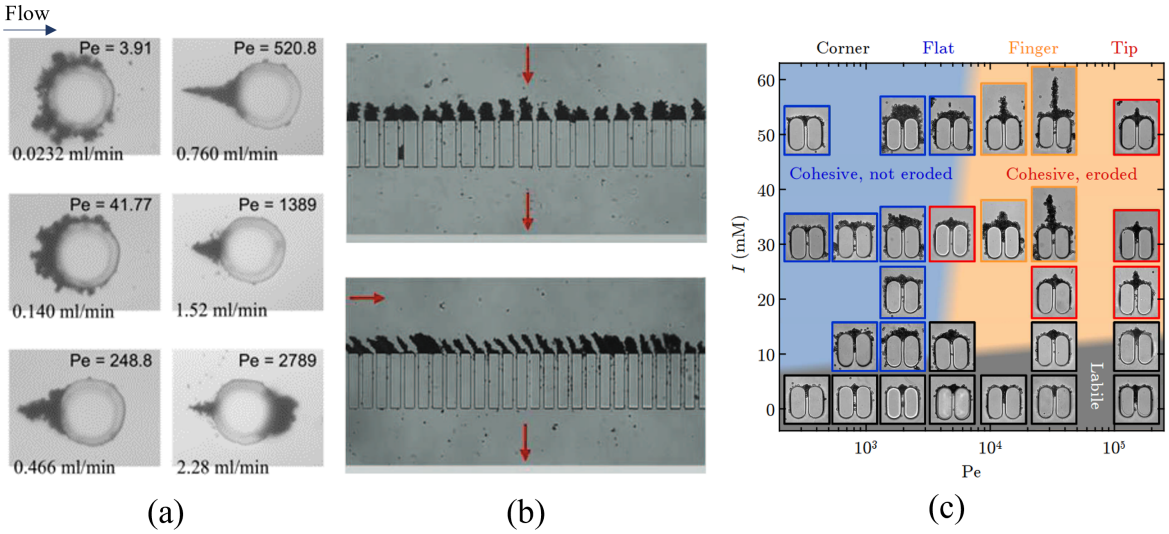

Figure 3.6: Examples of multilayer deposit morphologies observed under different flow and ionic strengths. (a) Deposition patterns on a single-grain collector at different Péclet numbers. Adapted from Kusaka et al. [2010]. (b) Dendrite formation at the entrance of a microfluidic filter (top) and effect of flow direction on dendrite orientation (bottom) [Agbangla et al., 2012a]. (c) Phase diagram of deposition morphologies around an obstacle as a function of ionic strength and Péclet number [de Saint Vincent et al., 2016].

Competition between deposition and erosion

The competition between deposition and erosion controls the development of particle deposits. This balance can be described by the competition between adhesive torque, acting normal to the surface (or deposited particle), and drag torque, acting tangentially [Torkzaban et al., 2007, Bergendahl and Grasso, 2000] (Fig. 3.7):

$$T_D = F_D l_D, \tag{3.2}$$
$$T_A = F_A l_A. \tag{3.3}$$

Here, F_D and F_A are the drag and adhesive forces, and l_D and l_A are their respective lever arms. When the adhesive torque exceeds the drag torque, particles remain attached and promote deposit growth. When the drag torque exceeds the adhesive torque, particles may detach, leading to erosion.

Quantifying clogging dynamics

When aggregate growth occurs, clogging dynamics are commonly described by the mean clogging time, $\langle t_{\text{clog}} \rangle$, defined from the fraction of constrictions that become blocked during the experiment. It has been shown that $\langle t_{\text{clog}} \rangle$ decreases with both the imposed pressure drop and the particle volume fraction [Wyss et al., 2006b, Sauret et al., 2014], following:

$$\langle t_{\text{clog}} \rangle \propto \frac{1}{C\,\Delta P}, \tag{3.4}$$

where C is the particle volume fraction and ΔP is the pressure drop across the system.

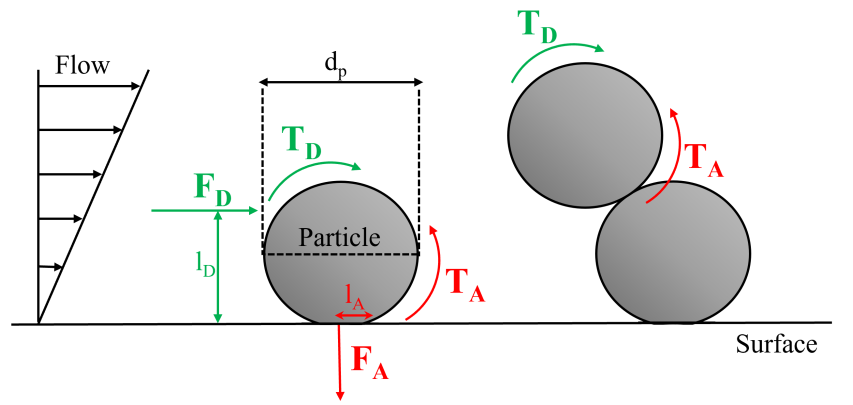

Figure 3.7: A schematic representation of the torques acting on a particle of diameter d_p in the vicinity of a surface or a previously deposited particle.

At the scale of a single constriction, clogging can also be related to a critical number of particles, denoted N^*, required to form a stable blockage. Experimental results suggest that this number scales as:

$$N^* \propto \frac{W^3 h}{6 d_p^4}, \tag{3.5}$$

where W is the constriction width, H is the channel depth, and d_p is the particle diameter. This critical number primarily reflects the geometric constraints of the constriction and corresponds to the number of particles needed to block it [Dersoir et al., 2015b, Wyss et al., 2006b].

3.1.4 Interplay of pore-scale clogging mechanisms

We have presented the different mechanisms responsible for particle deposition and pore clogging at the pore scale. The main characteristics of each clogging mechanism are summarized in Table 3.1.

Table 3.1: Comparison of the main clogging mechanisms observed in porous media, adapted from Dressaire and Sauret [2017b].

Characteristic	**Sieving**	**Bridging**	**Aggregation**
Size comparison (particle diameter d_p and channel width W)	$d_p \geq W$	$d_p \leq W$	$d_p \leq W$
Solid volume fraction in suspension	Low	High	Low
Dominant interactions	Geometric exclusion	Contact and hydrodynamic	Colloidal attraction
Clog formation mechanism	Single-particle blockage	Arch formation	Successive deposition (multilayer)

In realistic porous media, clogging rarely results from a single mechanism acting in isolation, but more often from the combined action of sieving, bridging, and aggregation (Fig. 3.8). Once particles start to deposit on a surface, the effective flow area within a constriction progressively

decreases. As multilayer deposition continues, the pore space becomes increasingly narrowed, which may ultimately lead to clogging by sieving or bridging depending on particle size, local geometry, and hydrodynamic conditions.

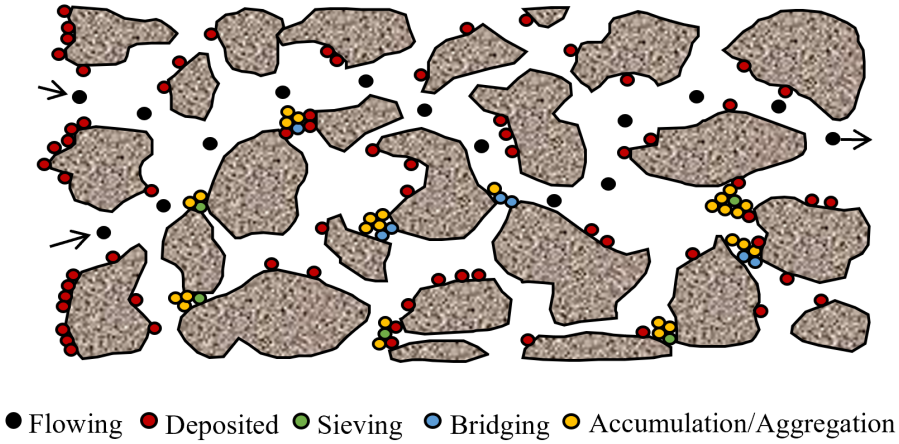

Figure 3.8: Schematic illustration of coupled clogging mechanisms in porous media. Flowing particles (black) may deposit on grain surfaces (red), progressively reducing the available flow area within constrictions. This promotes the emergence of multiple mechanisms, including sieving (green), bridging (blue), and aggregation (yellow), which can act simultaneously and lead to pore blockage. Adapted from Chauveteau et al. [1998].

Once clogging has developed within the porous medium through different retention mechanisms, the process is referred to as deep-bed filtration. With continued injection of low-quality water containing suspended particles, deposits may progressively accumulate from the interior of the porous structure toward the inlet. This buildup can eventually reach the entrance of the porous domain and form an external filter cake, as illustrated in Fig. 3.9b. Such a cake further hinders fluid entry into the porous medium, leading to reduced injectivity and an additional decrease in the effective permeability of the formation. In borehole configurations, this external deposit forms along the wellbore wall, as schematically shown in Fig. 3.9a.

In the remainder of this chapter, the literature on clogging is reviewed through the main factors known to control particle deposition and pore blockage. The following sections synthesize results obtained in rock cores, reconstructed porous media, and micromodels, in order to highlight how these parameters affect the underlying mechanisms and the resulting impairment of the porous medium.

3.2 Factors influencing particle deposition and clogging in porous media

In this section, we review the key factors controlling particle deposition and clogging, based on experimental observations reported in the literature.

3.2.1 Fluid chemistry

Flow in subsurface porous formations is subject to a wide range of conditions. Parameters such as as ionic strength, pH, and temperature, can significantly influence particle transport, deposition, and the resulting injectivity and effective permeability of the system.

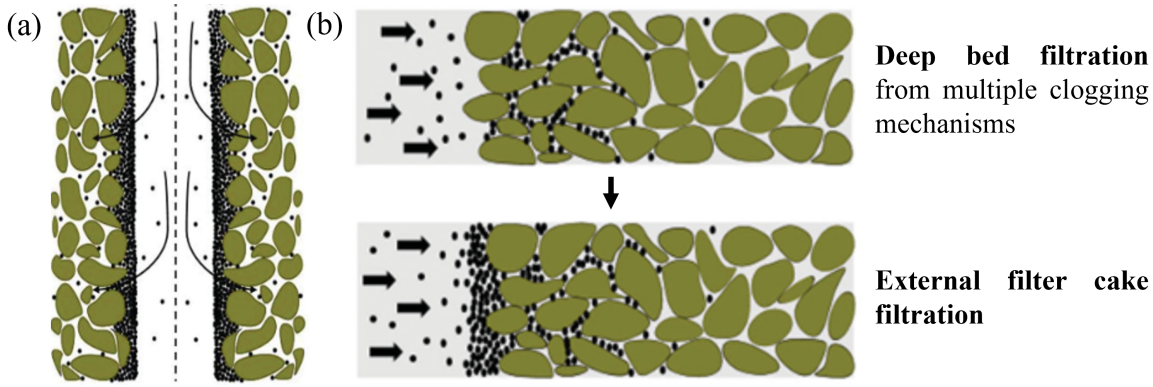

Figure 3.9: (a) Schematic illustration of well impairment caused by the injection of low-quality water containing suspended particles, showing deep-bed filtration within the porous formation and external filter cake formation under radial flow. (b) Progressive transition from deep-bed filtration to external filter cake formation as deposits accumulate toward the inlet in a one-dimensional porous medium. Adapted from Tale et al. [2021].

Ionic strength

Ionic strength characterizes the concentration of ions in the fluid and depends on both their concentration and valency. Numerous studies have investigated the effect of ionic strength on colloid retention in porous media composed of quartz grains [Pelley and Tufenkji, 2008, Sang et al., 2013, Gerber et al., 2019], glass beads in flow cells [Kuznar and Elimelech, 2007b], and parallel channel in a 2D microfluidic array [Agbangla et al., 2012b].

Under both saturated and unsaturated conditions, Sang et al. [2013] showed that increasing ionic strength (NaCl) leads to higher deposition rates of carboxylated polystyrene particles, as illustrated in Fig. 3.10a. Similarly, Pelley and Tufenkji [2008] reported that increasing ionic strength (KCl) enhances the attachment efficiency of latex particles over a range of particle sizes (Fig. 3.10b).

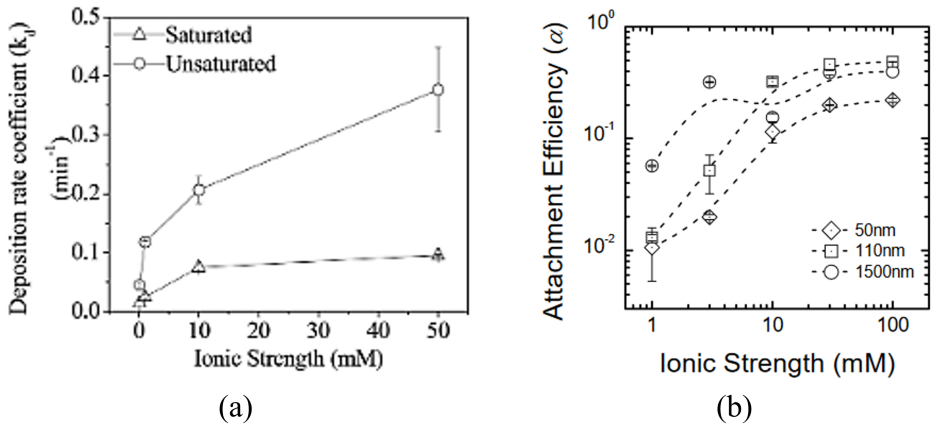

Figure 3.10: Effect of ionic strength on particle deposition and attachment in porous media. (a) Deposition rate coefficient of carboxylated polystyrene particles under saturated and unsaturated conditions as a function of NaCl concentration [Sang et al., 2013]. (b) Attachment efficiency of latex particles of different sizes as a function of ionic strength (KCl) [Pelley and Tufenkji, 2008].

Kuznar and Elimelech [2007a] showed that the location and extent of particle deposition strongly depend on ionic strength (Fig. 3.11). At low ionic strength (1 mM KCl), no particle deposition was observed due to strong electrostatic repulsion. At intermediate ionic strengths (10–30 mM), partial screening of electrostatic interactions leads to the formation of a secondary energy minimum, in which particles can be temporarily trapped. Under these conditions, particles are preferentially transported toward the rear of the collectors and accumulate in downstream stagnation regions when their energy is insufficient to overcome the secondary minimum. At high ionic strength (100 mM), the electrostatic energy barrier is suppressed, enabling particles to attach directly to the collector surface without restriction. As a result, deposition occurs over the entire surface of the grains. These observations are consistent with the interaction energy profiles shown in Fig. 3.11b, where increasing ionic strength reduces the repulsive barrier and promotes particle attachment.

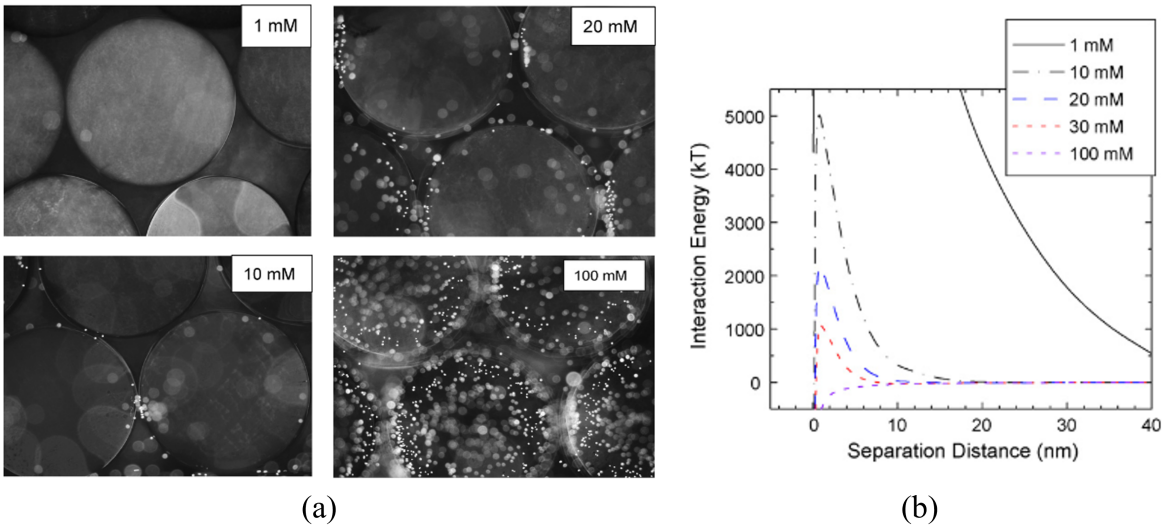

Figure 3.11: Effect of ionic strength on particle deposition and interaction energy. (a) Deposition patterns of 4.1 µm latex particles on glass beads at different KCl ionic strengths, with flow from right to left. (b) DLVO interaction energy profiles between latex particles and glass beads, showing a high repulsive barrier at low ionic strength (1 mM) and its disappearance at high ionic strength (100 mM). Adapted from Kuznar and Elimelech [2007a].

More recently, Gerber et al. [2019] confirmed that increasing ionic strength leads to enhanced particle retention (Fig. 3.12). They further showed that even at very low ionic strength ($I = 10^{-6}$ M), where interparticle interactions are dominated by strong electrostatic repulsion, particle deposition still occurs. In this regime, particles progressively accumulate on the surface of the grains over time, leading to gradual surface coverage.

However, in contrast to the observations of Kuznar and Elimelech [2007a], Gerber et al. reported a different preferential deposition pattern, with particles accumulating mainly on the upstream side of the collectors rather than in downstream stagnation regions. In addition, they showed that deposition does not proceed indefinitely, but instead approaches a plateau as surface coverage increases. This behavior is attributed to the evolution of the local hydrodynamic conditions near the grain surface. As the deposit layer grows, the effective surface geometry is modified, which increases hydrodynamic forces acting on incoming particles and reduces their probability of attachment.

This behavior has also been observed in 2D microfluidic systems. Agbangla et al. [2012b]

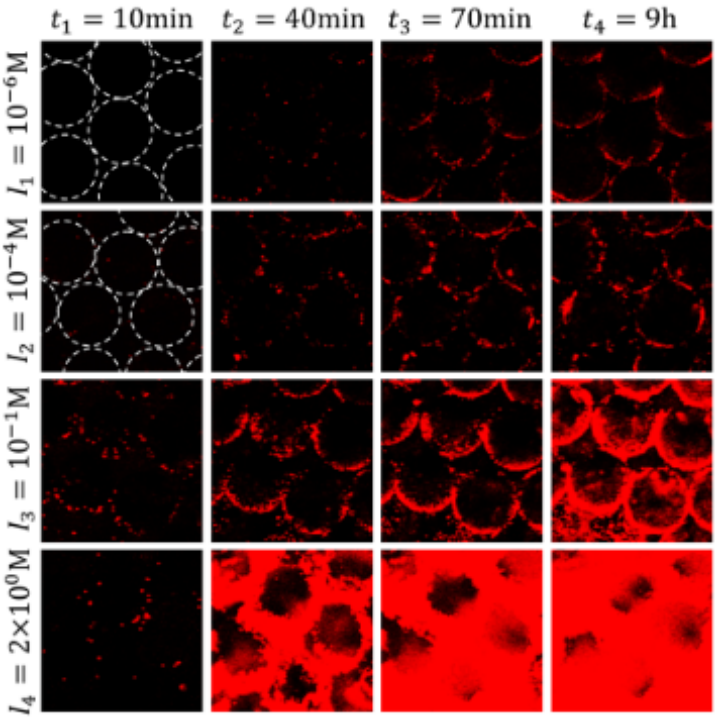

Figure 3.12: Confocal microscopy images of latex particle deposition (red) in the pore space between glass beads (black) at the entrance of a porous medium, for different ionic strengths and times. The flow is directed upwards. Adapted from Gerber et al. [2019].

showed that at zero ionic strength (0 mM KCl), almost no particle deposition is observed under dead-end filtration conditions (Fig. 3.13a), due to strong electrostatic repulsion between particles. In contrast, at high ionic strength (100 mM KCl), electrostatic screening promotes particle aggregation and deposition, leading to the formation of multilayer deposits (dendritic structures) developing upstream in the microfluidic array (Fig. 3.13b).

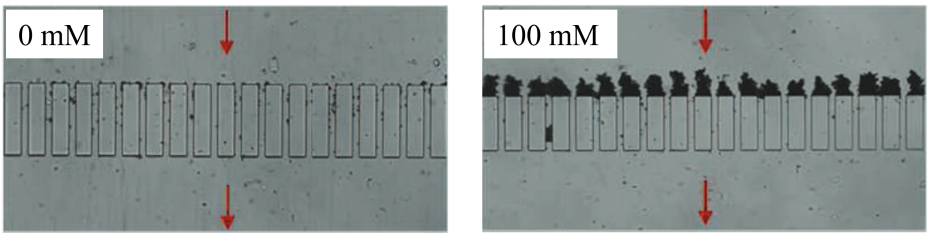

Figure 3.13: Effect of ionic strength on particle deposition in a 2D microfluidic array. (a) No particle deposition after 90 min of dead-end filtration with latex suspensions in ultra-pure water ($I = 0$ mM). (b) Formation of upstream multilayer deposits (dendrites) after 90 min at high ionic strength (100 mM KCl) under identical flow conditions. Flow is directed from top to bottom, and each channel has a width of 20 µm. Adapted from Agbangla et al. [2012b].

pH

pH is a key chemical parameter controlling colloidal deposition and aggregation in porous media. By modifying the surface charge of both particles and collector grains, pH directly affects the electrostatic interactions governing particle retention. In a study by Sadri et al. [2017], 100 nm polystyrene latex particles were injected through a porous column packed with soda-lime glass beads. Their results showed that the zeta potentials of both the particles and the collector surfaces vary with pH (Fig. 3.14a,b), which alters the interaction energy between them.

At low pH, the electrostatic repulsion barrier is strongly reduced and can even become attractive, as shown by the interaction energy profiles in Fig. 3.14c. Under these conditions, particles are more likely to aggregate and deposit on the collector surfaces, leading to stronger retention in the column. This is reflected in the normalized effluent concentration shown in Fig. 3.14d, where the lowest breakthrough is observed at pH 2. In contrast, at higher pH, stronger electrostatic repulsion limits aggregation and deposition, allowing particles to migrate more easily through the porous medium. Similar trends have been reported by Muneer et al. [2020], while Vaidya and Fogler [1990] showed that pore blockage may still occur under conditions favoring particle migration when hydrodynamic effects become dominant.

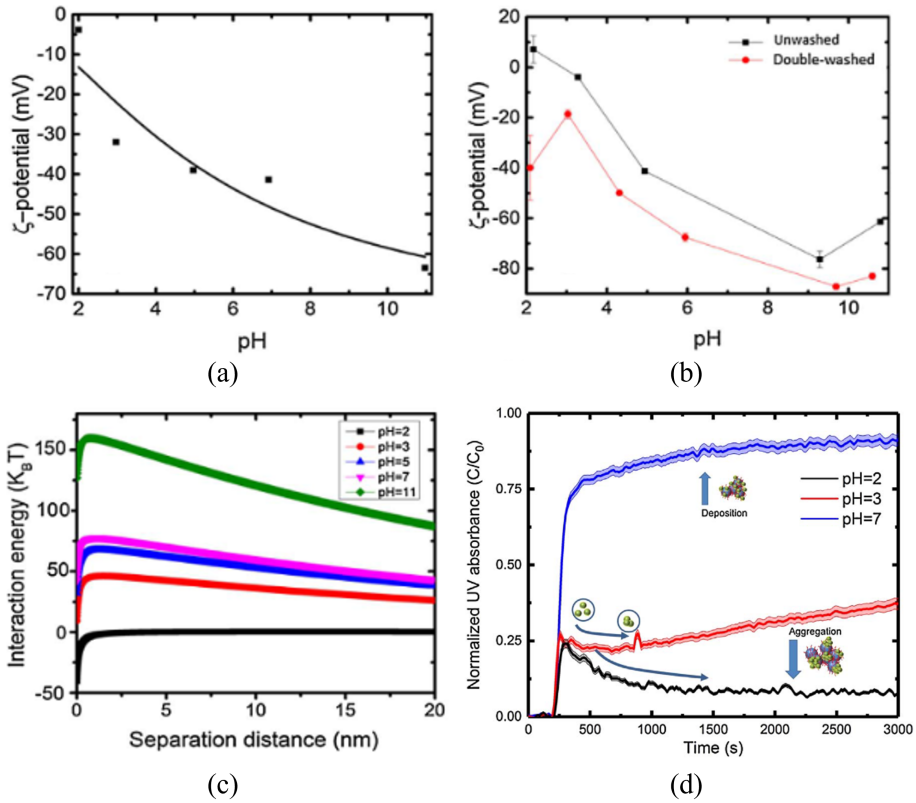

Figure 3.14: Effect of pH on surface charge, interaction energy, and particle retention in porous media. (a) Zeta potential of polystyrene particles as a function of pH. (b) Zeta potential of soda-lime glass beads as a function of pH. (c) Interaction energy profiles of polystyrene nanoparticles at different pH values, showing attractive interactions at low pH. (d) Normalized UV absorbance as a function of time for different pH conditions, illustrating stronger particle retention at low pH due to enhanced aggregation and deposition. Adapted from Sadri et al. [2017].

Temperature effects

Temperature influences the properties of the fluid, the particles, and the porous matrix [Rosenbrand et al., 2015]. They showed that increasing temperature modifies the dielectric properties of the fluid and the surface potential, thereby altering the electrical double layer (EDL) interactions between particles and the porous matrix (berea sandstone plugs). Under such conditions, heating may increase repulsive interactions and promote the mobilization of previously attached fines. In addition, increasing temperature reduces fluid viscosity, which can increase the hydrodynamic torque acting on attached particles and favor their detachment when it exceeds the adhesion torque. This mobilization leads to a redistribution of fines within the pore space, which may reduce permeability without necessarily corresponding to increased permanent deposition (Fig. 3.15). In this case, the permeability reduction was observed to be largely reversible when the temperature returns to its initial value.

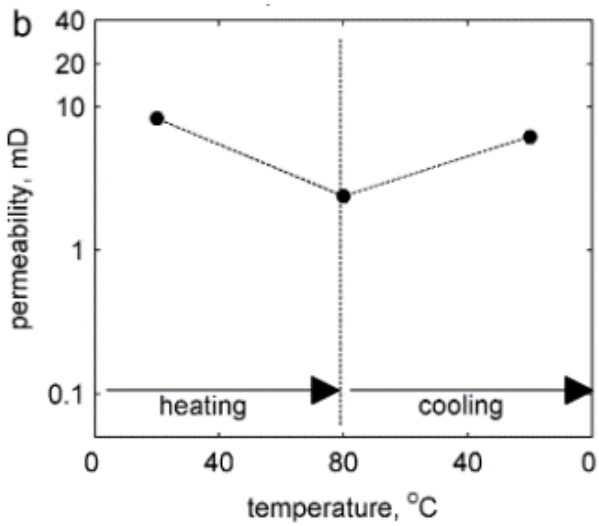

Figure 3.15: Heating causes a decline in the permeability of the Berea sandstone sample, and this reduction is reversible when the temperature is returned to its initial value. Adapted from Rosenbrand et al. [2015].

In a different thermal configuration, Yan et al. [2020] investigated particle deposition in a microchannel subjected to a temperature gradient (Fig. 3.16). Although the number of deposited particles increased with time under all tested conditions, they showed that the deposition rate per unit area decreased as the temperature gradient increased. These observations highlight the role of different mechanisms, from the redistribution of existing fines [Rosenbrand et al., 2015] to the deposition of suspended particles under a temperature gradient [Yan et al., 2020].

3.2.2 Properties of suspended particles

Particle surface charge and size ratio

The surface charge of particles, together with their size, plays an important role in permeability impairment. Litton and Olson [1996] investigated the effect of particle size and surface functionality by injecting modified latex particles into a quartz-grain column (Fig. 3.17). They showed that, for carboxyl-functionalized particles, the attachment efficiency increases with particle size over a range of ionic strengths (Fig. 3.17a). However, when comparing particles with different surface functionalities, they found that hematite particles, although smaller than the sulfate latex particles, exhibit a higher attachment efficiency (Fig. 3.17b). This behavior was attributed to the less

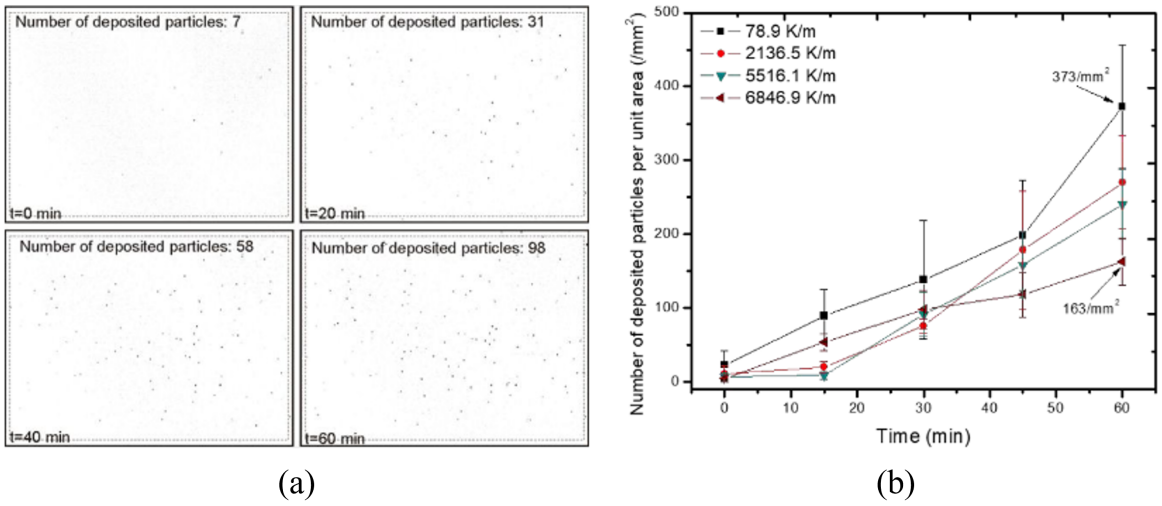

Figure 3.16: (a) Videomicroscopic images of 0.93 µm polystyrene particles captured with a 10× objective under an imposed temperature gradient of 6846.9 K/m at 0, 20, 40, and 60 min; particles are visible as black dots. (b) Evolution of the number of deposited particles per unit area with time for four different temperature gradients: 78.9, 2136.5, 5516.1, and 6846.9 K/m. Adapted from Yan et al. [2020].

negative surface charge of hematite compared with sulfate-functionalized particles, which promotes particle attachment.

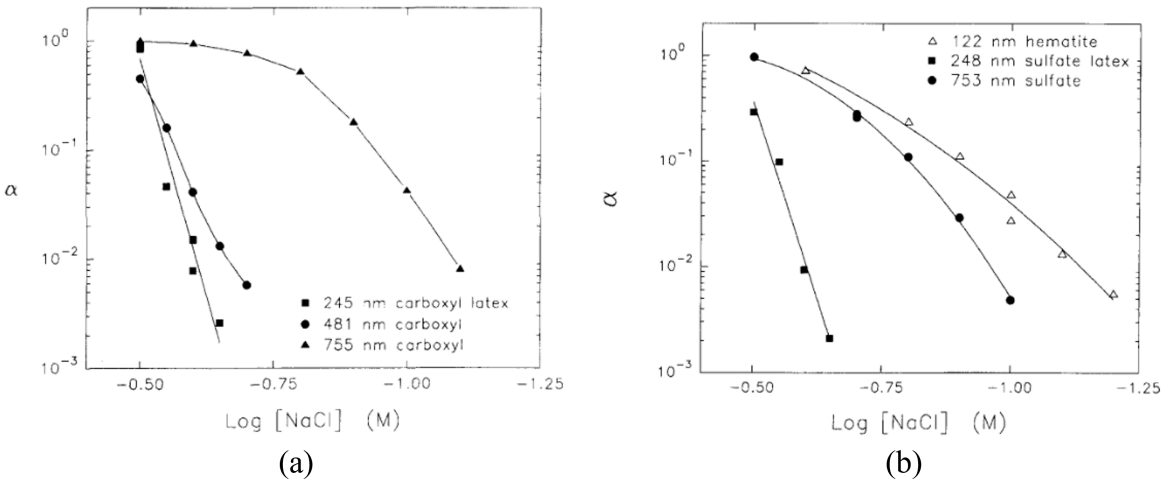

Figure 3.17: Effect of particle size and surface functionality on attachment efficiency in a quartz-grain column. (a) Attachment efficiency of carboxyl-functionalized particles of different sizes as a function of ionic strength, showing higher attachment for larger particles. (b) Attachment efficiency of particles with different surface functionalities as a function of ionic strength, showing that hematite particles exhibit higher attachment efficiency than larger sulfate latex particles. Adapted from Litton and Olson [1996].

It is also observed by Bennacer et al. [2017] that lower permeability recovery rates are associated with larger particle sizes across a range of flow velocities and ionic strengths (Fig. 3.18).

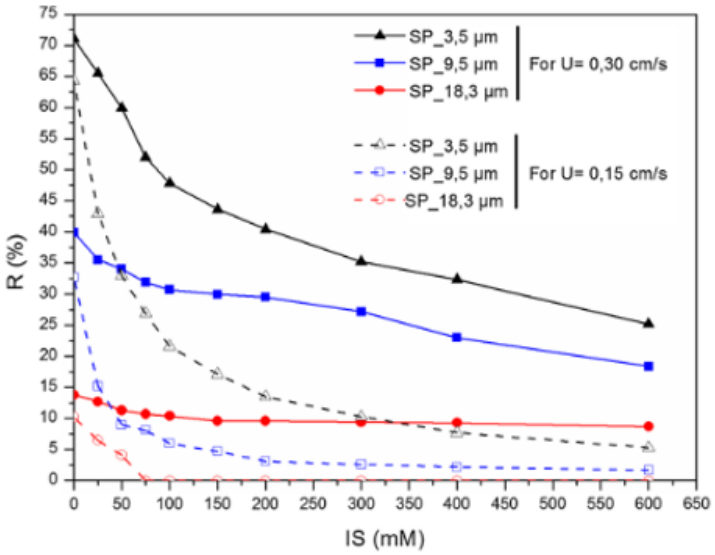

Figure 3.18: Effect of particle size, ionic strength, and flow velocity on the permeability recovery rate R. Larger particles are associated with lower recovery rates across the range of tested ionic strengths and flow velocities [Bennacer et al., 2017].

Concentration of particles

The concentration of particles injected into a porous domain is an important factor driving the behavior of clogging. Alem et al. [2015] experimentally demonstrated that, during the injection of a polydisperse suspension with particle sizes ranging from 1.7 to 40 µm into a sand column made of grains sieved from the Seine River, permeability impairment became more pronounced as the concentration of suspended particles increased (Fig. 3.19).

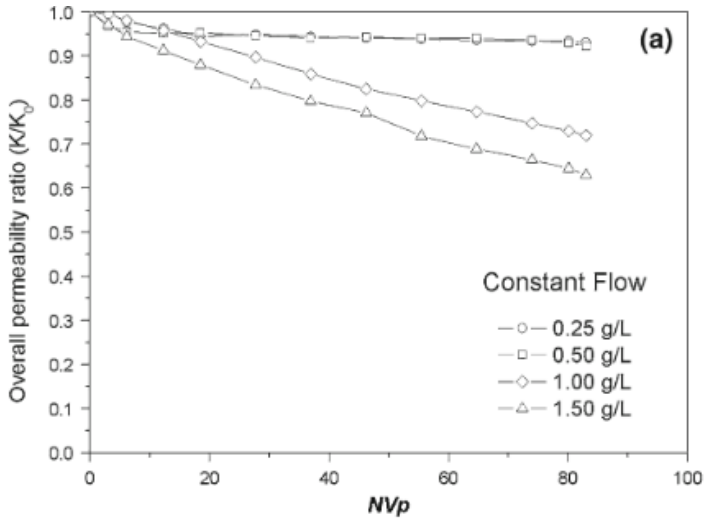

Figure 3.19: Evolution of the normalized permeability K/K_0 as a function of injected pore volumes NV_p for increasing particle concentrations under constant flow conditions [Alem et al., 2015]. Higher concentrations result in a faster permeability decline.

Moreover, Agbangla et al. [2012b] experimentally investigated the combined effect of particle volume fraction and flow velocity on clogging in a microfluidic dead-end filtration device composed of parallel channels (Fig. 3.20). Their results showed that for dilute suspensions, with a particle

volume fraction of about 5×10^{-4}, no clogging was observed over the range of flow velocities tested. As the particle volume fraction increased, particle deposition became more significant and clogging started to occur. Clogging was mainly observed at sufficiently high particle concentrations and high flow velocities, highlighting the coupled role of particle loading and hydrodynamic conditions in controlling deposition and clogging.

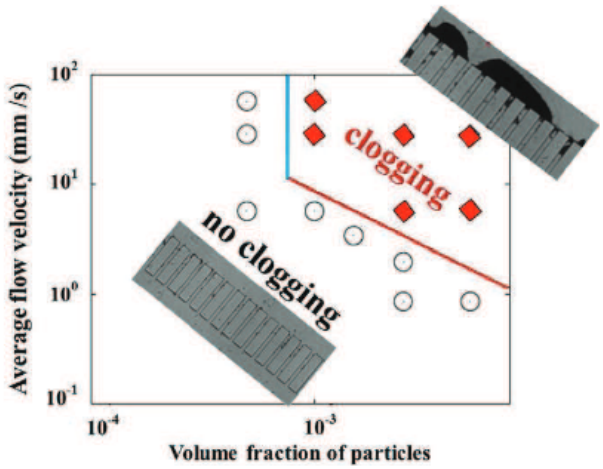

Figure 3.20: Experimental conditions leading to clogging in a dead-end microfluidic filtration system by injecting latex particles suspended in deionized water. The diagram maps the occurrence of clogging after 90 min of injection as a function of particle volume fraction and average flow velocity. Filled diamonds indicate conditions for which clogging was observed, whereas open circles correspond to conditions where no clogging occurred [Agbangla et al., 2012b].

3.2.3 Flow rate and injection protocols

The influence of flow rate on particle transport and retention in porous media has been extensively investigated by Bradford et al. [2007], Zhang et al. [2015], Li et al. [2008].

Using 1.1 µm latex colloids transported through quartz sand, Bradford et al. [2007] showed that the effect of flow rate depends strongly on the physicochemical conditions of the system. At an ionic strength of 56 mM, increasing the flow rate from approximately 0.1 to 0.45 cm/min led to lower particle retention for different grain sizes, as evidenced by the higher breakthrough concentrations shown in Fig. 3.21. Under these conditions, stronger hydrodynamic forces likely reduce particle retention by promoting detachment and limiting stable deposition.

However, this trend is not universal. At a lower ionic strength of 6 mM, the same study showed that increasing the flow rate could instead promote particle retention, as illustrated in Fig. 3.22. For example, the case $d_c/d_{50} = 0.008$ at 0.1 cm/min in Fig. 3.22(a) is comparable to the 360-Data case at 0.45 cm/min in Fig. 3.22(b), yet the latter exhibits a lower breakthrough concentration, indicating stronger retention. A similar tendency was reported by Agbangla et al. [2012b], whose results in Fig. 3.20 show that, for a given particle concentration, increasing the average flow velocity can promote the onset of clogging in latex suspensions injected in deionized water. These observations show that particle deposition and clogging are governed by a coupled effect of hydrodynamic and physicochemical conditions, rather than by flow rate alone.

Among the strategies proposed to mitigate particle-induced clogging in porous media, backwashing is one of the most commonly used approaches. This method consists of periodically reversing the flow once permeability has decreased, in order to restore throughput by destabilizing previously formed deposits [Lohaus et al., 2020, Zsirai et al., 2012]. At the pore scale, once

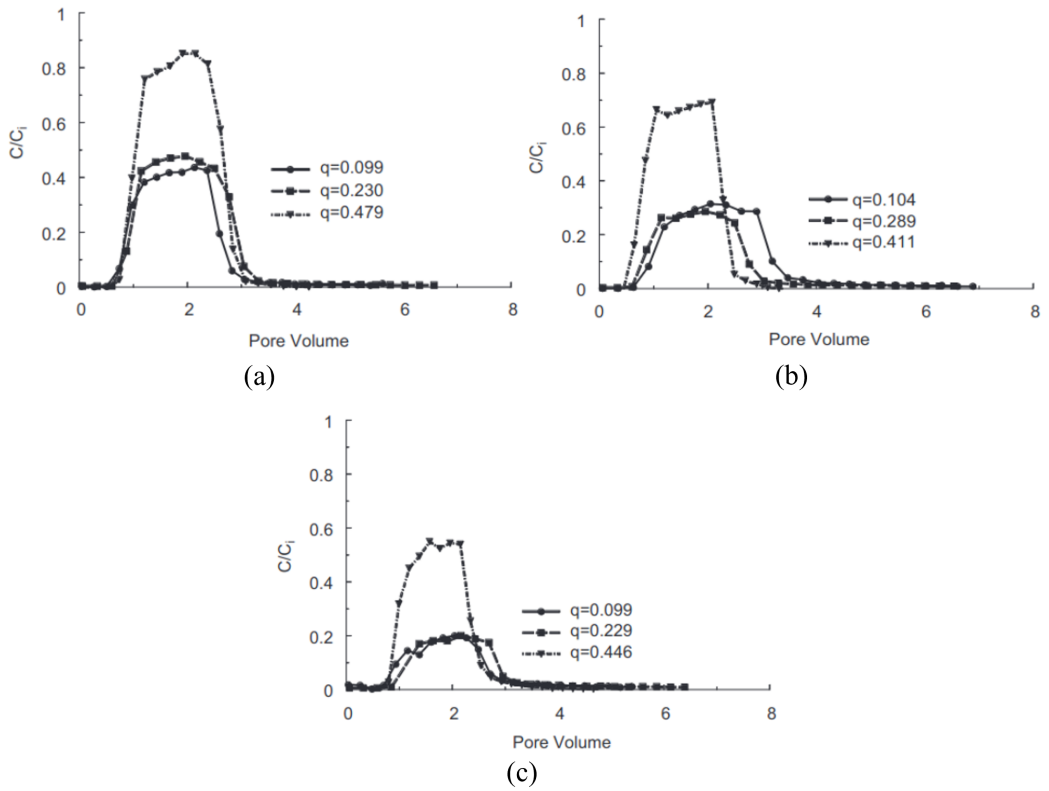

Figure 3.21: Breakthrough curves showing the retention of 1.1 µm latex colloids in quartz sand at an ionic strength of 56 mM for grain sizes of (a) 360 µm, (b) 240 µm, and (c) 150 µm. For each grain size, higher flow rates, ranging from approximately 0.1 to 0.45 cm/min, are associated with lower particle retention. Adapted from Bradford et al. [2007].

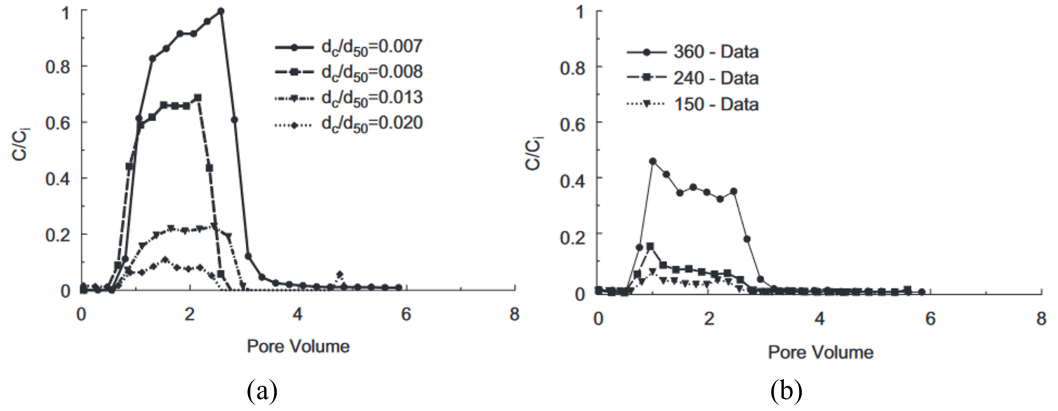

Figure 3.22: Concentration breakthrough curves showing particle retention at an ionic strength of 6 mM for flow rates of 0.1 cm/min in (a) and 0.45 cm/min in (b). The case $d_c/d_{50} = 0.008$ in (a) is comparable to the 360-Data case in (b), indicating greater particle retention at the higher flow rate. Adapted from Bradford et al. [2007].

clogging sets in at a constriction, particle accumulation upstream of the clog leads to the formation of clusters, which can be destabilized under reversed flow conditions. Using a combination of

microfluidic experiments and numerical simulations, Lohaus et al. [2020] showed that several mechanisms contribute to this process, including erosion of individual particles at lower reverse-flow intensities, and, at stronger reverse flow, partial cluster breakage (Fig. 3.23a) or cluster migration toward low-drag regions (Fig. 3.23b). These observations indicate that reverse-flow intensities higher than those responsible for clog formation are required for effective deposit destabilization.

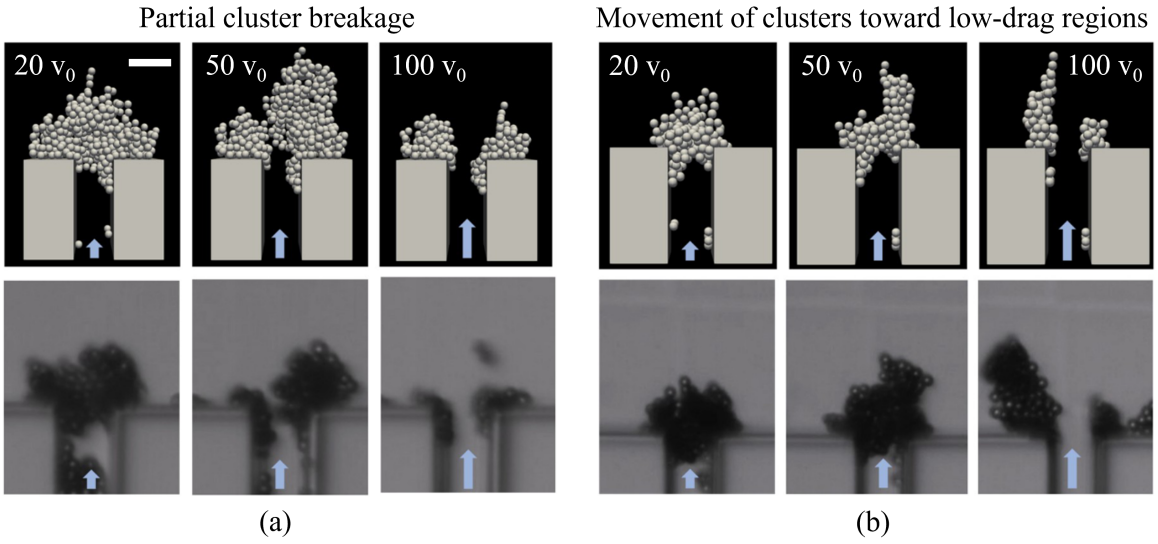

Figure 3.23: Dominant mechanisms observed during backwashing: (a) partial cluster breakage and (b) cluster migration toward low-drag regions. Top panels show the corresponding numerical simulation results for increasing reverse-flow intensity, while bottom panels show the microfluidic experiments for increasing reverse-flow velocity, from 0.1 μL/s to 6.7 μL/s. The scale bar represents 20 μm. Adapted from Lohaus et al. [2020].

Beyond backwashing applied after permeability loss, time-dependent injection protocols have been explored as a preventive strategy to delay clogging from the beginning of filtration. This approach is motivated by the idea that continuous hydrodynamic perturbations may prevent the formation of stable deposits. In this context, Dincau et al. [2022] investigated the effect of pulsatile flow in two-dimensional microfluidic channel arrays. Their results showed that, at relatively high ionic strength, sinusoidal pressure oscillations can extend the lifetime of the system before complete clogging occurs. They identified an optimal operating window for the oscillation amplitude, with an amplitude equal to 50% of the initial pressure drop providing the most effective mitigation. In contrast, a larger amplitude of 125%, involving flow reversal, did not improve mitigation during the early stage of the experiment and produced a response close to the continuous-flow case (Fig. 3.24a). This behavior was attributed to particle ejection from the formed filter cake and the subsequent redeposition of resuspended particles in downstream channels when flow resumes. At later times, however, the performance improved as the average flow rate decreased and particle ejection became less pronounced. In addition, for the optimal amplitude, increasing the oscillation frequency enhanced the mitigation effect, with 0.1 Hz leading to the slowest flow-rate decline, whereas 0.001 Hz remained close to the steady-flow condition (Fig. 3.24b).

These results highlight the potential of time-dependent forcing to delay clogging, while showing that its effect depends strongly on the imposed forcing conditions. Its behavior in heterogeneous porous media and under different physicochemical regimes remains to be clarified.

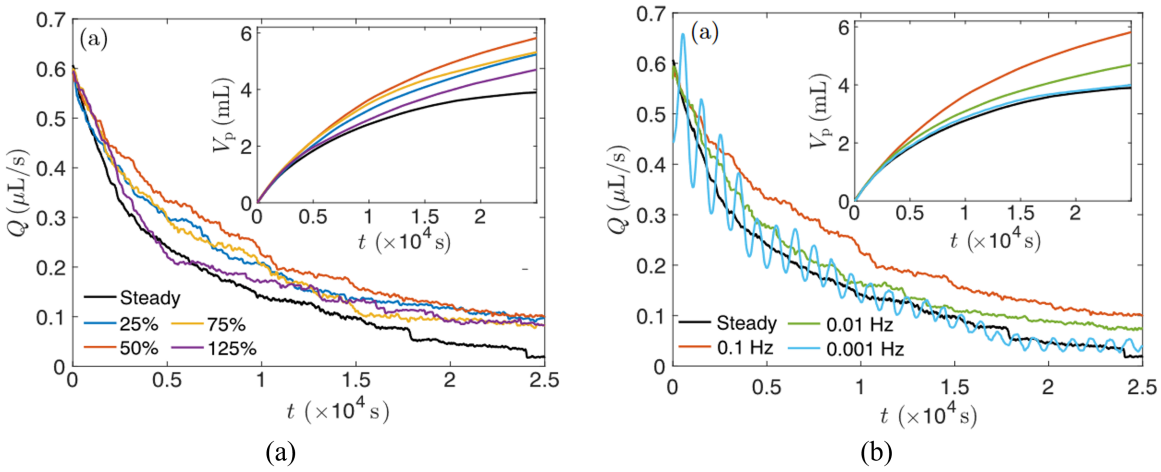

Figure 3.24: Effect of oscillatory flow on clogging mitigation in a two-dimensional microfluidic channel array, adapted from Dincau et al. [2022]. (a) Evolution of the flow rate with time for different oscillation amplitudes, showing that an amplitude of 50% of the initial pressure drop provides the most effective mitigation compared with steady flow, whereas an amplitude of 125% gives a response close to the continuous-flow case. (b) Evolution of the flow rate with time for different oscillation frequencies at a fixed amplitude of 50%, showing that 0.1 Hz yields the strongest mitigation, while 0.001 Hz remains close to the steady-flow case.

3.2.4 Influence of porous geometry and surface properties

Surface roughness

Surface roughness is an important morphological property that can significantly influence particle retention in porous media. Using micromodel experiments, Auset and Keller [2006] investigated the effect of collector roughness on colloid transport and showed that rough surfaces modify the local hydrodynamic conditions and the streamlines followed by particles, thereby increasing particle–collector interactions as increasing roughness reduce the magnitude of energy barrier, and promote more particles attaching to solid surfaces [Bradford and Torkzaban, 2013]. As illustrated in Fig. 3.25a, rough collectors promote greater particle deposition than smooth collectors. This trend is further supported by the higher collision efficiencies measured for rough surfaces over the range of ionic strengths investigated (Fig. 3.25b).

Surface chemical heterogeneity

Surface chemical heterogeneity of the porous matrix plays a key role in controlling colloid transport and deposition. Johnson et al. [1996] investigated the effect of geochemically heterogeneous sand grains by comparing clean and partially coated collectors in column experiments. As shown in Fig. 3.26, the presence of favorable surface patches strongly alters colloid mobility. In the absence of favorable deposition sites ($\lambda = 0\%$), particles exhibit nearly complete breakthrough, indicating negligible retention. However, as the fraction of favorable surface sites increases, breakthrough curves progressively deviate from this ideal transport behavior, reflecting enhanced particle deposition within the porous medium. These observations highlight that even a small fraction of chemically favorable surfaces can significantly increase colloid retention.

A similar behavior was reported by Guo et al. [2020], who investigated the transport of negatively charged carboxylate-modified polystyrene particles through microfluidic porous media

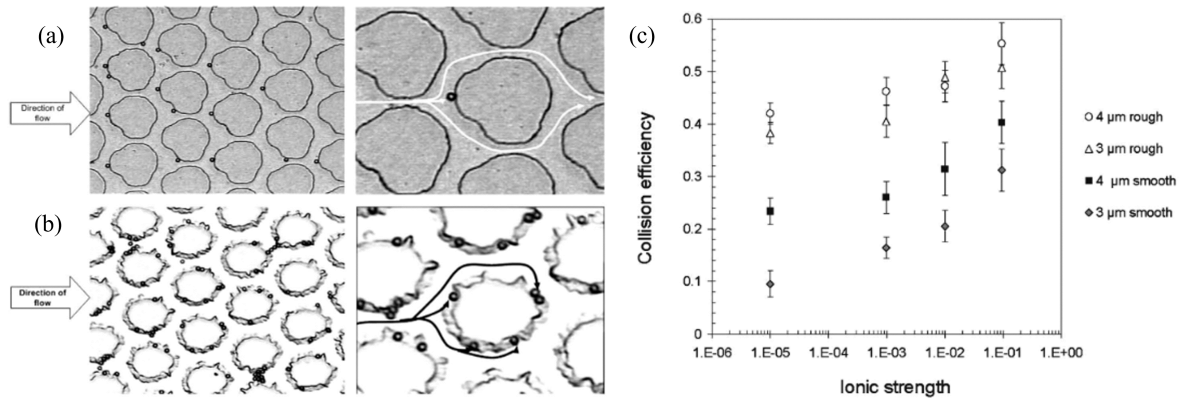

Figure 3.25: Effect of collector surface roughness on particle deposition and collision efficiency, adapted from Auset and Keller [2006]. Microscopic images compare particle deposition in micromodels composed of smooth collectors (a) and rough collectors (b), with hand-drawn streamlines illustrating the particle trajectories around collectors. Panel (c) shows the collision efficiency as a function of ionic strength for 3 µm and 4 µm particles flowing through smooth and rough micromodels. For both particle sizes and across the investigated ionic strengths, rough collectors exhibit higher collision efficiencies than smooth collectors, indicating enhanced particle–surface interactions in the presence of surface roughness.

composed of mixtures of positively and negatively charged collectors. Because the particles carried negatively charged carboxylate surface groups, they exhibited near-complete breakthrough when flowing through fully negatively charged collectors. However, as the fraction of positively charged collectors increased, particle deposition was promoted and breakthrough was progressively reduced. These results confirm that surface charge heterogeneity strongly controls particle transport and retention.

Tortuosity and connectivity

The geometrical organization of the porous medium, including connectivity and tortuosity, plays a key role in controlling particle transport and clogging. Bacchin et al. [2014] investigated these effects using microfluidic channel arrays with different levels of connectivity and tortuosity. As shown in Fig. 3.27a, in straight and disconnected channels, particle deposition mainly occurs at the entrance of the microseparators, while particles that do not deposit are efficiently transported downstream by the flow. In this configuration, deposition remains localized, and no significant accumulation occurs between channels.

When connectivity between channels is introduced (Fig. 3.27b), the flow distribution becomes heterogeneous, inducing transverse flows and velocity variations at the junctions. These hydrodynamic heterogeneities promote particle accumulation at specific locations and lead to a more spatially distributed deposition pattern.

In the presence of tortuosity (Fig. 3.27c), the flow paths become more complex, generating stagnation regions and preferential deposition zones upstream of the collectors. Over time, particles accumulate in these regions and progressively extend toward the inlet, eventually forming a filter cake. This demonstrates that tortuosity enhances internal clogging by promoting localized deposition and limiting particle transport through the porous network.

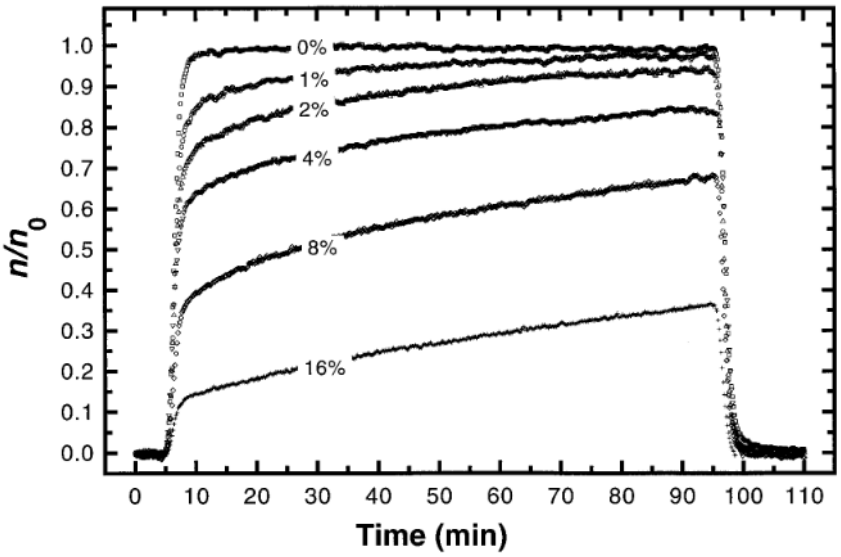

Figure 3.26: Breakthrough curves of colloidal particles in a sand column with varying degrees of surface chemical heterogeneity. The percentage indicates the fraction of iron oxyhydroxide-coated sand grains, which provide favorable sites for particle deposition. Increasing the fraction of coated grains leads to a progressive reduction in breakthrough concentration, demonstrating enhanced particle retention due to surface charge heterogeneity [Johnson et al., 1996]

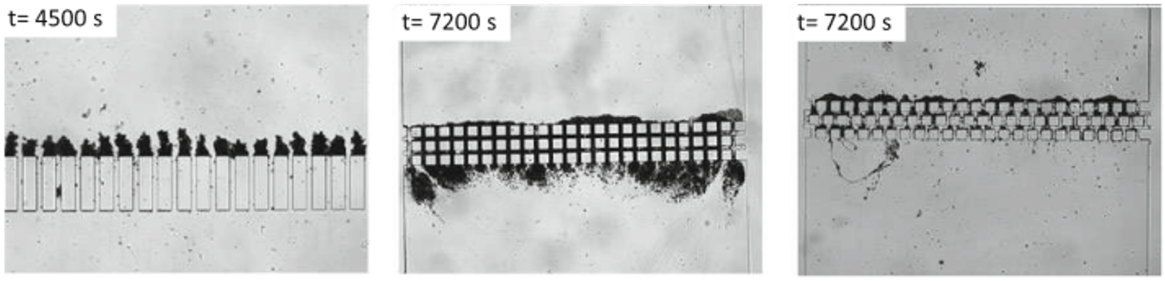

Figure 3.27: Effect of porous structure on particle deposition and clogging, adapted from Bacchin et al. [2014]. Images correspond to the final stage of filtration in microfluidic devices with (a) straight and disconnected channels, (b) connected channels, and (c) staggered (tortuous) channels. Increasing connectivity and tortuosity leads to more heterogeneous flow fields, promoting localized deposition, particle accumulation, and the development of internal clogging.

3.3 Techniques to investigate particle deposition and clogging in porous media

The role of the main parameters governing particle deposition and clogging has been widely reviewed in the previous section, but the level of understanding of the underlying mechanisms strongly depends on the techniques used to investigate these processes. Different approaches provide access to different levels of information, ranging from global measurements of retention and permeability decline to direct observations of particle transport, deposition, and clogging at the pore scale. In this section, we briefly review the main numerical and experimental approaches employed to study these phenomena.

3.3.1 Numerical approaches

Understanding permeability impairment induced by particle transport has motivated the development of several pore-scale numerical approaches. These methods aim to capture the complex interplay between hydrodynamics, particle transport, and retention mechanisms leading to several clogging mechanisms such as aggregation, sieving, and bridging. However, each modeling framework involves specific assumptions and limitations, particularly regarding the level of physical detail, computational cost, and the ability to represent large-scale porous structures.

High-fidelity Euler–Lagrange approaches explicitly resolve the fluid phase while tracking individual particles in a Lagrangian framework. Depending on the method used to solve the fluid phase, these approaches include CFD–DEM, where the Navier–Stokes equations are commonly discretized using methods such as the finite-volume method, and LBM–DEM, where the fluid dynamics are solved using the lattice Boltzmann method. In both cases, the discrete element method (DEM) is used to describe particle motion and particle–particle and particle–wall interactions.

CFD–DEM explicitly resolves fluid flow and particle dynamics at the pore scale, accounting for hydrodynamic interactions, particle–particle and particle–wall contacts, and colloidal forces [Tsuji et al., 1993, Sun, 2023, Fogouang et al., 2024, Maya Fogouang et al., 2025]. These models can reproduce a wide range of clogging mechanisms, including aggregation, sieving, and bridging, but remain computationally expensive for large domains representative of porous media. Direct particle-scale approaches have also been used to investigate particle straining in three-dimensional porous media. Mirabolghasemi et al. [2015] simulated straining in pore geometries reconstructed from X-ray microtomography images and compared the resulting filtration coefficients with particle-flooding experiments. Khan et al. [2017] further combined direct particle-scale simulations with a pore-network model and CT-imaged particle-flooding experiments to investigate the retention of bidispersed particles and the resulting porosity and permeability reduction. Particle-scale modeling has also been extended to three-dimensional rough-walled fractures for particulate and proppant transport [Zhang and Prodanović, 2019, Zhang, 2021]. These studies consider applications related to hydraulic fracturing and wellbore systems, generally involving higher flow rates than those investigated in the present work.

Lattice Boltzmann methods provide an alternative way of resolving the fluid phase within the same Euler–Lagrange framework when coupled with Lagrangian particle tracking or DEM. Their regular lattice formulation is particularly convenient for simulating flow through geometrically complex porous structures [Ladd, 1994]. Parvan et al. [2020] used LBM to simulate particle deposition and the resulting porosity and permeability reduction in porous structures obtained from X-ray tomography. More recently, Yin et al. [2024] coupled LBM with DEM to investigate clogging and unclogging associated with particle arch formation at pore constrictions. Like CFD–DEM, these approaches provide detailed information on pore-scale particle dynamics but remain computationally demanding for large three-dimensional domains.

Eulerian approaches describe particle transport using continuum equations for concentration, coupled with simplified retention formulations [Raoof et al., 2010, Seetha et al., 2017]. While computationally efficient and applicable at the representative elementary volume (REV) scale, these models do not explicitly resolve pore-scale mechanisms such as particle sieving and bridging.

Pore-network models (PNMs) provide an intermediate framework, representing the porous medium as a network of interconnected pores and throats [Blunt et al., 2013]. Depending on the formulation, PNMs can simulate particle transport either through Lagrangian particle tracking or Eulerian concentration-based approaches. These models are computationally efficient and allow for simulations at the REV scale, while incorporating key mechanisms such as deposition, aggregation, and sieving. PNMs have also been applied specifically to particle retention and formation damage. For example, Khan et al. [2017] used a pore-network model to describe the deposition of smaller

particles, coupled with direct particle-scale simulations for the retention of larger particles, and compared the resulting permeability impairment with particle-flooding experiments. However, accurately representing bridging remains challenging because the formation of a stable particle arch depends on the local pore geometry and on the collective configuration of several particles at a constriction.

Table 3.2 summarizes the main numerical approaches used to study particle clogging in porous media and compares both the clogging mechanisms they can represent and their ability to describe the system at the REV scale. The symbol ∼ indicates that the representation of the corresponding mechanism depends on the specific model formulation.

Table 3.2: Comparison of numerical approaches for modeling particle transport and clogging in porous media.

Method	Aggregation	Sieving	Bridging	REV scale
CFD–DEM (Euler–Lagrange)	✓	✓	✓	×
Euler–Euler	✓	×	×	✓
Pore-network models (PNM)	✓	✓	∼	✓

3.3.2 Experimental approaches

Conventional porous media experiments

Extensive experimental studies have been conducted to investigate filtration and clogging in conventional porous media, particularly through core-flood experiments. In these experiments, geological core samples are subjected to flow conditions representative of subsurface or reservoir environments. The temporal evolution of pressure drop is commonly monitored as a macroscopic indicator of clogging, from which changes in the permeability of the medium can be inferred [Ott et al., 2012, Unsal et al., 2018]. Similar approaches have also been used in other complex porous structures, such as membranes with cylindrical pores of varying sizes [Ramachandran and Fogler, 1999] and columns packed with beads [Mays and Hunt, 2005]. In such systems, particle retention is often estimated from the particle concentration measured at the outlet of the porous medium [Li et al., 2005, Gregory and Wishart, 1980]. While these approaches provide valuable macroscopic insights, they remain limited in resolving the fundamental pore-scale mechanisms governing particle deposition and clogging, as these media are generally opaque. In addition, the intrinsic geometric complexity and multiscale heterogeneity of natural porous media make it difficult to isolate the role of individual parameters and to directly interpret the observed behavior.

Advanced imaging techniques in porous media

To overcome these limitations, advanced imaging techniques have been developed to access the internal structure of porous media. X-ray microtomography enables three-dimensional reconstruction of particle distributions within the pore space, providing detailed spatial information [Gaillard et al., 2007, Bultreys et al., 2022]. In parallel, refractive index-matching methods combined with optical imaging allow transparent visualization of particle transport and deposition in model systems [Wiederseiner et al., 2011, Schneider et al., 2021, Bizmark et al., 2020]. Despite these advances, such techniques often involve significant experimental complexity and may suffer from limited temporal resolution or restricted control over flow and physicochemical conditions, which constrain systematic investigations.

Microfluidic micromodels

Microfluidic techniques, therefore, emerge as a powerful approach to investigate particle transport and clogging at the pore scale. They enable direct and real-time observation of particle trajectories, deposition events, and clogging dynamics at the scale of individual pores. Microfluidic porous media, or micromodels, are transparent devices composed of interconnected pore networks, typically designed using computer-aided design and implemented using a range of materials such as glass, silicon, polydimethylsiloxane (PDMS), or PMMA through different microfabrication approaches [Auset and Keller, 2004, Chrysikopoulos et al., 2011, Mohammadi et al., 2013, Gunda et al., 2011, Park et al., 2012]. Three-dimensional porous micromodels can also be obtained by packing glass beads [Datta et al., 2013]. These systems differ in their dimensionality as well as in their mechanical, thermal, and chemical properties, which influence both fabrication constraints and flow behavior. Their small dimensions reduce material and fluid consumption and enable rapid and reproducible experiments. In addition, microfluidic platforms provide a high level of control over hydrodynamic and physicochemical conditions, as parameters such as flow rate, pressure, particle size, salinity, and surface properties can be systematically varied.

Fabrication methods The fabrication of microfluidic micromodels relies predominantly on lithographic techniques that enable precise control of pore-scale geometry. In particular, photolithography is widely used to transfer a predefined pattern onto a photoresist layer deposited on a substrate, forming a solid microstructured mold. This mold is commonly used as a template for replica molding of elastomeric materials such as PDMS, in a process referred to as soft lithography [Whitesides et al., 2001]. This approach enables rapid and reproducible fabrication of two-dimensional micromodels with high geometric fidelity. Alternatively, rigid micromodels can be constructed directly from patterned photoresist or etched substrates such as glass or silicon, which are less prone to deformation under pressure but require more complex fabrication procedures [Beaumont et al., 2013]. As a result, a trade-off exists between fabrication simplicity and mechanical stability, which must be considered when designing experiments.

Geometry design and flow heterogeneity Beyond material selection, the geometry of the porous network plays a central role in controlling flow distribution and particle transport at the pore scale. Microfluidic micromodels can be designed with a wide range of geometries, broadly classified into regular and irregular structures (Fig. 3.28). Regular geometries, such as arrays of pillars [Grate et al., 2012], cross-hatched grids [Osei-Bonsu et al., 2017], or idealized pore body–throat networks [Meybodi et al., 2011], provide simplified and well-controlled configurations that facilitate the investigation of fundamental mechanisms under homogeneous conditions. In contrast, irregular geometries, including interconnected channel networks or structures inspired by natural porous media, introduce spatial heterogeneity and tortuosity, leading to non-uniform velocity fields and preferential flow paths [Soudmand-asli et al., 2007, Gauteplass et al., 2015, Park et al., 2012].

This flow heterogeneity has direct implications for particle transport, as it promotes localized accumulation in specific regions such as constrictions and stagnation zones, which are known to play a key role in clogging dynamics. Many microfluidic studies have therefore focused on simplified and regular geometries, which allow precise control of flow conditions and facilitate mechanistic analysis [Kim et al., 2022, Delouche et al., 2020, Duchêne et al., 2020, Auset and Keller, 2006]. However, such configurations do not fully capture the geometric complexity of natural porous media. In contrast, heterogeneous and tortuous geometries introduce spatial variability in flow fields, which is essential to reproduce realistic particle transport and clogging behavior [Esneu et al., 2025a,b].

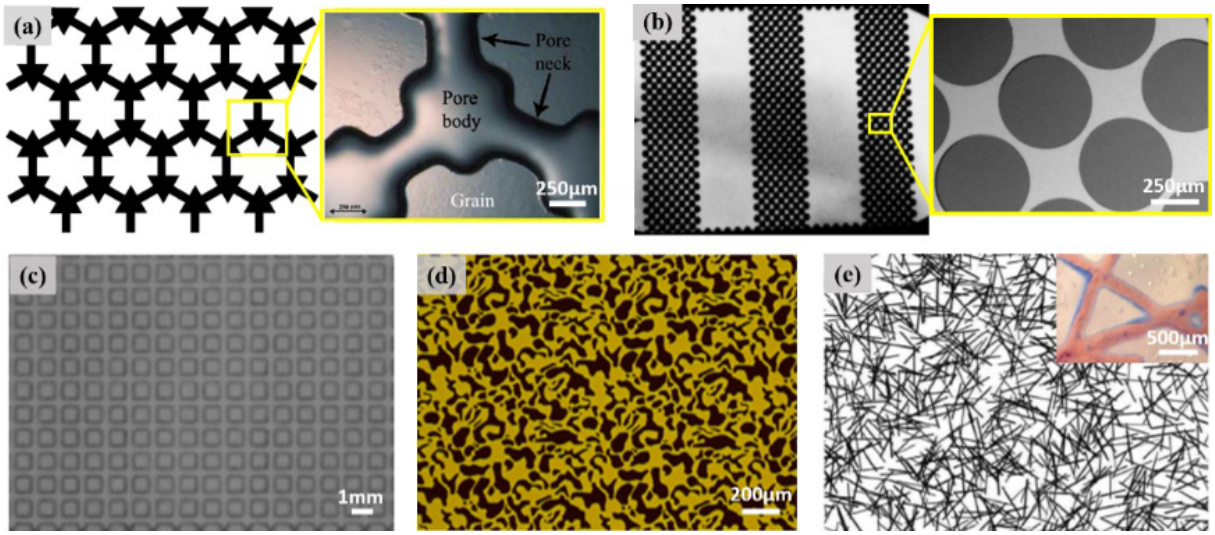

Figure 3.28: Examples of regular and irregular two-dimensional porous geometries used in microfluidic micromodels: (a) pore body–throat network [Meybodi et al., 2011], (b) regular pillar array [Grate et al., 2012], (c) cross-hatched grid [Osei-Bonsu et al., 2017], (d) irregular pattern representing a thin section of real rock [Gauteplass et al., 2015], and (e) irregular interconnected channels [Soudmand-asli et al., 2007]. Reproduced from Anbari et al. [2018].

In this context, microfluidics combined with heterogeneous porous geometries provides a suitable framework to investigate clogging mechanisms under conditions that are closer to those encountered in subsurface systems.

3.4 Research gaps and scientific questions

The review presented above highlights major advances in the understanding of particle transport and clogging in porous media. However, several important limitations remain when considering heterogeneous porous systems representative of subsurface environments. In particular, most studies rely either on macroscopic indicators, such as permeability decline or breakthrough curves, which do not resolve how deposits organize and evolve within the pore space, or on pore-scale investigations performed in simplified geometries that do not capture the heterogeneity and tortuosity of realistic porous media. As a result, the spatial organization of clogging, the respective roles of the dominant deposition regimes, and the extent to which their impact on permeability impairment can be predicted or controlled remain unclear. These limitations motivate the research gaps and scientific questions addressed in this thesis:

Gap 1: limited pore-scale understanding of aggregation-driven deposition patterns in heterogeneous porous media. In adhesion-dominated regimes, aggregation-driven clogging is commonly described as a progressive buildup of particles at pore constrictions through successive deposition events. Previous studies have shown that, under such conditions, aggregation may also produce finger-like or dendritic deposits in simplified geometries. However, the formation of these deposits in heterogeneous porous networks, their preferential localization in stagnation regions, and their interaction with the local flow field remain poorly understood.

Scientific question 1: *Under which pore-scale flow conditions do dendritic deposits form in heterogeneous porous media, and how do they contribute to permeability reduction?*

Gap 2: limited understanding of the mechanisms governing bridging-induced clogging in heterogeneous porous media. Pore bridging is a well-established mechanism contributing to particle retention and permeability reduction in porous media. Previous studies have shown that parameters such as flow conditions, particle concentration, and pore-scale confinement can influence bridging-induced clogging. However, in heterogeneous porous networks, how these parameters interact to control the onset and evolution of bridging remains insufficiently understood. This question is particularly relevant in a hydrodynamic-dominated regime, where aggregation-driven deposition is reduced, and clogging is primarily governed by flow and geometric confinement.

Scientific question 2: *How do flow conditions, particle properties, and pore-scale confinement interact to control bridging-induced clogging and the resulting permeability reduction in heterogeneous porous media?*

Gap 3: lack of predictive frameworks coupling pore-scale experiments and pore-network modeling. Although pore-network models have been widely used to investigate transport and permeability evolution in porous media, they often rely on simplified or purely theoretical clogging rules and are rarely constrained by direct pore-scale experimental observations in realistic heterogeneous geometries. In particular, there is still a lack of predictive frameworks capable of incorporating probabilistic bridging laws and reproducing the permeability impairment observed experimentally in microfluidic porous networks.

Scientific question 3: *Can a pore-network modeling framework informed by pore-scale experiments reproduce the dynamics of permeability impairment induced by hydrodynamic pore bridging in heterogeneous porous media?*

Gap 4: limited understanding of the effect of time-dependent flow forcing across different deposition regimes in heterogeneous porous media. Most existing studies focus on particle deposition and clogging under steady injection conditions, whereas fewer investigate how these processes are modified by time-dependent flow forcing. Recent works have shown that oscillatory or pulsatile injection can affect particle retention and permeability evolution, particularly in simplified geometries and under adhesion-dominated conditions. However, its effect across different deposition regimes remains insufficiently understood, especially in heterogeneous porous media where aggregation-dominated and hydrodynamic-dominated behaviors may arise under different physicochemical and flow conditions.

Scientific question 4: *How does time-dependent flow forcing affect particle deposition, clogging dynamics, and permeability evolution across different deposition regimes in heterogeneous porous media?*

3.5 Research strategy and thesis organization

To address these questions, we adopt a pore-scale experimental and analysis framework based on direct visualization in heterogeneous microfluidic porous media, combined with flow measurements, image-based analysis, and pore-scale simulations, all of which are presented in the next chapter. This integrated framework enables the identification of dominant clogging mechanisms and the quantification of their impact on permeability under controlled physicochemical and hydrodynamic conditions, including time-dependent forcing.

The following chapters investigate clogging across different deposition regimes. Chapter 5 examines aggregation-driven deposition and the formation of dendritic structures in heterogeneous porous networks (Question 1). Chapter 6 focuses on hydrodynamic bridging and its control by flow conditions, particle properties, and pore-scale confinement, while coupling experiments with

pore-network modeling (Questions 2 and 3). Chapter 7 analyzes the effect of time-dependent flow forcing on clogging dynamics across regimes (Question 4). Finally, Chapter 8 explores how clogging-induced flow alterations contribute to the mobilization of trapped contaminants in porous media, providing a broader perspective on the implications of these mechanisms.

Chapter 4

Materials and Methods

This chapter presents a detailed description of the experimental and numerical approaches developed to investigate particle transport, clogging, and flow dynamics in microfluidic porous media. We begin with a description of the geometric designs used, ranging from single-grain collectors to heterogeneous and tortuous media models, along with the microfabrication method used to produce PDMS microfluidic devices. Next, we outline the characteristics of particle suspensions, including particle properties and the use of density-matched carrier fluids. We then present the experimental apparatus used throughout our work, covering flow control strategies, sensing instruments, as well as the optical imaging methods employed for real-time observation of the processes occurring in the porous domain. Subsequently, image processing techniques are used to evaluate how porosity and spatial particle deposition evolve throughout the experiments. A dedicated section addresses the hydraulic behavior of the PDMS devices, including how their deformation impacts flow resistance and permeability along with the way of calculating permeability for our geometric models in use. Finally, we present the numerical simulation workflow, detailing how pore-scale models are built, solved, and used to assess how clogging alters local transport and overall flow connectivity.

4.1 Design and fabrication of microfluidic porous models

Microfabrication is the technique used to produce the microfluidic devices employed in our flow experiments. The technique is based on soft lithography [Xia and Whitesides, 1998], which is a common technique in microfluidics. It involves the design of porous media geometry and the fabrication of a master wafer. The PDMS (PolyDiMethylSiloxane) is then poured on the master wafer and bonded to a glass slide to obtain the final microfluidic device. The next sections will give a detailed description of the design specifications and the fabrication techniques.

4.1.1 Geometric definition of the designed porous configurations

In this study, we investigate two classes of microfluidic geometries designed to progressively increase structural complexity. The first consists of a *single-grain collector* configuration, where a cylindrical obstacle is placed within a straight microchannel to isolate local hydrodynamic and adhesive effects around an individual collector. The second class comprises *heterogeneous tortuous porous domains*, engineered to reproduce key geometric characteristics of natural subsurface media, including spatial disorder, pore-size variability, and constriction heterogeneity. These geometries enable the investigation of particle transport and clogging mechanisms under realistic pore-network conditions.

All photomask layouts are generated using KLayout, a computer-aided design (CAD) tool widely employed in photolithography-based microfabrication.

The three fabricated models are denoted as $M1$, $M2$, and $M3$. Model $M1$ corresponds to the single-grain configuration, whereas $M2$ and $M3$ represent heterogeneous porous domains with distinct pore-scale statistics. Their principal geometric characteristics are summarized in Table 4.1, including porosity (ϕ), representative pore and constriction length scales derived from image analysis, and an apparent permeability K_{app}. The methodology used to determine these quantities, particularly the hydraulic characterization leading to K_{app}, is detailed in Chapter 4.5.

Table 4.1: Geometric and hydraulic characterization of the three microfluidic models, where K_{app} is the apparent permeability, CSD is the constriction size distribution, and PSD is the pore size distribution.

Model	**Porosity** ϕ	K_{app} **(m^2)**	**Depth (µm)**	**CSD mean (µm)**	**PSD mean (µm)**
M1	N/A	3.3×10^{-11}	20	40	100
M2	0.48	2.96×10^{-12}	20	45	100
M3	0.47	1.8×10^{-12}	20	20	73

Single-grain-collector geometry

The single-grain-collector device ($M1$) has a straight inlet channel of width 500 µm that tapers into a converging section and then to a narrow throat of width 100 µm (Fig. 4.1). A single cylindrical obstacle (hereafter referred to as a "grain") is placed at the center of the throat to form a well-defined collector. The channel then diverges to a width of 500 µm downstream of the obstacle.

The inlet and outlet ports are designed to be slightly wider than 500 µm to ensure reliable punching with a 500 µm biopsy punch and to avoid damaging the patterned area during microfabrication. The total length of the device is 21 mm.

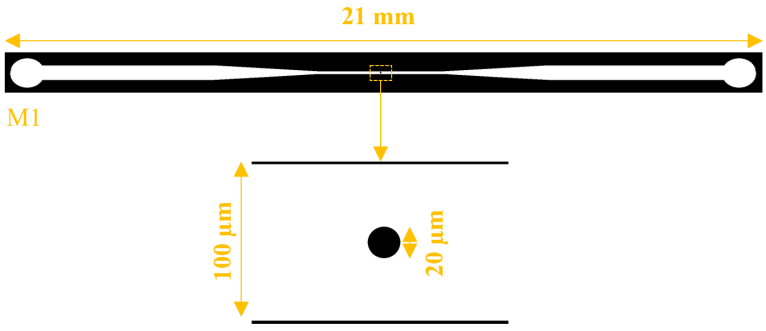

Figure 4.1: Schematic of the single-grain-collector microfluidic geometry ($M1$). A 500 µm-wide inlet channel converges to a 100 µm-wide throat containing a centered cylindrical collector (grain), followed by a diverging section returning to 500 µm.

Heterogeneous tortuous geometries

To investigate particle transport and clogging in realistic pore networks, we design two heterogeneous tortuous porous micromodels that mimic key geometrical features of natural subsurface formations. Each device consists of three main sections: an inlet manifold, a central porous domain, and a symmetric outlet manifold, which promotes a homogeneous distribution of flow across the porous region and limits boundary effects.

We create the inlet/outlet manifolds in KLayout and design them to progressively distribute the flow across the porous domain. To introduce spatial disorder while avoiding artificial periodicity, we generate large, non-repetitive porous patterns in MATLAB using an image-quilting workflow [Efros and Freeman, 2023], in which a large domain is constructed by stitching together smaller texture patches. We then import the resulting binary geometry into KLayout and merge it into the final photomask layout.

The two micromodels (Fig. 4.2a,b) share the same overall footprint (36 mm long and 6 mm wide) and the same layout: inlet and outlet networks (11.5 mm each) connected to a 12 mm porous domain through 0.5 mm transition zones. While their porosities are nearly identical, 48% for model (a), referred to as $M2$ throughout the thesis, and 47% for model (b), referred to as $M3$, we intentionally differentiate their internal pore space statistics. In particular, $M3$ is designed with smaller pores and narrower throats than $M2$, yielding a more constrictive network for comparison. We quantify pore-scale metrics (pore diameters and constriction lengths) from 2D image analysis using an in-house MATLAB workflow and ImageJ skeleton analysis (Listings A.1 and A.2). The resulting distributions are fitted with log-normal models to extract representative parameters (e.g., modes and arithmetic means), as reported in Fig. 4.2.

These two geometries therefore provide controlled yet distinct pore-scale environments, enabling a systematic investigation of how pore and throat size distributions influence particle deposition, clogging dynamics, and permeability evolution.

4.1.2 Photolithographic fabrication of the master wafer

The master wafers used to fabricate the microfluidic devices were produced at the Renatech LAAS-CNRS using standard SU-8 photolithography in a cleanroom environment. The process follows established fabrication protocols, including spin-coating, UV exposure through a photomask, and development, without modification. An overview of the procedure is provided in Fig. 4.3.

The process starts by cleaning and dehydrating a 4-inch silicon wafer. A uniform layer of SU-8 epoxy photoresist is then spin-coated onto the wafer to obtain a final structure height of 20 µm, which corresponds to the channel depth. Solvents are evaporated to partially solidify the resist by a soft bake on a hot plate to ensure good adhesion and uniform resist thickness. Subsequently, a chrome-coated glass photomask with the predefined features is aligned above the wafer, and the photoresist is exposed to UV light. The exposed regions crosslink and become insoluble in the developer solution. After exposure, the wafer is post-exposure baked to complete the crosslinking of the exposed SU-8. It is then developed in SU-8 developer (typically propylene glycol monomethyl ether acetate, PGMEA), which removes the unexposed photoresist. This yields a negative 3D master wafer of the final predefined patterns, which is subsequently used for soft lithography as detailed in Chapter 4.1.3. Before casting PDMS, we silanize the master wafer in vapor phase using TCP (trichloro(1H,1H,2H,2H-perfluorooctyl)silane) to render the surface hydrophobic and facilitate demolding. We also provide in the Appendix the complete mask layouts for both designs: the single-grain-collector geometry ($M1$) replicated 19 times (Fig. A.2) and the heterogeneous tortuous porous-domain layouts, with 4 replicas of each configuration ($M2$ and $M3$) (Fig. A.3).

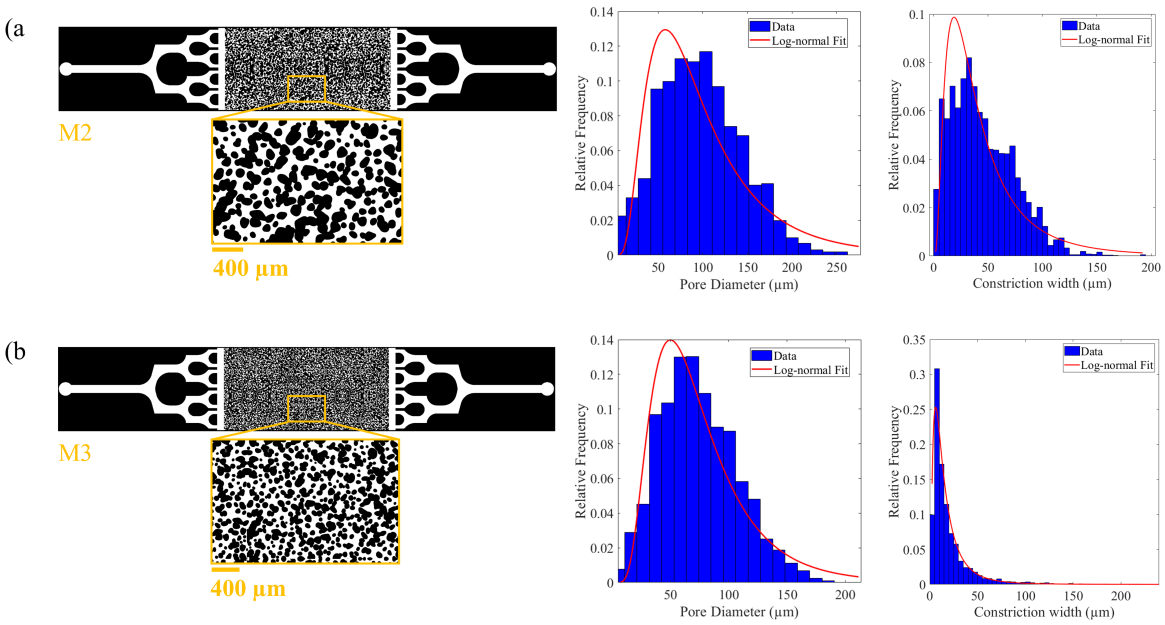

Figure 4.2: Two microfluidic porous micromodels used in this study, referred to throughout the thesis as M2 and M3, and their geometric characterization. Panels (a) and (b) show the full chip layouts of M2 and M3, respectively, where black denotes the solid matrix and white the pore space. Each device consists of an inlet manifold and an outlet manifold (11.5 mm each) connected by a central porous region (12 mm), for an overall footprint of 36 mm × 6 mm. The zoomed views highlight the disordered grain packing within the porous region. The histograms on the right show the pore-diameter and constriction-width distributions obtained from the 2D image analysis, with log-normal fits shown as solid red curves. In M2, the pore-diameter distribution peaks around ~ 60 μm (mean ~ 97 μm), and the constriction widths peak near ~ 19 μm (mean ~ 45 μm). In M3, pores are overall smaller (mode ~ 50 μm; mean ~ 73 μm), and the constrictions are substantially tighter, with the distribution clearly shifted toward smaller widths (mode ~ 5 μm; mean ~ 20 μm).

4.1.3 Microfluidic devices in PDMS

Following the microfabrication of the master wafer containing the predefined geometries of the pores, fabrication of the PDMS chips is the next step (Fig. 4.3). PDMS, a popular material in soft lithography, possesses homogeneity, isotropicity, optical transparency, flexibility, and biocompatibility [Whitesides et al., 2001]. Particularly, we prepare PDMS using the base to curing agent ratio 10:1.

Then, after mixing PDMS thoroughly, we take it for degassing in a vacuum chamber to remove all air bubbles that may affect bonding and imaging. Next, we pour the degassed mixture of PDMS over the master wafer and cure it at 65 °C for 1.5 hours, followed by an overnight rest at room temperature to complete the crosslinking. The cured PDMS replica is carefully peeled from the reusable master wafer and trimmed to match the dimensions of the glass slide. Inlet and outlet ports are then punched at the designated locations using 0.5 mm biopsy punches. The port diameter is selected to match the stainless-steel fluidic connectors, which are coupled to Tygon tubing with an internal diameter of 0.5 mm. The detailed specifications of the fluidic connectors are provided in Chapter 4.3.

Before bonding, the PDMS replica is cleaned in an ultrasonic bath with ethanol and ultrapure

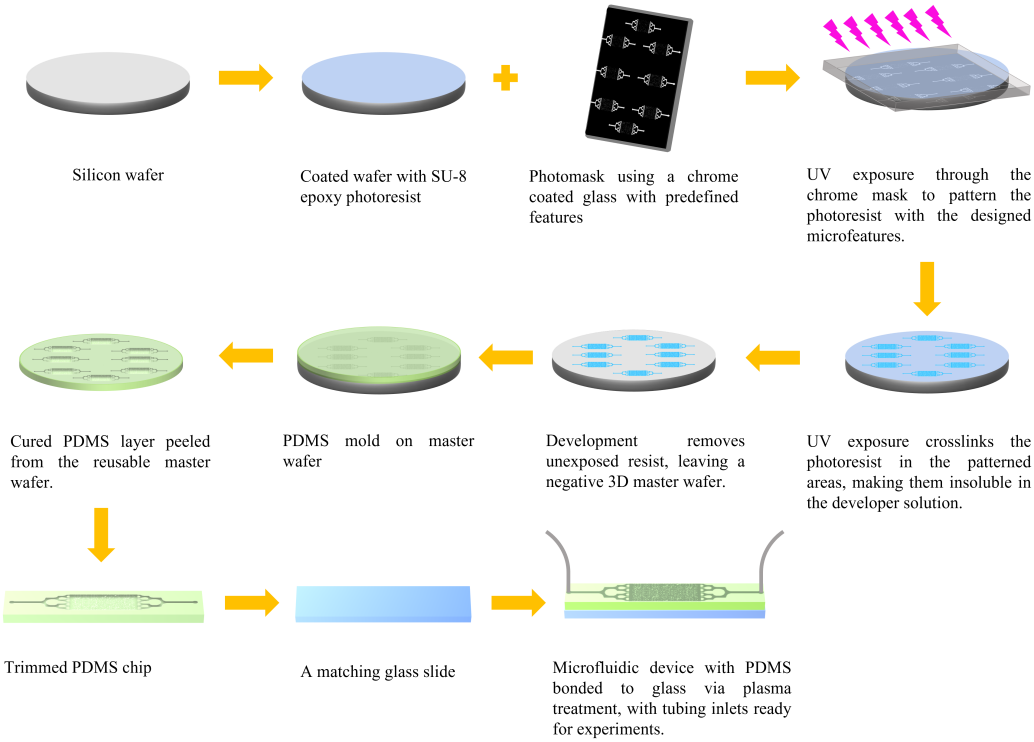

Figure 4.3: Step-by-step schematic of the microfabrication workflow. The master wafer is produced by patterning SU-8 photoresist on a silicon wafer using standard photolithography with the predefined microfeatures. The resulting reusable negative mold is then used for soft lithography: PDMS is cast, cured, and demolded to obtain the patterned replica, which is finally bonded to a substrate (glass slide) to form the microfluidic device used in the experiments.

water for 30 minutes. To assemble the device, the PDMS layer and a microscope glass slide are exposed to oxygen plasma for 35 s, which generates silanol (–OH) groups on the PDMS surface and enables strong, irreversible covalent bonding upon contact. Depending on the desired wettability, additional conditioning is applied before flow experiments: for hydrophilic conditions, the bonded device is placed in the plasma chamber for an additional 5 minutes and experiments are performed immediately; for hydrophobic conditions, the bonded device is placed in an oven at 120 °C for at least 3 hours to obtain stable and reproducible hydrophobicity [Dersoir et al., 2015b].

4.2 Particle suspensions: composition and key properties

This section describes the composition and key physical and interfacial properties of the particle suspensions used in this study. We first introduce the characteristics of the colloidal particles, including their size, material, and surface functionalization. We then detail the formulation of the density-matched carrier fluid used to limit sedimentation and ensure stable particle transport during flow experiments. Finally, we outline the preparation of the particle suspensions and the control of their electrostatic properties, which together define the initial conditions governing particle transport, deposition, and clogging in the microfluidic porous media.

Particle properties The particles used in this thesis are Polybead® Carboxylate Microspheres, which are monodisperse polystyrene spheres functionalized with surface carboxyl groups and manufactured by *Polysciences, Inc.* Two particle sizes are employed: 4.5 µm and 6 µm in diameter, with coefficients of variation (CV) of 7% and 10%, respectively. Both types of microspheres are supplied as 2.6% solids (w/v) in aqueous suspension. The characteristics of these particles are summarized in Table 4.2.

Table 4.2: Properties of the particles used in the experiments.

Property	**Description**
Material	Polystyrene
Surface functionalization	Carboxyl (-COOH) groups
Diameter	4.5 µm and 6 µm
Coefficient of variation (CV)	7% and 10%
Aqueous suspension	2.6% and 2.7% solids (w/v)
Density	1.05 g/cm^3

Density-matched carrier fluid Avoiding particle sedimentation during flow experiments requires matching the buoyant properties of the bulk density of the suspended particles with those of the surrounding fluid. According to Archimedes' principle, a spherical particle immersed in a fluid experiences an upward buoyant force equal to the weight of the displaced fluid. In our experiments, these body forces cancel out, as we ensured that $\Delta\rho = \rho_f - \rho_p = 0$, where ρ_f and ρ_p represent the fluid and particle densities, thereby eliminating sedimentation. Density matching between the fluid and the polystyrene microspheres is achieved by mixing 78% ultrapure water with 22% glycerol by weight, resulting in a suspension with a bulk density of approximately 1.05 g/cm^3, closely matching that of the particles. The resulting fluid also exhibits a dynamic viscosity ranging from 1.45 to 1.9 mPa·s, depending on the room temperature. Depending on the experimental conditions, the density-matched carrier fluid is either used in its salt-free form or mixed with NaCl to obtain final concentrations of 1 mM and 100 mM, allowing the investigation of electrostatic interactions.

Preparation of particle suspensions The initial weight/volume percentage (w/v %) of the particle suspensions is provided by the manufacturer, as summarized in Table 4.2. To obtain the desired particle concentrations for the experiments, these stock suspensions are diluted using the previously prepared density-matched carrier fluid. The volumes of stock solution and carrier fluid are adjusted to reach the specific weight fractions required for each experimental condition. In addition, zeta-potential measurements were conducted using a Malvern Zetasizer to assess the electrostatic properties of the particle suspensions. These measurements were performed by a colleague in collaboration with the Karlsruhe Institute of Technology (KIT, Germany), yielding values of approximately −69 mV for the salt-free case and −21.3 mV in the presence of 100 mM NaCl.

4.3 Experimental apparatus

Optical system The experiments are carried out on a standard optical microscope (Nikon ECLIPSE Ti2) equipped with objective lenses of 2×, 4×, 10×, 20×, and 40× magnification. Images are recorded with a high-speed FASTEC HS7 camera, which captures sequences at up to 2500 frames per second with a resolution of 1920×1080 pixels.

Fluid injection and control Fluid injection is performed using two types of systems, depending on the configuration: a syringe pump (KD Scientific, KDS Legato™ 101) compatible with syringe volumes from 0.0005 mL to 10 mL, and pressure-driven injection setups. Pressure is regulated either with an Elveflow OB1 Mk4 Microfluidic Flow Controller (0–200 mbar), which enables both continuous and oscillatory injection at a prescribed frequency, or with a FLUIGENT EZ FLOW controller (0–1000 mbar) for continuous injection.

Flow and pressure measurements Flow conditions are monitored using two complementary approaches. In one setup, continuous pressure measurements are obtained using an in-line microfluidic pressure sensor (Fluigent EIPS1000, range −1000 to 1000 mbar, mean accuracy 10–20 mbar, i.e., 1.0–2.0% of full scale). In a second setup, the flow rate is measured with a mini CORI-FLOW (ML120V00) ultra-low-flow Coriolis mass flow meter, designed for full-scale ranges between 5 and 200 g/h and a minimum measurable flow of 50 mg/h (corresponding to approximately 0.8 μL/min to 3.17 mL/min for a carrier-fluid density of 1.05 g/cm^3). This covers the range explored in this work and provides a mass-flow accuracy of ±0.2% of the reading.

Fluidic connections In all configurations, fluidic connections are assembled with Tygon tubing (1/16 in OD × 0.020 in ID, i.e., 0.51 mm ID) and accessories supplied by Darwin Microfluidics. The PDMS chips are connected using 23G stainless-steel connectors (Microfluidic Fittings 23G Steel Tubing PDMS Adapters Kit), compatible with 0.5 mm ID Tygon microfluidic tubing. When required, a reusable microfluidic valve (1/16 in OD, 0.020 in ID) is used to rapidly stop the flow or inject a fluid. Besides, fluid switching is also performed with a 4-port manual valve; among the available modes (diagonal, right-angle "L", and single "T" flow), we use the "T" configuration with two inlets and one outlet.

Experimental configurations The injection modes (flow-rate control, pressure-driven forcing, and the two-phase-flow protocol) as well as the associated data acquisition procedures are detailed in their relevant chapters, where they are presented in direct connection with the research objectives and analysis methods.

4.4 Image analysis

The image analysis workflow is designed to extract quantitative, spatially resolved metrics of particle deposition and pore-space evolution during clogging. Specifically, it enables (i) identification of immobile particle deposits, (ii) estimation of porosity evolution with time, and (iii) determination of the spatial distribution of particle deposition within the porous medium.

4.4.1 Image acquisition workflow

Image sequences are recorded at selected pore volumes or times during the injection process, depending on the purpose of the experiment. The frame rate of image acquisition is varied based on the analysis type, with lower frame rates used in qualitative analysis and higher frame rates used in deposition dynamics analysis.

With the lowest available magnification objective (×2), the field of view of the FASTEC camera is restricted to 1080 pixels in length, which corresponds to a length of about 5.5 mm. Since this is less than half of the porous field, the entire field is captured by taking three successive image sequences at different streamwise locations. A 300-pixel overlap is maintained between the sequences to ensure alignment and continuity.

After acquisition, each image stack is analyzed in ImageJ with the *Z-projection* tool and average intensity option (Fig. 4.4a). This procedure enhances the signal of immobile (deposited) particles while suppressing the contribution from moving particles. The averaged images are then combined along the x-axis using a tiling algorithm developed from standard image-stitching methods [Preibisch et al., 2009], resulting in a single reconstructed 2D image of the entire porous region (Fig. 4.4b). This combined image is used as the foundation for all image analyses.

4.4.2 Image-based porosity evaluation

Once the full stitched image of the porous domain is obtained (Fig. 4.4b), the three phases that are part of the system, namely the deposited particles, the pore space, and the solid grains, are then identified using image segmentation. It is noted that the pore space and solid grains may have similar grayscale values; a dedicated segmentation procedure is applied to reliably separate these phases. The resulting segmented image (Fig. 4.4c) clearly distinguishes particles (black), pore space (gray), and grains (white).

Following segmentation, adaptive binarization is applied to isolate the deposited particles, which appear as white regions in the binary image (Fig. 4.4d). This enables us to monitor the reduction of pore space because of deposited particles and measure the change in porosity with time, denoted as $\phi(t)$.

As porosity is calculated based on 2D projections, this calculation cannot accurately capture the 3D stacking of particles within the channel depth, which is constant at 20 µm. For 4.5 µm particles, a maximum of about 4-5 layers can be stacked. When only two layers are deposited, the 2D binarization process underestimates the porosity by about 15%. For 6 µm particles, a maximum of about 3-4 layers can be stacked within the channel depth; when less than two layers are deposited, this translates to an underestimation of porosity by about 20-25%.

In regions where particles span the entire channel height, this 2D simplification becomes valid, and the estimation remains accurate. Moreover, optical observations show clear flow redirection around deposited structures, suggesting that clogging often involves full-depth stacking, which minimizes the impact of this approximation. This analysis, therefore, offers a time-dependent estimation of the effective porosity $\phi(t)$ during clogging.

4.4.3 Spatial distribution of particle deposition along the porous domain

Unlike the image-based porosity evaluation, which requires full phase segmentation to quantify pore-space reduction, the streamwise deposition analysis is designed to capture relative spatial trends in particle accumulation at the macroscopic scale. For this purpose, a simplified grayscale-threshold approach is adopted. Because the objective here is to compare deposition localization along the flow direction at a fixed clogging state rather than to compute absolute porosity values, this method provides a robust alternative to full segmentation.

For qualitative and quantitative analysis of deposition profiles, the final stitched image at the clogging reference state is processed using a custom Python routine. The same grayscale mapping (brightness and contrast settings) is applied to all images to ensure consistent intensity values across experimental conditions. In the processed images, deposited particles correspond to low grayscale intensities, whereas the pore space and solid grains correspond to higher intensities. Accordingly, the grayscale histogram computed over the porous domain exhibits a bimodal distribution (Fig. 4.5), with a narrow low-intensity peak associated with deposited particles and a broader high-intensity peak associated with the background (pore space and grains). The particle phase is isolated using a global intensity threshold, I_{th}, defined as the first local minimum of the smoothed histogram following the low-intensity peak. This criterion allows deposited particles to be identified while minimizing the inclusion of background pixels.

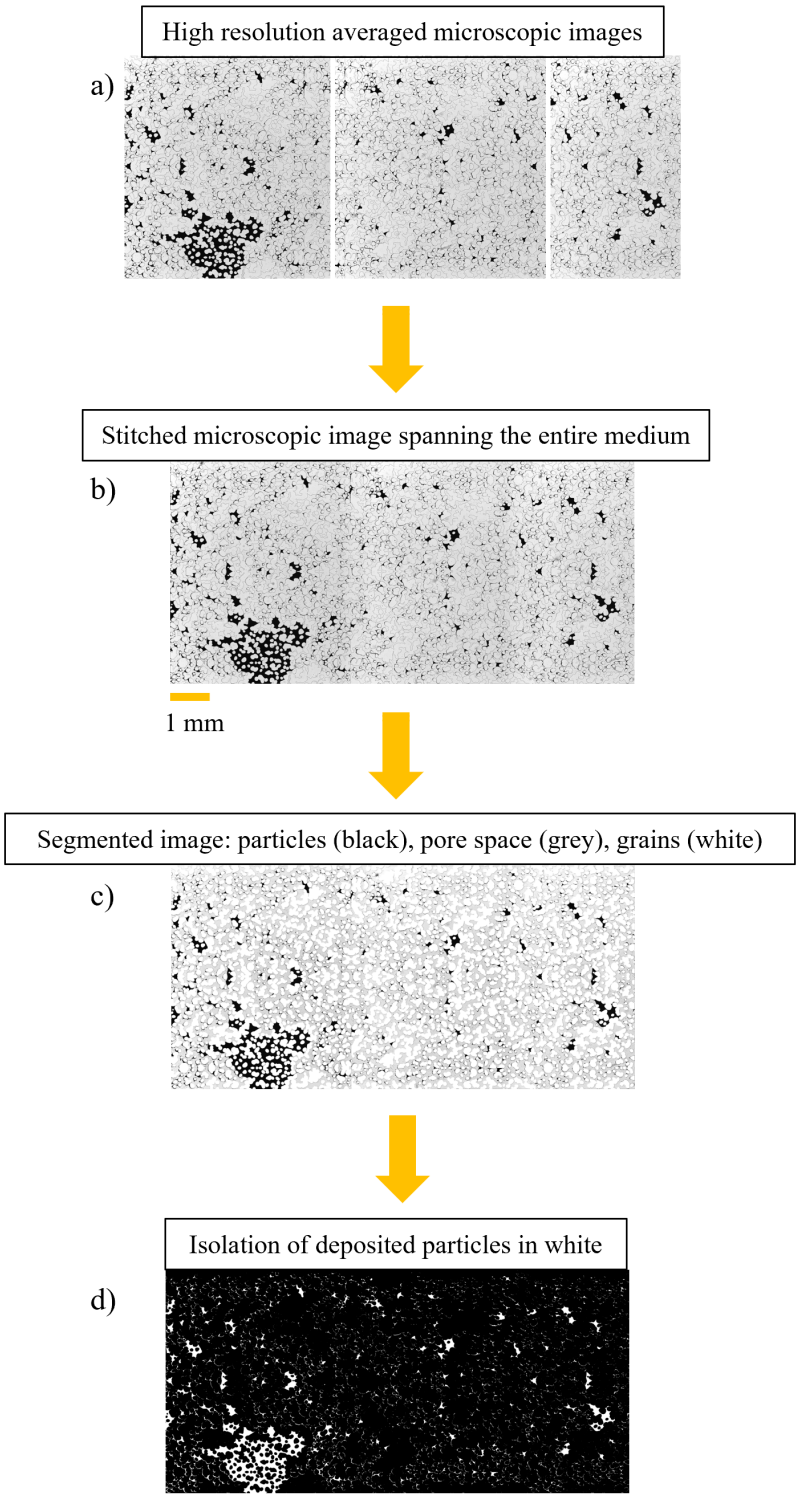

Figure 4.4: (a) Consecutive time-averaged images highlighting deposited particles (black), with pore space and solid grains appearing in varying shades of gray. (b) Reconstructed 2D view of the entire porous domain obtained by stitching the images in (a). (c) Segmented image distinguishing deposited particles (black), pore space (gray), and solid grains (white). (d) Binary image isolating deposited particles (white), used to quantify pore-space reduction and porosity evolution.

Each stitched image is then divided into ten equal segments along the streamwise (x) direction. The number of particle-classified pixels is counted within each segment and normalized by the total number of pixels in the full image. This yields a spatially resolved deposition profile, allowing comparison across experimental conditions and highlighting whether clogging remains localized near the inlet or progressively invades the porous medium.

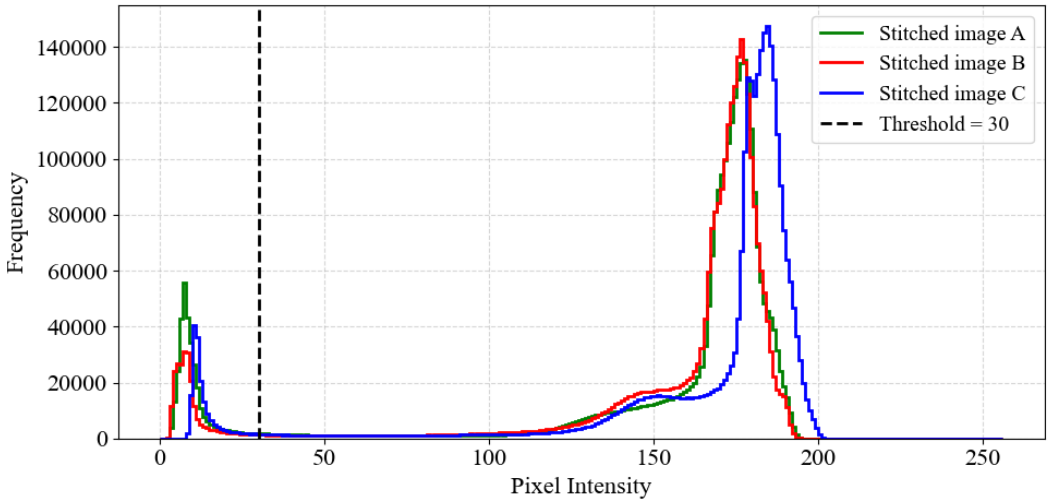

Figure 4.5: Grayscale pixel intensity histograms from representative images used to determine the particle detection threshold. A value of 30 (dashed line) reliably separates deposited particles from pore space and solid grains.

4.5 Hydraulic characterization of the microfluidic devices

This section presents the hydraulic characterization of the microfluidic devices used in our study, which are presented in Table 4.1. We first determine the range of imposed pressures over which the device exhibits a linear flow response, such that PDMS deformation remains negligible. Defining this operating window ensures that all hydraulic measurements are consistent and directly comparable. Within this regime, we then estimate the apparent permeabilities of the different models, which serves as the baseline for interpreting the flow, transport, and clogging dynamics presented in the following chapters.

4.5.1 Identification of the linear hydraulic regime and PDMS deformation threshold

PDMS microfluidic devices are known to deform when the imposed pressure becomes sufficiently large because of the elastic nature of the polymer. This effect has been reported in the microfluidics literature and can result in changes in hydraulic measurements, summarized by the device resistance, by effectively changing the channel cross-section [Gervais et al., 2006, Hardy et al., 2009]. Identifying the pressure range over which such deformation remains negligible is therefore essential to ensure that pressure-dependent changes in channel geometry do not bias the hydraulic measurements reported in this work.

We quantify this operating range with a simple pressure–flow calibration performed in the pressure-controlled configuration. We perform these measurements over the $M3$ model, where we increase the imposed pressure in 50 mbar steps up to 550 mbar. After each pressure step, we wait 1 minute while recording the flow rate at 1 Hz, and we define the steady-state flow rate as the

average over this stabilization period (Fig. 4.6). The measured flow rate increases linearly with the imposed pressure up to an onset of 250 mbar (Fig. 4.6); beyond this onset, the measured flow rate deviates from the linear fit, suggesting the onset of PDMS deformation. In this regime, the effective channel cross-section does not change with pressure, and the hydraulic resistance can therefore be considered constant, leading to more reliable experiments for comparison and for deposition and clogging. In contrast, pressure-induced deformation would modify the channel cross-sectional area and thus the local velocity and shear conditions, potentially biasing particle deposition dynamics and the apparent evolution of permeability.

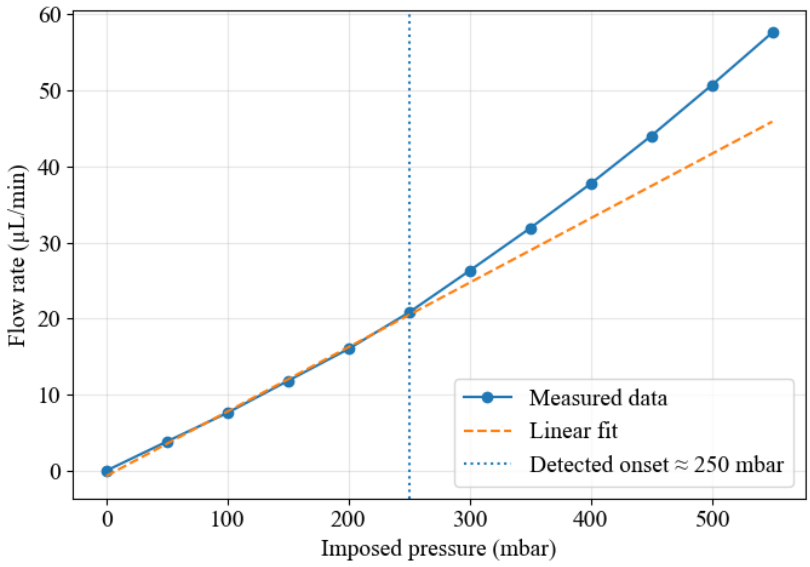

Figure 4.6: Flow-rate response to increasing imposed pressure in the PDMS microfluidic device $M3$. The flow rate scales linearly with pressure up to ~ 250 mbar (negligible PDMS deformation); beyond this onset, deviations from linearity indicate PDMS deformation.

4.5.2 Apparent permeability estimation

Having identified the operating pressure range over which the PDMS microfluidic device operates without deformation, we can now estimate an apparent permeability. Within this linear hydraulic regime, the flow response follows Darcy's law.

The apparent permeability of the microfluidic device is estimated using a rearranged form of Darcy's law,

$$K_{\text{app}} = \frac{Q\,\mu\,L}{\Delta P\,A}, \tag{4.1}$$

where K_{app} is the apparent permeability (m^2), L is the length of the porous domain in the flow direction (m), ΔP is the measured pressure drop across the microfluidic device, and Q is the corresponding volumetric flow rate.

The apparent permeabilities K_{app} for the $M2$ and $M3$ models are quantified based on Eq. 4.1 from the experimentally measured flow rate and pressure drop, and are reported in Table 4.1. However, for $M1$, as pressure sensors were not mounted during the single-grain collector experiments, we estimate the permeability using a Hele–Shaw (parallel-plate) approximation, $K \approx H^2/12$, where the smallest dimension controlling the resistance is the channel depth ($H = 20\ \mu\text{m}$).

4.6 Pore-scale simulation for post-processing microfluidic results

Numerical simulations are used as a post-processing tool to complement the microfluidic experiments. While experiments provide direct observation of particle deposition and clogging, simulations enable quantitative characterization of the flow field within complex pore geometries and how it reorganizes as clogging develops.

4.6.1 Simulation strategy: Darcy–Brinkman–Stokes approach

Direct numerical simulation of the Stokes equations on pore-resolved geometries would require explicit meshing of all solid–fluid interfaces. Although accurate, such an approach becomes computationally expensive for complex microfluidic porous networks and is not well-suited for handling evolving geometries due to particle deposition and clogging.

To overcome these limitations, we adopt a Darcy–Brinkman–Stokes (DBS) formulation [Soulaine and Tchelepi, 2016], which allows both fluid and solid regions to be treated within a unified continuum framework. In this approach, the porous medium is represented as a spatially varying permeability field, avoiding the need for body-fitted meshes and enabling straightforward incorporation of deposited particles.

Because the microfluidic device has a shallow finite depth, a depth-averaged two-dimensional formulation is adopted. Under creeping-flow conditions, the depth-averaged velocity field $\mathbf{U}$ satisfies

$$0 = -\nabla P + \rho_f \mathbf{g} + \frac{\mu}{\phi}\nabla^2\mathbf{U} - \mu K^{-1}\mathbf{U} - \mu\frac{12}{H^2}\mathbf{U}, \tag{4.2}$$

where $K(\mathbf{x})$ is the spatially varying permeability field derived from the image-based reconstruction.

The different terms in Eq. (4.2) represent distinct physical mechanisms. The term $-\mu K^{-1}\mathbf{U}$ represents the permeability-induced resistance term associated with the porous structure and deposited particles. This term varies spatially and enables the distinction between open pores and solid regions. The additional term $-\mu\frac{12}{H^2}\mathbf{U}$ corresponds to the Hele–Shaw correction.

The total resistance to flow is therefore decomposed into two contributions: an in-plane resistance associated with pore geometry and clogging, and an out-of-plane resistance associated with depth confinement (Hele–Shaw term).

The DBS model exhibits the correct asymptotic behavior:

- In open space regions (Fig. 4.7) ($\phi = 1$, $K \to \infty$), the geometric resistance term vanishes, and the equation reduces to the 2D depth-averaged Stokes equation.

- In solid grain or particle deposition regions (Fig. 4.7), a very small permeability ($K = 10^{-15}$ m^2) is assigned, making the permeability-induced resistance term dominant and forcing the velocity to approach zero, which mimics an effective no-slip condition.

Simulations are performed using the `porousMedia4Foam` toolbox [Soulaine et al., 2021b], which is specifically designed for solving such hybrid flow formulations.

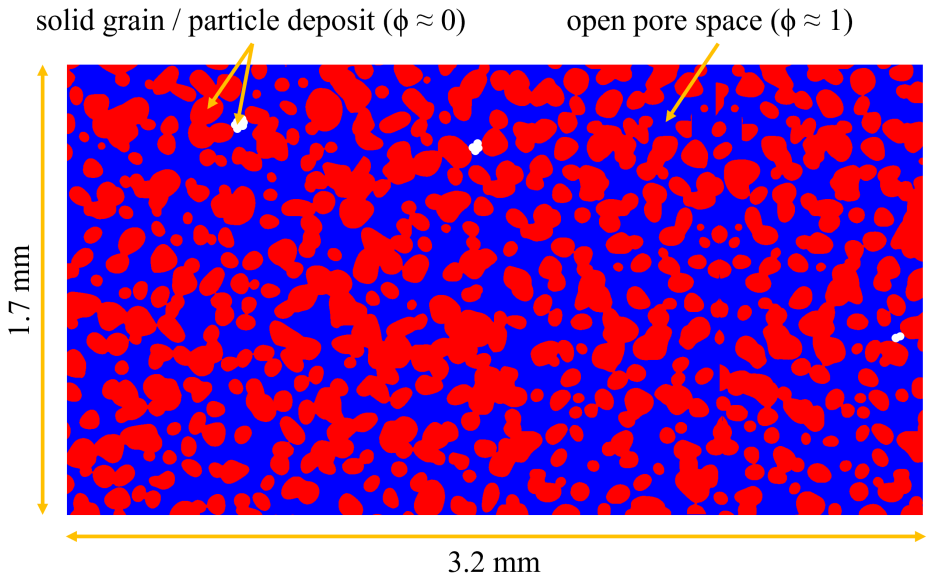

Figure 4.7: Representation of the porous medium on a Cartesian grid. Blue corresponds to open pore space ($\phi = 1$ and $K^{-1} = 0$ m^{-2}), while red and white corresponds to solid grains and particle deposits respectively ($\phi = 0.01$ and $K^{-1} = 1 \times 10^{15}$ m^{-2}).

4.6.2 From microfluidic images to simulation

The computational domains are directly constructed from high-resolution binary images of the microfluidic porous media, with a spatial resolution of approximately 4.5–5 μm per pixel. These images are obtained from experiments and represent the pore structure in a binary form, where the solid phase is separated from the pore space (Fig. 4.7).

A MATLAB-based workflow is used to convert the binary images into a Cartesian computational grid, avoiding the need for complex mesh generation. Each pixel is assigned local properties based on its phase. This permeability assignment allows deposited particles, identified experimentally, to be directly incorporated into the simulation as impermeable regions. As a result, clogging is naturally represented through local reductions in permeability.

To minimize boundary effects and better represent the experimental conditions, inlet and outlet extensions are added to the computational domain.

4.6.3 Outcomes of the simulations: Flow-field visualization and impact of clogging

Velocity fields and streamline distributions are extracted to quantify how clogging modifies flow pathways. Figure 4.8 compares the initial particle-free porous structure with the clogged configuration obtained after incorporating the experimentally observed deposits. The presence of deposited particles induces a strong reorganization of the flow, characterized by flow focusing and local acceleration within the remaining open pores. For consistency, the same velocity scale is used in both cases, highlighting regions of intensified flow.

In addition, the simulations enable a quantitative evaluation of permeability and its evolution with porosity. By progressively incorporating the experimentally observed deposits into the computational domain, changes in pore space due to particle deposition and clogging are reflected in the effective permeability extracted from the simulations. Through Darcy's law, this permeability

can then be related to the corresponding pressure drop, allowing the hydraulic consequences of clogging to be quantified.

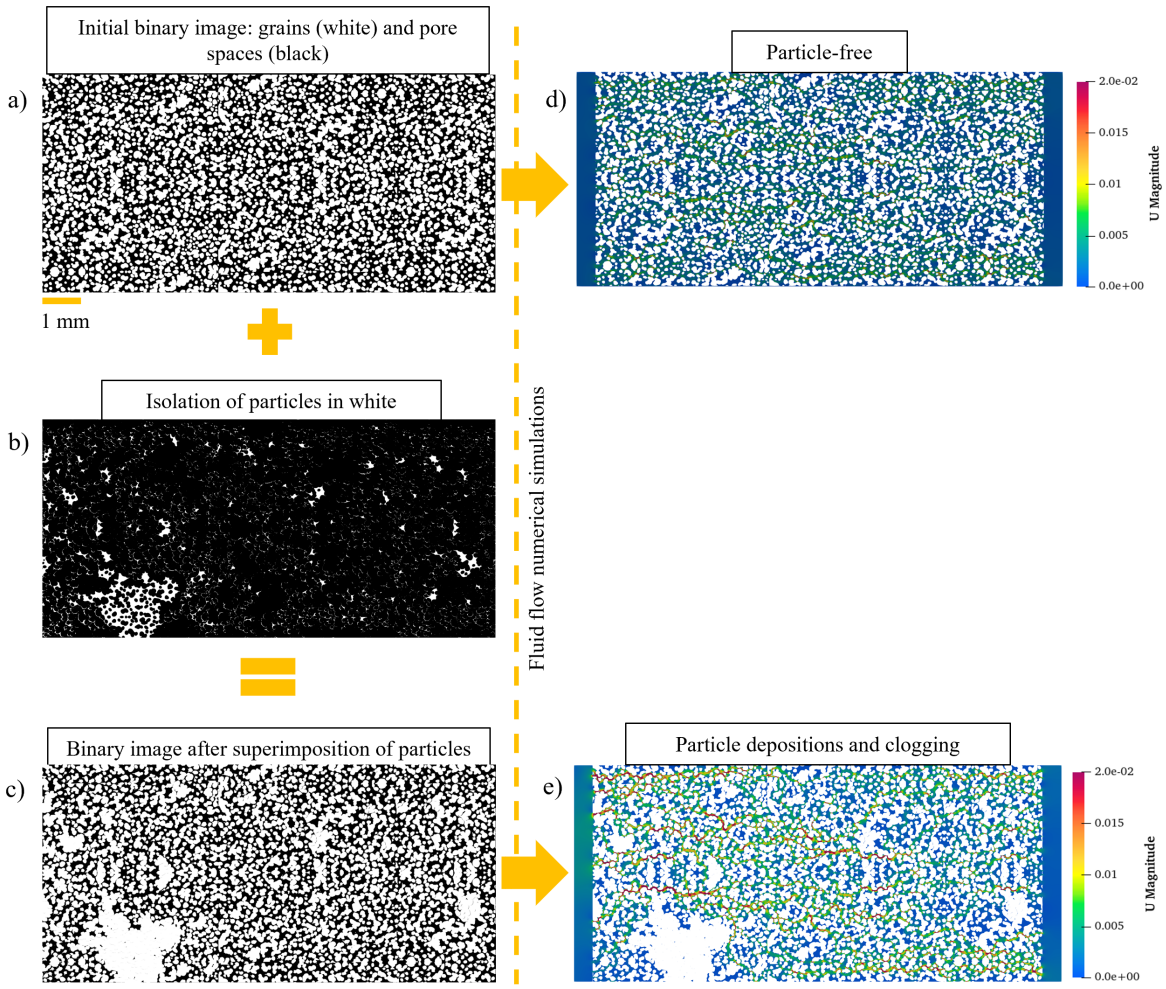

Figure 4.8: (a) Original binary image of the entire porous domain, with solid grains shown in white and the pore space in black. (b) Segmented binary image of deposited particles only, isolated from the experimental images and shown in white. (c) Combined binary image of the deposited particles from (b) superimposed on the initial porous structure in (a), representing the experimentally modified binary image of the porous domain. (d) Simulation result for fluid flow using the initial domain (free of particles), indicating the basic distribution of streamlines with velocities between 0 and 0.02 m/s. (e) Fluid flow simulation on the modified domain with deposited particles, showing how clogging affects fluid flow patterns, with redirection and regions of increased velocity magnitude.

Chapter 5

Progressive colloidal clogging mechanism by dendritic build-up in porous media

This chapter builds on the first research gap identified in Chapter 3, concerning the limited pore-scale understanding of aggregation-driven deposition patterns in heterogeneous porous media. It investigates the formation of dendritic structures under adhesion-dominated conditions and examines how their development within tortuous porous networks contributes to permeability reduction. The results presented in this chapter are adapted from Okaybi et al. [2025].

5.1 Introduction

The physics of colloidal transport within confined environments is fundamental to both natural and engineered systems. For example, in groundwater flow, colloid mobility and subsequent pore clogging can influence water quality and alter flow paths within aquifers, directly impacting filtration effectiveness [Ryan and Elimelech, 1996]. Similarly, in geothermal reservoirs, particle clogging reduces the permeability, leading to a decline in efficiency in performance [You et al., 2015, Maya Fogouang et al., 2025]. This issue also arises in other applications, such as microfiltration membranes used for particle removal [Gopal et al., 2006], as well as in micro-engineered systems, porous structures, and micro-reactors, where clogging limits flow and system performance [Dressaire and Sauret, 2017a, Liu et al., 2019, Chen et al., 2015]. Therefore, understanding the underlying physics of colloidal deposition and clogging is crucial for overcoming major limitations in various industrial applications.

Particle clogging occurs through three mechanisms [Dressaire and Sauret, 2017a]: sieving, where the pore constriction is too small for a particle to flow through [Sauret et al., 2014, 2018, Duchêne et al., 2020, Majekodunmi and Hashmi, 2022]; bridging, where multiple particles simultaneously arrive at a constriction and form a bridge [Marin et al., 2018, Vani et al., 2022, Hafez et al., 2021, Vani et al., 2024]; and progressive clogging or aggregation, where particles successively deposit near a wide constriction, narrowing the channel and ultimately causing blockage [Wyss et al., 2006a, Dersoir et al., 2015a, 2019, 2017]. The key point to describing the progressive clogging mechanism lies in understanding how particle deposits evolve from initial layers to the formation of multilayer buildups on the walls of the constriction. Achieving effective control over this process, however, presents a significant challenge. It requires a deep understanding of the complex interplay between flow hydrodynamics [Bacchin et al., 1995, Torkzaban et al., 2007] and adhesion forces, which include electrostatic interactions between particles and surfaces [Bacchin et al.,

2011, Torkzaban et al., 2007] as well as the effects of Brownian motion. The most widely used framework for capturing these electrostatic interactions is the Derjaguin-Landau-Verwey-Overbeek (DLVO) theory [Derjaguin, 1941b, Verwey, 1947]. It models adhesion forces as the combined effect of attractive Van der Waals forces and repulsive electrostatic interactions from overlapping electric double layers, which dictate particle-particle and particle-surface interactions [Fogouang et al., 2024], ultimately influencing deposition. Ramachandran and Fogler [1998] investigated the critical conditions for multilayer deposition in a particle-pore surface system, emphasizing the interplay between flow rate and ionic strength. They demonstrated experimentally that higher salt concentrations screen surface charges on flowing sub-micron particles [Ryde et al., 1991], weakening the electrostatic repulsion barrier. This reduction allows particles to deposit onto previously deposited ones, which act as additional collectors — solid grains or deposited particles within the porous medium onto which flowing particles can attach due to hydrodynamic and adhesive interactions — leading to multilayer formation. They found that for a particle to deposit, its velocity must exceed a critical threshold to overcome the repulsion barrier and move close enough for adhesion forces to take effect. As ionic strength increases, repulsive forces diminish, lowering the critical velocity required for deposition. At sufficiently high salt concentrations, the repulsion barrier vanishes at small separation distances, meaning that a particle can only deposit if its velocity remains below a certain threshold.

Kusaka et al. [2010] studied deposition morphology around a cylindrical obstacle in a microfluidic channel at high salt concentrations, revealing that at low Péclet numbers (low advection relative to diffusion), deposits formed uniformly across the upstream half of the collector. As the Péclet number increases, deposition concentrated at the front stagnation point, eventually forming finger-like dendritic structures. These structures were velocity-dependent: at higher Péclet numbers, dendrites became smaller, and deposition shifted to the rear of the collector. Building on these findings, studies on a one-dimensional (1D) array of aligned pores [Agbangla et al., 2012a] and an isolated obstacle [de Saint Vincent et al., 2016] examined the conditions for dendritic growth, emphasizing the effects of salt concentration and flow dynamics. Both studies showed that dendrites form under high salt concentrations and relatively high flow velocities. de Saint Vincent et al. [2016] further explained that erosion induces lateral particle detachment, promoting dendritic growth along the upstream centerline of the pore. However, dendritic growth was suppressed as flow velocity increased further due to particle detachment at the centerline. These studies highlight the importance of balancing salt concentration and flow conditions for dendrite formation, with excessively high velocities disrupting their growth. However, they do not define a criterion beyond which dendritic growth is significantly hindered.

Bacchin et al. [2014] investigated how different 2D pillar array configurations (straight, connected, and staggered) influence clogging mechanisms. They found that dendritic structures exclusively formed at the entrance of the straight pore array, with no internal clogging, consistent with previous work by Bacchin et al. [2011]. In contrast, the staggered and connected arrays showed an absence of dendritic build-ups upstream of the pillars. Instead, clogging occurred through successive particle accumulation on the upstream sides of individual pillars, eventually forming a cake layer that blocked the entrance. Despite these insights, the formation of dendrites within heterogeneous porous media and their impact on flow dynamics remain poorly understood. In particular, there is no clear evidence on how dendrite buildup contributes to pore clogging.

Understanding how particle deposition leads to clogging in porous media requires direct visualization of transport mechanisms at the pore scale [Wyss et al., 2006a]. Microfluidic devices offer a powerful tool for this purpose, as they enable the fabrication of transparent two-dimensional (2D) [Duffy et al., 1998] and three-dimensional (3D) [Accardo et al., 2018] models with diverse geometric features. These devices allow for high-resolution, real-time observation of transport mechanisms in microchannels while providing rapid analysis, minimal sample consumption, and

cost efficiency [Manz et al., 1992, Whitesides, 2006]. While microfluidic devices have been extensively used to study particle deposition and clogging, including in porous-like media with realistic geometries[Liu et al., 2019, Soumane, 2021, He et al., 2025], most studies have not addressed the emergence of dendritic structures in such environments or their role in inducing clogging and altering flow behavior. To address this gap, we combine microfluidic experiments with flow simulations to investigate three key aspects of dendrite formation and its impact on clogging in heterogeneous tortuous porous media. First, we examine how dendritic structures progressively develop within the medium, altering flow dynamics and, in some regions, leading to dendrite-induced clogging. Second, we identify the conditions that promote dendrite formation by correlating detailed velocity profiles from flow simulations with the critical velocity for particle detachment, determined through a torque balance between hydrodynamic and adhesive forces. Finally, we assess how dendrite formation and clogging influence permeability loss by analyzing permeability-porosity relationships derived from experimental data.

The structure of the paper is as follows. In Section 5.2, we describe the materials and methods, including the fabrication of PDMS microfluidic devices, the preparation of particle suspensions, and the setup for flow experiments and imaging. We also present the methodology for determining the critical velocity for particle detachment and the post-processing techniques used in computational fluid flow analysis. In Section 5.3, we present and discuss our results, starting with experimental evidence of dendrite clogging, followed by an analysis of the conditions that favor dendrite formation, and concluding with an evaluation of its impact on porous media properties. Finally, we summarize the key findings of this study and their broader implications.

5.2 Materials and Methods

We present microfluidic systems designed to investigate dendrite formation and its role in clogging within porous media. Our approach includes preparing particle suspensions, setting up experiments with integrated advanced imaging techniques, and identifying critical velocities for particle detachment. We also develop a new methodology to augment our experimental findings using computational microfluidics.

5.2.1 PDMS microfluidic devices

This study employs two microfluidic system designs to explore deposition patterns, focusing on dendritic structures and their influence on pore clogging.

The primary design is a heterogeneous tortuous porous model ($M2$) (Fig. 4.2a). Its design workflow, properties, and dimensions, as well as the extraction of internal pore statistics (pore-size distribution and constriction-size distribution), are presented in Chapter 4.1.1. The geometric and hydraulic properties of this model are summarized in Table 4.1, with a porosity of $\phi_0 = 0.48$, an experimentally determined permeability of $K_0 = 2.96 \times 10^{-12}$ m^2, a mean arithmetic pore diameter of 100 µm, and a mean arithmetic constriction diameter of 43 µm.

The second design is a single-grain collector system ($M1$), designed to investigate the underlying processes driving the build-up of dendritic structures. The specifications of this model are presented in Chapter 4.1.1, where a grain of 20 µm diameter is placed within a channel of width 100 µm. Similar to the porous domain, the single-grain collector system maintains a depth of 20 µm.

The PDMS microfabrication workflow used to produce these devices is described in detail in Chapter 4.1.3. After bonding the PDMS replica to a glass slide, the assembled microchip is exposed to oxygen plasma for at least 5 minutes to render the surface hydrophilic before performing the experiments.

5.2.2 Particle suspension

Carboxylate polystyrene latex particles with a diameter of 4.5 µm are used in this study (Table 4.2). The suspension concentration is prepared by diluting the stock solution in a density-matched fluid (see Chapter 4.2) to minimize the effects of gravity, achieving a final volume fraction of 1.25×10^{-3}. To control the electrostatic repulsion between particles and between particles and walls, a NaCl concentration of 100 mM is used, which is below the critical coagulation concentration of 157 mM [Guo et al., 2024]. Before each experiment, the suspension is sonicated for 30 minutes in an ultrasonic bath to break apart any pre-formed aggregates prior to injection.

5.2.3 Flow experiments and imaging

We inject particle suspension into the microfluidic device previously saturated with 100 mM NaCl solution using a KD Scientific syringe pump at a controlled flow rate, as shown in Figure 5.1. All the experimental parameters with their corresponding values are listed in Table 5.1. The flow conditions are carefully controlled to ensure a creeping flow regime, with a Reynolds number $\mathrm{Re} = \rho V \mathcal{L}/\mu$ <1. V represents the characteristic velocity at the feeding channel just before the single-grain collector and the porous domain. $\mathcal{L}$ is the characteristic length chosen as the depth (H) across both microfluidic devices. Additionally, we evaluate the Péclet number ($\mathrm{Pe} = (3\pi d_p \mu \mathcal{L} V)/(k_B T)$), which quantifies the contribution of advection to diffusion for suspended particles. In our experiments, the Péclet number exceeds 2.9×10^5, indicating that particle transport is dominated by advection rather than diffusion. We also evaluate the Stokes number ($\mathrm{St} = (\rho_p d_p^2 V)/(18\mathcal{L}\mu)$), which quantifies the influence of inertial effects on particle transport. It is defined as the ratio of the particle's characteristic time scale to the fluid's characteristic time scale and is calculated to be $\mathrm{St} < 6.5 \times 10^{-3}$. Since this value is well below 10^{-2}, inertial effects are negligible for the suspended particles [Espinosa-Gayosso et al., 2012].

The microfluidic device is positioned on an inverted microscope (Nikon ECLIPSE Ti2 microscope platform) connected to a high-speed FASTEC (HS7) camera to capture image sequences at a specific depth using magnifications of $2\times, 4\times, 10\times$, and $20\times$ after a certain number of pore volumes is injected. At selected pore volumes during the experiment, we recorded sequences of 300 images at 300 frames per second. The image acquisition workflow used to filter out moving particles, retain only deposited particles from sequential images of the porous domain, and tile them into a single stitched image [Preibisch et al., 2009] at a given injected pore volume is detailed in Chapter 4.4.1. Porosity over time, $\phi(t)$, is measured by adaptive binarization of these images, which allows us to track changes in porosity due to particle deposition. The workflow of Image-based porosity evaluation estimated from 2D images is detailed in Chapter 4.4.2.

Additionally, we have installed two inline pressure sensors from FLUIGENT on both sides of the microfluidic device to monitor pressure differentials continuously throughout the experiment. These pressure readings are instrumental in calculating the permeability of the porous domain over time, $K(t)$, which is then normalized against the initial permeability, K_0.

5.2.4 Critical velocity for particle-surface and particle-particle detachment

We aim to identify a critical velocity that determines whether a particle will attach to or detach from a collector surface or an already deposited particle. Establishing this criterion helps us understand the mechanisms driving different deposition patterns and the processes underlying their formation. As aggregates grow in linear low-shear regimes, we consider the stability of particles at stagnation regions along with the flow direction. Given that rolling is the predominant mechanism of particle detachment [Bergendahl and Grasso, 1998, Tsai et al., 1991, Torkzaban et al., 2007], the torque on an attached particle results from a balance between adhesive forces acting

Table 5.1: Parameters for fluid properties, particle characteristics, surface properties, and force calculations in the experimental and simulation setup. The annotations p and s refer to the particle and surface collector, respectively

Fixed parameters	**Value**
Particle and carrier fluid density, ρ	1050 kg/m^3
Depth of the microfluidic device, H	20 µm
Dynamic viscosity, μ,	1.83 mPa.s
Particle diameter, d_p	4.5 µm
Boltzmann constant, k_B	1.38×10^{-23} J/K
Temperature, T	293 K
Adhesive force (particle-surface), F_A^{p-s}	2.3×10^{-8} N
Adhesive force (particle-particle), F_A^{p-p}	3.4×10^{-8} N
Poisson ratio (surface), υ_s	0.5
Poisson ratio (particle),υ_p	0.35
Young modulus (surface), E_s	2 MPa
Young modulus (particle), E_p	3 GPa
Elastic constant (surface) [Johnson et al., 1971], $k^s = \frac{1-\upsilon_s^2}{\pi E_s}$,	1.2×10^{-7}
Elastic constant (particle) [Johnson et al., 1971], $k^p = \frac{1-\upsilon_p^2}{\pi E_p}$	9.3 $\times 10^{-11}$
Composite Young's modulus (particle-surface) [Johnson et al., 1971], $K^{p-s} = \frac{4}{3\pi(k^p+k^s)}$	3.56 MPa
Composite Young's modulus (particle-particle) [Johnson et al., 1971], $K^{p-p} = \frac{4}{3\pi(k^p+k^p)}$	2.28 GPa
Variable parameters	**Value**
Flow rate through porous domain, Q	8, 20 µL/min
Flow rate through single-grain collector, Q	1, 5, 10 µL/min

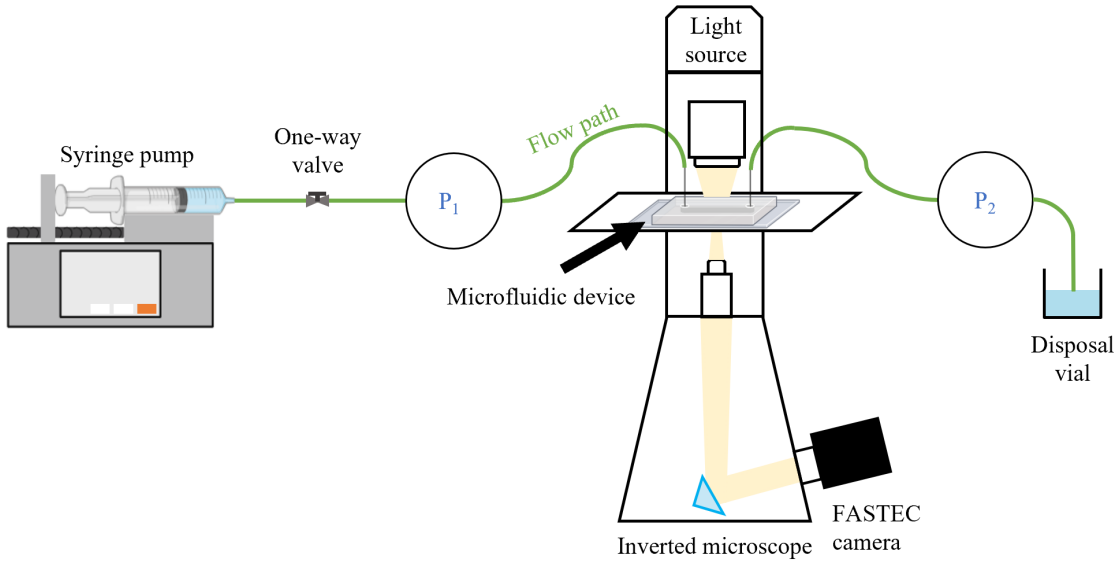

Figure 5.1: Schematic of the microfluidic setup. A syringe pump drives the particle suspension through the microfluidic device, in which pressure sensors monitor the pressure drop (ΔP) across the porous medium. The outlet flow is collected in a vial. An inverted microscope equipped with a high-speed FASTEC camera captures real-time imaging of particle deposition and clogging dynamics. Some elements were created with BioRender.com.

normal to the surface (or deposited particle) and drag forces acting tangentially. The adhesive force tends to bind a particle to the surface while the drag force tends to mobilize it. Under laminar conditions, the drag force acting on a spherical particle reads as $F_D = (1.7)(3\,\pi\,\mu\,d_p V_x^f)$ where V_x^f is the fluid velocity [Goldman et al., 1967, O'neill, 1968]. The drag force is effective at $1.4(d_p/2)$, reading an applied torque of $T_D = 1.4\,(d_p/2)F_D$ [Sharma et al., 1992]. On the other hand, the adhesive force, F_A, is calculated as the sum of Van der Waals and electric double-layer potentials (see Chapter 2.5.2 and the corresponding appendix in A.1) acting between particles or between a particle and a surface divided by an approximated separation distance of 0.2 nm [Israelachvili, 2011]. The adhesive torque for attached particles is expressed as $T_A = F_A \cdot l_x$, where l_x represents the contact radius between the particle and either a surface or another particle. The contact radius is defined as $l_x = (F_A(d_p/2)/4K^{p-i})^{1/3}$ and depends on the particle size and the material properties of both the particle and the surface [Torkzaban et al., 2007]. Here, K^{p-i} represents the composite Young's modulus, which describes the elastic properties at the contact interface—either between two particles or between a particle and the collector surface [Johnson et al., 1971]. The critical detachment velocity, (V_x^c), is obtained by balancing the hydrodynamic and the adhesive torques. It reads:

$$V_x^c = \frac{F_A \left(\frac{F_A(d_p/2)}{4K^{p-i}}\right)^{1/3}}{(1.4 \times 1.7)(3\pi\mu(d_p^2/2))}, \tag{5.1}$$

where all the parameters with their corresponding values are defined and listed in Table 5.1. The subscripts p and i denote the particle and either another particle or the surface, respectively.

5.2.5 Post-processing using computational microfluidics

We perform direct fluid flow simulations to complement and enhance our experiments by providing deeper insights into the fluid dynamics within our microfluidic devices. These simulations generate detailed velocity profiles, helping to identify stagnation regions that favor particle deposition. Additionally, they enable us to map the redirection of fluid streamlines after accounting for experimentally observed particle deposition and clogging. To achieve this, we first convert an experimental binary image of the entire porous domain, with a resolution of 5 µm/pixel, into a computational grid. In this grid, permeability is penalized by assigning very low values to grains and deposited particles, while high values are assigned to pore spaces, following the approach described in Soulaine and Tchelepi [2016], Soulaine et al. [2021a], with additional details provided in Chapter 4.6. Fluid flow is then simulated using porousMedia4Foam, an OpenFOAM-based package dedicated to multi-scale flow and transport in porous media [Soulaine et al., 2021b]. We solve the 2D Stokes equation while incorporating the Hele-Shaw correction term, which accounts for the effect of the microchannel's finite depth. The Hele-Shaw approximation simplifies the flow into a depth-averaged 2D equation by introducing an effective permeability term proportional to $H^2/12$. This correction ensures that the simulated flow regime remains consistent with the experimental conditions. The simulations assume saturated, incompressible flow with no-slip boundary conditions at grain surfaces. Fixed inlet velocities, along with constant fluid density and viscosity, are set to match experimental parameters presented in Table 5.1.

5.3 Results and Discussion

In this section, we demonstrate how the continuous growth of dendrites leads to dendrite-induced clogging. We then analyze the conditions that favor dendrite formation using both a single-grain collector and a tortuous porous domain at different flow rates. Finally, we investigate the impact of flow rate on the hydraulic properties of the porous domain.

5.3.1 Experimental evidence of dendrite clogging

We introduce the particle suspension with a 100 mM NaCl concentration into the porous domain at two flow rates: 8 µL/min and 20 µL/min. These flow rates correspond to velocities of 1.1 mm/s and 2.7 mm/s, respectively, in the feeding channel just before the porous domain. The high salt concentration in our flow experiments reduces electrostatic repulsion between particles, promoting multi-layer particle deposition, as noted by Ryde et al. [1991]. The chosen flow rates correspond to a Péclet number range of $\mathcal{O}\left(10^5 - 10^6\right)$ within the porous domain. According to Bacchin et al. [2011], this range is conducive to multi-layer particle build-up in stagnation regions, where low shear allows for the formation of dendritic structures. In our porous domain—characterized by highly connected, tortuous pathways and varying grain sizes—these conditions could similarly facilitate dendritic growth. A key question arises: can these structures develop sufficiently to bridge neighboring grains and ultimately clog the pores? To analyze the resulting clogging mechanisms, we capture time-sequenced images of the experiments, allowing us to investigate how different flow rates influence pore clogging and deposition patterns.

We identify a new progressive clogging mechanism termed "dendrite clogging". Unlike typical clogging patterns involving progressive aggregation and deposition at two deposition sites at the entrance of the pore [Dersoir et al., 2015a, Wyss et al., 2006a], dendrite clogging arises from the presence of dendrites (elongated structures) that grow across the pore from a single deposition site—the tip of the dendrite. To illustrate this process, Figure 5.2a shows averaged images from a sequence of captured frames, highlighting a specific region of interest within the porous domain. These images correspond to different pore volumes injected (PVs) of the particle suspension at a

flow rate of 8 µL/min. After 435 PVs, multiple clogging events appear in the region, with a notable initial dendrite forming at the front stagnation zone of a grain facing the flow (highlighted by a dotted red box). By 1225 PVs, additional particles accumulate on the existing deposits, causing the dendrite to extend upstream into the pore. After 1664 PVs, we observe a further extension of the dendrite significantly reducing the gap between its tip and the adjacent grain (both annotated in the figure) without complete pore-clogging, allowing particles to still flow through, as shown in Movie_Figure_3a_8_µL/min_1664_PVs; see Appendix Section A.5, and the corresponding video in the supplementary material of Okaybi et al. [2025]. Finally, by 2225 PVs, the continuous buildup of the dendritic structure leads to complete pore-clogging and redirection of the local pathway, which is shown in Movie_Figure_3a_8_µL/min_2225_PVs; see the Appendix A.5, and the corresponding video in the supplementary material of Okaybi et al. [2025]. In addition, we have observed and tracked the progression of dendrite-induced clogging across several regions of the porous domain (see Appendix A.4). Agbangla et al. [2012a] observed that the orientation of dendrites is based on the flow direction in a 2D straight array of pores. To validate this in a more complex and tortuous porous domain, we extract streamlines from velocity profiles obtained from numerical simulations at an 8 µL/min flow rate (Figure 5.3), before and after injecting 2225 PVs of the particle suspension, with deposited particles shown in black. Figure 5.3a shows the initial flow field at the beginning of the experiment. Figure 5.3b illustrates the flow field after clogging has occurred. Our results confirm that dendrite orientation, highlighted in the yellow-circled areas, closely follows the streamlines shaped by the flow direction and gradually modifies them as the dendrites grow. As highlighted in the red-dotted box, the continuous build-up of dendrites leads to clogging, forcing a complete redirection of the local flow path of particles, which strongly contrasts with the initial streamline configuration observed in Figure 5.3a.

In the same region of interest within the porous domain (Figure 5.2b), the experiment conducted at a flow rate of 20 µL/min exhibits multiple clogging events but no dendrite formation or dendrite-induced clogging. From 482 PVs to 2348 PVs, the absence of a dendritic structure within the highlighted red box suggests that dendrite clogging does not occur at this higher flow rate. This can be attributed to the increased shear at 20 µL/min, which is 2.5 times higher than at 8 µL/min, effectively limiting dendrite growth. This finding aligns with previous experimental observations in de Saint Vincent et al. [2016] and Kusaka et al. [2010], where a higher Péclet number was shown to inhibit the development of elongated dendritic structures along the centerline of the collector.

5.3.2 Conditions for dendrite formation

In the previous section, we demonstrated how dendrite formation progressively leads to clogging as more particles accumulate with increasing PVs. We also observed that higher flow rates generate greater shear stress at front stagnation regions, disrupting particle-particle attachment and preventing dendritic growth. To further investigate the conditions that promote dendrite formation, we focus on a single-grain collector geometry, which allows us to isolate and quantify the factors governing dendrite emergence in porous media. We emphasize that the single-grain collector was not designed to replicate the full complexity of the porous medium, but rather to isolate the hydrodynamic and adhesive conditions necessary to initiate dendritic build-up. Although the 20 µm cylindrical grain is smaller than the grains in the porous domain, this controlled geometry enables a focused analysis of the initial stages, promoting dendrite formation and multilayer growth.

To achieve this, we conduct experiments by injecting particle suspensions at flow rates ranging from 1 µL/min to 10 µL/min, corresponding to velocities between 8.3 mm/s and 83 mm/s in the feeding channel just before the single-grain collector. We maintain the same salt concentration (100 mM) as in the porous domain experiments to ensure consistency. To analyze deposition

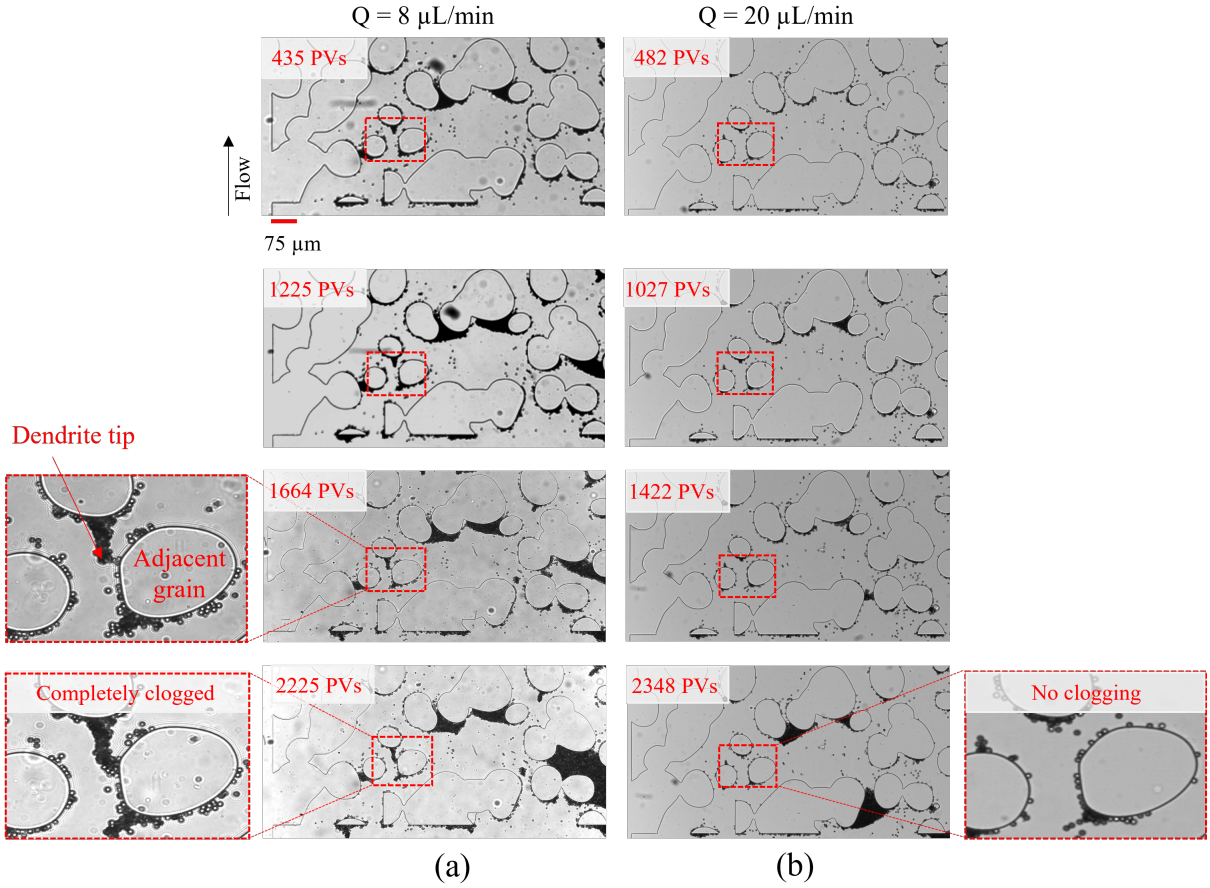

Figure 5.2: Averaged images from experiments conducted at two flow rates, (a) 8 µL/min and (b) 20 µL/min, capturing a section of the porous domain at different pore volumes and highlighting distinct clogging mechanisms. In (a), multiple clogging regions emerge, with a particular focus on the progressive development of dendritic clogging. An initial dendrite forms after 435 PVs (highlighted in a red dotted box), extending upstream by 1225 PVs. By 1664 PVs, the dendrite tip advances further toward the adjacent grain (annotated in the magnified side image), eventually leading to complete pore clogging as the structure continues to grow, constricting the local flow pathway. In (b), multiple clogging events occur, but no dendrite formation or dendrite-induced clogging is observed in the same region, even after injecting 2348 PVs.

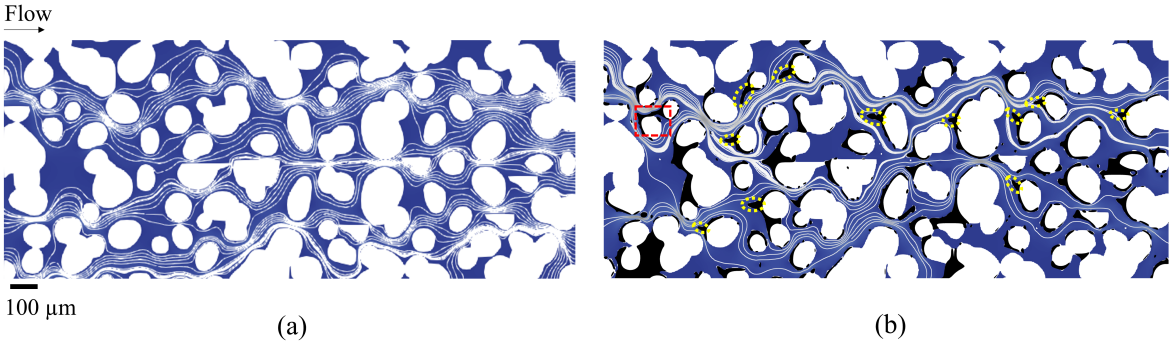

Figure 5.3: Streamlines extracted from fluid flow simulations at an 8 µL/min flow rate, showing particle deposits in black and grains in white. (a) Flow field at the beginning of the experiment, illustrating the initial streamline configuration. (b) Flow field after 2225 PVs of particle suspension injection, where dendritic structures (circled in yellow) are seen growing into the pore space. These deposits progressively distort the surrounding streamlines. The red-dotted box highlights a region where dendrite-induced clogging causes a complete redirection of particle flow, contrasting with the initial pattern in (a). Additional clogging mechanisms throughout the domain are also observed to contribute to local flow redirection.

patterns, we record image sequences after 2500 PVs injected through the single-grain collector geometry, roughly aligning with the endpoint of the porous domain experiments for comparison. In Figure 5.4a, at a flow rate of 1 µL/min, particles predominantly attach at the front stagnation region, facing the flow, leading to a progressive buildup and the formation of dendrites. At 5 µL/min, deposition is limited to a monolayer on the collector surface in the upstream stagnation region, with no significant particle-particle attachment. At 10 µL/min, no deposition occurs at the upstream stagnation region. Instead, as particles approach this zone, they experience a velocity drop, causing them to roll along the collector's sides before settling at the rear stagnation region.

To establish a quantitative basis for our experimental observations, we calculate the critical detachment velocity using Equation 5.2, which balances the adhesive torque that binds a particle to a collector surface or previously deposited particle against the drag torque that mobilizes it. Our results suggest that for a particle to attach to a collector surface, its velocity (V_x^f) must remain below the threshold $V_x^c(p-s) = 8.3$ mm/s. In comparison, attachment to a previously deposited particle requires a lower threshold, with V_x^f needing to stay below $V_x^c(p-p) = 1.6$ mm/s. Both values are calculated at a separation distance of one particle radius. In Table 5.2, we present the normalization of the simulated fluid flow velocity (V_x^f) with the calculated critical velocities $V_x^c(p-s)$ and $V_x^c(p-p)$. Our results show that particle−collector surface attachment is favored in the three experiments performed as $V_x^f/V_x^c\,(p-s) < 1$. However, the location of these attachments is highly dependent on the hydrodynamic force. At flow rates of 1 µL/min and 5 µL/min, particles tend to deposit at the front stagnation regions where $V_x^f/V_x^c\,(p-s)$ remains relatively low. In contrast, at 10 µL/min, when the fluid velocity approaches this threshold ($V_x^f/V_x^c\,(p-s) \approx 1$), particles begin to roll along the surface, reducing their contact area and weakening adhesive forces. This rolling motion continues until they reach the rear stagnation point, where adhesive forces are re-established, promoting stable deposition. Particle deposition in the rear stagnation zones of the collector observed in our experiments aligns with the findings of Kusaka et al. [2010], which indicate that at sufficiently high flow rates, particles preferentially accumulate at the rear of the collector.

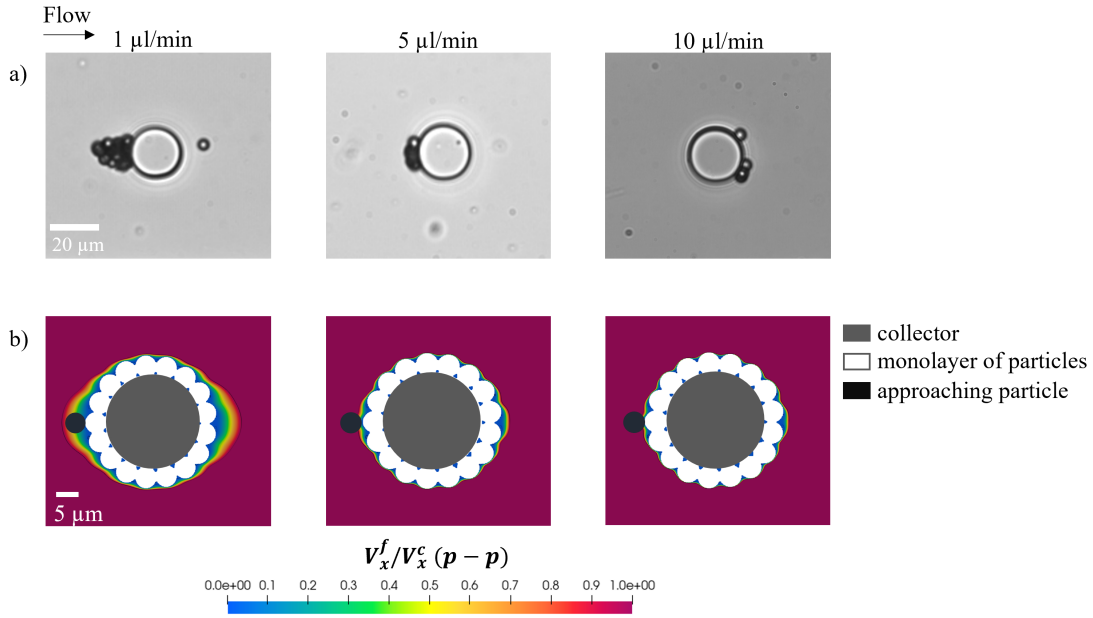

Figure 5.4: (a) Images captured after 2500 PVs under 100 mM salt concentration, illustrating the different deposition patterns achieved on a single-grain collector geometry at flow rates ranging from 1 µL/min to 10 µL/min. At 1 µL/min, particles progressively build up at the upstream stagnation region of the collector surface, forming a dendrite. At 5 µL/min, a monolayer of depositions forms with no particle−particle attachment observed. At 10 µL/min, no deposits are observed at the upstream stagnation region; instead, particles decelerate in this region, roll along the collector surface, and attach at the rear stagnation region. (b) Simulated fluid velocity fields normalized by the critical velocity for particle–particle detachment ($V_x^f/V_x^c(p\text{-}p)$). The simulations include both the collector and an explicit monolayer of deposited particles. At 1 µL/min, the upstream stagnation region is wide enough to accommodate an additional particle, promoting multilayer buildup. As the flow rate increases, this region compresses and becomes too narrow to support further deposition, explaining the absence of dendrites at higher flow rates.

For dendritic structures to develop, a monolayer of deposits must first form at the front stagnation regions, observed only at 1 µL/min and 5 µL/min. However, dendrite formation occurred only at the lower flow rate (1 µL/min), where the fluid velocity remains below the threshold for particle–particle attachment where $V_x^f/V_x^c(p\text{-}p) < 1$ (Table 5.2). To analyze particle–particle attachment, we assume in our analysis that an initial monolayer of particles forms along the collector surface, represented as "monolayer of particles" in Figure 5.4b. This monolayer serves as a prerequisite for initiating multilayer deposition by providing a foundation for further buildup.

In Figure 5.4b, we perform fluid flow simulations to extract the velocity profile and normalize it by the critical velocity threshold for particle–particle detachment. This allows us to define cone-shaped stagnation regions that promote multilayer build-up. In these regions, adhesive forces dominate over hydrodynamic forces, promoting particle aggregation and the formation of multilayer deposits, which eventually can develop into elongated dendritic structures. In contrast, higher shear forces outside these zones suppress aggregation, limiting particle–particle attachment along the sides of the grain. We also highlight the effect of increasing flow rate on the compression of these front stagnation regions. At 1 µL/min, the stagnation region is large

Table 5.2: Ratios of simulated fluid velocity (V_x^f) to the critical detachment velocity for particle-collector surface attachment ($V_x^c\,(p-s)$) and particle-particle attachment ($V_x^c\,(p-p)$) at a separation distance of one particle radius, across flow rates ranging from 1 µL/min to 10 µL/min

Flow rate (µL/min)	1	5	10
$V_x^f/V_x^c\,(p-s)$	0.08	0.4	0.8
$V_x^f/V_x^c\,(p-p)$	0.4	2	4

enough to accommodate one particle diameter, illustrated by the "approaching particle" shown in Figure 5.4b. However, as the flow rate increases, these regions compress, becoming too small to accommodate even a single particle. Since dendrites formed only at 1 µL/min, as experimentally observed in Figure 5.4a, this suggests that dendrite formation requires a stagnation region large enough to accommodate at least one particle diameter, promoting directional multilayer build-up — a flow-dependent criterion that highlights the critical role of the cone-shaped stagnation zone. Our findings align with those of van der Wee et al. [2023], who reported that active microrollers preferentially accumulate in hydrodynamically defined low-velocity zones around cylindrical obstacles, analogous to the cone-shaped stagnation regions identified in our study. While their system involves active particles, it reinforces the broader conclusion that flow-defined structures govern preferential particle accumulation regardless of the deposition mechanism.

In the context of the porous domain, we similarly assume that an initial monolayer of particles forms along the grain surfaces, serving as a base for further multilayer buildup. Applying this analysis — and the flow-dependent criterion extracted from the single-grain collector geometry — to the porous domain, we find that at 8 µL/min the cone-shaped stagnation region, annotated in the magnified image in Figure 5.5a, can accommodate approximately 1.5 particle diameters. If this criterion indeed holds in the porous geometry, dendrite formation should occur, which is confirmed by superimposing the final particle deposits from the experiment onto the $V_x^f/V_x^c, (p\text{-}p)$ profile. In contrast, at 20 µL/min, as shown in the magnified image in Figure 5.5b, the front stagnation region compresses to the point where it can no longer accommodate even a single particle. Consistently, superimposing the final particle deposits onto the $V_x^f/V_x^c, (p-p)$ profile reveals no dendritic structures but rather a predominant monolayer of particles surrounding the grains.

From both the single-grain collector and porous domain analyses, we conclude that dendrite formation requires a cone-shaped stagnation region large enough to accommodate at least one particle diameter, promoting directional multilayer build-up.

5.3.3 Impact on porous media properties

We have shown that dendrites form under specific conditions and play a role in clogging. Understanding how particle deposition and clogging affect porosity and permeability is essential. Porosity is determined from binary images of the porous domain captured at different pore volumes of particles injected (PVs), while permeability changes are inferred from pressure drop measurements (ΔP) taken during experiments performed at flow rates of 8 µL/min and 20 µL/min.

In Figure 5.6, the normalized pressure difference ($\Delta P/\Delta P_0$) increases over time in both experiments, reflecting progressive particle deposition and clogging. At a flow rate of 8 µL/min, the normalized pressure difference is consistently higher than at 20 µL/min, indicating greater deposition and clogging at lower flow rates due to reduced particle velocity. Both experiments show a rapid increase in $\Delta P/\Delta P_0$ during the first 800 PVs, followed by a gradual rise until it stabilizes between 1400 PVs and 2400 PVs. The experiment is terminated after 2400 PVs, as

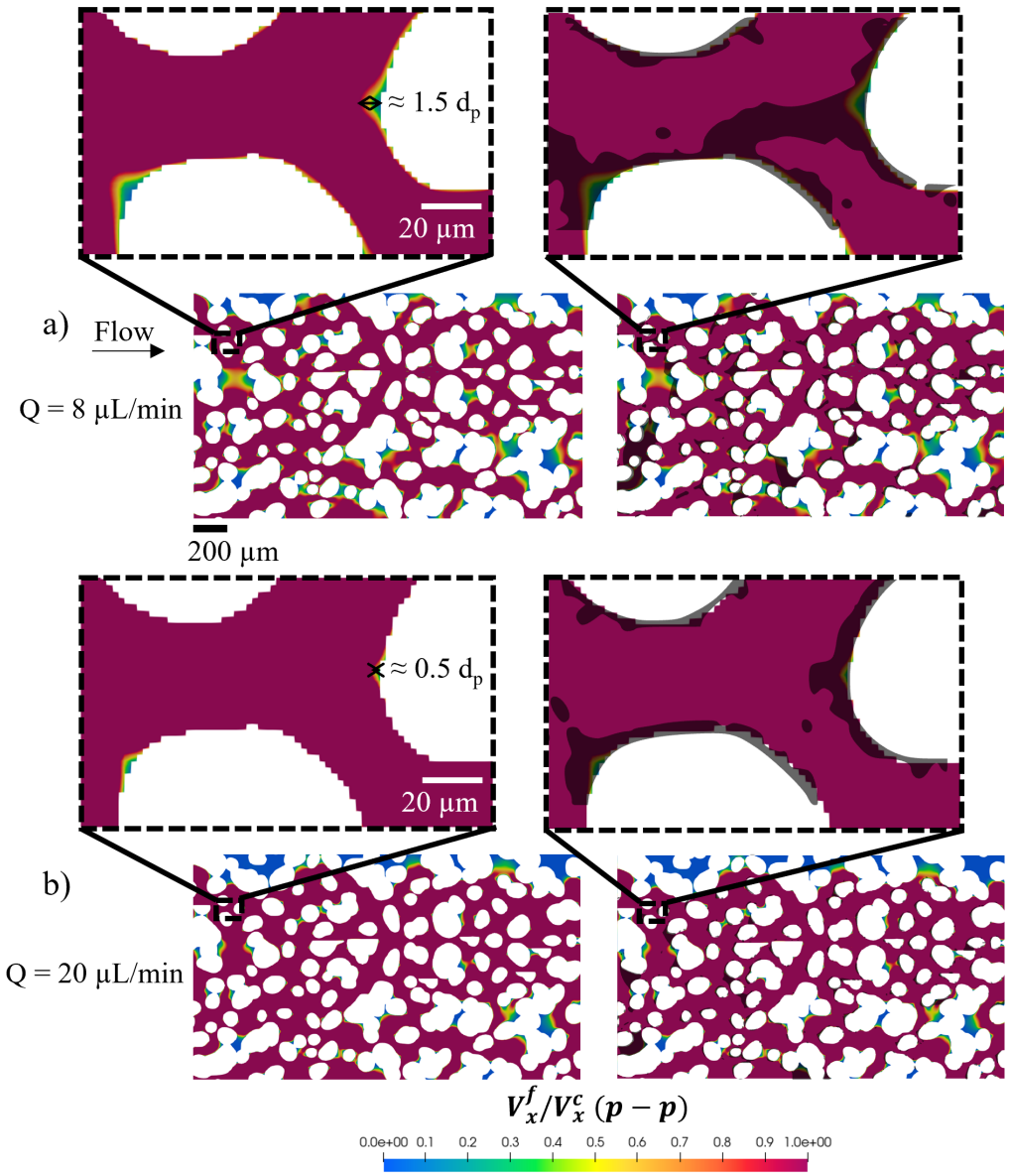

Figure 5.5: Fluid flow velocity profiles obtained by simulations and normalized by the critical velocity for particle-particle detachment ($V_x^f/V_x^c\,(p-p)$) at flow rates of 8 µL/min (a) and 20 µL/min (b). (a) The magnified image shows a stagnation region that accommodates approximately 1.5 particle diameters. The adjacent image overlays the experimental deposition pattern onto the normalized velocity profile, highlighting dendrite formation and build-up in the front stagnation regions. The progression of dendrite growth leading to clogging is shown in the magnified image. (b) The magnified image shows a stagnation region that accommodates only 0.5 particle diameters. The adjacent image shows the superimposition of the experimental deposition pattern on the normalized velocity profile, illustrating the absence of dendrites in the front stagnation regions within the porous domain. This emphasizes the critical role of stagnation region size in initiating dendrite growth, as the region is too small to accommodate a single particle diameter.

further changes in ΔP become negligible.

We compare our experimental data to established permeability models to quantify the relationship between permeability and porosity. The Kozeny-Carman equation is a widely used model that relates permeability to porosity based on an idealized flow representation through packed granular media [Kozeny, 1927, Carman, 1939]. However, it assumes uniform particle deposition and a homogeneous pore structure, which does not accurately capture the complexity of clogging in our system. In particular, our experiments reveal that permeability decline is influenced by localized dendritic growth and heterogeneous deposition patterns, leading to deviations from the smooth permeability reduction predicted by the Kozeny-Carman model.

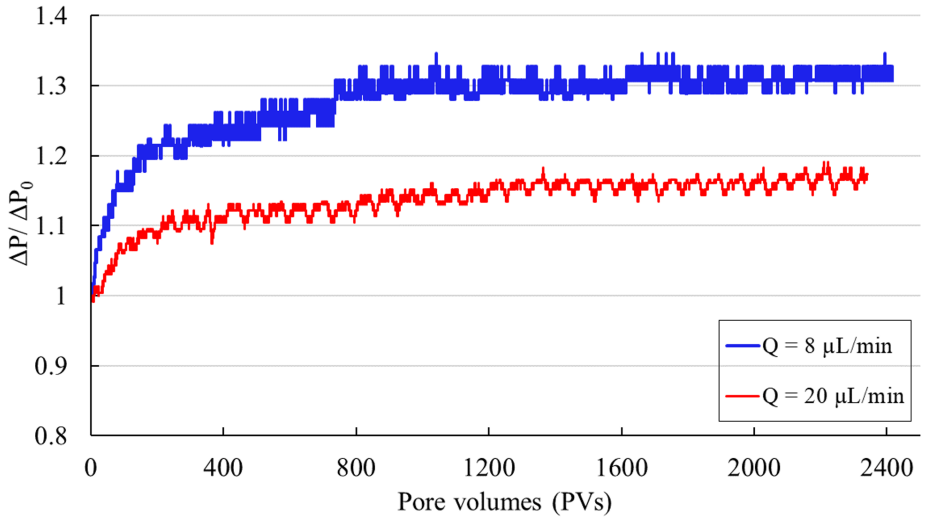

Figure 5.6: The normalized pressure drop ($\Delta P/\Delta P_0$) across the porous domain after injecting multiple pore volumes (PVs) is shown for two flow rates, Q = 8 µL/min and Q = 20 µL/min. In both experiments, $\Delta P/\Delta P_0$ builds up due to particle deposition and clogging, with consistently higher values at Q = 8 µL/min. During the first 800 PVs, the pressure difference rises rapidly before gradually stabilizing between 1400 PVs and 2400 PVs in both cases.

Given these limitations, we use the Verma-Pruess model, a power law extension of the Kozeny-Carman model, originally proposed by Verma and Pruess [1988] and later reformulated by Ott et al. [2015]. This model was initially developed to describe permeability reduction caused by mineral precipitation and biofilm accumulation, where solid deposits gradually obstruct pore spaces [Hommel et al., 2018]. Since both mineral precipitation and dendrite formation and clogging follow the same localized, structure-dependent pattern of modifying and blocking the flow, the Verma-Pruess model is a good choice for describing permeability loss in our system. This nonlinear model better reflects the permeability-porosity relationship observed in our experiments:

$$\frac{K - K_C}{K_0 - K_C} = \left(\frac{\Phi - \Phi_C}{1 - \Phi_C}\right)^{\tau}, \tag{5.2}$$

where $\Phi = \phi/\phi_0$ represents the normalized porosity, where ϕ is the actual porosity and ϕ_0 is the initial porosity. Likewise, K is the actual permeability, K_0 is the initial permeability, and K_C is the critical (or minimum) permeability reached due to particle deposition and clogging at a critical reduced porosity, Φ_C.

A key advantage of the Verma-Pruess model is that it incorporates K_C and Φ_C, which allow us to describe the experimentally observed stabilization of permeability and porosity. By assigning $\Phi_C = 0.864$ and $\Phi_C = 0.944$, corresponding to the final porosities observed at the end of the

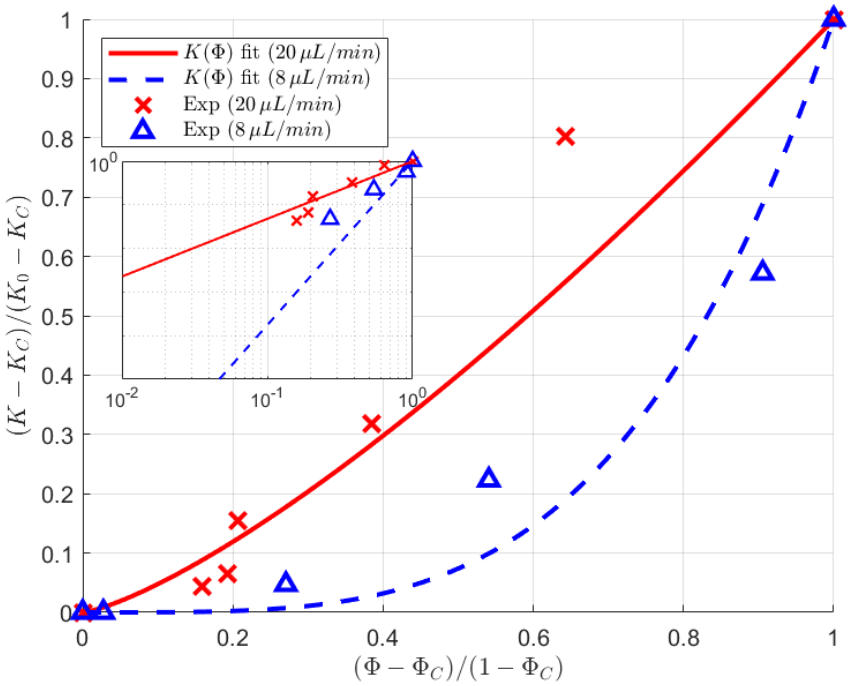

Figure 5.7: The permeability-porosity relationships ($K(\Phi)$) describing the experimental observations for the two flow rates Q = 8 µL/min (blue) and Q = 20 µL/min (red) are shown along with their corresponding fitting curves. These curves accurately capture the experimental trends using the Nonlinear Least Squares method with a robust bisquare weighting, achieving R-squared values of 0.995 and 0.982 for Q = 8 µL/min and Q = 20 µL/min, respectively. The data for Q = 8 µL/min clearly shows a steeper permeability decline, with an exponent $\tau = 3.75$, compared to $\tau = 1.32$ for Q = 20 µL/min. This indicates a more pronounced particle deposition and clogging effect at lower flow rates. An inset shows the same data on a log–log scale, confirming the power-law behavior through the linearity of the trend in logarithmic coordinates.

8 µL/min and 20 µL/min experiments, we obtain K_C/K_0 values of 0.764 and 0.867, respectively. Figure 5.7 presents the experimentally obtained permeability-porosity relationship for the two flow rates, 8 µL/min and 20 µL/min, and their respective fitting curves. Each data point corresponds to a distinct pore volume injected during a single continuous experiment at a given flow rate. Separate experiments were conducted for each flow rate, and the data were analyzed independently. In the final plot, we selected data points that correspond to similar injected pore volumes across experiments to facilitate meaningful comparison between flow rates. The fitting curves effectively describe the experimental data trends, yielding exponents of $\tau = 3.75 \pm 0.66$ for 8 µL/min and $\tau = 1.32 \pm 0.27$ for 20 µL/min. The higher exponent at 8 µL/min reflects a more abrupt permeability loss, consistent with more pronounced effects of particle depositions and clogging inferred from the pressure measurements. To confirm the power-law behavior, a log–log representation of the same data is provided as an inset in Figure 5.7, and demonstrating that the experimental relationship is not linear on a standard plot.

These findings highlight the critical role of flow rate in governing clogging mechanisms and deposition patterns. At a moderate flow rate of 8 µL/min, dendritic structures emerge in the front stagnation regions begin to alter local streamlines and redirect flow even before complete pore blockage occurs, as shown in Figure 5.3 and the supplementary video (Movie_Figure_3a_ 8_µL/min_ 1664_PVs) [Okaybi et al., 2025]. In some regions, these dendrites continue to grow, as observed in Figure 5.2 and the Appendix A.4, ultimately leading to full pore blockage and significant redirection of the local flow due to dendrite-induced clogging. These effects—both before and after dendrite clogging—combined with the fact that lower particle velocities at 8 µL/min promote increased deposition through additional clogging mechanisms, contribute to a more pronounced permeability decline. In contrast, at the higher flow rate of 20 µL/min, dendrite formation is suppressed, and particle deposition is less pronounced due to higher velocities, resulting in a more gradual permeability decline. Together, these results demonstrate the effectiveness of the Verma–Pruess model in capturing deposition patterns and underscore how hydrodynamic conditions regulate particle accumulation and clogging behavior in porous media.

5.4 Conclusions

From industrial uses like microfluidic filtration to natural processes like groundwater filtration, clogging in porous media plays a critical role in many diverse systems. Our study provides new insights into how dendritic structures drive clogging in porous media, highlighting a distinct mechanism where deposition extends progressively from a single deposition site to bridge pore spaces. Unlike clogging by aggregation, dendrite clogging emerges due to flow-dependent stagnation zones that enable multilayer deposition within them. This finding advances our understanding of permeability loss in complex porous environments and suggests that clogging dynamics are not solely dictated by particle accumulation but also by the evolving interplay between hydrodynamics and deposition patterns.

Despite these advances, key questions remain. The impact of particle surface properties, such as charge and roughness, on dendrite stability is not yet fully understood. Another open question concerns the role of fixed-pressure conditions in dendrite formation. Under such conditions, the flow rate gradually decreases as clogging progresses. Assuming the system initially satisfies our flow-dependent criterion for dendritic growth, we expect that the velocity weakening over time would reduce the adjacent high-shear zones responsible for sustaining directional growth. This reduction in shear could promote multilayer deposition along the sides of the growing dendrite, eventually burying the tip and transitioning the structure into a flattened or radially symmetric deposit. Additionally, while our experiments provide direct observations in two-dimensional porous networks, a natural extension would be to investigate the extent to which dendrite formation

and dendrite-driven clogging translate to three-dimensional environments. Addressing these aspects will refine predictive models and inform strategies for mitigating clogging in complex porous systems. Extending these insights to broader porous environments could enhance filtration efficiency, optimize subsurface flow, and improve microfluidic performance, ultimately contributing to better clogging control in both natural and engineered systems.

Chapter 6

Permeability impairment by hydrodynamic pore bridging: Probabilistic pore-network modeling and microfluidic experiments

This chapter builds on the second and third research gaps identified in Chapter 3, concerning the limited understanding of bridging-induced clogging in heterogeneous porous media and the lack of predictive frameworks coupling pore-scale experiments with pore-network modeling. It investigates hydrodynamic pore bridging under conditions where aggregation is limited, to clarify how flow conditions, particle properties, and pore-scale confinement control the onset and evolution of clogging, and how these processes translate into permeability impairment. The chapter is based on Soulaine et al. [2026]; the corresponding experimental dataset is publicly available in Okaybi et al. [2026a].

6.1 Introduction

Permeability impairment caused by the flow of suspended particles is a critical mechanism in various industrial processes, including filtration, groundwater flow, and subsurface engineering. For instance, the detachment and mobilization of fines—small sand or clay particles loosely adhered to pore walls—by hydrodynamic forces and changes in fluid salinity [Khilar and Fogler, 1984, Cerda, 1987, Khilar et al., 1990] can significantly reduce permeability near wells. This phenomenon poses a serious threat to the productivity of geothermal and oil reservoirs, often requiring costly remediation treatments or even leading to the abandonment of affected wells.

Three primary mechanisms are responsible for pore clogging during the flow of particle suspension: (i) sieving, (ii) bridging, and (iii) particle aggregation [Dressaire and Sauret, 2017b]. Sieving occurs when particles are physically excluded from entering a pore due to their size [Sauret et al., 2014]. Bridging refers to the formation of arch-like structures by a few particles arriving simultaneously at a pore entrance where the flow converges [Ramachandran and Fogler, 1998]. Aggregation involves the gradual accumulation of colloidal particles, driven by long-range electrochemical interactions between the fluid, the particles, and the solid matrix [Dersoir et al., 2019]. A secondary process associated with aggregation involves the progressive growth of dendritic structures that ultimately result in pore plugging [Okaybi et al., 2025]. During operation, these clogging mechanisms may co-occur, and their combined effects can exacerbate system performance degradation [Wyss et al., 2006b].

This study focuses on clogging by bridging – a phenomenon observed in micromodel experiments since the late 1970s, though it was not well understood at the time [Muecke, 1979]. Later experiments using straight and constricted microtubes demonstrated that stable particle arches can form and obstruct flow, even at low particle concentrations [Sharp and Adrian, 2005]. Bridging occurs when hydrodynamic forces overcome repulsive interactions and balance contact forces between particles and between particles and the pore walls. Numerous studies have investigated the influence of particle size and concentration, flow rate, and pore geometry on the onset of arch formation. A breakthrough was achieved by Goldsztein and Santamarina [2004a], who found that clogging by arch formation typically occurs after a certain amount of volume of fluid is extracted. Based on that, Wyss et al. [2006b] defines a critical number of particles that need to pass through a pore throat before clogging. Notably, this number was found to be largely independent of flow rate but highly sensitive to pore geometry—specifically the particle-to-throat size ratio, the pore-to-throat radius ratio, and the smoothness of the throat [Souzy et al., 2020, Marin et al., 2018, Janda et al., 2008]. These findings have been confirmed by numerous experimental and numerical studies on clogging at the single-pore scale [Agbangla et al., 2012b, 2014, Dersoir et al., 2015b]. They laid the foundation for probabilistic laws linking arch formation to particle-to-throat size ratio and particle concentration [Ortega-Roano et al., 2023, Vani et al., 2022]. More recently, Vani et al. [2024] highlighted the role of throat angle in facilitating bridging, which led Fogouang Maya et al. [2025] to propose a new stochastic model that predicts pore clogging probabilities based on suspension properties, throat angle, and the particle-to-throat size ratio. The model incorporates two fitting parameters that capture the influence of pore geometry and has demonstrated strong predictive capability across a wide range of simulation and experimental conditions. These probabilistic laws of clogging have been developed for individual pore throats, but a significant gap remains in using them to predict permeability impairment at the scale of a rock, where the microstructure consists of a heterogeneous network of interconnected pores.

The prediction of permeability impairment by particle suspensions through numerical simulation remains in its infancy. While high-fidelity pore-scale simulations are now feasible, they are still highly computationally demanding. Among the most advanced approaches in this field are four-way coupled Computational Fluid Dynamics–Discrete Element Methods (CFD-DEM), which combine the grid-based – or lattice-based – solution of the Navier–Stokes equations in the pore space with Lagrangian tracking of solid particle transport and retention [Tsuji et al., 1993, Ladd, 1994]. Modern CFD-DEM frameworks account for the feedback of particle presence on the fluid flow, and incorporate the mechanical interactions between particles and pore walls [Sun, 2023, Fogouang Maya et al., 2025, Mondal et al., 2016] as well as colloidal interaction forces [Samari-Kermani et al., 2021, 2020, Fogouang et al., 2024, Li et al., 2023]. Therefore, these frameworks are capable of simulating a wide range of pore-clogging mechanisms, including sieving, bridging, and particle aggregation. However, because they explicitly resolve all contact and long-range interactions, such simulations are computationally intensive and, at present, are not feasible for modeling particle migration and retention across large domains representative of the three-dimensional structure of a core sample [Mirabolghasemi et al., 2015].

An alternative approach widely adopted in porous media research and engineering to compute permeability from digital rock images is the use of pore-network models (PNMs) [Blunt et al., 2013]. In this approach, the rock microstructure is approximated as a network of interconnected nodes – corresponding to pore bodies – and cylindrical throats [Fatt, 1956]. A wide variety of PNMs have been proposed to simulate particulate transport and retention in porous media. Eventually, they should be able to predict not only the permeability response and the effluent concentration during deep bed filtration, but also the mapping of pores plugged by particles under varying particle size distributions and concentrations, flow rates, fluid pH, and salinity. The first PNM to simulate formation damage caused by injection of particles has been proposed by Todd et al. [1984] using

a simplified approach to particle transport and retention. Since this pioneering work, PNMs for particulate transport have evolved significantly and become increasingly sophisticated. Two main modeling approaches have emerged. On the one hand, particle tracking methods explicitly simulate the motion of individual particles through the network [Meng and Yang, 2019, Rege and Fogler, 1987, Feng et al., 2015]. On the other hand, Eulerian approaches compute the particle concentration by solving an advection–diffusion-retention equation within the network [Lin et al., 2021, Seetha et al., 2017, Tang and Raoof, 2024].

The particle tracking approach in PNM provides a discrete, Lagrangian framework in which particle trajectories and retention behavior are governed by local flow conditions and probabilistic rules [Meng and Yang, 2019]. A key challenge in early implementations was the redistribution of particle paths at network bifurcations. [Rege and Fogler, 1987] addressed this using a flow-biased probabilistic algorithm, where particles choose exit throats based on the relative flow distribution, favoring pathways with higher flow rates. While their model accounted for a range of particle sizes, it was limited to simulating clogging by sieving (size exclusion). This framework was later extended by Rege and Fogler [1988, 1991], who introduced both straining of particles larger than pore throats and probabilistic deposition at solid walls for smaller particles, thereby capturing a broader spectrum of retention mechanisms. Follow-up studies have built on this approach, refining deposition models to assess how particle and network characteristics influence permeability damage [Siqueira et al., 2003, Feng et al., 2015]. More recent advancements, such as the model by Yang and Balhoff [2017], incorporate surface roughness and detailed particle–surface interactions to improve predictions of particle capture. Collectively, these efforts have significantly enhanced our understanding of how microscale transport phenomena contribute to permeability decline. However, while particle-tracking PNMs have proven effective at simulating pore clogging by sieving and deposition, modeling clogging by bridging remains a persistent challenge.

Eulerian approaches in PNMs solve advection–dispersion equations for particle concentrations within pore bodies and throats, coupled with mechanistic descriptions of particle retention processes. Originally introduced to simulate reactive transport at the pore scale – such as surface reaction kinetics and molecular adsorption onto pore walls [Raoof et al., 2010, 2013] – this framework has since been extended to account for particulate transport and clogging phenomena. A key advantage of the Eulerian formulation is its ability to capture hydrodynamic dispersion within throats, which is critical for accurately predicting the spreading and mixing of particles. Mehmani and Tchelepi [2017] demonstrated that Eulerian PNM approaches can reliably reproduce results from direct numerical simulations of passive scalar transport, validating their suitability for transport modeling in heterogeneous porous structures. Building on this foundation, Seetha et al. [2017] developed a PNM framework that integrates advective–diffusive transport with size-dependent retention mechanisms, enabling the simulation of aggregation-driven clogging. Lin et al. [2024] employed a similar PNM to investigate the impact of colloid deposition on breakthrough curves and retention profiles across pore networks. In addition to deposition kinetics, Lin et al. [2021] introduced straining and a hydrodynamic bridging criterion: clogging is predicted if the cumulative projected area of retained colloids exceeds the cross-sectional area of the pore throat. With their framework, they were able to investigate, by simulation, the impact of particle size and concentration, flow rate, and fluid chemistry on permeability reduction. Tang and Raoof [2024] further advanced this modeling framework by considering the number of particles passing through a throat before forming an arch that plugs the pores, as proposed by Wyss et al. [2006b]. Li et al. [2021b] proposed a probabilistic PNM in which the bridging probability is controlled by particle concentration, pore-to-particle size ratio, and friction, and is calibrated against CFD–DEM simulations. While these studies have significantly enhanced our understanding of pore-scale clogging mechanisms, the probability law governing this particle threshold does not explicitly account for pore geometry. Moreover, their predictive capabilities

have yet to be validated against experimental observations, leaving a gap between modeling and empirical evidence.

In this paper, we investigate permeability impairment due to particle bridging using both microfluidic experiments and pore-scale modeling. The use of microfluidic devices that replicate the complexity of natural porous media [Roman et al., 2016], combined with state-of-the-art imaging and post-processing methods [Roman et al., 2025], enables the assessment of permeability impairment due to particle clogging. We present a novel pore-network model that incorporates the probabilistic nature of hydrodynamic pore bridging. It accounts for key parameters influencing bridging, including particle size and concentration, the particle-to-throat size ratio, and the pore-to-throat radius ratio. The structure of the paper is as follows. In Section 6.2, we introduce the developed pore-network model along with the CFD-DEM-based approach used to calibrate the bridging probability law. We also describe the microfluidic experiments conducted to support and validate the numerical results. In Section 6.3, we compare experimental and numerical results on the injection of suspensions into porous media, highlighting the emergence of pore bridging and the resulting permeability impairment. Finally, we conclude with a summary of the main findings and an outlook on future research directions.

6.2 Materials and Methods

In this section, we present the numerical and experimental framework developed to investigate hydrodynamic bridging in porous media. We begin by describing the geometry of the porous medium used in both simulations and experiments. Next, we describe the microfluidic experiments designed to assess the robustness and predictive capability of the model. Finally, we introduce our novel pore-network model, which incorporates a probabilistic law for arch formation at pore entrances.

6.2.1 Heterogeneous porous geometry

We use a heterogeneous porous geometry that mimics the complexity and heterogeneity of subsurface environments, which is essential for investigating particle transport and clogging phenomena. In this study, we use the $M3$ heterogeneous tortuous porous geometry shown in Fig. 4.2. The design procedure, generation method, and detailed pore-scale statistical characterization of this geometry are described in the Materials and Methods chapter (Chapter 4.1.1).

6.2.2 Flow experiments and image analysis

Fabrication of PDMS Microfluidic devices are then fabricated following standard soft lithography procedures using polydimethylsiloxane (PDMS) [Whitesides et al., 2001]. The complete fabrication workflow—from PDMS preparation to irreversible bonding of the PDMS replica to a glass slide—is described in Chapter 4.1.3. To ensure stable and reproducible surface hydrophobicity during experiments, the assembled devices are placed in an oven at 120 °C for at least 3 hours prior to use [Dersoir, 2015].

Particle suspensions The particles used in this study have diameters of either 4.5 µm or 6 µm and are suspended in a density-matched carrier fluid. The particle properties, suspension preparation, and density-matching procedure are detailed in Chapter 4.2. The particle suspensions used here have volume fractions of 0.2% and 0.3%, depending on the experimental conditions. The viscosity of the final mixture is approximately 1.45 mPa·s. The two-dimensional arithmetic mean constriction width of the porous geometry is approximately $W \simeq 20$ µm, as presented in Table. 4.1. The corresponding confinement ratio, W/d_p, therefore ranges from 3.33 to 4.44 depending on the

particle diameter. Under these salt-free conditions, particle–particle and particle–wall interactions are weakly screened, and bridging can be initiated at constrictions, ultimately leading to clogging.

Flow experiments The experiment begins by saturating the microfluidic device with a particle-free, density-matched fluid to eliminate trapped air and ensure consistent initial conditions (see Figure 6.1 for a schematic of the experimental setup). Flow is driven using a pressure controller (FLUIGENT EZ FLOW) connected to a reservoir containing the particle suspension, with experiments conducted at two different pressure drops, 100 mbar and 150 mbar, so that flow remains in the creeping-flow regime at low Reynolds number. As discussed in Chapter 4.5, PDMS deformation is not desirable because it can affect particle deposition and clogging behavior by altering the hydraulic resistance through dilation of the channel walls. We ensure that all experiments were conducted at inlet pressures below the predefined threshold, identified to be around 250 mbar. The suspension is delivered through 0.5 mm inner diameter Tygon tubing, which passes through a one-way valve. This valve is essential when switching between particle-free fluid and particle suspension, as it prevents air from entering the flow path. Once the particle suspension reaches the entrance of the porous domain, the experiment is initiated. The flow rate is continuously monitored over time using a Coriolis flow sensor (Bronkhorst) positioned downstream of the microfluidic device. The flow sensor records data at 1-second intervals, but due to sensor-induced fluctuations, we apply an additional smoothing step using a Python script. A moving average with a 50-second window is used to consistently smooth the flow rate data across all experiments [Dincau et al., 2022]. The experiment continues until full clogging occurs, which is defined as the point at which the flow rate drops to 85% of its initial value.

Image analysis To monitor the evolution of clogging over time, image sequences are recorded at selected time points throughout the experiment. Since the field of view of the camera covers less than the full length of the porous domain, several sequences are acquired at consecutive locations along the flow direction (x-axis). Each sequence is temporally averaged to highlight only the immobile (deposited) particles while removing those in motion, and the resulting averaged images are stitched together to reconstruct a complete 2D view of the porous domain. The full acquisition and processing workflow is described in Chapter 4.4.

To quantify how particle deposition varies along the flow direction, a custom Python script is used to analyze the final stitched images of the porous domain. All images are processed using the same grayscale contrast settings, applied once clogging is reached—defined here as the point when the flow rate drops to 85% of its initial value. Deposited particles are identified by grayscale thresholding (see Chapter 4.4 for details), and each stitched image is divided into ten equal segments along the streamwise (x) direction. The number of particle-classified pixels is counted within each segment and normalized by the total number of pixels in the full image. The resulting distribution is plotted, allowing direct comparison of particle deposition patterns along the x-direction for different experimental conditions.

6.2.3 Pore-network model with probability of bridging

The modeling approach, including its numerical implementation and the calibration of the bridging probability, was developed and implemented by my co-authors. It is included here to provide a complete description of the methodology used in the article and to contextualize the experimental results presented in this chapter.

Flow model In a pore-network model, the microstructure is represented as a collection of pore bodies interconnected by cylindrical throats. The volumetric flow rate, Q_{ij}, through the

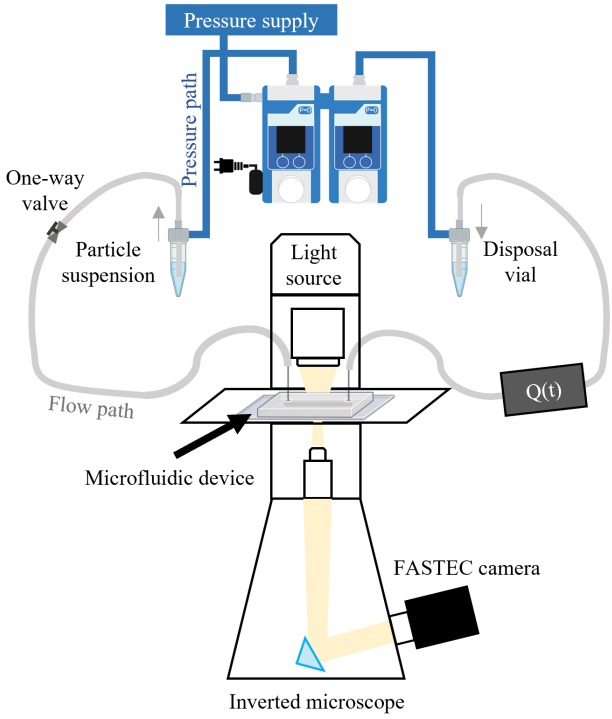

Figure 6.1: Schematic of the experimental setup used for flow experiments. A pressure controller drives the injection of particle suspension from a reservoir through tubing equipped with a one-way valve, which facilitates fluid switching without introducing air bubbles. The flow enters the microfluidic device mounted on an inverted microscope platform, where image sequences are recorded over time using a high-speed camera. A flow rate sensor positioned downstream continuously monitors the decline in flow rate due to pore clogging. The fluid then exits into a disposal vial.

throat connecting pore i to pore j is approximated using a Hagen–Poiseuille–type relation for rectangular sections:

$$Q_{ij} = \frac{\alpha_{ij}\left(D_{ij}, H\right)}{\mu L_{ij}}\left(P_i - P_j\right), \tag{6.1}$$

where α_{ij} is the geometric hydraulic conductance factor, H is the micromodel thickness, D_{ij} is the two-dimensional diameter of the throat, L_{ij} is its length, μ is the suspension viscosity, and P_i and P_j are the fluid pressure in pore i and j, respectively. For a throat with a rectangular cross-section, as commonly encountered in microfluidic devices, the geometric hydraulic conductance factor is $\alpha_{ij} = \frac{HD_{ij}^3}{12}$ if $D_{ij} < H$ and $\alpha_{ij} = \frac{H^3 D_{ij}}{12}$ if $D_{ij} > H$, corresponding to the parallel-plate (wide-slit) limit in each orientation. For solid volume fraction below the jamming transition, the suspension viscosity reads [Zarraga et al., 2000],

$$\mu\left(C\right) = \mu_f \frac{\exp\left(-2.34C\right)}{\left(1 - C/C_m\right)^3}, \tag{6.2}$$

where μ_f is the fluid viscosity, C is the particle concentration and $C_m \approx 0.62$ is the maximum packing density [Zarraga et al., 2000].

Due to mass conservation at each pore, the net flow into pore i must be zero, leading to the

condition:

$$\sum_{j}^{N_i} Q_{ij} = 0, \tag{6.3}$$

where N_i denotes the number of neighboring pores connected to pore i.

Constant pressures are applied at the inlet and outlet boundaries. These boundaries may correspond either to the inlet/outlet of the porous domain itself or to those of the intricate injection channels. In the latter case, the injection channels are represented using pore bodies and throats. All other boundaries parallel to the main flow direction are treated as no-flow boundaries.

The flow equations, combined with mass conservation at each pore and the imposed boundary conditions, result in a linear system that determines the pressure in all pore bodies. This system is solved numerically using MATLAB and is updated at every time step.

Transport model We use the Mixed-Cell Method to solve the advection-dispersion equation governing the evolution of the particle volume fraction throughout the network. In this method, pores are seen as control volumes over which mass balance is imposed. We have,

$$V_i \frac{dC_i}{dt} = \sum_{j=1}^{N_i} Q_{ij}^c, \tag{6.4}$$

where Q_{ij}^c is the mass flux through the pore throat ij. This flux includes both advective and diffusive contributions. Using a first-order upwind scheme for the advective term, the total flux is expressed as:

$$Q_{ij}^c = \mathcal{H}\left(\delta P_{ij}\right) Q_{ij} C_j + \mathcal{H}\left(-\delta P_{ij}\right) Q_{ij} C_i + \mathcal{D}_{ij} S_{ij} \frac{C_j - C_i}{L_{ij}}, \tag{6.5}$$

where $\mathcal{H}\left(\cdot\right)$ is the Heaviside function used to implement upwinding based on the sign of pressure difference, δP_{ij}, in the throat [Mehmani and Balhoff, 2015], $S_{ij} = hD_{ij}$ is the throat cross-sectional area, and $\mathcal{D}_{ij}$ is the effective diffusion coefficient. The latter accounts for Taylor-Aris dispersion in the throat [Aris, 1956, Taylor, 1953, Dentz and Carrera, 2007] using,

$$\mathcal{D}_{ij} = \mathcal{D}_m + \frac{min(h, D_{ij})^2}{4\mathcal{D}_m} U_{ij}^2 \left(\frac{2}{105} - \sum_{n=1}^{\infty} \frac{18}{(n\pi)^6} \exp\left(-4 \left(\frac{n\pi}{min(h, D_{ij})} \right)^2 \mathcal{D}_m t \right) \right), \tag{6.6}$$

where $U_{ij} = \frac{Q_{ij}}{S_{ij}}$ is the average velocity in the throat and the particle diffusion coefficient, $\mathcal{D}_m$, is given by Stokes-Einstein relationship, $\mathcal{D}_m = \frac{k_B T}{3\pi\mu_f d_p}$, k_B and T being the Boltzmann constant and temperature, respectively.

The jamming transition, C_{jam}, bounds the particle concentration and is defined as the concentration at which the suspension becomes immobile. Its value is always lower than the packing density, C_m, and depends on the shear stress, and therefore varies with pore geometry, particle size and concentration, and flow rate [Blanc et al., 2018, Lobry et al., 2018, d'Ambrosio et al., 2025].

Hydrodynamic bridging criterion Bridging occurs when a stable arch of particles forms across a pore throat. The number of particles, n, required to form such an arch depends on the particle size and the throat diameter. It is estimated as:

$$n = \left\lfloor \frac{D}{d_p} \right\rfloor + 1, \tag{6.7}$$

where $\lfloor \cdot \rfloor$ is the floor function (i.e., the greatest integer less than or equal to the argument) and D/d_p is the throat-to-particle diameter ratio.

The probability of forming a stable arch that clogs a pore is governed by N^*, the number of particles that pass through a throat before clogging occurs. Wyss et al. [2006b] has demonstrated that this number is independent of the flow rate. This number depends on the probability of clogging according to [Zuriguel et al., 2005],

$$N^* = \frac{(1 - P_{clog})}{P_{clog}}. \tag{6.8}$$

Building on recent work from my co-authors [Fogouang Maya et al., 2025], the probability of forming a stable arch of n particles reads,

$$P_{clog}\,(n) = k \frac{[(n-1)C]^{n-1}}{(n-1)! \times C_m^{n-1} \times \exp\left(\frac{(n-1)C}{C_m}\right)} \left(\frac{d_p}{D}\right)^n (\sin\theta)^\alpha \times \exp\left(\left(\frac{C}{C_m}\right)^{n^3}\right). \tag{6.9}$$

This discrete stochastic model for predicting pore-clogging probabilities was established under the assumption of a creeping-flow regime (low Reynolds number) for a suspension of monodisperse spherical particles. We also assume smooth particle surfaces and smooth pore walls (no roughness effects). The model was established and validated in Fogouang Maya et al. [2025] using more than 700 CFD–DEM simulations in which particle size, particle concentration, particle-to-throat diameter ratio, and constriction angle were systematically varied. We verified that the predictions of this law are consistent with the probability density function of particle escaping before clogging obtained from both the CFD–DEM simulations and the experimental datasets of Vani et al. [2022], Marin et al. [2018], Vani et al. [2024]. In contrast with the probability laws proposed in the literature [Marin et al., 2018, Vani et al., 2022, Ortega-Roano et al., 2023], Eq. (6.9) depends on the particle concentration C, the maximal packing concentration C_m, and geometric parameters including the throat angle θ, and the particle-to-throat diameter ratio $\frac{D}{d_p}$. The PNM computes the particle concentration within the throat at each time step. The throat angle is determined from the pore geometry and is given by $\tan\theta = \frac{R_i - R_{ij}}{L_{ij}/2}$, where R_i and R_{ij} are the pore and throat radius, respectively. Eq. (6.9) involves two fitting parameters, k and α, that reflect the packing morphology, the shape of the channel, and the particle friction. It has been shown that these parameters are independent of flow rate, particle size, throat angle, and particle concentration, in the limit of the semi-dilute suspensions [Fogouang Maya et al., 2025]. The fitting parameters entering the clogging probability law, $k = 0.3$ and $\alpha = 0.6$, are calibrated using four-way coupled CFD–DEM simulations of suspension injection through a single pore, performed by my co-authors within an OpenFOAM-based framework [Fogouang Maya et al., 2025].

In the PNM, we begin by computing the number of particles required to form a clogging arch in each throat ij, using Eq. (6.7). This calculation is performed only once at the beginning of the simulation, as the suspension is monodisperse. At each time step, we evaluate the clogging probability for every throat using Eq. (6.9), and determine the number of particles that must pass the constriction before clogging, N^*, using Eq. (6.8). If a throat is smaller than the particle diameter, we set $N^* = 1$. Simultaneously, we track the cumulative number of particles that have passed through each pore. Once this number exceeds N^* the likelihood of clogging is considered high, and the throat conductance factor is replaced by $\alpha_{ij} = D_{ij} H \frac{d_p^2 (1 - C_{jam})^3}{180 C_{jam}^2}$ which corresponds to an estimate of the permeability of a throat clogged by packed bed of beads, based on the Kozeny-Carman relationship.

6.3 Results and discussion

In this section, we investigate permeability impairment in a heterogeneous medium during the injection of a monodisperse suspension. We conduct microfluidic experiments to investigate the impact of injection pressure, particle size, and concentration on clogging dynamics. Finally, this high-resolution experimental dataset is used to assess the predictive robustness of the proposed pore network model.

6.3.1 Permeability damage of hydrodynamic pore-bridging via microfluidics

Microfluidic experiments are conducted to investigate how injection pressure, particle size, and particle concentration affect permeability impairment and particle deposition patterns resulting from hydrodynamic pore bridging. A total of five experiments are performed: a base case with a replicate to assess reproducibility, and three additional cases in which flow conditions and suspension properties are systematically varied. Starting from the base case, each parameter is varied by a factor of 1.5, except for particle size, which is varied by a factor of 1.33, to assess the influence of each parameter on permeability impairment fairly. The parameters for each case are summarized in Table 6.1. Each experiment is initiated by saturating the porous micromodel with a particle-free, density-matched fluid to ensure consistent initial conditions. The particle-laden suspensions are then injected at controlled pressure drops using a pressure-driven system.

Plot color	**Pressure drop** ΔP (mbar)	**Concentration** C (%)	**Particle size** d_p (µm)	**Jamming concentration** C_{jam} (%)
Blue	150	0.3	6	0.61
Dashed blue	150	0.3	6	
Red	150	0.3	4.5	0.613
Green	150	0.2	6	0.6145
Purple	100	0.3	6	0.612

Table 6.1: Cases investigated using microfluidic experiments and pore-network modeling.

Base configuration and pore-scale deposition dynamics A suspension containing 0.3% of 6µm particles is injected into the heterogeneous micromodel by applying a pressure difference of $\Delta P = 150$ mbar, and the injection is maintained until complete clogging occurs. Full clogging is observed approximately 10 minutes after the start of the injection. Time-lapse images of the experiment are presented in Figure 6.2. Yellow arrows in the magnified insets of the experimental images indicate the last constriction to become clogged before complete blockage of the micromodel occurs.

At early times, particles flow freely through the porous domain. Some particles are deposited at stagnation points around solid grains, while a few others become trapped by sieving in pore throats narrower than 6µm, as shown in the magnified inset. After 131 seconds, several black regions appear, indicating throats that have become blocked, followed by the progressive filling of the associated pore spaces with particles depositing on both sides of the constriction marked by yellow.

As time progresses, the accumulation intensifies, and larger regions become densely packed with particles. Clogging becomes increasingly pronounced near the inlet, where a filter cake begins to form after 394 seconds. Regarding the constriction of interest, we observe particles depositing and spanning the 2D cross-section of the constriction; however, a gray streamline is still visible downstream in the averaged images at 394 s and 525 s, indicating residual particle flow.

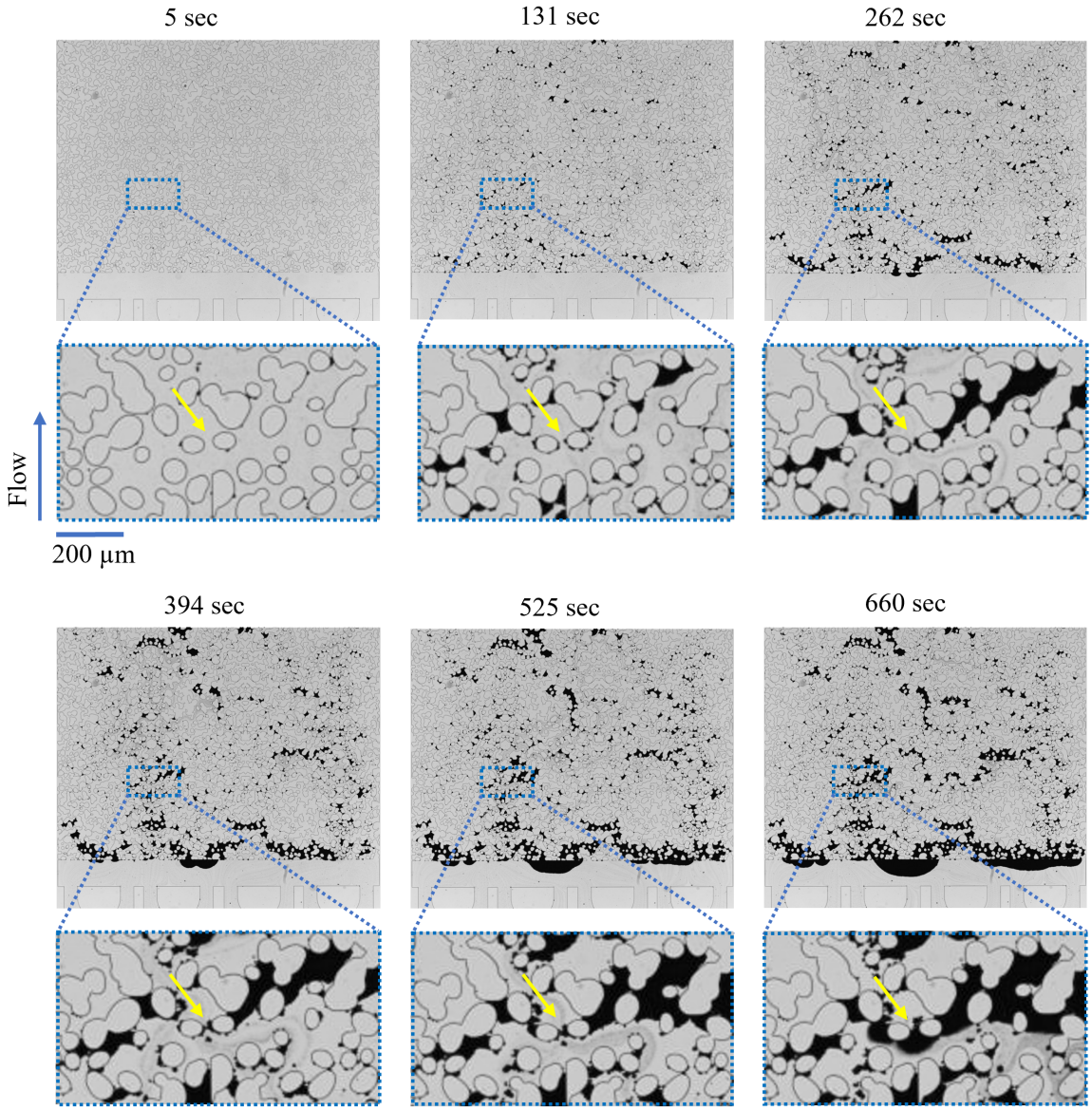

Figure 6.2: Time-lapse images of the base configuration in the first section of the porous domain, showing how particle deposition progressively develops over time until the domain becomes fully clogged. The insets show a constant magnified view of a selected region highlighted by a yellow arrow, indicating a constriction where particles gradually accumulate over time until the pore is completely blocked after 660 seconds.

Multiple filter cakes subsequently develop and expand until, by 660 seconds, the inlet is completely obstructed. In addition, the constriction of interest shows a clear and complete blockage of particle flow. The spatial profile of deposited particle concentration along the longitudinal axis at the time of clogging is shown by the blue curve in Figure 6.3, confirming that most clogging occurs near the inlet, within the first quarter of the micromodel's length, which corresponds to the field of view shown in the time-lapse images.

This experiment was repeated once to assess the reproducibility of the results. The two experiments show excellent agreement. As shown in Figure 6.4, the permeability reduction follows

nearly identical trends in both cases, with complete clogging occurring after approximately 10 minutes. A comparison of the particle deposition maps at full clogging (see Fig. 6.3) reveals a surprisingly high level of similarity between the two replicates: the clogged regions and blocked pores are nearly identical. This consistency is likely due to the disordered nature of the porous medium, which tends to yield more reproducible flow patterns than ordered or highly structured systems [Zami-Pierre et al., 2018]. This replication reinforces our confidence in the reproducibility of results obtained for other experimental configurations.

Effect of injection pressure, particle size, and concentration In addition to the base case, three further experiments are carried out, each varying a single parameter—flow rate, particle size, or particle concentration—by a factor of approximately 1.5. The results are summarized in Figure 6.3. For each experimental condition, the progression of particle deposition over time is shown for the entire porous domain. We also show the mean deposition profiles along the x-axis after complete clogging. They correspond to the dotted boxes.

The experiment performed at a lower pressure difference, shown in violet, exhibits only a minimal filter cake near the inlet, with a greater amount of deposition occurring in the second quarter of the domain. The reduced pressure difference slows the clogging process, enabling particles to penetrate deeper into the porous medium and accumulate within internal pores before eventual blockage at the inlet. This observation aligns with the concept that a constant number of particles, N^*, must traverse a pore before an arch forms to clog a throat [Wyss et al., 2006a]. Since N^* remains constant, a lower flow rate results in a longer time required for clogging to occur.

Among all experiments, the one carried out with a particle concentration reduced by a factor of 1.5 (see green plots) exhibits the highest overall deposition in the porous domain. It has the most pronounced accumulation at the inlet, forming a large filter cake. This behavior can be explained by the fact that a high pressure difference combined with 6 µm particles promotes the formation of a filter cake, while the reduced concentration delays the onset of clogging in certain constrictions. As a result, particles continue to deposit on the previously formed filter cakes near the inlet while simultaneously migrating deeper into the domain, progressively filling pores, particularly within the first half of the porous structure, until complete clogging of the flow is eventually reached.

The experiment shown in red uses particles with a diameter of 4.5 µm instead of 6 µm in the base case. The deposition profile follows a similar overall trend with a more pronounced filter cake near the inlet and a significant deposition in the second quarter of the domain. Since the particles are smaller by a factor of 1.33, a larger number of them, n, are required to form an arch.

From these experiments, a general trend emerges: higher injection pressures lead to greater particle deposition near the inlet [Elmøe et al., 2009, Chen et al., 2025], resulting in the formation of filter cakes whose intensity varies depending on the other parameters specific to each experiment. Regarding particle size and particle concentration, both parameters strongly influence the intensity of deposition in the porous domain before complete clogging occurs. A higher amount of deposition is observed in the case of a lower suspension concentration, which is consistent with the understanding that a larger number of particles is required to form a stable bridging arch across a single pore throat [Vani et al., 2022]. This delays the onset of complete clogging, allowing more particles to migrate and accumulate behind already clogged pores. In contrast, reducing the particle size relative to the base configuration results in a higher overall deposition than the base case, yet still lower than the deposition observed in the experiment with a reduced particle concentration. This is attributed to the smaller particle diameter, which increases the ratio of pore width to particle size and thus requires more time for clogging to develop [Vani et al., 2022, Wyss et al., 2006a, Dersoir et al., 2015a].

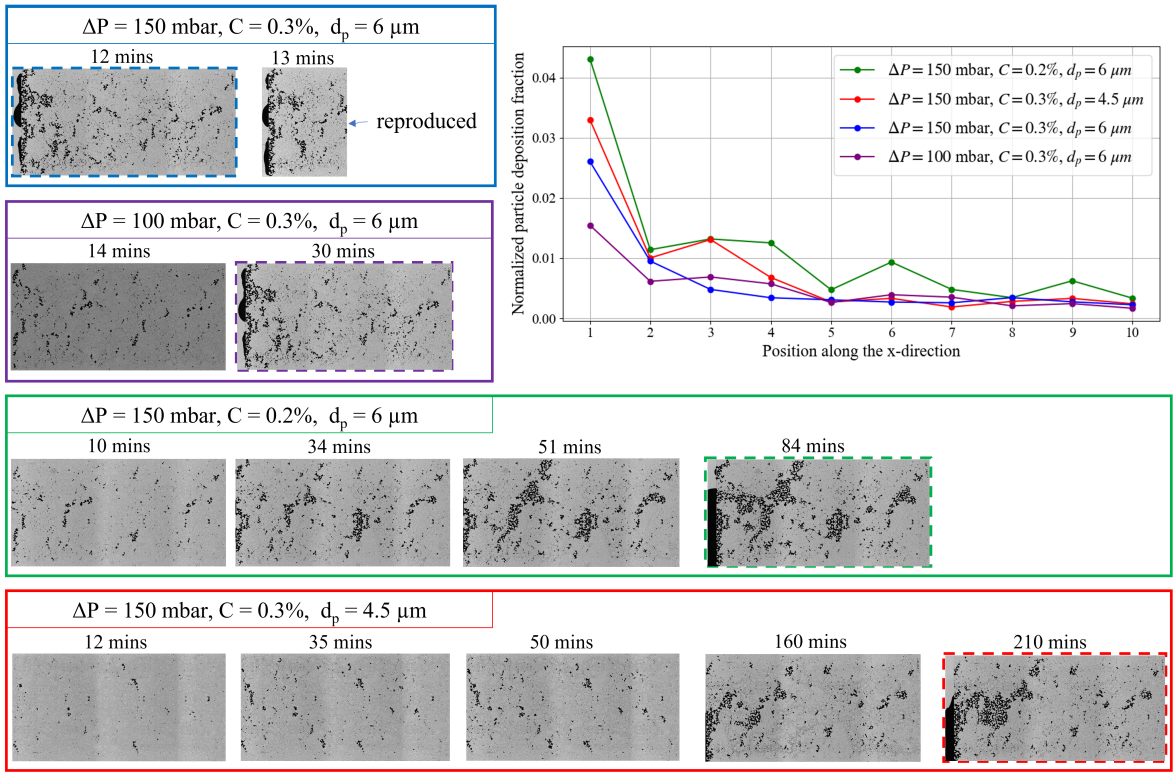

Figure 6.3: Time-lapse averaged stitched experimental images of the porous domain under different experimental conditions, with each condition distinguished by a separate color. The corresponding plot shows the normalized particle deposition fraction from the final stitched images, highlighted by dotted boxes, as a function of position along the x-direction for each experimental condition.

Permeability impairment Real-time flow rate measurements for the different experimental conditions are acquired downstream and processed using a moving-average smoothing algorithm to reduce sensor noise. The resulting evolution of permeability impairment is presented in Fig. 6.4 for the 4 experimental conditions.

The base configuration depicted in blue shows the fastest permeability decline, with complete clogging occurring after approximately 750 seconds. The replication of this experiment yields an identical permeability impairment curve. Reducing the injection pressure by a factor of 1.5 (violet curve) results in a decline that is approximately twice as slow. A 1.5-fold reduction in particle concentration (green curve) leads to an even slower decline, about seven times slower than in the base case. The slowest permeability decline is observed for the experiment using particles that are 1.33-fold smaller (red curve), with complete clogging occurring approximately seventeen times later than in the base case.

The stepwise sharp declines observed in the permeability curves are likely associated with the progressive clogging of major flow paths within the porous domain. Each steep drop corresponds to the complete blockage of a main flow line, with the final steep drop marking the clogging of the last remaining primary flow path. This pattern appears in almost all experiments, except in the baseline case, where the permeability shows a consistently steep decline from the start.

These results indicate that, among the parameters investigated, particle size has the strongest influence on permeability impairment, followed by particle concentration, and finally injection pressure. This experimental dataset will serve as a reference to assess the ability of our probabilistic PNM to capture permeability impairment caused by particle bridging.

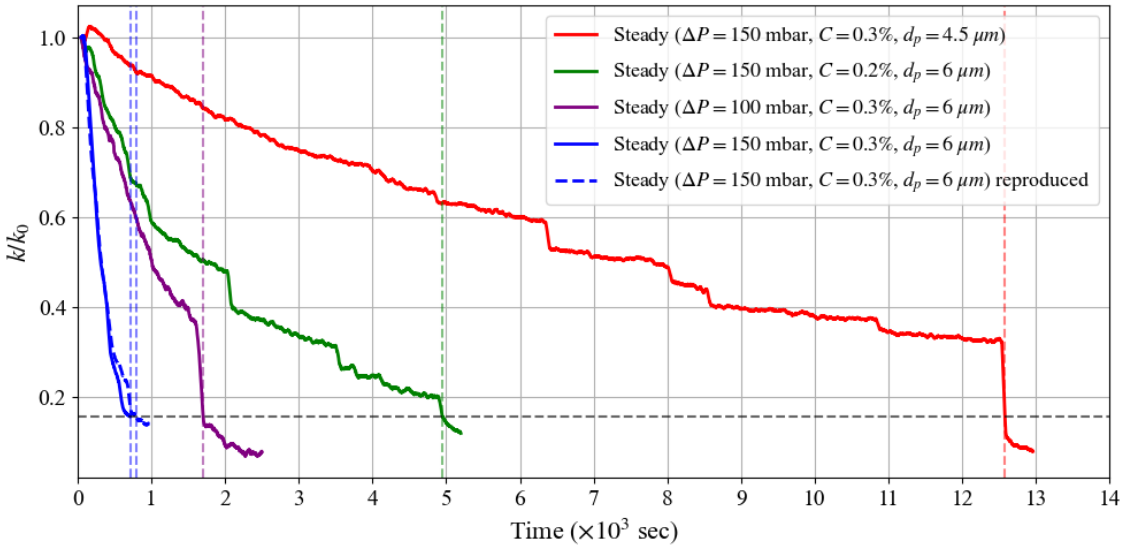

Figure 6.4: Evolution of permeability impairment over time for the different experimental conditions, each represented by a different color. The light black horizontal line indicates the 85% decline in initial permeability, while the vertical lines in corresponding colors mark the time at which each experiment reaches this threshold, indicating the onset of complete particle clogging.

6.3.2 Permeability impairment in PNM with probabilistic bridging law

Our novel pore-network model is employed to simulate pore clogging induced by particle bridging. The two-dimensional network is extracted from the micromodel geometry defined in Figure 4.2b. The resulting network spans 12 mm × 6 mm and is made of 5835 pores and 8952 throats. Consistent with the microfluidic experiments, four cases are considered: a base configuration and three additional cases in which a single parameter is varied relative to the base case (see Table 6.1).

The base case involves the injection of a suspension containing 0.3% particles with a diameter of 6 µm under a constant pressure difference of 150 mbar applied between the inlet and outlet. The time step is constrained by a Courant–Friedrichs–Lewy (CFL) $CFL \leq 0.5$. The jamming transition, C_{jam}, is obtained by trial and error. Snapshots of the baseline simulation are shown in Fig. 6.5. At the beginning of the simulation, the suspension is transported through the network. The probability of clogging and the expected number of particles, N^*, passing through a throat before clogging are computed at every time step for every throat. Once the cumulative number of particles per throat goes above N^*, the corresponding throat is clogged, and the conductance of the throat decreases significantly. After a throat is clogged, the upstream adjacent pore accumulates particles until the packing value is reached. Over time, clusters of clogged pores and throats develop within the network. The evolution of permeability is presented in plain blue line in Fig. 6.6. We observe an excellent agreement with the microfluidic measurements for $C_{jam} = 0.61$: the curves almost overlap, and both predict an 80% reduction in permeability after approximately 600 seconds.

Three additional PNM simulations are performed, each varying one parameter – particle size, particle concentration, or the pressure difference between the inlet and outlet. First, we use particle of 4.5µm instead of 6µm. The resulting permeability impairment develops more slowly than in the base case, consistent with experimental observations (see red curve in Fig. 6.6). This behavior is expected because a greater number of smaller particles, n, is required to form a stable bridging arch, thereby reducing the overall probability of clogging. Similar to microfluidic results, the curve displays a stepwise decline, reflecting the fact that when a primary flow pathway is

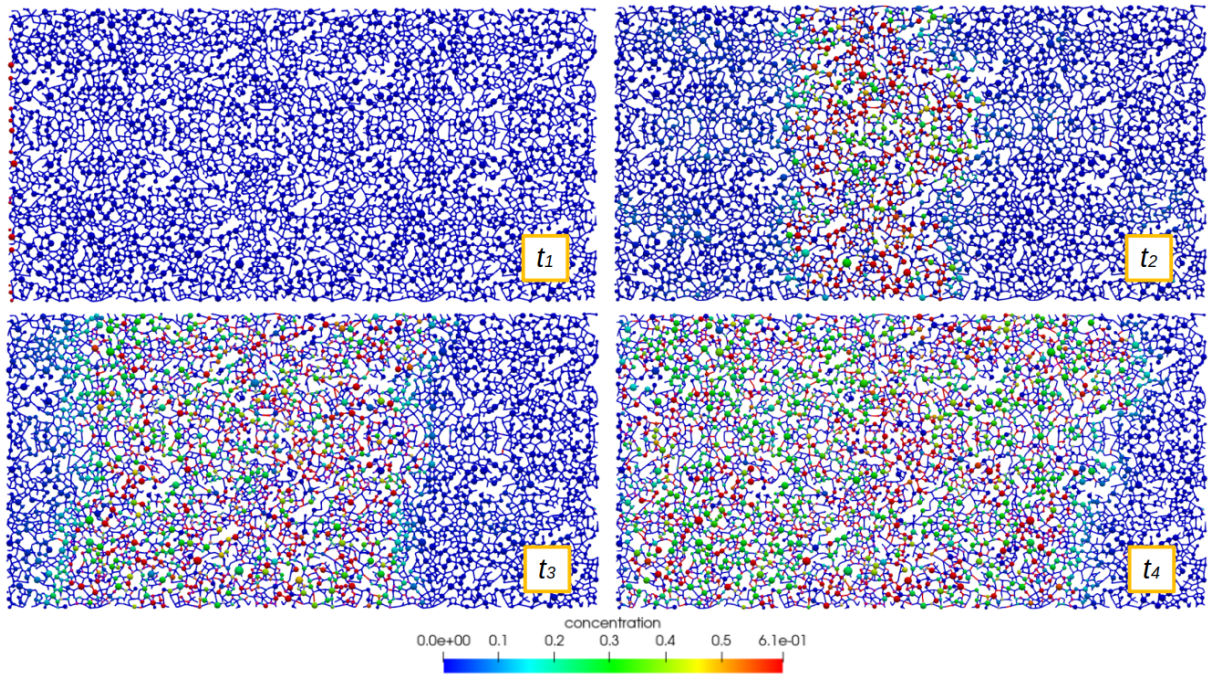

Figure 6.5: Snapshots of pore clogging obtained by probabilistic pore-network modeling for the baseline case. The throats in red are clogged. $t_1 = 0$s, $t_2 = 50$s, $t_3 = 100$s, and $t_4 = 700$s.

blocked, the fluid is forced to reroute through secondary channels with higher hydraulic resistance. Then, we inject a suspension with 0.2% of particles instead of 0.3%. The resulting permeability decline curve is plotted in green in Fig. 6.6. Finally, the pressure difference between the network inlet and outlet was reduced by a factor 1.5 (see violet curve in Fig. 6.6). In agreement with microfluidic experiments, the permeability reduction is delayed compared with the baseline, and the effect is less pronounced than for the small-particle case.

In all the cases, the permeability exhibits a stair-wise decline reflecting the blockage of preferential flow paths and the subsequent diversion of the suspension toward more resistive pore throats. Some discrepancies are nevertheless observed in the sequence of local clogging events, as evidenced by abrupt permeability drops that do not perfectly coincide with those measured experimentally. These differences can be attributed to several factors. First, the heterogeneous microstructure – in particular the pore geometry – is only approximately captured during the network extraction, and the transport laws used in the 2D model are themselves subject to modeling uncertainties. Second, additional physical mechanisms, such as shear-induced migration, may influence particle transport at bifurcations between adjacent throats but are not accounted for in the PNM simulations. Moreover, the jamming criterion in the PNM is imposed globally over the entire network, whereas it should ideally be defined locally at the throat scale, depending on constriction geometry and local shear conditions. Despite these limitations, the predicted clogging timescale remains in the same order of magnitude as that observed experimentally.

Overall, the simulations reproduce permeability impairment trends consistent with those observed in the microfluidic experiments. This set of results demonstrates the capability of the PNM approach, when coupled with an appropriate probability law for arch formation, to robustly capture the clogging dynamics by hydrodynamic bridging. Most previous PNMs were restricted to simulating clogging through sieving and the accumulation of particle layers driven by aggregation. By introducing a probabilistic treatment of arch formation, our approach now enables PNMs to capture the full spectrum of pore-clogging processes including bridging.

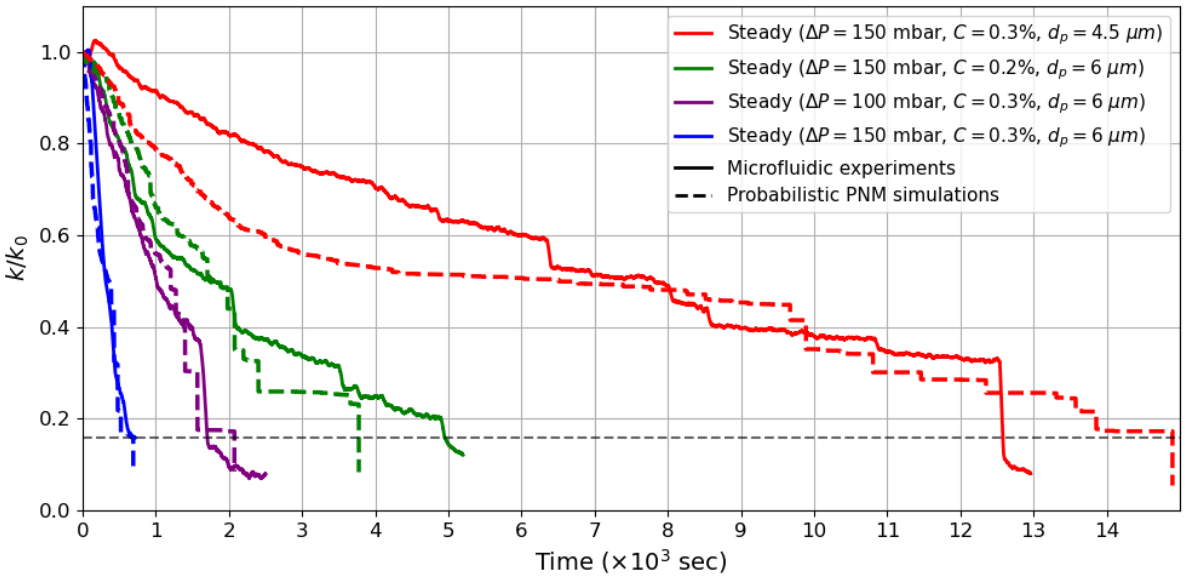

Figure 6.6: Evolution of permeability impairment for the different conditions, each represented by a different color, obtained with PNM simulations (dashed line) and microfluidic experiments (plain line).

6.4 Conclusions

Permeability impairment in heterogeneous porous media remains a long-standing challenge with significant implications for numerous industrial and environmental processes. In this study, we used both microfluidic experiments and pore-scale modeling to investigate the mechanisms of clogging induced by particle injection.

The microfluidic results show that permeability impairment driven by hydrodynamic pore bridging proceeds through a stepwise process, reflecting the sudden blockage of preferential flow paths by stable particle arches forming at pore constrictions. The experiments further demonstrate that particle size and concentration strongly control the onset and progression of clogging, while the imposed pressure difference primarily affects the timescale of permeability reduction. In particular, smaller particles significantly delay permeability impairment, an effect that is more pronounced than that of a reduced pressure drop.

We introduce a novel probabilistic pore-network model that quantifies the likelihood of stable particle arch formation within pore throats. The law of probability accounts for the particle-to-throat diameter ratio, the particle concentration and the pore constriction angle. Its fitting parameters are calibrated in a data-driven manner using high-fidelity CFD-DEM simulations. This constitutes a key advantage over previous probabilistic models, as it eliminates ad-hoc or case-specific tuning and yields a framework that is more predictive, generalizable, and physically interpretable. Both the microfluidic experiments and PNM simulations exhibit similar trends in permeability impairment, confirming the validity of the probabilistic PNM developed in this study to model clogging driven by hydrodynamic bridging.

State-of-the-art PNMs have so far been able to simulate pore clogging through sieving and the progressive aggregation of particles at pore walls, but they have not captured hydrodynamic bridging properly. This study demonstrates that probabilistic PNMs can successfully represent this mechanism, thereby extending the capability of PNMs to describe all three pore-clogging processes during the injection of particle-laden flows in porous media. The simulations, however, were conducted in two dimensions. While extending the PNM framework to three dimensions

is straightforward for solving flow and transport, the validity of the probability law in 3D remains uncertain. Further work is needed to clarify this aspect. In this context, CFD-DEM simulations can be employed to calibrate the probability law in three dimensions, and in-situ imaging techniques, such as time-lapse X-ray microtomography, will provide high-resolution datasets to validate PNM predictions.

Chapter 7

From clogging mitigation to clogging acceleration: particle deposition under oscillatory flow in microfluidic porous media

This chapter builds on the fourth research gap identified in Chapter 3, concerning the limited understanding of the effect of time-dependent flow forcing on particle deposition and clogging in heterogeneous porous media. It investigates how oscillatory injection modifies clogging dynamics across different deposition regimes, including both aggregation-dominated and hydrodynamic-dominated conditions, and examines how these effects translate into changes in permeability evolution. The results presented in this chapter are adapted from Okaybi et al. [2026b].

7.1 Introduction

The transport and retention of fine particles in confined environments is a widespread phenomenon spanning multiple scales and porous media contexts. Across applications—from biological circulation [Vahidkhah et al., 2016, PATNAIK et al., 1994] to groundwater transport [Ryan and Elimelech, 1996, Bradford et al., 2002, Jeong et al., 2018], aquifer storage and recovery [Jeong et al., 2018], geothermal injection [Song et al., 2020], oil production [Khilar and Fogler, 1983, Mungan, 1965], irrigation networks [Ait-Mouheb et al., 2019], and membrane filtration and subsurface bioremediation [Eddaoui and Soulaine, 2026]—particle accumulation progressively reduces permeability and flow capacity. Under continuous injection, deposits typically persist once formed, so restoring circulation and transport after clogging is rarely straightforward and often requires medium replacement or disruptive cleaning. This motivates the development of mitigation strategies that delay clogging and extend the lifetime of porous media, which in turn requires understanding the pore-scale mechanisms governing particle deposition and blockage.

At the pore scale, particle retention results from the competition between hydrodynamic forces (e.g., drag) and interfacial interactions [Torkzaban et al., 2007, Okaybi et al., 2025]. The latter are commonly described by Derjaguin–Landau–Verwey–Overbeek (DLVO) theory [Derjaguin, 1941a, Verwey, 1947], which represents the sum of van der Waals attraction and electrostatic double-layer forces. Varying ionic strength tunes electrostatic screening, thereby shifting the interaction balance toward adhesion at high salinity and toward repulsion in salt-free conditions [Ramachandran and Fogler, 1998, Ryde et al., 1991, Torkzaban et al., 2007]. Geometric confinement, quantified by the constriction-to-particle size ratio (W/d_p), primarily governs which clogging mechanisms

are geometrically admissible, whereas interfacial interactions control particle attachment and the stability of deposited or bridged structures. When $W/d_p < 1$, sieving (straining) dominates [Delouche et al., 2021, Sauret et al., 2014, Majekodunmi and Hashmi, 2022]. At intermediate W/d_p, bridging may occur when multiple particles form a stable arch at a constriction despite being individually smaller than the entrance [Bielinski et al., 2021, Vani et al., 2022, Hsu et al., 2021, Soulaine et al., 2026]. This phenomenon is most likely for $W/d_p \approx 2.5$–3.33, as reported by Sharp and Adrian [2005]. For $W/d_p \gg 1$, clogging is governed by adhesive deposition through progressive surface buildup to closure [Dersoir et al., 2015a, 2017, Okaybi et al., 2025]. In realistic porous networks, variations in (W/d_p), hydrodynamics, and interfacial interactions allow these mechanisms to coexist and compete. The resulting outcomes are further modulated by *i.* particle volume fraction, which sets particle arrival statistics at constrictions [Wyss et al., 2006a, Fogouang Maya et al., 2025, Marin et al., 2018, Vani et al., 2022], and *ii.* pore-network tortuosity, which enhances flow-path complexity and local flux heterogeneity [Bacchin et al., 2014, Kampel et al., 2009].

Together, these clogging mechanisms lead to permeability and injectivity decline, progressively compromising the efficiency of the flow system. To mitigate this damage, mechanical and chemical strategies are widely implemented. Upstream filtration captures particles before they reach critical constrictions but requires additional infrastructure and maintenance [Hube et al., 2020, Hoslett et al., 2018, Aljuboury et al., 2017]. Chemical treatments suppress mineral precipitation and biofouling, yet involve handling risks, continuous dosing, and potential ecological impacts [Trooien et al., 1998, Bertelli et al., 2018, Wang et al., 2019]. In subsurface systems, chemical–mechanical interventions such as acid fracturing can restore injectivity but must be carefully controlled to avoid re-clogging or environmental risks [Yudin et al., 2024, Saripalli et al., 1999, Zang et al., 2019]. These approaches are largely preventive or reactive, often costly, and may interrupt normal operation.

An alternative strategy is to modify the hydrodynamic conditions that govern clog formation and stability. In many filtration settings, backwashing/backflushing is applied as a discrete regeneration step. Flow is shortly reversed and/or hydrodynamic stresses are transiently increased after performance has degraded to dismantle partially formed deposits and restore throughput [Zsirai et al., 2012, Lohaus et al., 2020]. The same principle—periodically disturbing the local force balance that stabilizes particle clogging—also motivates oscillatory forcing applied from the start of filtration. In this approach, cyclic modulation of pressure or flow rate imposes repeated hydrodynamic perturbations whose frequency and amplitude can be tuned [Dincau et al., 2020]. Such forcing can perturb nascent deposits throughout operation. It has been reported to delay deposit stabilization and system-scale clogging while maintaining throughput across a range of applications, including groundwater redevelopment [Bichara, 1988], irrigation systems [Zhang et al., 2017], blood microfiltration [McFaul et al., 2012, Cheng et al., 2016, Lee et al., 2018, Yoon et al., 2016], and microfluidic filtration systems [Dincau et al., 2022].

More specifically, in microfluidic colloidal filtration studies under saline conditions, deposit stability is commonly interpreted within an adhesion-dominated framework, in which attachment reflects a balance between hydrodynamic and adhesive forces [Torkzaban et al., 2007]. In this regime, increasing shear can promote detachment by overcoming adhesive forces [Schwarze et al., 2019]. Oscillatory forcing can intermittently exceed the detachment threshold, triggering partial-erosion events. Their effectiveness depends on the forcing amplitude and frequency, which can mitigate clogging and reveal critical operating windows with maximal mitigation, as reported in two-dimensional microfluidic channel arrays [Dincau et al., 2022]. It remains unknown whether such oscillation-induced mitigation extends to heterogeneous porous domains across physicochemical regimes. This knowledge gap is especially relevant in weakly saline or salt-free conditions, where reduced ionic screening may shift clogging toward mechanically dominated

bridging. In that regime, increased particle flux can accelerate near-simultaneous arrivals at constrictions and promote blockage [Agbangla et al., 2012a, Sendekie and Bacchin, 2016, Dressaire and Sauret, 2017a], yet the response of these dynamics to oscillatory forcing in heterogeneous porous networks remains largely unexplored.

To address this gap, we employ microfluidic technology to fabricate heterogeneous, tortuous porous networks that mimic subsurface geometries while enabling direct pore-scale visualization. Microfluidic devices provide high-resolution, real-time observation of transport and clogging processes in a cost-efficient and highly reproducible manner [Manz et al., 1992, Whitesides, 2006]. We combine controlled variation of salinity and forcing frequency with real-time imaging and macroscopic measurements of flow-rate decline and injectivity loss. We systematically compare continuous and oscillatory injection under an imposed time-dependent driving pressure difference $\Delta P(t)$ while continuously measuring the resulting flow rate $Q(t)$. This framework allows us to determine whether oscillatory forcing mitigates or enhances clogging in heterogeneous porous domains and to quantify the dependence of the response on physicochemical regime and frequency.

The paper is organized as follows. In Section 7.2, we describe the microfluidic porous-network geometry and fabrication, the particle suspensions, the generation and monitoring of oscillatory forcing, and the experimental and imaging protocols. In Section 7.3, we present and analyze the baseline clogging behavior under continuous injection across salt concentrations. We then analyze and compare continuous and oscillatory injection at various frequencies under saline, weakly saline, and salt-free conditions using both pore-scale visualization and macroscopic injectivity measurements. We conclude by summarizing the main findings and discussing their implications for subsurface filtration and injectivity management.

7.2 Materials and Methods

We start by introducing the micromodel design and fabrication, together with its main hydraulic and mechanical characteristics. We then describe the particle suspensions and the method used to generate and monitor pulsatile flows. Finally, we detail the experimental procedure, including hydrodynamic characterization and the image acquisition and processing workflow used to investigate clogging under continuous and oscillatory injection, while also considering different salinity conditions.

7.2.1 PDMS microfluidic devices

A heterogeneous porous geometry that mimics the complexity and heterogeneity of subsurface environments is employed in this study, which is essential for investigating particle transport and clogging phenomena. In this study, we use the $M3$ heterogeneous tortuous porous geometry shown in Fig. 4.2. The design procedure and generation method are presented in (Chapter 4.1.1). Besides, the geometric and hydraulic properties of this model are summarized in Table 4.1.

The geometry is replicated in poly(dimethylsiloxane) (PDMS) using standard soft-lithography techniques, resulting in a uniform channel depth of $H = 20$ μm. The pore volume of the porous domain is ~ 0.76 μL. Fabrication protocols and surface-treatment procedures are also described in detail in Chapter 4.1.3. Prior to each experiment, devices are baked at 120 °C for at least 3 hours to ensure consistent surface properties [Dersoir et al., 2015a].

PDMS compliance can affect hydraulic resistance at elevated pressures [Gervais et al., 2006, Hardy et al., 2009]. Based on the device calibration reported in Chapter 4.5 and Fig. 4.6, all experiments are conducted at $\Delta P < 250$ mbar, where no measurable deformation-induced change in hydraulic resistance is observed; resistance variations therefore solely reflect particle transport and clogging rather than elastic deformation.

7.2.2 Particle suspensions

We use monodisperse polystyrene particles with a diameter (d_p) of 6 μm, coated with carboxyl groups (Table 4.2). The preparation of the particle suspensions in the density-matched fluid used in this study is detailed in Chapter 4.2. The final weight fraction (w/w) of the diluted suspension is 0.3%, with an approximate viscosity of $\mu \approx 1.9$ mPa $\cdot$ s. For experiments involving salt, NaCl is added to the density-matched carrier fluid to achieve final concentrations of 1 mM and 100 mM. To minimize particle aggregation, the suspension is sonicated for at least 30 minutes prior to each experiment.

7.2.3 Oscillatory flow generation and monitoring

The oscillatory flows used in our experiments are generated as sinusoidal pressure waveforms, representing the superposition of a steady component and a harmonic oscillation. They are expressed as $\Delta P(t) = \Delta P_0 + \delta P \sin(\omega t)$, where $\Delta P_0 = 100$ mbar is the mean pressure, $\delta P = 50$ mbar is the oscillation amplitude, and $\omega = 2\pi f$ is the angular frequency corresponding to the imposed frequencies $f = 0.1$ and 0.01 Hz. In all pulsatile experiments, the oscillation amplitude is kept constant, and only the forcing frequency is varied in order to investigate the effect of frequency on clogging dynamics under identical peak pressure gradients solely. The values of ΔP_0 and δP are chosen such that PDMS deformation remains negligible and no measurable damping of the oscillatory response occurs during the injection stage.

The pressure profiles are generated using an Elveflow OB1 Mk4 microfluidic flow controller (Fig. 7.1). The resulting volumetric flow rate is continuously measured at the outlet using a mini CORI-FLOW (ML120V00) Coriolis mass flow meter (Bronkhorst). The operating range and accuracy of these apparatus are detailed in Chapter 4.3, which covers our experimental range. Because the imposed forcing introduces oscillations and measurement noise in the flow-rate signal (acquired at 1 s intervals), raw data are smoothed using a rolling-average filter implemented in Python (Fig. 7.1b). The window length, which corresponds to the number of data points used to compute the rolling mean (or moving average), is selected to help smooth the signal by averaging over a defined time period, effectively reducing noise and fluctuations. For continuous injection and $f = 0.1$ Hz, a window length of 50 s (50 data points) is used, while for $f = 0.01$ Hz, a window length of 100 s (100 data points) is chosen. The window length is selected to ensure consistency across continuous and oscillatory injection conditions, allowing for comparability in data smoothing. For $f = 0.1$ Hz, the 50-second window captures approximately 5 cycles, while for $f = 0.01$ Hz, the 100-second window corresponds to 1 full cycle of oscillation. The window lengths are sufficient to capture a stable baseline for normalization. The smoothed flow rate is normalized by a reference value Q_0 to obtain the dimensionless ratio Q/Q_0, where Q_0 is defined as the mean flow rate over the initial smoothing window (first 50 s or 100 s, depending on f). We quantify the variability of the initial mean flow rate Q_0 across all performed experiments in this study and observe a maximum deviation of 7% at different frequencies, which we consider acceptable for ensuring consistent initial hydraulic conditions. For example, the values of Q_0 in the three experimental conditions presented in Fig. 7.1b correspond to 5.76, 6.02, and 5.7 μL/min for continuous, $f = 0.1$ Hz, and $f = 0.01$ Hz, respectively. As illustrated in Fig. 7.1b, the measured flow-rate signal oscillates at the imposed frequency, with no visible phase drift and no marked attenuation during the initial stage of injection. This indicates that, over the investigated frequency range, the pressure waveform is effectively transmitted through the system and accurately captured by the flow-rate sensor. At higher frequencies, however, the flow response can become attenuated and phase-shifted relative to the imposed pressure, as reported by Dincau et al. [2022]. Accordingly, the maximum forcing frequency is limited to 0.1 Hz to ensure that the flow rate remains synchronized with the imposed pressure signal.

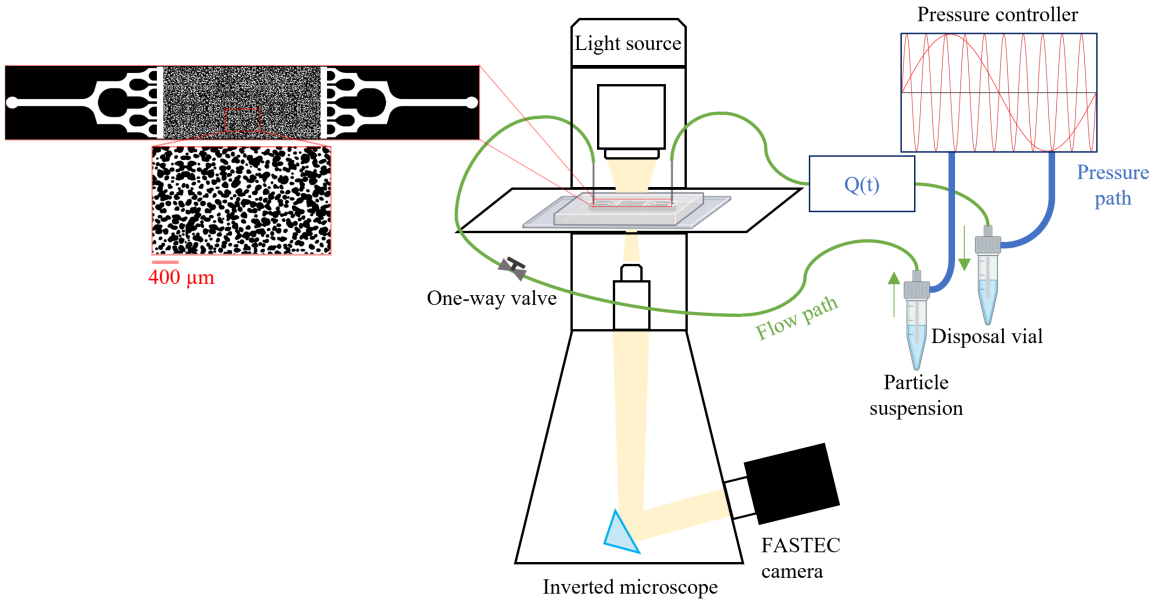

(a)

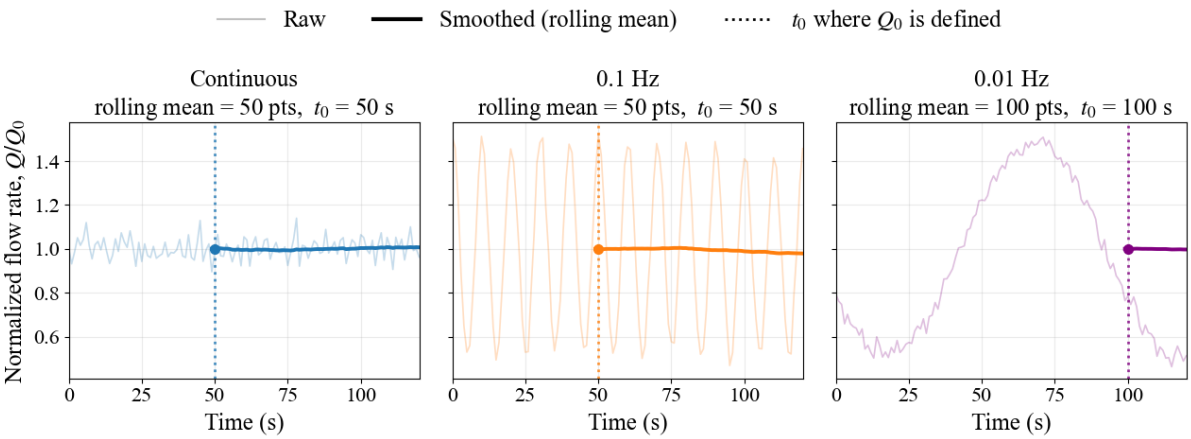

(b)

Figure 7.1: (a) Schematic of the oscillatory-flow experiments. The microfluidic device layout is shown on the left, with a magnified view of the heterogeneous porous domain highlighted below. A pressure controller applies a programmed pressure waveform at frequency f by pressurizing a sealed inlet reservoir, thereby driving flow through the microfluidic chip (pressure path in blue; flow path in green). The resulting volumetric flow rate $Q(t)$ is measured downstream using a flow sensor. The chip is mounted on an inverted microscope for real-time imaging. (b) Flow-rate preprocessing and normalization procedure. Raw flow-rate signals (light curves) are smoothed using a rolling mean (thick curves). The reference flow rate Q_0 is computed at t_0 over the initial smoothing window (50 s for continuous and 0.1 Hz; 100 s for 0.01 Hz), and the signal is normalized to obtain Q/Q_0.

7.2.4 Flow experiments

Each experiment begins by saturating the microfluidic device with the predefined background particle-free fluid. Once full saturation is achieved, the reservoir containing the particle suspension is connected, and particle injection is initiated according to the predefined flow protocol (continuous or oscillatory pressure waveforms). The overall experimental configuration, including the pressure controller, microfluidic chip, flow sensor, and optical imaging system, is shown in Fig. 7.1a. When particles reach the region just upstream of the porous domain, flow-rate recording is activated downstream of the microfluidic device, and image acquisition is started using a high-speed FASTEC camera mounted on an inverted Nikon ECLIPSE Ti2 microscope. Each experimental run is terminated once the normalized flow rate reaches a critical threshold, denoted by θ, such that $Q(t)/Q_0 < \theta$, with $\theta = 0.17$. This corresponds to complete clogging, where no particles from the suspension are observed flowing at the outlet. The value of θ was determined empirically from repeated experiments. The resulting $Q(t)/Q_0$ time series is used to quantify the temporal evolution of injectivity impairment. We denote by t_θ the time at which the threshold is first reached and define the cumulative injected volume up to this state as $V_\theta = \int_0^{t_\theta} Q(t)\,\mathrm{d}t$, computed from the measured flow-rate signal.

To characterize the flow and transport regime, we evaluate the Reynolds, particle Péclet, Stokes, and Womersley numbers. Using the measured flow rates and a characteristic length scale $\mathcal{L} = h = 20\ \mu m$ (comparable to the mean constriction size reported in [Soulaine et al., 2026]), the Reynolds number $Re = \frac{\rho U \mathcal{L}}{\mu}$ remains small for all imposed pressure drops ($Re < 10^{-2}$), confirming operation in the creeping-flow (Stokes) regime. Particle transport is quantified using the particle Péclet number, $Pe_p = \frac{U\mathcal{L}}{D_p}$, which compares advective transport to Brownian diffusion of the suspended particles. The fluid velocity U is used in the calculation of Pe_p because it represents the dominant driving force of particle transport in the flow. The particle diffusivity is estimated from the Stokes–Einstein relation, $D_p = \frac{k_B T}{3\pi\mu d_p}$, where k_B is the Boltzmann constant and T is the temperature (293 Kelvin). Using this relation, we obtain $D_p \sim 4 \times 10^{-14}\ \mathrm{m^2\,s^{-1}}$. Based on the initial velocity U_0, we obtain $Pe_{p,0} \sim 10^5$ to 10^6. Even at the clogging threshold ($Q/Q_0 = \theta = 0.17$), the Péclet number remains $\mathcal{O}(10^4)$ because advection dominates in regions behind the clogs, where particles continue to flow due to residual flow and fill the voids, despite no particles being observed at the outlet. The Stokes number $St = \frac{\rho_p d_p^2 U}{18\mu\mathcal{L}}$ remains $< 10^{-4}$, indicating negligible particle inertia and tracer-like behavior of the suspended particles. For oscillatory forcing, the Womersley number $Wo = \sqrt{\frac{\omega h^2 \rho}{\mu}}$ remains well below unity over the explored frequency range ($Wo \lesssim 10^{-2}$), indicating that viscous diffusion dominates over unsteady inertia and that the velocity field redevelops within each oscillation cycle.

7.2.5 Image acquisition and deposition analysis

Image sequences are acquired at selected time points using an inverted microscope (FASTEC camera, $\times 2$ objective). Because a single field of view does not span the full porous domain, three adjacent regions are recorded sequentially along the main flow direction (x-direction). For each region, the image sequence is temporally averaged to suppress mobile particles and retain only immobile (deposited) particles. The resulting averaged frames are then stitched into a single mosaic, yielding a full 2D representation of the porous region at the considered time. The full acquisition and processing workflow is described in Chapter 4.4.

For the qualitative and quantitative analysis of deposition profiles, the final stitched image at the clogging reference state t_θ is processed using a custom Python routine detailed in Chapter 4.4.3, in which deposited particles correspond to low grayscale intensities, whereas the pore space and solid grains correspond to higher intensities. To quantify the streamwise distribution of deposits,

the reconstructed domain is divided into ten equal segments along the flow direction, and the number of particle pixels in each segment is normalized by the total number of pixels in the stitched image. This procedure yields the normalized streamwise deposition profile used to compare deposition patterns under different salinity and forcing conditions.

7.3 Results and Discussion

In this section, we first establish the baseline clogging behavior under continuous injection for different ionic strengths. We then compare continuous and pulsatile injection to determine how oscillatory forcing modifies clogging dynamics across frequencies and salinities. Finally, we analyze pore-scale deposition profiles and connect them to the observed macroscopic injectivity response. For clarity, only one representative microscopic image is shown for each condition, selected from replicate experiments performed under consistent conditions, as showing both replicates would reduce figure readability without adding qualitative information.

7.3.1 Baseline clogging under continuous injection

We first establish a hydraulic reference by performing continuous-flow experiments at a fixed imposed pressure difference $\Delta P = 100$ mbar for three ionic strengths (100 mM, 1 mM, and 0 mM). Each condition is repeated twice to assess reproducibility. Injectivity loss is monitored through the normalized flow rate Q/Q_0 (top panel of Fig. 7.2) and the cumulative injected volume (bottom panel of Fig. 7.2). For quantitative comparison across salinities, all conditions are evaluated at the common clogging state $Q/Q_0 = \theta = 0.17$, from which we extract the threshold time t_θ and the cumulative injected volume V_θ.

A clear monotonic dependence on ionic strength is observed, with good reproducibility between replicas. At 100 mM (red curves), Q/Q_0 decreases most rapidly, yielding $t_\theta \sim 1120$ s and $V_\theta = 43.4 \pm 4.2$ μL. Reducing ionic strength to 1 mM (blue curves) delays clogging ($t_\theta \sim 3320$ s) and increases the injected volume to $V_\theta = 131.3 \pm 32.3$ μL, corresponding to an increase of about 205% relative to 100 mM. Under salt-free conditions (0 mM, black curves), the slowest injectivity decline is observed, with $t_\theta \sim 8300$ s and $V_\theta = 294.8 \pm 0.9$ μL, i.e. about 125% more than at 1 mM and about 586% more than at 100 mM. This ordering is consistent with established colloidal filtration behavior: increasing ionic strength enhances electrostatic screening, promotes aggregation, and accelerates pore-spanning bridge formation, thereby reducing injectivity [Bradford et al., 2007, Torkzaban et al., 2008, Dersoir et al., 2015b, Sendekie and Bacchin, 2016, Dressaire and Sauret, 2017b, Xinqiang et al., 2019, Mesticou et al., 2016, Bennacer et al., 2017].

To relate this injectivity trend to pore-scale deposition, we extract streamwise deposition profiles at t_θ (Fig. 7.3). For clarity, Fig. 7.3 presents one representative stitched image for each salinity, whereas the corresponding streamwise deposition profiles are calculated from both replicates and reported as replicate-averaged curves. Unless otherwise stated, the same procedure is applied to all subsequent deposition profiles obtained under different conditions in Section 7.3.2 and Section 7.3.3. The profiles show inlet-biased retention for all salinities, with deposition decreasing downstream along the porous domain. The downstream extent of deposition nonetheless increases as ionic strength decreases from 100 mM to 0 mM. At first glance, this salinity-dependent footprint may appear counterintuitive, since column-scale studies often report enhanced retention at higher ionic strength due to reduced electrostatic repulsion and stronger attachment [Bradford et al., 2007, Torkzaban et al., 2008]. The key distinction here is that deposition is compared at a fixed clogging state ($Q/Q_0 = \theta$), rather than after injecting the same volume. Because clogging occurs much earlier at high salinity (smaller V_θ), fewer particles have the opportunity to penetrate downstream before hydraulic failure is reached.

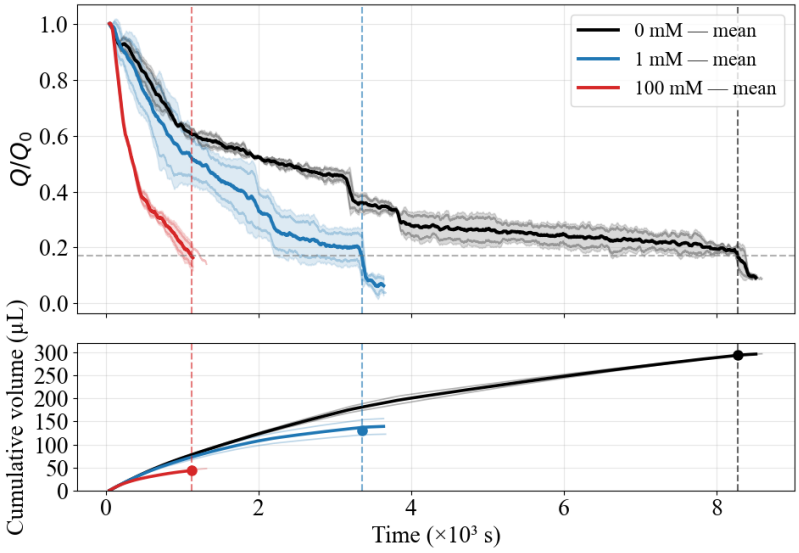

Figure 7.2: Injectivity decline under continuous forcing at different ionic strengths. Top: Normalized flow rate Q/Q_0 versus time for 0 mM (black), 1 mM (blue), and 100 mM (red). For each salinity, two independent replicates ($n = 2$) are shown as faint lines together with their mean (thick line). The horizontal dashed line marks the clogging threshold $Q/Q_0 = \theta = 0.17$, and vertical dashed lines indicate the corresponding threshold times t_θ. Bottom: Cumulative injected volume $V(t) = \int_0^t Q(t)\,\mathrm{d}t$; markers indicate $V_\theta = V(t_\theta)$. Increasing ionic strength accelerates injectivity decline and reduces V_θ.

The confinement ratio of the present porous domain further clarifies this behavior. With a mean constriction-to-particle size ratio $W/d_p \sim 3$–4, clogging occurs in a strongly confined pore-scale regime where aggregation and hydrodynamic pore bridging can coexist and directly obstruct constrictions. In contrast, the column systems reported in [Bradford et al., 2007, Torkzaban et al., 2008] involve grain-to-particle size ratios at least one order of magnitude larger, where deposition is predominantly governed by progressive adhesive build-up to grain surfaces up to blockage. Under the present confined conditions, electrostatic screening at high salinity accelerates aggregation and promotes rapid upstream bridge formation [Sendekie and Bacchin, 2016, Dressaire and Sauret, 2017b], leading to early hydraulic failure. Conversely, at low ionic strength, delayed aggregation postpones bridge formation, requiring substantially larger injected volumes to reach $Q/Q_0 = \theta$. This extended injection permits deeper particle penetration and more progressive pore filling upstream of the ultimately clogged constrictions before the system is completely blocked. The larger downstream deposition extent observed at 0 mM therefore primarily reflects delayed hydraulic failure (larger V_θ) rather than stronger adhesive attachment.

Having established reproducible baseline behavior under continuous injection for each salinity, we use these datasets as reference states for the subsequent oscillatory experiments. For each salinity, we then impose sinusoidal pressure oscillations at prescribed frequencies f (with fixed peak pressure amplitude) and assess whether pulsation mitigates clogging (increases t_θ and V_θ relative to the baseline) or instead accelerates injectivity decline.

7.3.2 Mitigation under oscillatory forcing in screened conditions

We investigate the effect of oscillatory forcing in the presence of electrostatic screening (100 mM and 1 mM) by imposing sinusoidal pressure oscillations around the same mean pressure ($\Delta P_0 = 100$

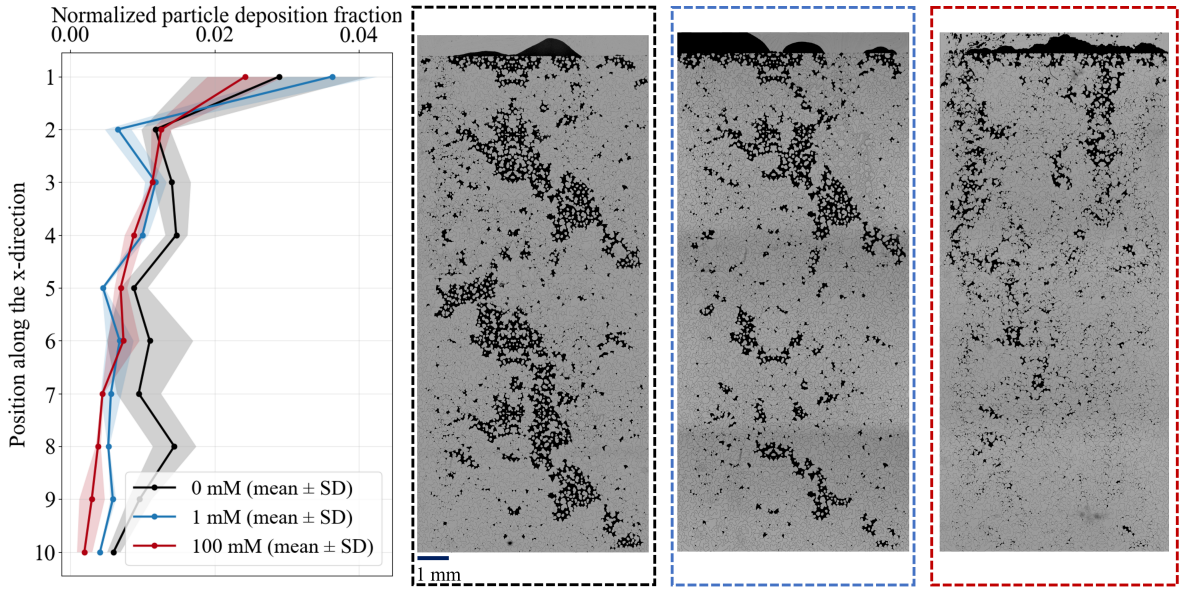

Figure 7.3: Streamwise deposition profiles at t_θ for different ionic strengths. Deposited particles are shown in black (pore space and grains in light grey). One representative stitched image is displayed for each salinity, whereas deposition profiles are obtained from two independent replicates ($n = 2$) and plotted as replicate-mean-averaged curves. Deposition is inlet-biased for all salinities, with downstream extent increasing as ionic strength decreases (0 mM > 1 mM > 100 mM).

mbar) with amplitude $\delta P = 50$ mbar at $f = 0.01$ and 0.1 Hz, following the protocol described in Section 7.2.3. For each salinity, pulsatile cases are compared with the continuous-injection reference using t_θ, V_θ, and the mitigation factor $\Gamma(f) = V_\theta(f)/V_{\theta,\mathrm{cont}}$ (Table 7.1), where $V_{\theta,\mathrm{cont}}$ is the injected volume at the clogging threshold under continuous injection. Here, $\Gamma > 1$ indicates mitigation and $\Gamma < 1$ indicates accelerated clogging relative to continuous forcing. Unless stated otherwise, t_θ and V_θ denote replicate-averaged metrics ($n = 2$), and Γ is computed from the corresponding replicate-averaged V_θ.

Table 7.1: Clogging metrics at threshold ($Q/Q_0 = \theta = 0.17$) for different salinity and forcing conditions.

Salinity	Forcing	t_θ (s)	V_θ (μL)	Γ
100 mM	Continuous	1123	43.40	–
	0.01 Hz	1300	51.83	1.20
	0.1 Hz	2417	78.38	1.81
1 mM	Continuous	3324	131.3	–
	0.01 Hz	5203	214.6	1.64
	0.1 Hz	3541	198.0	1.51
0 mM	Continuous	8300	294.0	–
	0.01 Hz	10707	370.0	1.26
	0.1 Hz	5315	227.5	0.77

For both salinities and both investigated frequencies, sinusoidal forcing delays hydraulic failure relative to continuous injection (Figs. 7.4, 7.5), yielding mitigation factors $\Gamma > 1$ (Fig. 7.6). At

100 mM (Fig. 7.4), the threshold time increases from $t_\theta \sim 1123$ s under continuous forcing to ~ 1300 s at $f = 0.01$ Hz and ~ 2417 s at $f = 0.1$ Hz. The cumulative injected volume at the clogging threshold correspondingly increases from $V_\theta = 43.40 \pm 4.15$ μL to ~ 52 μL and 78.4 ± 13.8 μL at 0.01 and 0.1 Hz, respectively, corresponding to $\Gamma = 1.2$ and 1.81. At $f = 0.01$ Hz, replication was limited to a single experiment due to material availability and experimental time constraints; this result is therefore reported as an indicative trend rather than a statistically robust estimate. Over the tested frequencies, both t_θ and V_θ increase monotonically with f, indicating enhanced mitigation within this range.

At 1 mM (Fig. 7.5), a similar mitigation response is observed. The threshold time increases from $t_\theta \sim 3324$ s under continuous injection to ~ 5203 s at $f = 0.01$ Hz and ~ 3541 s at $f = 0.1$ Hz. The injected volume at threshold likewise increases from $V_\theta = 131.3 \pm 32.3$ μL to 214.6 ± 17.8 μL and 198.0 ± 18.8 μL, yielding $\Gamma = 1.64$ and 1.51, respectively. While both oscillatory frequencies mitigate clogging relative to continuous injection, the replicate-averaged metrics indicate only a marginal advantage of $f = 0.01$ Hz over $f = 0.1$ Hz.

The spatial deposition patterns at the common clogging state provide complementary insight into the mitigation mechanism. For both salinities, deposition remains predominantly inlet-biased under all forcing protocols (Figs. 7.4c and 7.5c). However, compared to continuous injection, sinusoidal forcing produces a broader downstream deposition footprint. Because deposition is evaluated at a fixed clogging state ($Q/Q_0 = \theta$), the downstream footprint primarily reflects the cumulative injected volume V_θ. Consequently, the larger injected volumes under oscillatory forcing translate into a redistribution of deposited particles over a larger fraction of the porous domain. Hydraulic failure is therefore delayed not by eliminating deposition, but by spatially redistributing it.

A consistent physical interpretation is that cyclic pressure modulation alters the balance between aggregation-driven accumulation and shear-induced destabilization. In screened saline conditions, DLVO energy barriers are reduced, and particle attachment is energetically favorable. During the low-pressure portion of the cycle, reduced velocities promote deposition and cluster growth in stagnation regions [de Saint Vincent et al., 2016]. During the subsequent high-pressure phase, transiently elevated shear stresses increase the hydrodynamic torque acting on weakly attached clusters and nascent bridges [Schwarze et al., 2019, Torkzaban et al., 2007]. These stress excursions may intermittently approach the detachment threshold [Okaybi et al., 2025], limiting irreversible consolidation near pore entrances. The resulting cyclic build-up and partial erosion shift the effective hydraulic-failure condition to larger injected volumes.

Mitigation under pulsatile forcing has previously been reported in parallel-channel microfluidic arrays at a single ionic strength (100 mM) [Dincau et al., 2022]. Our results in a heterogeneous, tortuous porous micromodel show the same qualitative behavior at 100 mM, including stronger mitigation at the higher of the two tested frequencies (0.1 Hz versus 0.01 Hz). Quantitatively, the sensitivity to frequency is pronounced at 100 mM: increasing f from 0.01 to 0.1 Hz produces a strong increase in Γ (by $\sim 50\%$). Mitigation also persists when electrostatic screening is reduced to 1 mM, as both oscillatory cases yield $\Gamma > 1$; however, the same frequency increase produces only a weak change and slightly reduces Γ (by $\sim 8\%$). This contrast suggests that the frequency dependence of mitigation weakens, and may even reverse, as electrostatic screening is reduced.

7.3.3 Frequency-driven regime inversion in salt-free conditions

In the absence of added salt, the response to oscillatory forcing differs from the finite-salinity cases (Fig. 7.7). Under continuous injection, the clogging state is reached at $t_\theta \sim 8300$ s, corresponding to an injected volume $V_\theta = 294.8 \pm 0.9$ μL. At low frequency ($f = 0.01$ Hz), oscillatory forcing delays clogging relative to the continuous reference: the threshold time increases to $t_\theta \sim 10707$ s, corresponding to $V_\theta = 370 \pm 5.32$ μL and a mitigation factor $\Gamma = 1.26$. In contrast, at higher

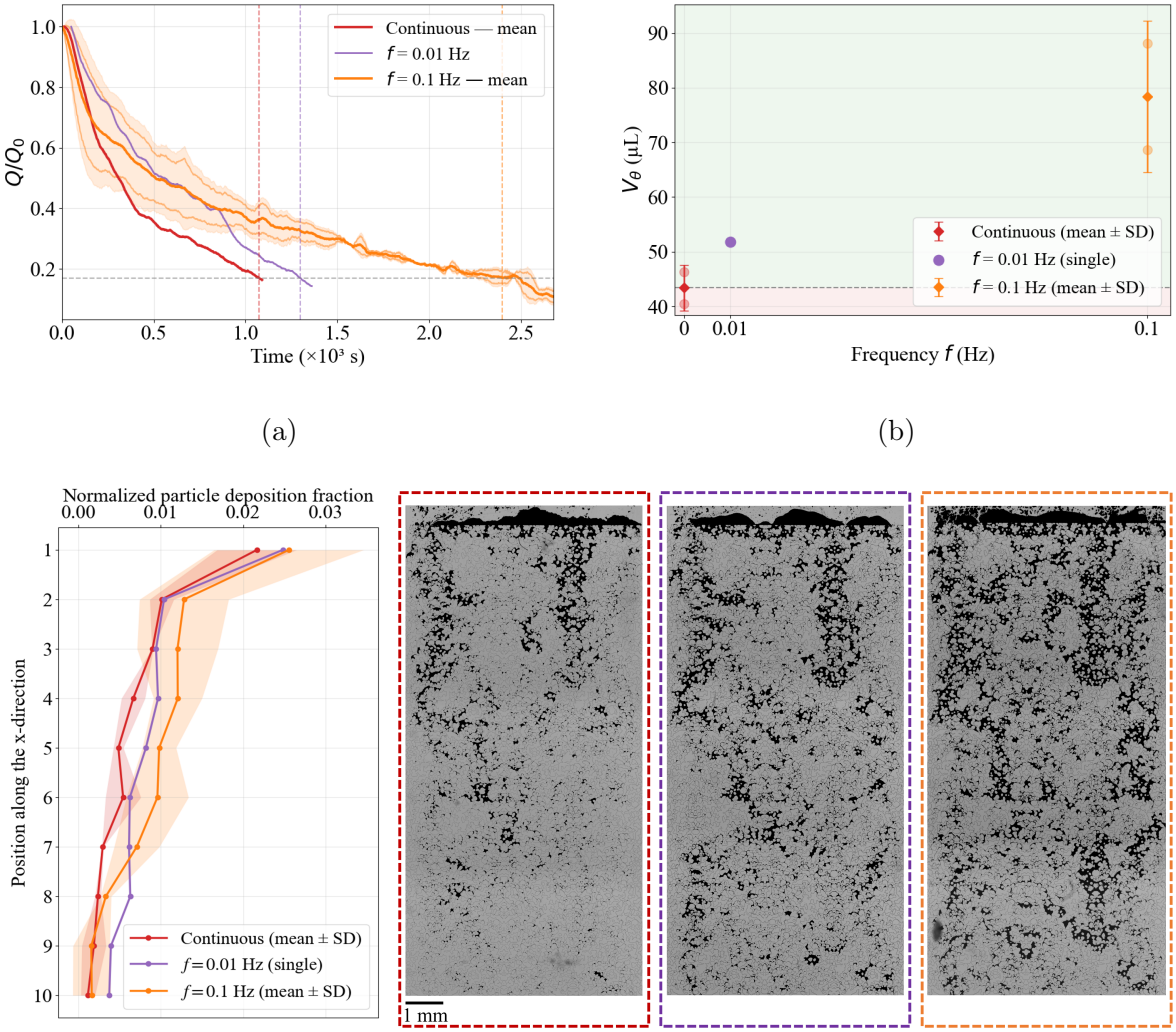

Figure 7.4: Injectivity decline (a) and injected volume at the clogging threshold (V_θ) (b) for 100 mM under continuous injection (red) and oscillatory forcing at $f = 0.01$ Hz (purple) and $f = 0.1$ Hz (orange). The green-shaded region denotes the mitigation regime, where V_θ for both frequencies exceeds the continuous reference. (c) Streamwise deposition profiles for continuous and oscillatory forcing. For all forcing conditions, deposition is strongly inlet-biased and decreases downstream along the porous domain. Relative to continuous injection, sinusoidal forcing increases downstream deposition coverage. Although local profile reversals may appear near the outlet, oscillatory forcing overall increases the downstream deposition extent compared to continuous injection.

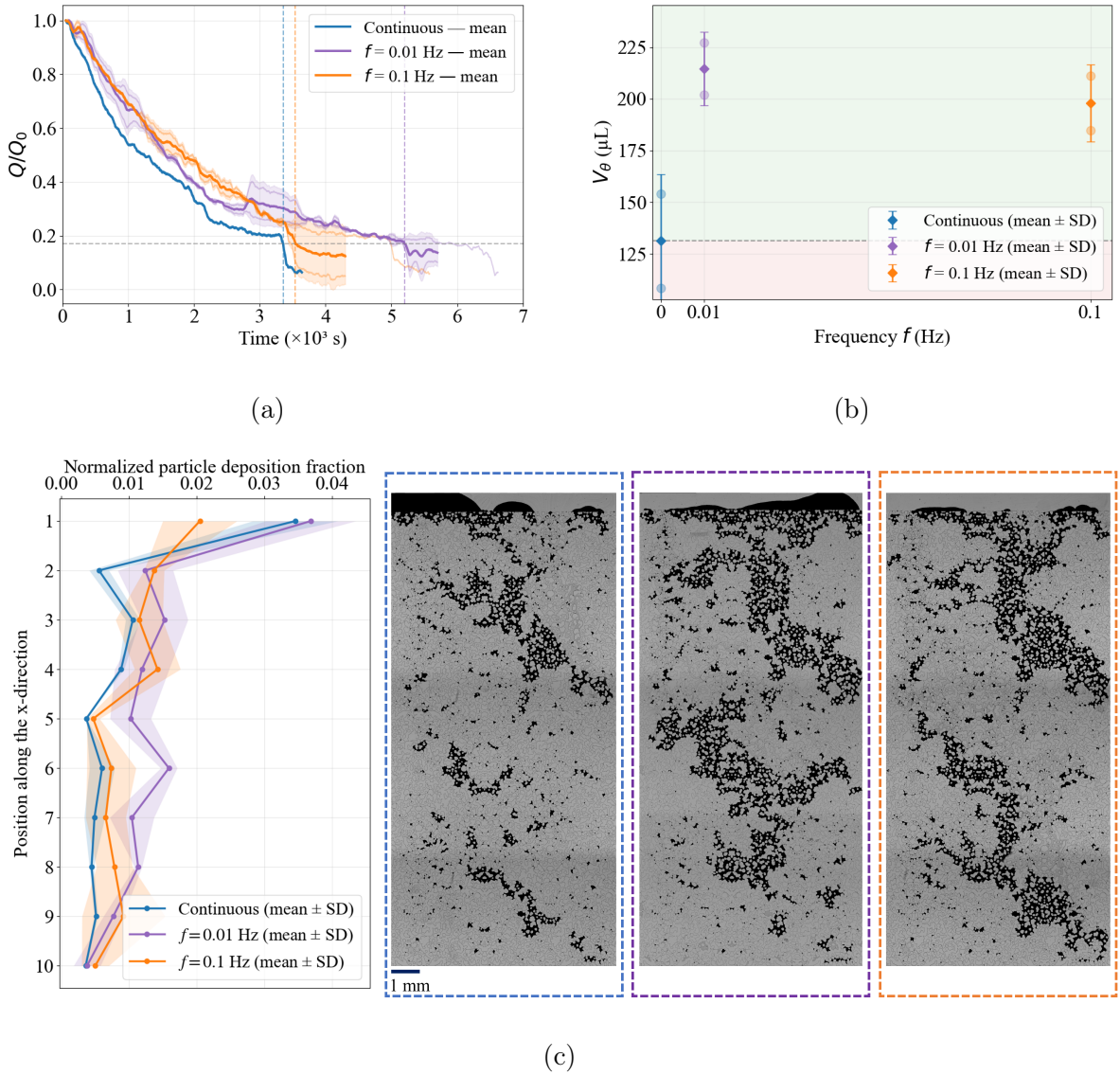

Figure 7.5: Injectivity decline (a) and injected volume at the clogging threshold (V_θ) (b) for 1 mM under continuous injection (blue) and oscillatory forcing at $f = 0.01$ Hz (purple) and $f = 0.1$ Hz (orange). The V_θ for the two frequencies fall in the mitigation regime, where it exceeds the continuous reference. (c) Streamwise deposition profiles under continuous and oscillatory forcing. For all conditions, deposition remains strongly inlet-biased and decreases downstream along the porous domain. Relative to continuous injection, sinusoidal forcing increases the downstream deposition coverage with a slightly higher deposition footprint at 0.01 Hz than at 0.1 Hz.

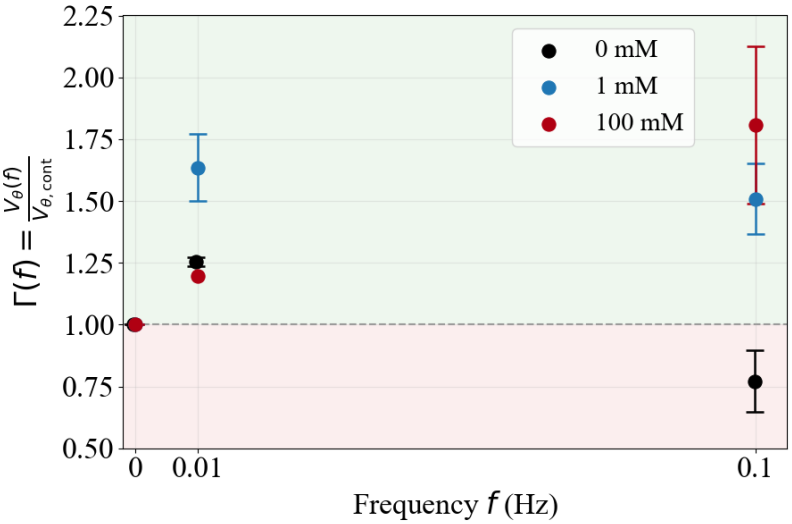

Figure 7.6: Mitigation factor $\Gamma(f) = V_\theta(f)/V_{\theta,\mathrm{cont}}$ versus oscillation frequency for 0 mM, 1 mM, and 100 mM. The dashed line marks $\Gamma = 1$ (continuous injection); shaded regions indicate mitigation ($\Gamma > 1$) and acceleration ($\Gamma < 1$). Oscillations enhance transport at 1 mM and 100 mM for both frequencies, whereas the 0 mM case shows a regime inversion from mitigation at 0.01 Hz to acceleration at 0.1 Hz. The continuous-injection reference point at $\Gamma = 1$ for 100 mM is slightly shifted horizontally for visualization purposes only, to avoid overlap with the corresponding points for 0 mM and 1 mM at the same reference condition. Error bars denote variability across repetitions.

frequency ($f = 0.1$ Hz) the effect reverses: the threshold time decreases to $t_\theta \sim 5315$ s, and the injected volume correspondingly drops to $V_\theta = 227.5 \pm 36.9$ μL, yielding $\Gamma = 0.77$. These trends are reproducible across the two independent repetitions performed at each frequency. In contrast to the finite-salinity regimes, the salt-free case shows a frequency-driven inversion, transitioning from mitigation at $f = 0.01$ Hz to acceleration at $f = 0.1$ Hz.

Despite the clear inversion observed in V_θ, the deposition profiles at the clogging state (Fig. 7.7c) remain qualitatively similar and predominantly inlet-controlled, with profiles that largely overlap and occasionally intersect along the domain. This indicates that the final deposition footprint alone does not fully capture the frequency effect in the salt-free regime. Note that only one stitched image at t_θ is available for $f = 0.01$ Hz due to an acquisition interruption during the second replicate. The flow-rate measurements nevertheless support the hydraulic reproducibility, and the available deposition image is representative of the observed behavior.

Sensitivity to frequency turns to be highly pronounced in the salt-free regime, where Γ decreases by approximately 39% when the frequency increases from 0.01 Hz to 0.1 Hz, reflecting the transition from mitigation at low frequency to acceleration at higher frequency. A similar directional trend is observed at 1 mM, where increasing the frequency from 0.01 Hz to 0.1 Hz also slightly reduces Γ (by $\sim 8\%$), although both oscillatory conditions remain within the mitigation regime. This comparison suggests that the sensitivity to frequency evolves progressively with ionic strength and reflects changes in the dominant clogging dynamics. In the salt-free limit, strong electrostatic repulsion suppresses aggregation and the system approaches a mechanically dominated regime. Given the average confinement ratio of the present micromodel ($W/d_p \sim 3$–4), clogging is then primarily governed by hydrodynamic pore bridging, where blockage arises from particle crowding and geometrically constrained collisions at pore constrictions [Dressaire and

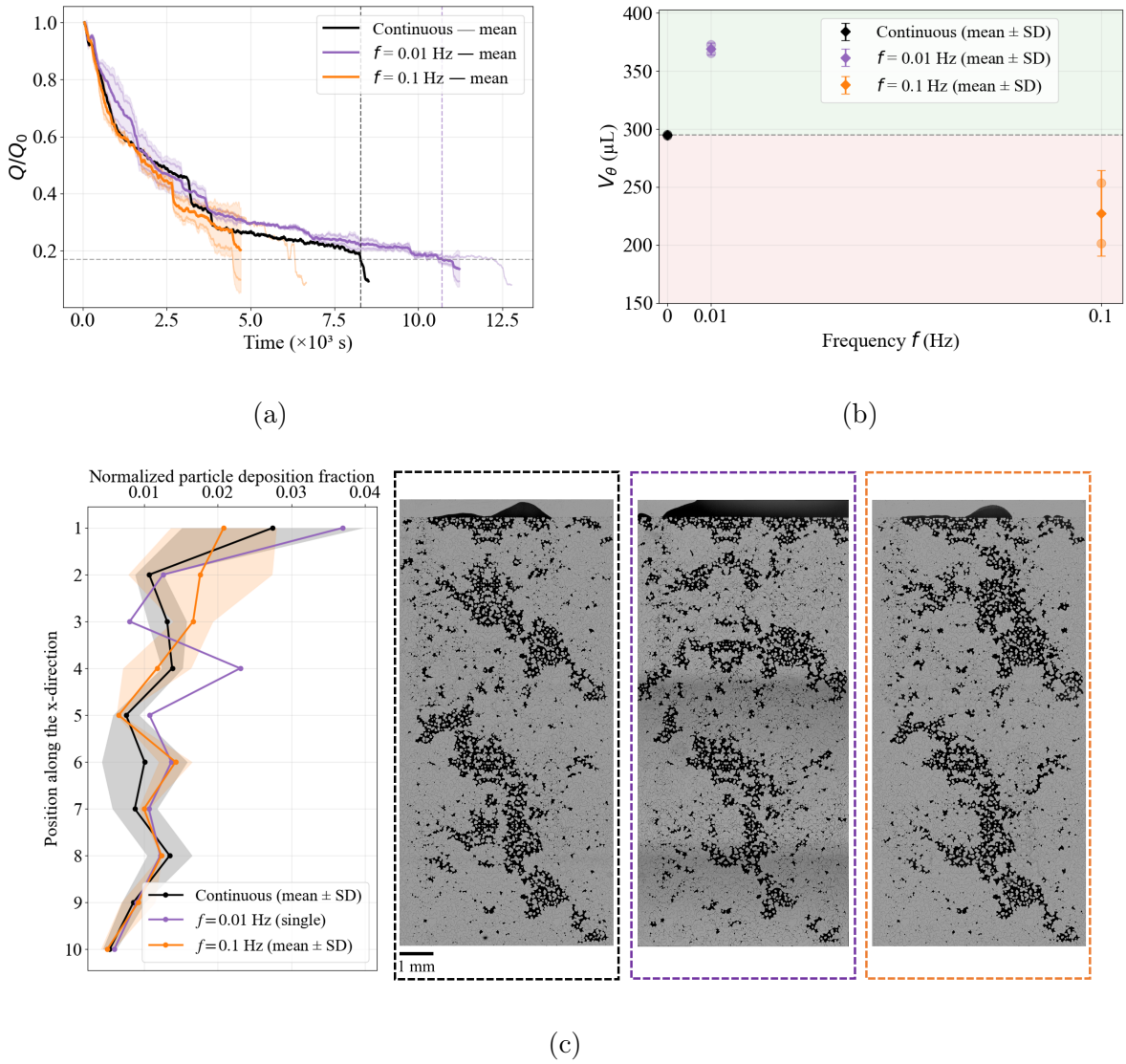

Figure 7.7: Injectivity decline (a) and injected volume at the clogging threshold (V_θ) (b) for 0 mM under continuous injection (black) and oscillatory forcing at $f = 0.01$ Hz (purple) and $f = 0.1$ Hz (orange). The $f = 0.01$ Hz condition falls in the mitigation regime (V_θ exceeding the continuous reference), whereas $f = 0.1$ Hz falls in the clogging-acceleration regime (red-shaded region). (c) Streamwise deposition profiles under continuous and oscillatory forcing. For all conditions, deposition remains strongly inlet-biased and decreases downstream along the porous domain. No clear qualitative distinction between forcing protocols emerges, as the profiles partially overlap and intersect along several regions of the domain.

Sauret, 2017a, Sauret et al., 2018, Majekodunmi and Hashmi, 2022].

The influence of oscillatory forcing in this mechanically dominated regime is therefore governed by the cumulative hydrodynamic loading imposed prior to blockage. Using the replicate-averaged clogging time t_θ, the number of oscillation cycles experienced before reaching the clogging threshold is $N_{\mathrm{cyc},\theta} = f\, t_\theta$, yielding approximately 115 cycles at 0.01 Hz and 530 cycles at 0.1 Hz. Normalizing by the replicate-averaged transported volume V_θ gives the cycling intensity

$$\mathcal{I}_\theta = \frac{f\, t_\theta}{V_\theta},$$

which increases from 0.30 ± 0.03 cycles/μL at 0.01 Hz to 2.32 ± 0.15 cycles/μL at 0.1 Hz. The higher frequency, therefore, imposes nearly an order-of-magnitude greater cyclic loading per unit injected volume, suggesting that the cumulative hydrodynamic loading experienced prior to clogging plays a central role in controlling the response to oscillatory forcing.

In the 0 mM case, in repulsive colloidal systems, deposition is governed primarily by particle flux density rather than adhesive stabilization. Contraction microchannel experiments under such conditions [Kim et al., 2022] show that increasing flow rate intensifies deposition at constrictions despite elevated wall shear stresses, because the amplification of particle flux under geometric confinement dominates over shear-induced removal. When particles are advected from a wider region into a narrower constriction, the reduction in cross-sectional area increases local velocity and thus particle flux density; clogging occurs once a critical crowding threshold is exceeded [Agbangla et al., 2012b, Bacchin et al., 2006]. In the present micromodel under repulsive conditions, the system operates close to the geometric bridging limit. Oscillatory forcing at $f = 0.1$ Hz repeatedly generates transient high-velocity peaks, substantially increasing instantaneous particle flux at constrictions relative to both continuous injection and the lower-frequency case. These frequent flux amplifications increase the probability of reaching the critical crowding condition, thereby accelerating mechanically driven pore bridging. By contrast, at $f = 0.01$ Hz, peak-velocity events occur less frequently, allowing nascent particle depositions to reorganize between loading cycles and delaying cumulative mechanical stabilization.

Taken together, these results demonstrate that the response to oscillatory forcing depends strongly on the physicochemical condition. While oscillations delay clogging under screened conditions and mitigation increases monotonically with frequency, this frequency sensitivity progressively reverses as electrostatic repulsion strengthens, eventually leading to a non-monotonic regime where higher-frequency forcing accelerates clogging instead of delaying it.

7.4 Conclusions

Clogging in porous media affects a wide range of applications, from groundwater transport and subsurface injection to industrial filtration processes. Understanding how hydrodynamic forcing influences clog formation is therefore important for developing strategies to extend the lifetime of such processes.

In this chapter, we investigated how the frequency of oscillatory pressure forcing modulates clogging dynamics in heterogeneous microfluidic porous networks across different salinity conditions. Our experiments reveal that the sensitivity of clogging dynamics to oscillatory forcing evolves systematically with ionic strength. Under strongly saline conditions, oscillatory forcing delays clogging relative to continuous injection, and mitigation becomes more pronounced as the forcing frequency increases within the explored range, consistent with previous observations in parallel microfluidic channel arrays [Dincau et al., 2022]. At weak salinity, oscillatory forcing relative to continuous injection still delays clogging at both tested frequencies; however, a slight inversion in performance emerges, with higher frequency marginally reducing the mitigation effect.

In the salt-free limit, this trend translates into a complete inversion of the response: low-frequency forcing still delays clogging, whereas higher-frequency oscillations accelerate blockage.

These results demonstrate that oscillatory forcing is not a universally beneficial mitigation strategy. Rather, its impact depends on the dominant clogging mechanism and the underlying physicochemical regime. Under screened conditions, clogging is governed primarily by aggregation-assisted deposition, where cyclic pressure fluctuations intermittently destabilize growing deposits and delay hydraulic failure. In contrast, in the salt-free condition, strong electrostatic repulsion suppresses aggregation and shifts the system toward mechanically dominated clogging, where pore bridging is driven by particle crowding under geometric confinement. In this regime, frequent velocity peaks generated by high-frequency oscillations increase particle flux toward constrictions and accelerate blockage. This mechanistic transition explains why oscillatory forcing accelerates blockage at higher frequencies in the salt-free limit.

These findings have implications for injection processes in natural porous formations by clarifying how oscillatory forcing interacts with physicochemical conditions to control clogging dynamics. In many subsurface systems, such as geothermal reservoirs or groundwater aquifers, dissolved salts promote electrostatic screening between suspended particles. It is important to note that most natural porous formations typically deal with saline fluids, rather than saline-free fluids. Under such conditions, our results suggest that oscillatory injection may mitigate clogging and delay hydraulic failure, potentially extending the operational lifetime of injection systems. At the same time, the response to oscillatory forcing depends strongly on the physicochemical environment. While our experiments provide direct observations in heterogeneous two-dimensional porous networks, an important next step is to examine whether these regime-dependent responses persist in three-dimensional porous media. Complementary studies in simplified pore geometries would further help isolate the mechanisms controlling the transition between mitigation and acceleration under oscillatory forcing. Exploring these directions will refine predictive models and optimize flow performance in complex porous systems.

Chapter 8

Two-phase microfluidic experiments toward investigating clogging-induced mobilization of trapped oil

This chapter extends the previous results toward two-phase flow conditions by exploring the implications of particle-induced clogging for the mobilization of trapped immiscible fluids in porous media. It presents the experimental progress achieved so far and discusses the main limitations encountered in assessing whether clogging-induced permeability reduction can enhance the displacement of capillary-trapped oil in heterogeneous, tortuous porous networks representative of subsurface formations.

8.1 Introduction

Significant attention has been directed by researchers towards studying colloidal transport, both for degrading and mobilizing trapped contaminants in groundwater [Phenrat et al., 2009, Zhao et al., 2016, Kanel et al., 2006], and for enhancing the recovery of trapped oil [Hussain et al., 2013, Zhang et al., 2014, Wu et al., 2013]. This interest arises because, after primary and secondary recovery processes, more than 90 % of the oil often remains trapped by capillary forces [Wardlaw and Cassan, 1979].

The enhanced mobilization of trapped immiscible fluids in the presence of colloids is driven by several mechanisms. One involves injecting surface-active particles, which localize at the immiscible fluid-fluid interface and reduce interfacial tension [Alomair et al., 2014, Salem Ragab and Hannora, 2015]. Another mechanism involves particles that are not necessarily surface-active but instead adsorb onto rock surfaces, altering the wettability of the formation from oil-wet to neutral or water-wet [Roustaei and Bagherzadeh, 2015, Li et al., 2015]. Additionally, particles can build disjoining pressure by spreading within wedge-shaped films in confined three-phase systems, such as oil-nanofluid-porous media [Zhang et al., 2014].

For these mechanisms to effectively mobilize trapped immiscible fluids, particles must travel freely through the porous media to bind and interact with specific fluid interfaces. However, particle deposition and clogging within porous media can hinder this process by limiting particle mobility. Paradoxically, deposition and clogging can also cause a permeability decline, increasing the pressure difference exerted on trapped fluids. In core-flood experiments, this increased pressure drop was suspected to increase the recovery of the trapped oil due to clogging, but visualization was impossible in opaque samples [Li et al., 2015]. Schneider et al. [2021] later demonstrated, using 3D transparent porous media and confocal microscopy, that colloidal deposition can mobilize

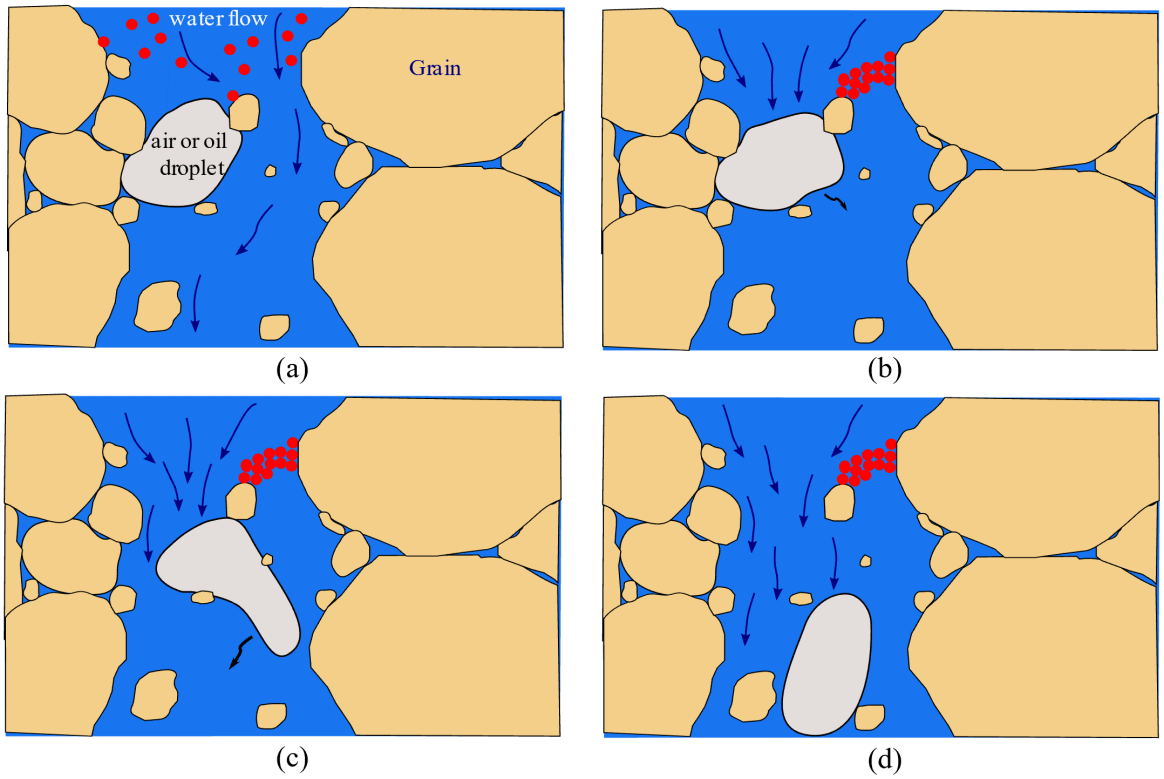

Figure 8.1: Schematic illustration of the mobilization of a trapped immiscible droplet (air or oil) in a porous medium in the presence of colloidal particles. (a) Colloidal particles (red) are transported by the flowing water past a trapped droplet. (b) Particle accumulation clogs a neighboring pore, increasing local flow resistance and viscous stresses. (c,d) The induced flow redistribution enhances hydrodynamic forces on the droplet, resulting in its deformation and eventual mobilization. Courtesy of Cyprien Soulaine.

trapped contaminants. The deposition reduces the effective cross-sectional area, increasing viscous forces at controlled flow rates, which can overcome the capillary forces trapping the oil. However, they did not observe pore clogging, leaving unanswered whether clogging enhances or hinders the mobilization of trapped oil droplets compared to non-clogging scenarios. To clarify the mechanisms involved, Fig. 8.1 presents a schematic representation of the expected coupling between particle transport, clogging, and droplet mobilization. As particles are transported by the flow, they may accumulate and clog adjacent pores, locally increasing flow resistance. This induces flow redistribution and enhances the viscous forces acting on nearby trapped droplets, potentially overcoming capillary forces and leading to their mobilization.

In this chapter, we investigate this question using microfluidic experiments under two-phase flow conditions. We examine how particle transport, deposition, and clogging affect pressure evolution, flow redistribution, and the mobilization of trapped oil. During this investigation, we encountered important limitations associated with PDMS-based micromodels, which are discussed to clarify the conditions required for reliable two-phase experiments.

8.2 Materials and Methods

This section describes the microfluidic two-phase experiments used to investigate how particle-induced pore clogging influences the mobilization of trapped immiscible fluids in heterogeneous porous media. We detail the porous geometry in use, the surface treatment used to control wettability, the properties of the wetting fluid and non-wetting oil fluids, and the flow protocol used to monitor pressure evolution and image the displacement process.

8.2.1 PDMS microfluidic device geometry

In this chapter, we use the $M3$ heterogeneous, tortuous porous domain shown in Fig. 4.2b. The design workflow, pore-scale geometric statistics, and fabrication procedure are described in Chapter 4.1.

We select this geometry because it provides a relatively low confinement ratio for the particles used in the two-phase experiments. Specifically, the ratio W/d_p lies in the range 3.33–4.44, depending on the particle diameter. Such confinement conditions promote pore bridging and clogging, which are required here to investigate whether clogging can enhance the mobilization of trapped immiscible fluids.

8.2.2 Surface treatment and wettability control

After irreversible bonding of the PDMS replica to a glass slide, we expose the assembled microfluidic device to oxygen plasma for at least 5 minutes to render the surface hydrophilic. We initiate the two-phase flow protocol immediately thereafter, such that the density-matched aqueous phase (DMF; see Chapter 4.2) can be considered the wetting fluid.

To further control wettability, as these experiments involve a non-wetting oil phase, we also conduct experiments using a poly(vinyl alcohol) (PVA) surface coating, following the approach proposed by Trantidou et al. [2017]. The use of PVA is intended to mitigate the hydrophobic recovery of PDMS, enable DMF to be used as the wetting fluid, and improve the stability of the two-phase experimental setup over the duration of the experiments.

8.2.3 Non-wetting fluids

As described above, the wetting fluid in these experiments is DMF. For the non-wetting phase, we use three different oils: silicone oil, paraffin oil, and Fluorinert. Their key properties at 20 °C are summarized in Table 8.1.

Table 8.1: Types and properties of the non-wetting oils used in the two-phase experiments (20 °C).

Type of oil	Density (g/mL)	Dynamic viscosity (cP)
Silicone oil	0.93	9.3
Paraffin oil	0.87	31.94
Fluorinet	1.88	5.0–5.5

8.2.4 Flow experiments

We aim to investigate the injection of particle suspensions into an initially unsaturated microfluidic porous medium under two-phase flow conditions. The optical setup (microscope, illumination, and camera) and the flow-rate-controlled injection setup are the same as in the single-phase injection experiments presented in Chapter 5. The pressure drop across the device is determined using

the same differential pressure sensing setup placed upstream and downstream of the microfluidic chip, as explained in Chapter 5.

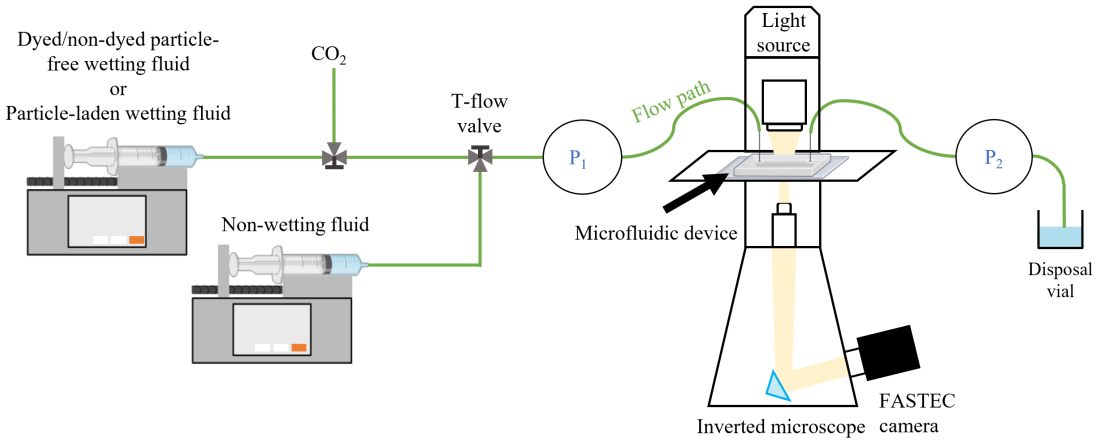

Figure 8.2: Schematic of the flow-rate–controlled two-phase microfluidic experimental setup with differential pressure sensing. CO_2 is injected to displace residual air before introducing the wetting and non-wetting fluids. Two syringe pumps supply the fluids and are selected via a valve network upstream of the microfluidic chip. The pressure drop across the porous domain is measured using upstream and downstream pressure sensors along the main flow path. The chip is mounted on an inverted microscope for real-time imaging with a FASTEC high-speed camera, and the effluent is collected downstream in a disposal vial.

The experimental protocol is outlined in Fig. 8.2. The experiment starts with CO_2 injection to displace and dissolve residual air. The porous domain is then saturated with a particle-free wetting fluid at a prescribed target flow rate, and the corresponding pressure drop is recorded as a baseline reference. A non-wetting fluid (oil) is then injected at a high flow rate to maximize oil saturation in the porous domain. At this stage, we capture an image of the initial oil-in-place (OIIP). Subsequently, a dyed, particle-free wetting fluid is injected at a lower flow rate, typically equal to that used during the initial saturation step, to mobilize the trapped oil; this step is referred to as waterflooding. Once the pressure difference across the microfluidic device stabilizes, waterflooding is considered to have reached its limit, as no further oil is mobilized under these conditions. The remaining trapped oil therefore defines a residual oil saturation within the porous structure.

We then replace the particle-free wetting fluid with a dyed, particle-laden wetting suspension and continue the injection at the same flow rate. Over time, we monitor the evolution of the pressure difference ($\Delta P(t)$) and acquire images of the porous domain at regular intervals. This enables us to investigate, in situ, how particle transport and pore clogging influence the mobilization of trapped oil.

8.3 Results and discussion

We first report that, in PDMS micromodels, waterflooding does not reach a stable limit of residual oil saturation due to oil uptake into PDMS, an effect observed for several oils with different uptake rates. We then present control waterflooding experiments in glass microchips (Micronit), which exhibit stable behavior after a finite injected volume, highlighting the absence of the

PDMS-related artifact.

8.3.1 Silicone oil uptake into PDMS prevents stable trapped-oil conditions

During waterflooding (injection of the wetting phase) in the PDMS porous micromodel, the pressure drop across the device does not reach a clear steady plateau, even after prolonged injection, suggesting that the distribution of the silicone oil continues to evolve. Yet, direct microscopic observations at the outlet do not reveal the release of oil droplets, indicating that the ongoing changes are not primarily due to advective oil production.

Instead, the real-time image sequence in Fig. 8.3 shows a progressive loss of visible silicone oil from the pore space, despite the absence of any connected pathway for the oil to escape from the field of view. This indicates that the silicone oil is being absorbed into the PDMS matrix. Such behavior is not unexpected, as similar uptake and swelling have been reported for PDMS in contact with organic liquids such as hydrocarbons, toluene, and dichloromethane [Lee et al., 2003]. These interactions highlight that PDMS is not well-suited for experiments involving such fluids.

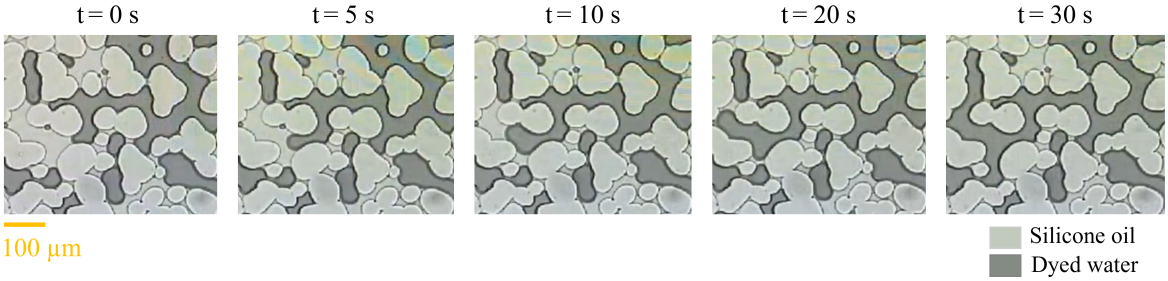

Figure 8.3: Real-time snapshots during waterflooding in a PDMS porous micromodel initially containing silicone oil. The images show the distribution of non-wetting fluid (light grey), dyed wetting fluid (dark grey), and grains (light grey). The dyed wetting phase invades the pore space while silicone oil progressively disappears, even though no connected pathway is available for oil to exit the field of view, consistent with oil uptake (infusion) into the PDMS matrix. Times indicate elapsed time since the start of recording.

8.3.2 Attempted mitigation of PDMS oil uptake using alternative oils

In a study by Dangla et al. [2010], PDMS is shown to readily swell in contact with silicone oil, whereas paraffin oil displays a lower infusion rate before reaching saturation. Motivated by these observations, we replace silicone oil with paraffin oil (properties in Table 8.1) and perform waterflooding experiments in a PDMS porous micromodel at a constant flow rate of 10 µL/min. The measured pressure difference ΔP as a function of injected pore volumes exhibits a characteristic two-stage evolution (Fig. 8.4). At early times, ΔP first increases slightly and then drops sharply, which is attributed to the mobilization and displacement of initially trapped oil once the applied pressure overcomes capillary resistance. This initial transient is followed by a more gradual and monotonic decrease in ΔP over a large number of injected pore volumes. Eventually, ΔP approaches the independently measured reference value corresponding to the fully water-saturated micromodel (red line) at the same imposed flow rate, indicating a progressive transition toward full wetting-phase saturation, consistent with gradual oil loss promoted by uptake (infusion) of paraffin oil into the PDMS matrix, which prevents the establishment of stable trapped-oil conditions before particle injection.

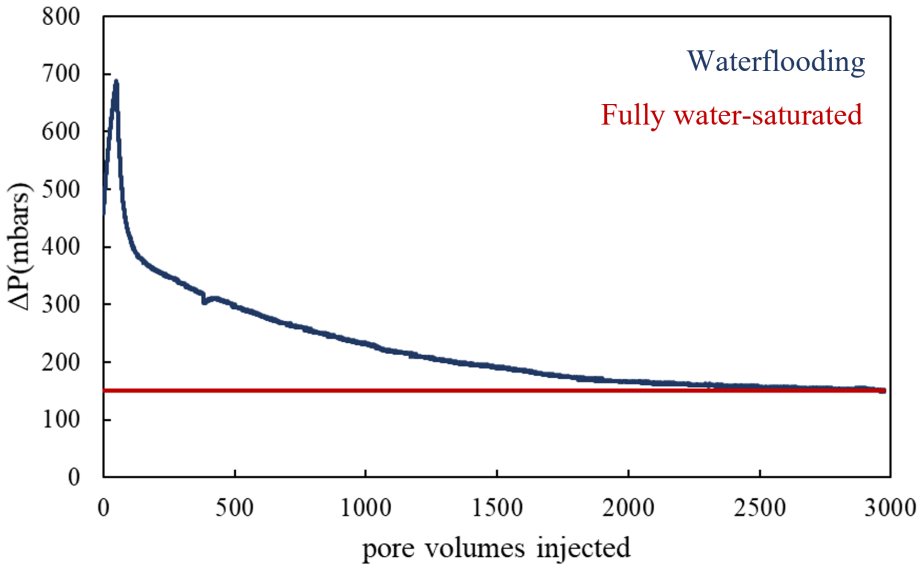

Figure 8.4: Pressure difference ΔP versus injected pore volumes during waterflooding at $Q = 10$ µL/min in a PDMS porous micromodel initially containing paraffin oil. After an initial transient, ΔP decreases monotonically and approaches the reference value corresponding to the fully water-saturated micromodel (red line), indicating a progressive transition toward full wetting-phase saturation.

After stable trapped oil cannot be maintained with either silicone or paraffin oil, we turn to fluorinated oil, which is reported to exhibit limited swelling and weaker affinity with PDMS [Karadimitriou et al., 2013]. A dedicated waterflooding experiment is performed using fluorinated oil at half the flow rate employed in the paraffin-oil case (5 µL/min), resulting in the injection of more than twice the number of pore volumes. Under these conditions, ΔP decreases more slowly and remains at higher values over a larger range of injected pore volumes compared with paraffin oil (Fig. 8.5), suggesting reduced oil loss. Nevertheless, ΔP does not reach a clear plateau over the explored pore-volume range and remains above the fully water-saturated reference value (red line), indicating that residual oil persists but its amount (and/or distribution) continues to evolve. Consequently, stable trapped-oil conditions cannot be robustly established in PDMS even when using fluorinated oil.

8.3.3 Establishing stable trapped oil conditions in hydrophilic glass EOR micromodels

To address the limitations associated with oil uptake in PDMS, we perform waterflooding experiments in heterogeneous tortuous glass EOR micromodels (Micronit), with a porosity of $\approx$ 53 % and a permeability of approximately 2.27×10^{-12} m^2 across the whole microfluidic device. Using silicone oil as the non-wetting phase, the pressure difference ΔP decreases rapidly during the early stages of waterflooding due to displacement of silicone oil and then reaches a stable plateau after approximately 180 injected pore volumes at a flow rate of 10 µL/min (Fig. 8.6). The plateau remains above the independently measured fully water-saturated reference value at the same flow rate, indicating that a residual oil phase persists in the porous domain.

This is supported by microscopy of a representative region of the porous domain (Fig. 8.7): the pore space is nearly fully oil-saturated prior to waterflooding, while after injecting 800 and 1600 pore volumes the spatial distribution of the oil phase remains similar, consistent with stable

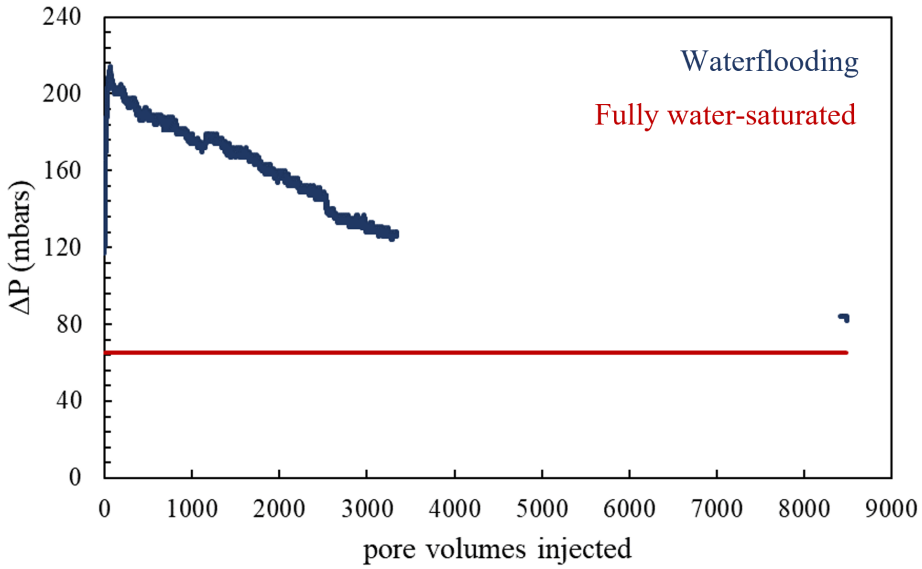

Figure 8.5: Pressure difference ΔP versus injected pore volumes during waterflooding at $Q = 5$ µL/min in a PDMS porous micromodel initially containing fluorinated oil. ΔP decreases gradually but remains above the fully water-saturated reference value (red line) and does not reach a clear plateau within the explored range, indicating that residual oil persists while the system continues to evolve.

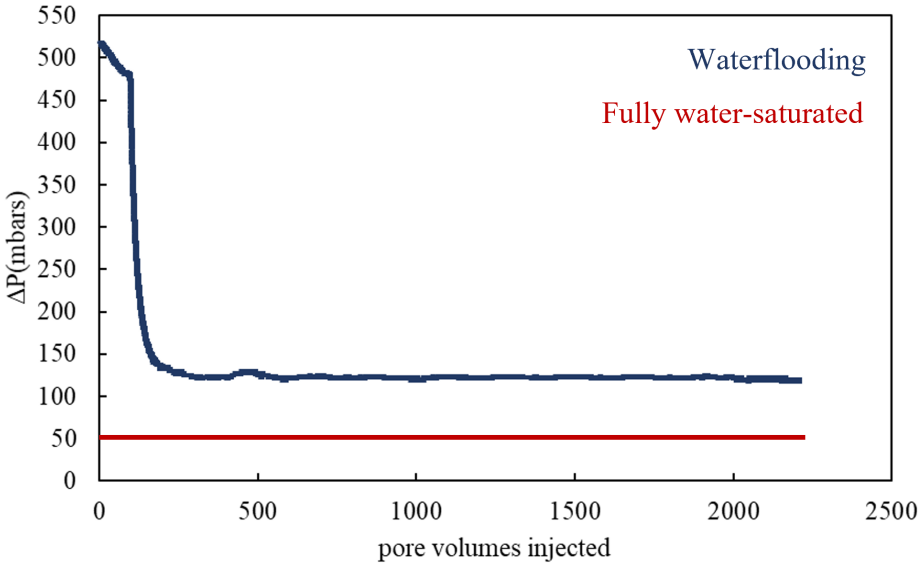

Figure 8.6: Pressure difference ΔP versus injected pore volumes during waterflooding at $Q = 10$ μL/min in a glass heterogeneous EOR micromodel (Micronit) initially containing silicone oil. After an initial transient, ΔP drops abruptly due to the mobilization of trapped oil in the chip and then reaches a plateau, from nearly 180 injected pore volumes until the end of the experiment at around 2300 pore volumes. This plateau, which remains above the red line representing full wetting-phase saturation, suggests the presence of residual trapped oil in the micromodel.

trapped-oil conditions.

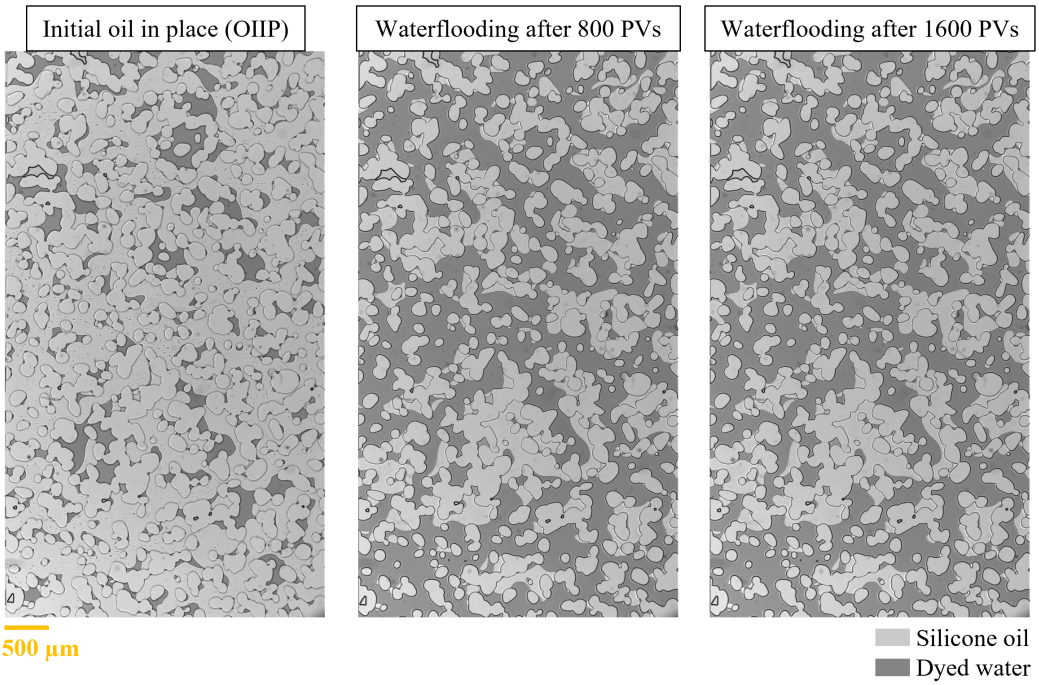

Figure 8.7: Microscopic images of a specific region in the Micronit glass microchip (EOR chip) during the waterflooding process after injecting different pore volumes. The images show the distribution of non-wetting fluid (light grey), dyed wetting fluid (dark grey), and grains (light grey). The images at 800 PVs and 1600 PVs indicate similar fluid distributions, confirming the establishment of steady trapped oil conditions.

8.4 Conclusions

The results above indicate that, during waterflooding in PDMS micromodels, an initial stage of oil mobilization and recovery is followed by a longer-term loss of the remaining capillary-trapped oil through uptake into the PDMS matrix for all oils tested (silicone, paraffin, and fluorinated oil), with kinetics that depend on the oil type. This motivates a transition from PDMS to glass micromodels for two-phase experiments, since glass eliminates oil uptake by the device material and enables stable trapped-oil conditions after waterflooding. Although commercial hydrophilic glass EOR chips (Micronit) provide a practical alternative, their characteristic constriction width is relatively large: the 2D arithmetic mean pore width is approximately 110 µm. For our particle sizes ($d_p = 4.5$ µm and 6 µm), this corresponds to confinement ratios $W/d_p \approx 24.4$ and 18.3, respectively. Such weak confinement is expected to delay pore-bridging and clogging events, thereby significantly increasing the experimental duration required to observe permeability impairment.

To better match the objectives and operating regime, we therefore need to fabricate in glass the same heterogeneous tortuous porous designs that we used in PDMS, with $M3$ being the most suitable due to its effective confinement ratios. While glass micromodels are commonly fabricated using wet-etching techniques, these methods impose constraints on achievable aspect ratios and limit the fabrication of highly confined and tortuous geometries. Reproducing our designs in glass requires more advanced microfabrication approaches that are still under development.

Reproducing these geometries in glass proved technically challenging within the fabrication routes explored during this work. The development of glass micromodels, therefore, remains a necessary next step for investigating particle-induced clogging under stable two-phase conditions.

Chapter 9

General conclusions and perspectives

This chapter summarizes the main findings of this thesis and discusses their implications for understanding, predicting, and controlling clogging in heterogeneous porous media. It also outlines perspectives for extending these results toward more realistic subsurface conditions and practical applications.

9.1 Conclusions

This thesis was motivated by the need to understand better how particle transport and deposition affect flow in porous media, with direct implications for injectivity loss in subsurface systems and the transport of contaminants such as colloids and microplastics. In such systems, permeability reduction results from complex pore-scale processes that remain difficult to predict in heterogeneous porous media due to their opacity. To address this, we investigated clogging mechanisms using microfluidic porous micromodels that mimic subsurface heterogeneity, enabling direct observation of particle deposition and its impact on flow. This approach allowed us to study clogging under controlled physicochemical and hydrodynamic conditions and to distinguish between adhesion-dominated and hydrodynamic-dominated regimes.

In the adhesion-dominated regime, this work advances the understanding of aggregation-driven clogging in heterogeneous porous media by identifying dendritic growth as a pore-scale mechanism of permeability impairment. We showed that clogging can proceed through the formation of dendritic structures that originate in stagnation regions and grow progressively upstream. Unlike classical aggregation-driven clogging, where particles progressively accumulate at the entrance of a constriction until it becomes blocked, dendritic clogging develops from a single deposition site and extends through directional multilayer growth toward an adjacent grain, eventually bridging the constriction. This mechanism is controlled by the local flow field, with dendrite orientation following streamlines and evolving as deposition modifies the flow. We further identified a pore-scale criterion for dendrite formation, showing that dendritic growth is promoted when the upstream stagnation region is sufficiently extended to sustain multilayer deposition under limited hydrodynamic shear, whereas increasing flow rate suppresses this condition. These results demonstrate that dendritic clogging develops under specific pore-scale flow conditions and progressively contributes to permeability decline.

In the hydrodynamic-dominated regime, this work advances the understanding of bridging-induced clogging in heterogeneous porous media by clarifying the respective roles of particle size, particle concentration, and flow conditions in controlling permeability impairment. This regime was isolated using a porous micromodel with an arithmetic mean constriction size of 20 µm, corresponding to a confinement ratio in the range $W/d_p \approx 3.3$ to 4.4 depending on particle size, which is favorable to hydrodynamic pore bridging. By varying particle size, particle

concentration, and imposed pressure difference by comparable factors, we assessed their respective influence on permeability decline. The results showed that particle size and concentration are the dominant parameters controlling the onset and evolution of clogging, whereas the imposed pressure difference mainly sets the timescale of permeability reduction. These experiments provided a benchmark dataset for bridging-dominated clogging in heterogeneous porous media, which was then used to develop and validate a pore-network model. Within this framework, hydrodynamic bridging was represented through a physically based probabilistic law, and the model successfully reproduced the main experimental trends of permeability decline observed under the different investigated conditions. This result highlights that the microfluidic experiments were essential not only for identifying the dominant factors controlling clogging, but also for providing the physical basis and reference data needed to construct a predictive pore-network modeling framework for bridging-induced permeability impairment in heterogeneous porous media.

Understanding particle clogging mechanisms and the factors controlling them is a prerequisite for proposing strategies to mitigate permeability impairment. In this context, this work advances the understanding of clogging dynamics in heterogeneous porous media by showing that time-dependent flow forcing cannot be considered a universal mitigation strategy, but instead acts differently depending on the dominant deposition regime. Under screened conditions, where aggregation and adhesion are promoted, oscillatory forcing delayed clogging and increased the injected volume required to reach the clogging threshold. This mitigation is attributed to the periodic increase in hydrodynamic stresses during the oscillation cycle, which promotes the detachment or destabilization of weakly attached deposits and thereby delays their progressive buildup. In many subsurface systems, such as geothermal reservoirs or groundwater aquifers, dissolved salts promote electrostatic screening between suspended particles. Under such conditions, our results suggest that oscillatory injection may mitigate clogging and delay hydraulic failure, potentially extending the operational lifetime of injection systems. In contrast, under repulsive conditions dominated by hydrodynamic deposition, the response became frequency-dependent: low-frequency oscillations delayed clogging, whereas higher-frequency forcing accelerated permeability decline. This regime inversion was linked to increased cyclic hydrodynamic loading and transient amplification of particle flux at pore constrictions, which promote mechanically driven bridging. These results show that the effect of dynamic forcing on permeability impairment must be interpreted in relation to the underlying deposition mechanism.

Taken together, these findings provide direct pore-scale evidence that permeability decline and injectivity loss in heterogeneous porous media arise from distinct clogging mechanisms whose relative importance depends on pore-scale geometry, flow conditions, and particle interactions. Predicting and controlling clogging in subsurface systems, therefore, requires approaches that identify the dominant mechanism under given physicochemical and hydrodynamic conditions, determine how this mechanism develops within the pore space, and relate it to the resulting evolution of permeability impairment and injectivity decline. Such an approach is necessary not only to interpret observed clogging dynamics but also to design mitigation strategies adapted to the governing regime, whether the objective is to delay permeability loss, preserve injectivity, or, conversely, exploit clogging-induced flow redistribution for specific applications, including the mobilization of trapped contaminants.

9.2 Perspectives

While this work provides new insights into clogging mechanisms in heterogeneous porous media, several extensions can be considered to further improve the understanding and applicability of these findings. In particular, future work should further explore the coupled evolution of pore structure and flow, which governs clogging dynamics across scales.

A first extension concerns the complexity of particle populations. The present study focuses on monodisperse spherical particles, which provide a controlled framework to isolate the governing mechanisms of deposition and clogging. However, natural and industrial systems typically involve polydisperse suspensions and particles with diverse shapes. Polydispersity can lead to selective transport and size-dependent retention, while non-spherical particles, such as microplastic fibers or fragments, may align with the flow, rotate, or enhance bridging probability. Investigating how particle size distribution and shape influence deposit structure and flow obstruction would provide a more realistic description of clogging in subsurface environments.

These aspects become even more critical when considering fractured porous media, particularly in enhanced geothermal systems, where fluid circulation is largely controlled by connected fracture networks in crystalline rocks, often granitic formations. The two-dimensional porous networks investigated in this thesis are not intended to reproduce the full geometrical complexity of such fractured geothermal reservoirs, but rather to provide a controlled platform in which particle deposition, clogging, and the resulting flow redistribution can be directly resolved at the pore scale. This ability to isolate and visualize individual mechanisms constitutes one of the main strengths of microfluidic approaches. However, translating these mechanisms to fractured geothermal reservoirs remains challenging because flow is concentrated within fracture networks whose hydraulic behavior depends on fracture aperture, roughness, orientation, density, and connectivity. Individual rough fractures can be reproduced in microfluidic devices, whereas reproducing a representative connected fracture network is considerably more difficult, particularly because the scale at which representative hydraulic behavior emerges in fractured rocks is not straightforward to define. Larger microfluidic systems may help bridge part of this scale gap, as demonstrated by core-scale micromodel approaches such as Mejia et al. [2020]. Complementary X-ray CT and micro-CT studies of fractured rocks could further provide realistic three-dimensional fracture geometries against which the pore-scale mechanisms identified using microfluidics can be tested. More generally, extending the present observations from two-dimensional to three-dimensional porous structures is an important step, since three-dimensional geometries introduce additional complexity in pore connectivity, flow redistribution, and deposit morphology. The spatial development and stability of clogging structures, as well as their impact on flow pathways, may therefore differ from those observed in the present two-dimensional systems, potentially affecting both dendritic growth and bridging conditions. Combining high-resolution microfluidic observations with fracture-specific micromodels and three-dimensional imaging of natural fractured rocks would thus provide a progressive route toward assessing how the mechanisms identified in this thesis translate to enhanced geothermal systems.

Beyond single-phase flow, a promising perspective concerns the role of clogging-induced flow redirection in multiphase systems containing trapped immiscible contaminants. As particle deposits progressively modify the pore structure, they can redirect local streamlines and locally increase viscous stresses. Under such conditions, these increased viscous forces may overcome the capillary forces that keep an immiscible phase trapped in place, leading to its mobilization. Investigating this coupling between clogging, flow redistribution, and capillary trapping could open new perspectives for remediation strategies based on the controlled mobilization of trapped contaminants.

Finally, further developments should focus on coupling pore-scale observations with larger-scale modeling approaches. While pore-network models provide a useful intermediate framework, integrating these results into continuum-scale descriptions remains a key challenge. Such multiscale approaches are required to incorporate the regime-dependent nature of clogging into field-scale predictions and to support the design of injection and remediation strategies.

Appendix A

Appendix

A.1 DLVO parameters and corresponding interaction profiles

Table A.1 lists the fixed parameters and their corresponding values used in the DLVO equations from Chapter 2, and Fig. A.1 presents the DLVO profiles for both particle-particle and particle-surface interactions.

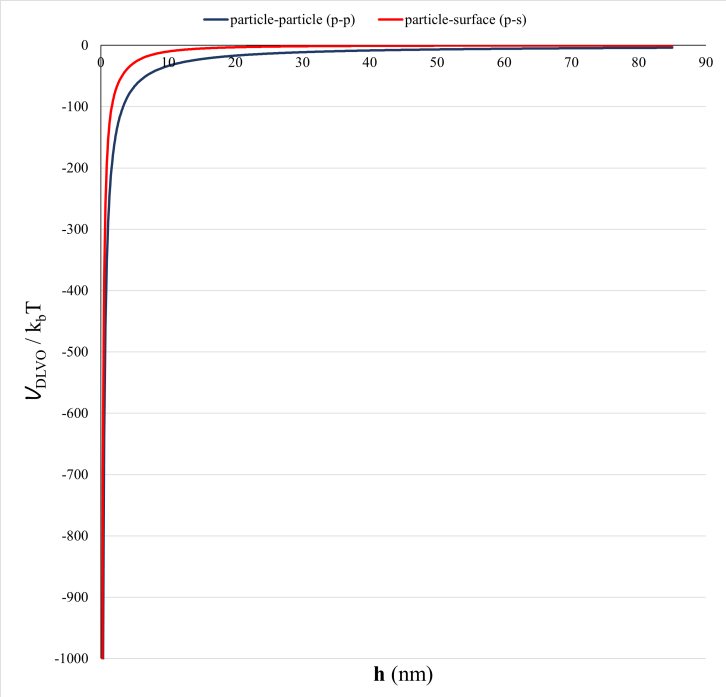

Figure A.1: DLVO profiles for particle-particle and particle-surface interactions as a function of separation distance (h) in nanometers (nm).

Table A.1: Parameters and their corresponding values used in the DLVO interaction potential approximations. The annotations p, m, and s refer to the particle, medium, and PDMS surface.

Fixed parameters	**Value**
Particle radius, a_p	2.25 µm
Vacuum permittivity, ε_0	8.85×10^{-12} C^2/Jm
Medium dielectric constant, ε_r	78.5 for water [Akerlof, 1932]
	40.2 for glycerol [Akerlof, 1932]
	70.1 (weighted average)
Boltzmann constant, k_B	1.38×10^{-23} J/K
Temperature, T	293 K
Avogadro's number, N_A	6.023×10^{23}
Electron charge, e	1.6×10^{-19} C
Hamaker constant, A	$A_{\text{polystyrene}} = 6.5 \times 10^{-20}$ J [Gong et al., 2001]
	$A_{\text{PDMS-surface}} = 4.4 \times 10^{-20}$ J [Drummond and Chan, 1997]
	$A_{\text{water}} = 3.7 \times 10^{-20}$ J [Gong et al., 2001]
	$A_{\text{glycerol}} = 1.38 \times 10^{-20}$ J [Israelachvili, 2011]
	$A_{medium} = A_{33} = 3.19 \times 10^{-20}$ J (weighted average)
$A_{131} = (\sqrt{A_{33}} - \sqrt{A_{11}})^2$	2.7×10^{-21} J (polystyrene–polystyrene)
$A_{132} = (\sqrt{A_{33}} - \sqrt{A_{11}})(\sqrt{A_{33}} - \sqrt{A_{22}})$	7.3×10^{-21} J (polystyrene–surface)
Retardation length, λ	100×10^{-9} m
Solution ionic strength, I	100 mM
Measured particle zeta potential, ζ_p	−21.3 mV
PDMS surface zeta potential, ζ_s	−23 mV [Mustin and Stoeber, 2016]
Reciprocal Debye length, $\kappa = \left(\frac{2\times10^3 N_A e^2 I}{\varepsilon_0 \varepsilon_r k_B T}\right)^{1/2}$	1.2×10^9 m

A.2 MATLAB scripts

A.2.1 Watershed-Based pore size distribution analysis

This MATLAB script extracts a pore size distribution from a segmented image of the porous medium using a watershed-based separation of pore regions. Pore areas are converted to equivalent diameters, and the resulting distribution is summarized with descriptive statistics and a log-normal fit. The script also exports the labeled pore map and the PSD plots used in this manuscript.

Listing A.1: MATLAB script used to compute pore size distribution using watershed segmentation

```
% Pore diameter distribution using watershed segmentation
% Based on Rabbani et al., 2014

clc; clear; close all;

% =========================
% GLOBAL STYLE (Times New Roman everywhere)
% =========================
set(groot, 'defaultTextFontName', 'Times New Roman');
set(groot, 'defaultAxesFontName', 'Times New Roman');
set(groot, 'defaultLegendFontName', 'Times New Roman');
set(groot, 'defaultTextInterpreter', 'tex');
set(groot, 'defaultAxesTickLabelInterpreter', 'tex');
set(groot, 'defaultLegendInterpreter', 'tex');

% =========================
% INPUT IMAGE + PARAMETERS
% =========================
A = imread('stitched-highresolution-rotated.tif');
Resolution = 2.04;  % um/pixel (printed later as um/pixel)
Bins = 20;
Conn = 8;

if ndims(A) == 3
    A = rgb2gray(A);
end

A = imbinarize(A);  % Ensure binary image
[s1, s2] = size(A);

A = bwmorph(A, 'majority', 10);
Poro = sum(~A(:)) / (s1 * s2);

% =========================
% WATERSHED SEGMENTATION
% =========================
D = -bwdist(A, 'cityblock');
B = medfilt2(D, [3 3]);
B = watershed(B, Conn);

% Isolate pores
Pr = zeros(s1, s2);
for I = 1:s1
    for J = 1:s2
        if A(I, J) == 0 && B(I, J) ~= 0
            Pr(I, J) = 1;
        end
    end
end

% Remove small regions and label
Pr = bwareaopen(Pr, 9, Conn);
[Pr_L, Pr_n] = bwlabel(Pr, Conn);

% =========================
% PORE AREAS -> EQUIV DIAM
% =========================
V = zeros(Pr_n, 1);
for I = 1:s1
```

```
    for J = 1:s2
        lab = Pr_L(I, J);
        if lab ~= 0
            V(lab) = V(lab) + 1;
        end
    end
end

D_pores = 2 * Resolution .* sqrt(V / pi);  % Equivalent diameter (um)
D_pores = D_pores(isfinite(D_pores) & D_pores > 0);  % safety for log()

% ==========================
% BASIC STATS (DATA)
% ==========================
Npores  = numel(D_pores);
minD    = min(D_pores);
maxD    = max(D_pores);

meanD   = mean(D_pores);     % arithmetic mean
medianD = median(D_pores);
stdD    = std(D_pores);

% ==========================
% HISTOGRAM MODE (DATA-BASED)
% ==========================
[counts_prob, edges_prob] = histcounts(D_pores, Bins, 'Normalization',
    'probability');
bin_centers_prob = edges_prob(1:end-1) + diff(edges_prob)/2;

[~, idxMode] = max(counts_prob);
mode_hist = bin_centers_prob(idxMode);
mode_hist_prob = counts_prob(idxMode);

% ==========================
% LOG-NORMAL FIT + DESCRIPTORS
% ==========================
mu_ln    = mean(log(D_pores));
sigma_ln = std(log(D_pores));

mode_logn   = exp(mu_ln - sigma_ln^2);
median_logn = exp(mu_ln);
mean_logn   = exp(mu_ln + 0.5*sigma_ln^2);

% ==========================
% PRINT EVERYTHING (TERMINAL)
% ==========================
um = char(181); % 'u' for terminal prints (ASCII-friendly)
fprintf('==============================\n');
fprintf('Pore diameter distribution (watershed)\n');
fprintf('==============================\n');
fprintf('Resolution: %.4f %sm/pixel\n', Resolution, um);
fprintf('Porosity (binary image): %.4f\n', Poro);
fprintf('Number of pores (labeled regions): %d\n', Pr_n);
fprintf('Number of valid pore diameters used: %d\n', Npores);
fprintf('Range: [%.2f, %.2f] %sm\n', minD, maxD, um);

fprintf('\n--- Data statistics (%sm) ---\n', um);
fprintf('Arithmetic mean: %.2f %sm\n', meanD, um);
fprintf('Median:          %.2f %sm\n', medianD, um);
fprintf('Std dev:         %.2f %sm\n', stdD, um);

```

```
fprintf('\n--- Histogram mode (data-based) ---\n');
fprintf('Bins: %d\n', Bins);
fprintf('Histogram mode (most probable bin center): %.2f %sm\n', mode_hist, um);
fprintf('Mode probability (bin height): %.4f\n', mode_hist_prob);

fprintf('\n--- Log-normal fit (based on log(D_pores)) ---\n');
fprintf('mu_ln = %.3f, sigma_ln = %.3f\n', mu_ln, sigma_ln);
fprintf('Log-normal mode (most probable size): %.2f %sm\n', mode_logn, um);
fprintf('Log-normal median (fit): %.2f %sm\n', median_logn, um);
fprintf('Log-normal mean (fit): %.2f %sm\n', mean_logn, um);

% =========================
% FIGURE 1: LABELED PORES + HISTOGRAM
% =========================
f = figure(1);
set(f, 'Position', [100 100 800 600], 'Color', 'w');

subplot(1, 2, 1)
RGB = label2rgb(Pr_L, 'jet', 'w', 'shuffle');
imshow(RGB);
imwrite(RGB, 'Output.png');

subplot(1, 2, 2)
edges = linspace(minD, maxD, Bins + 1);
Rel_Frequencies = histcounts(D_pores, edges, 'Normalization', 'probability');
bin_centers = edges(1:end-1) + diff(edges)/2;
bar(bin_centers, Rel_Frequencies, 1, 'FaceColor', 'b', 'EdgeColor', 'k');

xlabel(['Pore Diameter (' um 'm)'], 'Color', 'k',...
    'FontName', 'Times New Roman', 'FontSize', 20, 'Interpreter', 'tex');
ylabel('Relative Frequency', ...
    'FontName', 'Times New Roman', 'FontSize', 20, 'Interpreter', 'tex');

axis square;
set(gca, 'FontSize', 20, 'FontName', 'Times New Roman', ...
    'TickLabelInterpreter', 'tex');

exportgraphics(f, 'PoreSizeDistribution2.png', 'Resolution', 150);

% =========================
% FIGURE 2: HISTOGRAM + LOG-NORMAL FIT
% =========================
g = figure(2);
set(g, 'Position', [100 100 800 600], 'Color', 'w');

[counts, edges] = histcounts(D_pores, Bins, 'Normalization', 'probability');
bin_centers = edges(1:end-1) + diff(edges)/2;
hBar = bar(bin_centers, counts, 1, 'FaceColor', 'b', 'EdgeColor', 'k');
hold on;

x_fit = linspace(minD, maxD, 500);
logn_pdf = (1 ./ (x_fit * sigma_ln * sqrt(2*pi))) .* ...
    exp(-((log(x_fit) - mu_ln).^2) / (2*sigma_ln^2));
binw = edges(2) - edges(1);
logn_pdf = logn_pdf * binw;  % scale to probability/bin

hFit = plot(x_fit, logn_pdf, 'r-', 'LineWidth', 2);

xlabel('Pore Diameter (um)', ...
    'FontName', 'Times New Roman', 'FontSize', 20, 'Interpreter', 'none');

```

```
ylabel('Relative Frequency', ...
    'FontName', 'Times New Roman', 'FontSize', 20, 'Interpreter', 'none');


xlim([minD-2, maxD+2]);
axis square;
set(gca, 'FontSize', 20, 'FontName', 'Times New Roman', ...
    'TickLabelInterpreter', 'tex');

legend([hBar, hFit], {'Data', 'Log-normal Fit'}, ...
    'Location', 'best', 'FontName', 'Times New Roman', 'Interpreter', 'tex');

exportgraphics(g, 'PoreSizeDistribution_LogNormalOnly.png', 'Resolution', 150);
```

A.2.2 CSD (Constriction size distribution)

This MATLAB script processes the skeleton analysis output exported from ImageJ (Analyze Skeleton), and quantifies the distribution of branch (constriction) lengths. The script reads the CSV file `Branch information.csv`, converts branch lengths from pixels to micrometers using a fixed pixel-to-length calibration, removes non-physical values, and computes descriptive statistics, a probability histogram, and a log-normal fit. The resulting distribution and fit parameters are used to characterize the typical constriction length scale of the skeletonized structures.

Listing A.2: MATLAB script for computing the constriction (branch) length distribution

```
clear all; close all; clc;

% ==========================
% SETTINGS
% ==========================
pixel_to_micron = 2.4;              % um / pixel
csvFile = 'Branch information.csv';  % Analyze Skeleton output
columnName = 'BranchLength';         % change if needed

bin_width = 5;                       % um
nFitPts   = 500;                     % smooth curve resolution

% ==========================
% LOAD DATA
% ==========================
opts = detectImportOptions(csvFile);
data = readtable(csvFile, opts);

if ~ismember(columnName, data.Properties.VariableNames)
    error('Column "%s" not found. Available columns:\n%s', ...
        columnName, strjoin(data.Properties.VariableNames, ', '));
end

% Convert to microns
branch_lengths = data{:, columnName} * pixel_to_micron;   % now in um

% Remove invalid / non-positive values (protect log)
branch_lengths = branch_lengths(isfinite(branch_lengths) & branch_lengths > 0);

% ==========================
% BASIC STATS (DATA)
% ==========================
N            = numel(branch_lengths);
minLength    = min(branch_lengths);
```

```
maxLength    = max(branch_lengths);
meanLength   = mean(branch_lengths);     % arithmetic mean (um)
medianLength = median(branch_lengths);
stdLength    = std(branch_lengths);

% =========================
% HISTOGRAM (PROBABILITY)
% =========================
bin_edges = (floor(minLength/bin_width)*bin_width) : bin_width : ...
            (ceil(maxLength/bin_width)*bin_width + bin_width);

[counts, edges] = histcounts(branch_lengths, bin_edges);
probability = counts / sum(counts);
bin_centers = edges(1:end-1) + diff(edges)/2;
binw = edges(2) - edges(1);

% Histogram mode (most probable bin center)
[~, idxMode] = max(probability);
mode_hist = bin_centers(idxMode);
mode_hist_prob = probability(idxMode);

% =========================
% LOG-NORMAL FIT
% =========================
mu_ln    = mean(log(branch_lengths));
sigma_ln = std(log(branch_lengths));

mode_logn   = exp(mu_ln - sigma_ln^2);
median_logn = exp(mu_ln);
mean_logn   = exp(mu_ln + 0.5*sigma_ln^2);

x_fit = linspace(minLength, maxLength, nFitPts);
logn_pdf = (1 ./ (x_fit * sigma_ln * sqrt(2*pi))) .* exp(-((log(x_fit) -
    mu_ln).^2) / (2*sigma_ln^2));
logn_pdf_scaled = logn_pdf * binw;  % scale to probability per bin

% =========================
% PRINT EVERYTHING TO TERMINAL
% =========================
fprintf('==============================\n');
fprintf('Branch/Constriction Length Analysis\n');
fprintf('==============================\n');
fprintf('File: %s\n', csvFile);
fprintf('Column: %s\n', columnName);
fprintf('Pixel-to-micron: %.4f um/pixel\n', pixel_to_micron);
fprintf('N (valid entries): %d\n', N);
fprintf('Range: [%.2f, %.2f] um\n', minLength, maxLength);

fprintf('\n--- Data statistics (in um) ---\n');
fprintf('Arithmetic mean: %.2f um\n', meanLength);
fprintf('Median:          %.2f um\n', medianLength);
fprintf('Std dev:         %.2f um\n', stdLength);

fprintf('\n--- Histogram settings ---\n');
fprintf('Bin width: %.2f um\n', binw);
fprintf('Number of bins: %d\n', numel(probability));
fprintf('Histogram mode (most probable bin center): %.2f um\n', mode_hist);
fprintf('Mode probability (height of that bin): %.4f\n', mode_hist_prob);

fprintf('\n--- Log-normal fit (based on log(data)) ---\n');
fprintf('mu_ln:    %.4f\n', mu_ln);
```

```
fprintf('sigma_ln: %.4f\n', sigma_ln);
fprintf('Log-normal mode:   %.2f um\n', mode_logn);
fprintf('Log-normal median: %.2f um\n', median_logn);
fprintf('Log-normal mean:   %.2f um\n', mean_logn);

% =========================
% PLOT: HISTOGRAM + LOG-NORMAL FIT
% Keep ONLY legend entries: "Data" and "Log-normal Fit"
% =========================
figure('Position', [100 100 800 800]);
hold on;
xlim([0 240])

hBar = bar(bin_centers, probability, 1, 'FaceColor', 'b', 'EdgeColor', 'k');
hFit = plot(x_fit, logn_pdf_scaled, 'r-', 'LineWidth', 2);

grid off; box on;
set(gca, 'FontSize', 26);

% Axis labels
xlabel('Constriction width (um)');
ylabel('Relative Frequency');

% Legend in TOP-LEFT with box
lgd = legend([hBar, hFit], {'Data', 'Log-normal Fit'}, 'Location', 'northeast');
set(lgd, 'Box', 'on');

% Uncomment to save
% exportgraphics(gcf, 'HistCSD_LogNormal.png', 'Resolution', 200);
```

A.3 Complete mask layouts

We produce two negative 3D master wafers, both with the same microchannel depth of approximately 20 µm. The first wafer corresponds to the single-grain-collector geometry ($M1$), replicated 19 times on the mask shown in Fig. A.2. The second wafer is dedicated to the heterogeneous tortuous porous domains and includes two configurations ($M2$ and $M3$), each replicated 4 times on the mask shown in Fig. A.3. Both master wafers have a diameter of 10.5 cm.

A.4 Dendrite clogging at multiple locations within the porous domain

Fig. A.4 presents averaged experimental images capturing the progressive formation of a dendritic clog in a specific region of the porous domain at a flow rate of 8 µL/min, as the number of injected pore volumes (PVs) increases, leading to the complete clogging of the local flow pathway. Fig. A.5 further illustrates dendritic clogging occurring in two distinct regions: (a) after 2370 PVs and (b) after 2261 PVs, emphasizing the variability in dendrite-clogging dynamics within the porous domain.

A.5 Movies of the experiments

The movies were recorded using a FASTEC camera at 271 fps and are presented at a playback speed of 10 frames per second:

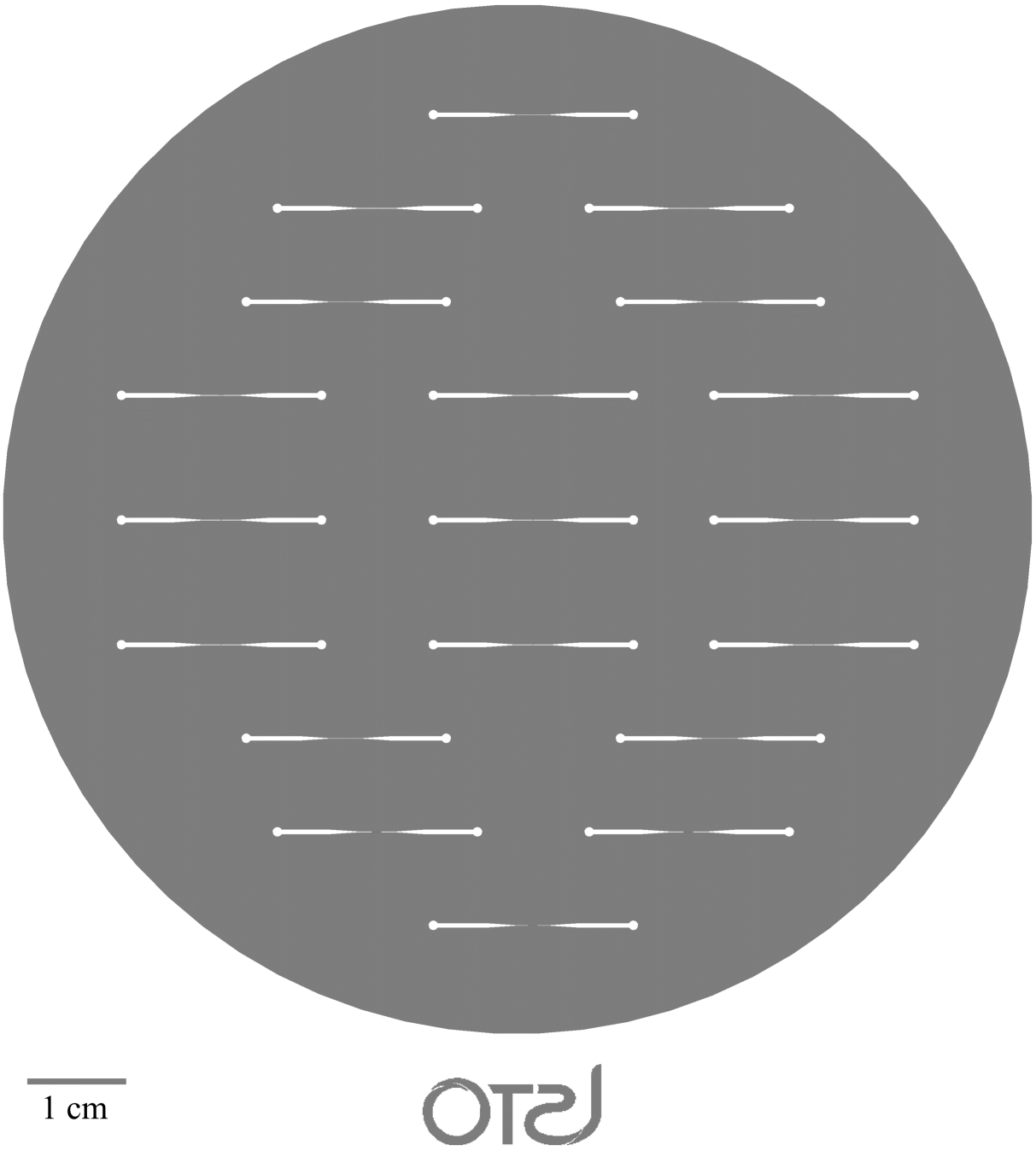

Figure A.2: Complete mask layout containing 19 replicas of the single-grain collector design ($M1$), where the gray regions represent the solid matrix (grains) and the white regions correspond to the pore space. The overall mask diameter is 10.5 cm.

- Movie corresponding to Fig. 5.2 in the main manuscript after 1664 PVs injected: `Movie_Figure_3a_8uL_min_1664_PVs` [Okaybi et al., 2025].
- Movie corresponding to Fig. 5.2 in the main manuscript after 2225 PVs injected: `Movie_Figure_3a_8uL_min_2225_PVs` [Okaybi et al., 2025].

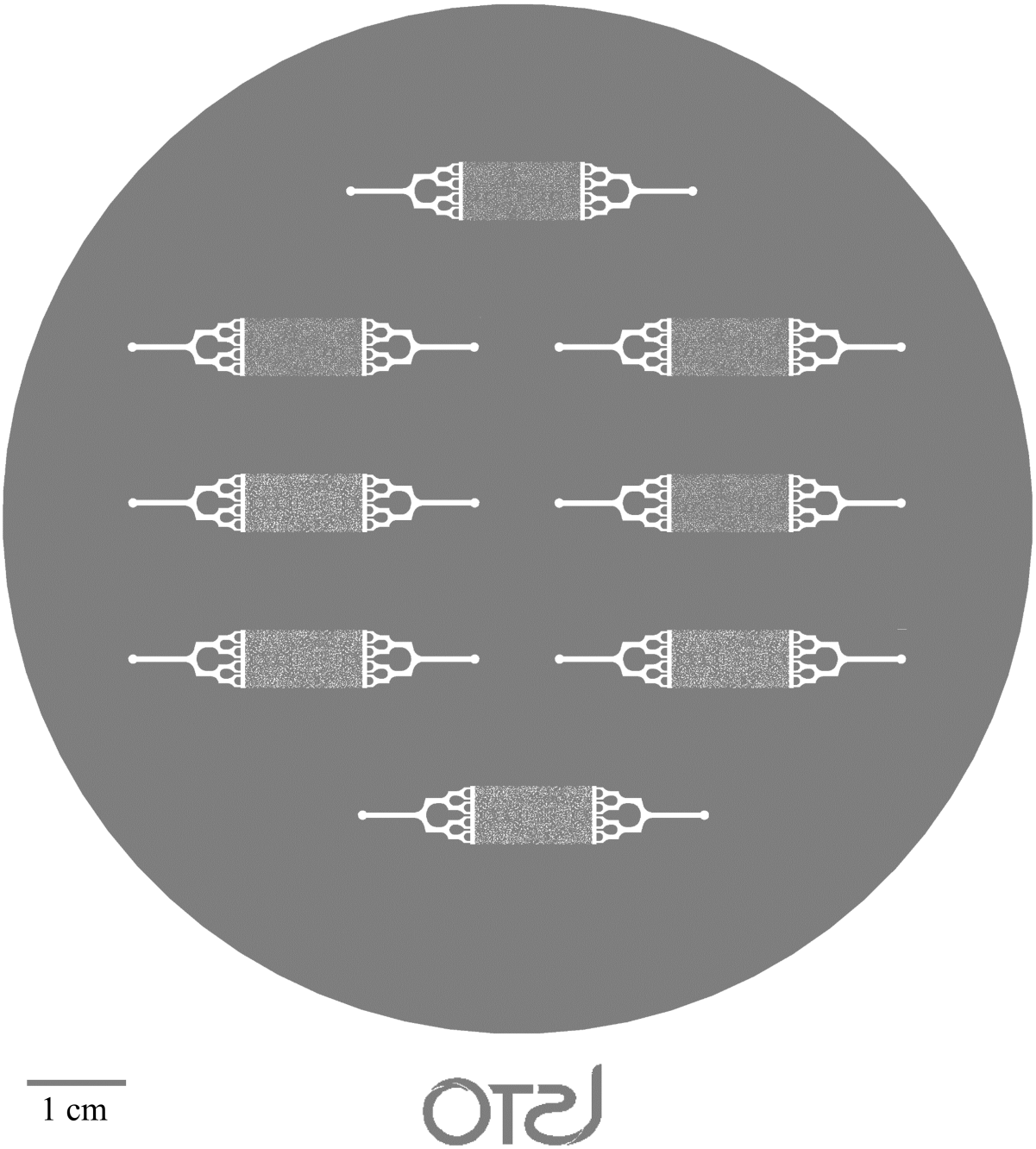

Figure A.3: Complete mask layout showing 8 replicas of the heterogeneous tortuous porous-domain designs (4 of $M2$ and 4 of $M3$). $M2$ and $M3$ differ in their internal pore-space statistics. Gray regions correspond to the solid matrix (grains), while white regions indicate the pore space. The mask diameter is 10.5 cm.

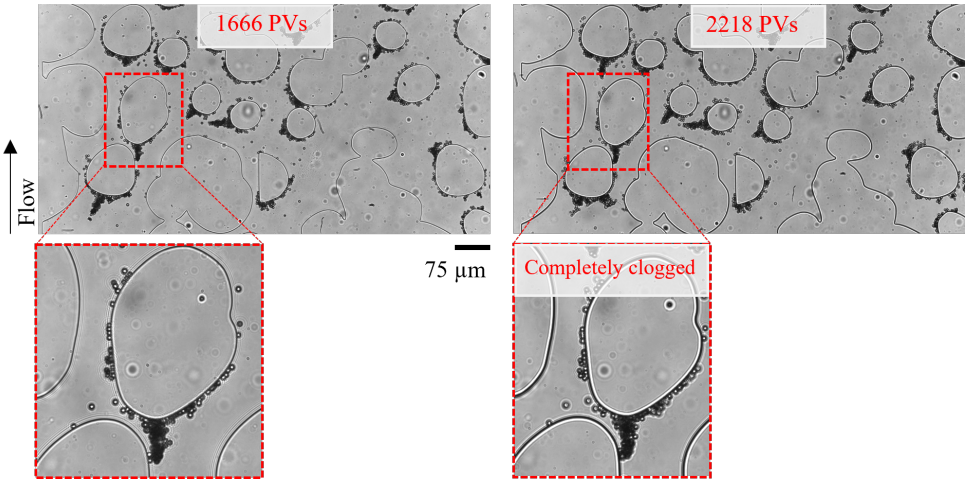

Figure A.4: Averaged experimental images at a flow rate of 8 µL/min, showing the progressive formation of a dendritic clog in a specific region of the porous domain over successive pore volumes of particle injection (PVs).

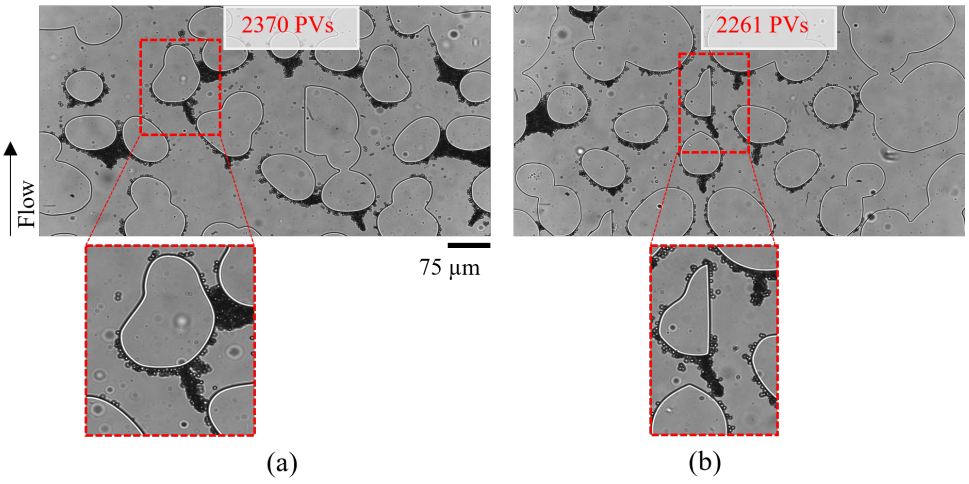

Figure A.5: Averaged experimental images at a flow rate of 8 µL/min, illustrating dendritic clogging in two distinct regions of the porous domain: (a) after 2370 pore volumes (PVs) of particle injection and (b) after 2261 PVs.

Bibliography

Angelo Accardo, Rémi Courson, Roberto Riesco, Vincent Raimbault, and Laurent Malaquin. Direct laser fabrication of meso-scale 2d and 3d architectures with micrometric feature resolution. *Additive Manufacturing*, 22:440–446, 2018.

Zbigniew Adamczyk, Barbara Siwek, Maria Zembala, and Peter Belouschek. Kinetics of localized adsorption of colloid particles. *Advances in Colloid and Interface Science*, 48:151–280, 1994.

Gbedo Constant Agbangla, Éric Climent, and Patrice Bacchin. Experimental investigation of pore clogging by microparticles: Evidence for a critical flux density of particle yielding arches and deposits. *Separation and purification technology*, 101:42–48, 2012a.

Gbedo Constant Agbangla, Éric Climent, and Patrice Bacchin. Experimental investigation of pore clogging by microparticles: Evidence for a critical flux density of particle yielding arches and deposits. *Separation and Purification Technology*, 101:42–48, November 2012b. ISSN 1383-5866. doi: 10.1016/j.seppur.2012.09.011. URL `https://www.sciencedirect.com/science/article/pii/S1383586612004868`.

Gbedo Constant Agbangla, Éric Climent, and Patrice Bacchin. Numerical investigation of channel blockage by flowing microparticles. *Computers & Fluids*, 94:69–83, 2014.

Nassim Ait-Mouheb, Juliette Schillings, Jafar Al-Muhammad, Ryad Bendoula, Séverine Tomas, Muriel Amielh, and Fabien Anselmet. Impact of hydrodynamics on clay particle deposition and biofilm development in a labyrinth-channel dripper. *Irrigation Science*, 37(1):1–10, 2019.

Gosta Akerlof. Dielectric constants of some organic solvent-water mixtures at various temperatures. *Journal of the American Chemical Society*, 54(11):4125–4139, 1932.

Abdellah Alem, Nasre-Dine Ahfir, Abdulghadir Elkawafi, and HuaQing Wang. Hydraulic operating conditions and particle concentration effects on physical clogging of a porous medium. *Transport in Porous Media*, 106(2):303–321, 2015.

DADA Aljuboury, P Palaniandy, HB Abdul Aziz, and SADA Feroz. Treatment of petroleum wastewater by conventional and new technologies-a review. *Glob. Nest J*, 19(3):439–452, 2017.

Osamah A Alomair, Khaled M Matar, and Yousef H Alsaeed. Nanofluids application for heavy oil recovery. In *SPE Asia Pacific oil and gas conference and exhibition*, pages SPE–171539. SPE, 2014.

Alimohammad Anbari, Hung-Ta Chien, Sujit S Datta, Wen Deng, David A Weitz, and Jing Fan. Microfluidic model porous media: Fabrication and applications. *Small*, 14(18):1703575, 2018.

Anton Paar. Potentiel zêta, n.d. URL `https://wiki.anton-paar.com/fr-fr/potentiel-zeta/`. Accessed: 2026-03-17.

R Aris. On the dispersion of a solute in a fluid flowing through a tube. *Proc. Roy. Soc. A.*, 235: 67–77, 1956.

Maria Auset and Arturo A Keller. Pore-scale processes that control dispersion of colloids in saturated porous media. *Water resources research*, 40(3), 2004.

Maria Auset and Arturo A Keller. Pore-scale visualization of colloid straining and filtration in saturated porous media using micromodels. *Water resources research*, 42(12), 2006.

Patrice Bacchin, Pierre Aimar, and Victor Sanchez. Model for colloidal fouling of membranes. *AIChE journal*, 41(2):368–376, 1995.

Patrice Bacchin, Pierre Aimar, and Robert W Field. Critical and sustainable fluxes: Theory, experiments and applications. *Journal of membrane science*, 281(1-2):42–69, 2006.

Patrice Bacchin, Aurélie Marty, Paul Duru, Martine Meireles, and Pierre Aimar. Colloidal surface interactions and membrane fouling: Investigations at pore scale. *Advances in colloid and interface science*, 164(1-2):2–11, 2011.

Patrice Bacchin, Quentin Derekx, Damien Veyret, Karl Glucina, and Philippe Moulin. Clogging of microporous channels networks: role of connectivity and tortuosity. *Microfluidics and nanofluidics*, 17:85–96, 2014.

Oliver Bajt. From plastics to microplastics and organisms. *FEBS Open bio*, 11(4):954–966, 2021.

Julien Beaumont, Hugues Bodiguel, and Annie Colin. Drainage in two-dimensional porous media with polymer solutions. *Soft Matter*, 9(42):10174–10185, 2013.

Lyacine Bennacer, Nasre-Dine Ahfir, Abdellah Alem, and HuaQing Wang. Coupled effects of ionic strength, particle size, and flow velocity on transport and deposition of suspended particles in saturated porous media. *Transport in porous media*, 118(2):251–269, 2017.

John Bergendahl and Domenico Grasso. Colloid generation during batch leaching tests: mechanics of disaggregation. *Colloids and Surfaces A: Physicochemical and Engineering Aspects*, 135(1-3): 193–205, 1998.

John Bergendahl and Domenico Grasso. Prediction of colloid detachment in a model porous media: hydrodynamics. *Chemical Engineering Science*, 55(9):1523–1532, 2000.

Claire Bertelli, Sophie Courtois, Marta Rosikiewicz, Philippe Piriou, Sébastien Aeby, Samuel Robert, Jean-François Loret, and Gilbert Greub. Reduced chlorine in drinking water distribution systems impacts bacterial biodiversity in biofilms. *Frontiers in microbiology*, 9:2520, 2018.

AF Bichara. Redevelopment of clogged recharge wells. *Journal of irrigation and drainage engineering*, 114(2):343–350, 1988.

Clément Bielinski, Othmane Aouane, Jens Harting, and Badr Kaoui. Squeezing multiple soft particles into a constriction: Transition to clogging. *Physical Review E*, 104(6):065101, 2021.

Navid Bizmark, Joanna Schneider, Rodney D Priestley, and Sujit S Datta. Multiscale dynamics of colloidal deposition and erosion in porous media. *Science advances*, 6(46):eabc2530, 2020.

Frédéric Blanc, Enzo D'Ambrosio, Laurent Lobry, François Peters, and Elisabeth Lemaire. Universal scaling law in frictional non-brownian suspensions. *Physical Review Fluids*, 3(11): 114303, November 2018. ISSN 2469-990X. doi: 10.1103/physrevfluids.3.114303.

Martin J. Blunt, Branko Bijeljic, Hu Dong, Oussama Gharbi, Stefan Iglauer, Peyman Mostaghimi, Adriana Paluszny, and Christopher Pentland. Pore-scale imaging and modelling. *Advances in Water Resources*, 51:197–216, 2013.

Scott A Bradford and Saeed Torkzaban. Colloid interaction energies for physically and chemically heterogeneous porous media. *Langmuir*, 29(11):3668–3676, 2013.

Scott A Bradford, Scott R Yates, Mehdi Bettahar, and Jirka Simunek. Physical factors affecting the transport and fate of colloids in saturated porous media. *Water resources research*, 38(12): 63–1, 2002.

Scott A Bradford, Saeed Torkzaban, and Sharon L Walker. Coupling of physical and chemical mechanisms of colloid straining in saturated porous media. *Water research*, 41(13):3012–3024, 2007.

G. Brans, A. van Dinther, B. Odum, C. G. P. H. Schroën, and R. M. Boom. Transmission and fractionation of micro-sized particle suspensions. *Journal of Membrane Science*, 290(1): 230–240, March 2007a. ISSN 0376-7388. doi: 10.1016/j.memsci.2006.12.045. URL `https://www.sciencedirect.com/science/article/pii/S0376738807000063`.

GBPW Brans, A Van Dinther, B Odum, CGPH Schroën, and RM Boom. Transmission and fractionation of micro-sized particle suspensions. *Journal of membrane science*, 290(1-2): 230–240, 2007b.

Mark Anthony Browne, Phillip Crump, Stewart J Niven, Emma Teuten, Andrew Tonkin, Tamara Galloway, and Richard Thompson. Accumulation of microplastic on shorelines woldwide: sources and sinks. *Environmental science & technology*, 45(21):9175–9179, 2011.

Tom Bultreys, Stefanie Van Offenwert, Wannes Goethals, Matthieu N Boone, Jan Aelterman, and Veerle Cnudde. X-ray tomographic micro-particle velocimetry in porous media. *Physics of Fluids*, 34(4), 2022.

PC Carman. Permeability of saturated sands, soils and clays. *The Journal of Agricultural Science*, 29(2):262–273, 1939.

C. M. Cerda. Mobilization of kaolinite fines in porous media. *Colloids and Surfaces*, 27(4): 219–241, 1987.

G Chauveteau, L Nabzar, and JP Coste. Physics and modeling of permeability damage induced by particle deposition. In *SPE International Conference and Exhibition on Formation Damage Control*, pages SPE–39463. SPE, 1998.

Yanbo Chen, Hao Liu, Yufeng Gao, Xiaowei Ye, Haowen Guo, Yunqi Gao, and Yandong Lv. Visualization of the microscopic mechanism of slurry infiltration and filter cake formation for slurry shield tunneling in saturated sand: A microfluidic chip experiment. *Transportation Geotechnics*, 51:101529, 2025.

Yizheng Chen, Jasmine C Sabio, and Ryan L Hartman. When solids stop flow chemistry in commercial tubing. *Journal of Flow Chemistry*, 5:166–171, 2015.

Yinuo Cheng, Xiongying Ye, Zengshuai Ma, Shuai Xie, and Wenhui Wang. High-throughput and clogging-free microfluidic filtration platform for on-chip cell separation from undiluted whole blood. *Biomicrofluidics*, 10(1), 2016.

Constantinos V Chrysikopoulos, Christina C Plega, and Vasileios E Katzourakis. Non-invasive in situ concentration determination of fluorescent or color tracers and pollutants in a glass pore network model. *Journal of Hazardous materials*, 198:299–306, 2011.

Faruk Civan. *Reservoir formation damage: fundamentals, modeling, assessment, and mitigation*. Gulf Professional Publishing, 2023.

Robert M Cohen. *Methods for monitoring pump-and-treat performance*. Robert S. Kerr Environmental Research Laboratory, Office of Research and . . . , 1994.

Lianghan Cong, Shuaiyi Lu, Pan Jiang, Tianqi Zheng, Ziwang Yu, and Xiaoshu Lü. Research progress on co2 as geothermal working fluid: A review. *Energies*, 17(21):5415, 2024.

National Research Council et al. Contaminants in the subsurface: Source zone assessment and remediation. 2005.

Guodong Cui, Fulong Ning, Bin Dou, Tong Li, and Qiucheng Zhou. Particle migration and formation damage during geothermal exploitation from weakly consolidated sandstone reservoirs via water and co2 recycling. *Energy*, 240:122507, 2022.

Joao P Da Costa, Ana R Nunes, Patrícia SM Santos, Ana V Girao, Armando C Duarte, and Teresa Rocha-Santos. Degradation of polyethylene microplastics in seawater: Insights into the environmental degradation of polymers. *Journal of Environmental Science and Health, Part A*, 53(9):866–875, 2018.

Rémi Dangla, François Gallaire, and Charles N Baroud. Microchannel deformations due to solvent-induced pdms swelling. *Lab on a Chip*, 10(21):2972–2978, 2010.

Sujit S Datta, Harry Chiang, TS Ramakrishnan, and David A Weitz. Spatial fluctuations of fluid velocities in flow through a three-dimensional porous medium. *Physical review letters*, 111(6): 064501, 2013.

Matthieu Robert de Saint Vincent, Manouk Abkarian, and Hervé Tabuteau. Dynamics of colloid accumulation under flow over porous obstacles. *Soft matter*, 12(4):1041–1050, 2016.

Albert Hendrik De Zwart. Investigation of clogging processes in unconsolidated aquifers near water supply wells. *Ponaen & Looyen BV, Delft*, 2007.

C Degueldre, H-R Pfeiffer, W Alexander, B Wernli, and R Bruetsch. Colloid properties in granitic groundwater systems. i: Sampling and characterisation. *Applied Geochemistry*, 11(5):677–695, 1996.

Nolwenn Delouche, Andrew B Schofield, and Hervé Tabuteau. Dynamics of progressive pore clogging by colloidal aggregates. *Soft Matter*, 16(43):9899–9907, 2020.

Nolwenn Delouche, JM Van Doorn, TE Kodger, AB Schofield, J Sprakel, and Hervé Tabuteau. The contribution of colloidal aggregates to the clogging dynamics at the pore scale. *Journal of Membrane Science*, 635:119509, 2021.

Marco Dentz and Jesus Carrera. Mixing and spreading in stratified flow. *Physics of Fluids*, 19(1), January 2007. ISSN 1089-7666. doi: 10.1063/1.2427089.

Boris V Derjaguin. Acta physicochim. *USSR*, 14, 1941a.

Boris V Derjaguin. Theory of the stability of strongly charged lyophobic sol and of the adhesion of strongly charged particles in solutions of electrolytes. *Acta phys. chim. URSS*, 14:633, 1941b.

Benjamin Dersoir. *La physique du colmatage: de la particule colloïdale au bouchon*. PhD thesis, Rennes 1, 2015.

Benjamin Dersoir, Matthieu Robert de Saint Vincent, Manouk Abkarian, and Hervé Tabuteau. Clogging of a single pore by colloidal particles. *Microfluidics and Nanofluidics*, 19:953–961, 2015a.

Benjamin Dersoir, Matthieu Robert de Saint Vincent, Manouk Abkarian, and Hervé Tabuteau. Clogging of a single pore by colloidal particles. *Microfluidics and Nanofluidics*, 19(4):953–961, October 2015b. ISSN 1613-4990. doi: 10.1007/s10404-015-1624-y. URL https://doi.org/10.1007/s10404-015-1624-y.

Benjamin Dersoir, Andrew Bruce Schofield, and Hervé Tabuteau. Clogging transition induced by self filtration in a slit pore. *Soft matter*, 13(10):2054–2066, 2017.

Benjamin Dersoir, AB Schofield, M Robert de Saint Vincent, and Hervé Tabuteau. Dynamics of pore fouling by colloidal particles at the particle level. *Journal of Membrane Science*, 573: 411–424, 2019.

Mary H Dickson and Mario Fanelli. *Geothermal energy: utilization and technology*. Routledge, 2013.

Brian Dincau, Emilie Dressaire, and Alban Sauret. Pulsatile flow in microfluidic systems. *Small*, 16(9):1904032, 2020.

Brian Dincau, Connor Tang, Emilie Dressaire, and Alban Sauret. Clog mitigation in a microfluidic array via pulsatile flows. *Soft Matter*, 18(9):1767–1778, 2022.

Emilie Dressaire and Alban Sauret. Clogging of microfluidic systems. *Soft matter*, 13(1):37–48, 2017a.

Emilie Dressaire and Alban Sauret. Clogging of microfluidic systems. *Soft Matter*, 13 (1):37–48, 2017b. doi: 10.1039/C6SM01879C. URL https://pubs.rsc.org/en/content/articlelanding/2017/sm/c6sm01879c. Publisher: Royal Society of Chemistry.

Calum J Drummond and Derek YC Chan. van der waals interaction, surface free energies, and contact angles: dispersive polymers and liquids. *Langmuir*, 13(14):3890–3895, 1997.

Charles Duchêne, Vasco Filipe, Sylvain Huille, and Anke Lindner. Clogging of microfluidic constrictions by monoclonal antibody aggregates: Role of aggregate shape and deformability. *Soft matter*, 16(4):921–928, 2020.

David C Duffy, J Cooper McDonald, Olivier JA Schueller, and George M Whitesides. Rapid prototyping of microfluidic systems in poly (dimethylsiloxane). *Analytical chemistry*, 70(23): 4974–4984, 1998.

E. d'Ambrosio, D. Gilbert, F. Blanc, C. Cohen, and E. Lemaire. Rheology of suspensions of cubic particles. *Journal of Rheology*, 69(6):807–828, September 2025. ISSN 1520-8516. doi: 10.1122/8.0001045.

Noura Eddaoui and Cyprien Soulaine. Modeling chemotaxis–biofilm competition during napl biodegradation in porous media. *Journal of Contaminant Hydrology*, 279:104904, 2026. ISSN 0169-7722. doi: https://doi.org/10.1016/j.jconhyd.2026.104904. URL https://www.sciencedirect.com/science/article/pii/S0169772226000653.

Alexei A Efros and William T Freeman. Image quilting for texture synthesis and transfer. In *Seminal Graphics Papers: Pushing the Boundaries, Volume 2*, pages 571–576. 2023.

Tobias D Elmøe, Antonio Tricoli, Jan-Dierk Grunwaldt, and Sotiris E Pratsinis. Filtration of nanoparticles: evolution of cake structure and pressure-drop. *Journal of Aerosol Science*, 40 (11):965–981, 2009.

Anne-Sophie Esneu, Pervez Ahmed, Guillaume Pilla, Vincent Ricordeau, Michele Bardi, and Jalila Boujlel. Quantitative investigation of colloidal flow and clogging kinetics in porous medium using laser-induced fluorescence. *Transport in Porous Media*, 152(2):15, 2025a.

Anne-Sophie Esneu, Boujlel Younsi Jalila, Erriguible Arnaud, Glockner Stéphane, Marlière Claire, Nabzar Lahcen, and Marre Samuel. Transport and clogging of colloidal particles: Effects of the concentration and geometry of a porous medium. *Journal of Rock Mechanics and Geotechnical Engineering*, 2025b.

Alexis Espinosa-Gayosso, Marco Ghisalberti, Gregory N Ivey, and Nicole L Jones. Particle capture and low-reynolds-number flow around a circular cylinder. *Journal of Fluid mechanics*, 710: 362–378, 2012.

European Environment Agency. Overview of contaminants affecting soil and groundwater in europe, 2009. URL `https://www.eea.europa.eu/en/analysis/maps-and-charts/overview-of-contaminants-affecting-soil-and-groundwater-in-europe`. Maps and charts, last modified 11 September 2024.

I. Fatt. The network model of porous media. *Transactions of the AIME*, 207(SPE-574-G):144–181, January 1956. doi: 10.2118/574-G.

Lisa S Fendall and Mary A Sewell. Contributing to marine pollution by washing your face: microplastics in facial cleansers. *Marine pollution bulletin*, 58(8):1225–1228, 2009.

Qihong Feng, Shang Li, Xiaodong Han, and Sen Wang. Network simulation for formation impairment due to suspended particles in injected water. *Journal of Petroleum Science and Engineering*, 133:384–391, 2015. ISSN 0920-4105. doi: 10.1016/j.petrol.2015.06.027.

Paul Fleuchaus, Bas Godschalk, Ingrid Stober, and Philipp Blum. Worldwide application of aquifer thermal energy storage–a review. *Renewable and Sustainable Energy Reviews*, 94: 861–876, 2018.

Laurez Maya Fogouang, Laurent André, Philippe Leroy, and Cyprien Soulaine. Particulate transport in porous media at pore-scale. part 2: Cfd-dem and colloidal forces. *Journal of Computational Physics*, 519:113439, 2024.

Laurez Fogouang Maya, Laurent André, and Cyprien Soulaine. Numerical investigation and stochastic modeling of particle bridging undervarious flow, pore, and particle properties. *Advances in Water Resources*, 206(105158), 2025. doi: 10.1016/j.advwatres.2025.105158.

Stephen Foster, Ricardo Hirata, Daniel Gomes, Monica D'Elia, and Marta Paris. Groundwater quality protection: a guide for water utilities, municipal authorities, and environment agencies: Proteccion de la calidad del agua subterranea: guia para empresas de agua, autoridades municipales y agencias ambientales. 2003.

Jean-François Gaillard, Cheng Chen, Susa H Stonedahl, Boris LT Lau, Denis T Keane, and Aaron I Packman. Imaging of colloidal deposits in granular porous media by x-ray difference micro-tomography. *Geophysical Research Letters*, 34(18), 2007.

Jarand Gauteplass, Kuldeep Chaudhary, Anthony R Kovscek, and Martin A Fernø. Pore-level foam generation and flow for mobility control in fractured systems. *Colloids and Surfaces A: Physicochemical and Engineering Aspects*, 468:184–192, 2015.

Gaetan Gerber, M Bensouda, David A Weitz, and Philippe Coussot. Self-limited accumulation of colloids in porous media. *Physical review letters*, 123(15):158005, 2019.

Thomas Gervais, Jamil El-Ali, Axel Günther, and Klavs F Jensen. Flow-induced deformation of shallow microfluidic channels. *Lab on a Chip*, 6(4):500–507, 2006.

Arthur Joseph Goldman, Raymond G Cox, and Howard Brenner. Slow viscous motion of a sphere parallel to a plane wall—i motion through a quiescent fluid. *Chemical engineering science*, 22 (4):637–651, 1967.

Barry Goldstein, Gerardo Hiriart, Jeff Tester, Luis Gutierrez-Negrin, Ruggero Bertani, Christopher Bromley, Ernst Huenges, Arni Ragnarsson, Mike Mongillo, John W Lund, et al. Geothermal energy, nature, use, and expectations. In *Renewable Energy Systems*, pages 772–782. Springer, 2013.

Guillermo H. Goldsztein and Juan C. Santamarina. Suspension extraction through an opening before clogging. *Applied Physics Letters*, 85(19):4535–4537, November 2004a. ISSN 1077-3118. doi: 10.1063/1.1818342.

Guillermo H Goldsztein and Juan C Santamarina. Suspension extraction through an opening before clogging. *Applied physics letters*, 85(19):4535–4537, 2004b.

Yong-Kuan Gong, Kenichi Nakashima, and Renliang Xu. A novel method to determine effective charge of polystyrene latex particles in aqueous dispersion. *Langmuir*, 17(9):2889–2892, 2001.

Renuga Gopal, Satinderpal Kaur, Zuwei Ma, Casey Chan, Seeram Ramakrishna, and Takeshi Matsuura. Electrospun nanofibrous filtration membrane. *Journal of Membrane Science*, 281 (1-2):581–586, 2006.

David C Grahame. The electrical double layer and the theory of electrocapillarity. *Chemical reviews*, 41(3):441–501, 1947.

Jay W Grate, Ryan T Kelly, Jonathan Suter, and Norm C Anheier. Silicon-on-glass pore network micromodels with oxygen-sensing fluorophore films for chemical imaging and defined spatial structure. *Lab on a Chip*, 12(22):4796–4801, 2012.

John Gregory. Approximate expressions for retarded van der waals interaction. *Journal of colloid and interface science*, 83(1):138–145, 1981.

John Gregory and A James Wishart. Deposition of latex particles on alumina fibers. *Colloids and Surfaces*, 1(3-4):313–334, 1980.

Naga Siva Kumar Gunda, Bijoyendra Bera, Nikolaos K Karadimitriou, Sushanta K Mitra, and S Majid Hassanizadeh. Reservoir-on-a-chip (roc): A new paradigm in reservoir engineering. *Lab on a Chip*, 11(22):3785–3792, 2011.

Yang Guo, Jincheng Lou, Jae Kyoung Cho, Nils Tilton, Jaehun Chun, Wooyong Um, Xiaolong Yin, Keith B Neeves, and Ning Wu. Transport of colloidal particles in microscopic porous medium analogues with surface charge heterogeneity: experiments and the fundamental role of single-bead deposition. *Environmental Science & Technology*, 54(21):13651–13660, 2020.

Yihui Guo, Ning Tang, Lan Lu, Na Li, Tingting Hu, Jiayin Guo, Jingyi Zhang, Zhuotong Zeng, and Jie Liang. Aggregation behavior of polystyrene nanoplastics: Role of surface functional groups and protein and electrolyte variation. *Chemosphere*, 350:140998, 2024.

Junhyuk Ha and Jun-Yeop Lee. Characterization of aquifer colloids and dissolved organic matters in kurt granitic groundwater system. *Nuclear Engineering and Technology*, 57(4):103322, 2025.

Ahmed Hafez, Qi Liu, Thomas Finkbeiner, Raed A Alouhali, Timothy E Moellendick, and J Carlos Santamarina. The effect of particle shape on discharge and clogging. *Scientific reports*, 11(1):3309, 2021.

Brian S Hardy, Kawika Uechi, Janet Zhen, and H Pirouz Kavehpour. The deformation of flexible pdms microchannels under a pressure driven flow. *Lab on a Chip*, 9(7):935–938, 2009.

Haiyang He, Xiaofeng Xiong, Ting Wu, Ran Hu, Yi-Feng Chen, and Zhibing Yang. Pore-scale study of particle transport and clogging mechanisms in a porous micromodel. *Separation and Purification Technology*, page 131929, 2025.

RTWDW Hogg, To Wo Healy, and Douglas W Fuerstenau. Mutual coagulation of colloidal dispersions. *Transactions of the Faraday society*, 62:1638–1651, 1966.

Johannes Hommel, Edward Coltman, and Holger Class. Porosity–permeability relations for evolving pore space: a review with a focus on (bio-) geochemically altered porous media. *Transport in Porous Media*, 124(2):589–629, 2018.

John Hoslett, Theoni Maria Massara, Simos Malamis, Darem Ahmad, Inge Van Den Boogaert, Evina Katsou, Balsam Ahmad, Heba Ghazal, Stefaan Simons, Luiz Wrobel, et al. Surface water filtration using granular media and membranes: A review. *Science of the Total Environment*, 639:1268–1282, 2018.

Chiao-Peng Hsu, Hasan Emre Baysal, Görel Wirenborn, Gustaf Mårtensson, Lisa Prahl Wittberg, and Lucio Isa. Roughness-dependent clogging of particle suspensions flowing into a constriction. *Soft Matter*, 17(31):7252–7259, 2021.

Selina Hube, Majid Eskafi, Kolbrún Fríða Hrafnkelsdóttir, Björg Bjarnadóttir, Margrét Ásta Bjarnadóttir, Snærós Axelsdóttir, and Bing Wu. Direct membrane filtration for wastewater treatment and resource recovery: A review. *Science of the total environment*, 710:136375, 2020.

F Hussain, A Zeinijahromi, P Bedrikovetsky, A Badalyan, T Carageorgos, and YJJOPS Cinar. An experimental study of improved oil recovery through fines-assisted waterflooding. *Journal of Petroleum Science and Engineering*, 109:187–197, 2013.

International Renewable Energy Agency. Renewable capacity highlights 2025, 2025. URL `https://www.irena.org/-/media/Files/IRENA/Agency/Publication/2025/Mar/IRENA_DAT_RE_Capacity_Highlights_2025.pdf`. Accessed: 2026-03-06.

Jacob N Israelachvili. *Intermolecular and surface forces*. Academic press, 2011.

Tomihisa Iwasaki, JJ Slade, and Wm E Stanley. Some notes on sand filtration [with discussion]. *Journal (American Water Works Association)*, 29(10):1591–1602, 1937.

Robert B Jackson. The integrity of oil and gas wells. *Proceedings of the National Academy of Sciences*, 111(30):10902–10903, 2014.

A. Janda, I. Zuriguel, A. Garcimartín, L. A. Pugnaloni, and D. Maza. Jamming and critical outlet size in the discharge of a two-dimensional silo. *EPL (Europhysics Letters)*, 84(4):44002, November 2008. ISSN 1286-4854. doi: 10.1209/0295-5075/84/44002.

Hoon Young Jeong, Seong-Chun Jun, Jeong-Yong Cheon, and Minji Park. A review on clogging mechanisms and managements in aquifer storage and recovery (asr) applications. *Geosciences Journal*, 22(4):667–679, 2018.

Kenneth Langstreth Johnson, Kevin Kendall, and AAD Roberts. Surface energy and the contact of elastic solids. *Proceedings of the royal society of London. A. mathematical and physical sciences*, 324(1558):301–313, 1971.

Philip R Johnson and Menachem Elimelech. Dynamics of colloid deposition in porous media: Blocking based on random sequential adsorption. *langmuir*, 11(3):801–812, 1995.

Philip R Johnson, Ning Sun, and Menachem Elimelech. Colloid transport in geochemically heterogeneous porous media: Modeling and measurements. *Environmental science & technology*, 30(11):3284–3293, 1996.

Ieva Kaminskaite, Sandra Piazolo, Andy R Emery, Nicholas Shaw, and Quentin J Fisher. The importance of physiochemical processes in decarbonisation technology applications utilizing the subsurface: a review. *Earth Science, Systems and Society*, 2(1):10043, 2022.

Guido Kampel, Guillermo H Goldsztein, and Juan C Santamarina. Particle transport in porous media: the role of inertial effects and path tortuosity in the velocity of the particles. *Applied Physics Letters*, 95(19), 2009.

Sushil Raj Kanel, Jean-Mark Greneche, and Heechul Choi. Arsenic (v) removal from groundwater using nano scale zero-valent iron as a colloidal reactive barrier material. *Environmental science & technology*, 40(6):2045–2050, 2006.

NK Karadimitriou, Michiel Musterd, PJ Kleingeld, MT Kreutzer, SM Hassanizadeh, and V Joekar-Niasar. On the fabrication of pdms micromodels by rapid prototyping, and their use in two-phase flow studies. *Water Resources Research*, 49(4):2056–2067, 2013.

Hasan J. Khan, Maryam S. Mirabolghasemi, Hongtao Yang, Maša Prodanović, David A. DiCarlo, and Matthew T. Balhoff. Study of formation damage caused by retention of bi-dispersed particles using combined pore-scale simulations and particle flooding experiments. *Journal of Petroleum Science and Engineering*, 158:293–308, 2017. doi: 10.1016/j.petrol.2017.08.061.

K. C. Khilar and H. S. Fogler. The existence of a critical salt concentration for particle release. *Journal of Colloid and Interface Science*, 101(1):214–224, September 1984. doi: 10.1016/0021-9797(84)90021-3. URL `https://ui.adsabs.harvard.edu/abs/1984JCIS..101..214K`.

Kartic C Khilar and H Scott Fogler. Water sensitivity of sandstones. *Society of Petroleum Engineers Journal*, 23(01):55–64, 1983.

Kartic C. Khilar, R. N. Vaidya, and H. S. Fogler. Colloidally-induced fines release in porous media. *Journal of Petroleum Science and Engineering*, 4(3):213–221, January 1990. doi: 10.1016/0920-4105(90)90011-Q. URL `https://ui.adsabs.harvard.edu/abs/1990JPSE....4..213K`.

Dae Yeon Kim, Seon Yeop Jung, Young Jin Lee, and Kyung Hyun Ahn. Effect of colloidal interactions and hydrodynamic stress on particle deposition in a single micropore. *Langmuir*, 38(19):6013–6022, 2022.

Chun-Han Ko and Menachem Elimelech. The "shadow effect" in colloid transport and deposition dynamics in granular porous media: measurements and mechanisms. *Environmental science & technology*, 34(17):3681–3689, 2000.

Josef Kozeny. Ueber kapillare leitung des wassers im boden. *Sitzungsberichte der Akademie der Wissenschaften in Wien*, 136:271, 1927.

Rakesh Kumar and Prabhakar Sharma. Microplastics pollution pathways to groundwater in india. *Curr. Sci*, 120:249, 2021.

Yasuyuki Kusaka, Jérôme FL Duval, and Yasuhisa Adachi. Morphology and breaking of latex particle deposits at a cylindrical collector in a microfluidic chamber. *Environmental science & technology*, 44(24):9413–9418, 2010.

Zachary A Kuznar and Menachem Elimelech. Direct microscopic observation of particle deposition in porous media: Role of the secondary energy minimum. *Colloids and Surfaces A: Physicochemical and Engineering Aspects*, 294(1-3):156–162, 2007a.

Zachary A. Kuznar and Menachem Elimelech. Direct microscopic observation of particle deposition in porous media: Role of the secondary energy minimum. *Colloids and Surfaces A: Physicochemical and Engineering Aspects*, 294(1):156–162, February 2007b. ISSN 0927-7757. doi: 10.1016/j.colsurfa.2006.08.007. URL `https://www.sciencedirect.com/science/article/pii/S0927775706006194`.

Anthony J. C. Ladd. Numerical simulations of particulate suspensions via a discretized boltzmann equation. i: Theoretical foundation. ii: Numerical results. *Journal of Fluid Mechanics*, 271: 285–339, 1994. ISSN 0022-1120; 1469-7645/e.

DJ Lapworth, Nicole Baran, ME Stuart, K Manamsa, and J Talbot. Persistent and emerging micro-organic contaminants in chalk groundwater of england and france. *Environmental Pollution*, 203:214–225, 2015.

Jessamine Ng Lee, Cheolmin Park, and George M Whitesides. Solvent compatibility of poly (dimethylsiloxane)-based microfluidic devices. *Analytical chemistry*, 75(23):6544–6554, 2003.

Yonghun Lee, Dong-Min Kim, Zhenglin Li, Dong-Eun Kim, and Sung-Jin Kim. Pulsatile plasma filtration and cell-free dna amplification using a water-head-driven point-of-care testing chip. *Lab on a Chip*, 18(6):915–922, 2018.

Philippe Leroy and Alexis Maineult. Exploring the electrical potential inside cylinders beyond the debye–hückel approximation: a computer code to solve the poisson–boltzmann equation for multivalent electrolytes. *Geophysical Journal International*, 214(1):58–69, 2018.

Haoting Li, Shuyan Wang, Xi Chen, Lei Xie, Baoli Shao, and Yimei Ma. Cfd-dem simulation of aggregation and growth behaviors of fluid-flow-driven migrating particle in porous media. 231: 212343, 2023. ISSN 2949-8910. doi: 10.1016/j.geoen.2023.212343.

Peiyue Li, Hui Qian, Jianhua Wu, Jie Chen, Yiqian Zhang, and Hongbo Zhang. Occurrence and hydrogeochemistry of fluoride in alluvial aquifer of weihe river, china. *Environmental earth sciences*, 71:3133–3145, 2014.

Peiyue Li, D Karunanidhi, T Subramani, and K Srinivasamoorthy. Sources and consequences of groundwater contamination. *Archives of environmental contamination and toxicology*, 80:1–10, 2021a.

Shidong Li, Mindaugas Genys, Kun Wang, and Ole Torsæter. Experimental study of wettability alteration during nanofluid enhanced oil recovery process and its effect on oil recovery. In *SPE Reservoir Characterisation and Simulation Conference and Exhibition*. OnePetro, 2015.

Xiqing Li, Pengfei Zhang, CL Lin, and William P Johnson. Role of hydrodynamic drag on microsphere deposition and re-entrainment in porous media under unfavorable conditions. *Environmental science & technology*, 39(11):4012–4020, 2005.

Yusong Li, Yonggang Wang, Kurt D Pennell, and Linda M Abriola. Investigation of the transport and deposition of fullerene (c60) nanoparticles in quartz sands under varying flow conditions. *Environmental science & technology*, 42(19):7174–7180, 2008.

Zihao Li, Hongtao Yang, Zhuang Sun, D. Nicolas Espinoza, and Matthew T. Balhoff. A probability-based pore network model of particle jamming in porous media. *Transport in Porous Media*, 139:419–445, 2021b. ISSN 0169-3913. doi: 10.1007/s11242-021-01673-4.

Dantong Lin, Liming Hu, Scott Alan Bradford, Xinghao Zhang, and Irene M. C. Lo. Pore-network modeling of colloid transport and retention considering surface deposition, hydrodynamic bridging, and straining. *Journal of Hydrology*, 603:127020, December 2021. doi: 10.1016/j.jhydrol.2021.127020. URL `https://ui.adsabs.harvard.edu/abs/2021JHyd..60327020L`.

Dantong Lin, Minpeng TANG, Xinghao ZHANG, Scott Alan BRADFORD, and Liming Hu. Exploring coupled effects of attachment, blocking, straining, and clogging in a pore network model. *SSRN*, (4896182), 2024. doi: 10.2139/ssrn.4896182.

Gary M Litton and Terese M Olson. Particle size effects on colloid deposition kinetics: evidence of secondary minimum deposition. *Colloids and Surfaces A: Physicochemical and Engineering Aspects*, 107:273–283, 1996.

Qi Liu, Budi Zhao, and J Carlos Santamarina. Particle migration and clogging in porous media: a convergent flow microfluidics study. *Journal of Geophysical Research: Solid Earth*, 124(9): 9495–9504, 2019.

Xueling Liu, Xin Jiang, Jinsong Liu, Jun Li, and Wanyi Li. The effect of the injection salinity and clay composition on aquifer permeability. *Applied Thermal Engineering*, 118:551–560, 2017.

Laurent Lobry, Elisabeth Lemaire, Frédéric Blanc, Stany Gallier, and François Peters. Shear thinning in non-brownian suspensions explained by variable friction between particles. *Journal of Fluid Mechanics*, 860:682–710, December 2018. ISSN 1469-7645. doi: 10.1017/jfm.2018.881.

J Lohaus, F Stockmeier, P Surray, J Lölsberg, and M Wessling. What are the microscopic events during membrane backwashing? *Journal of Membrane Science*, 602:117886, 2020.

Douglas M Mackay, Paul V Roberts, and John A Cherry. Transport of organic contaminants in groundwater. *Environmental science & technology*, 19(5):384–392, 1985.

Olukayode T Majekodunmi and Sara M Hashmi. Flow dynamics through discontinuous clogs of rigid particles in tapered microchannels. *Scientific Reports*, 12(1):22587, 2022.

Andreas Manz, D Jed Harrison, Elisabeth MJ Verpoorte, James C Fettinger, Aran Paulus, Hans Lüdi, and H Michael Widmer. Planar chips technology for miniaturization and integration of separation techniques into monitoring systems: capillary electrophoresis on a chip. *Journal of Chromatography A*, 593(1-2):253–258, 1992.

Adele Manzella, Agnes Allansdottir, and Anna Pellizzone. *Geothermal energy and society*. Springer, 2019.

Alvaro Marin, Henri Lhuissier, Massimiliano Rossi, and Christian J Kähler. Clogging in constricted suspension flows. *Physical Review E*, 97(2):021102, 2018.

Re Martin. Clogging issues associated with managed aquifer recharge methods. *IAH Commission on managing aquifer recharge, Australia*, pages 26–33, 2013.

Laurez Maya Fogouang, Laurent André, and Cyprien Soulaine. Particulate transport in porous media at pore-scale. part 1: Unresolved-resolved four-way coupling cfd-dem. *Journal of Computational Physics*, 521:113540, 2025.

David C Mays and James R Hunt. Hydrodynamic aspects of particle clogging in porous media. *Environmental science & technology*, 39(2):577–584, 2005.

Sarah M McFaul, Bill K Lin, and Hongshen Ma. Cell separation based on size and deformability using microfluidic funnel ratchets. *Lab on a chip*, 12(13):2369–2376, 2012.

Daene C McKinney and Min-Der Lin. Pump-and-treat ground-water remediation system optimization. *Journal of Water Resources Planning and Management*, 122(2):128–136, 1996.

Alan D McNaught, Andrew Wilkinson, et al. *Compendium of chemical terminology*, volume 1669. Blackwell Science Oxford, 1997.

Sharon B Megdal. Invisible water: the importance of good groundwater governance and management. *NPJ Clean Water*, 1(1):15, 2018.

Yashar Mehmani and Matthew T. Balhoff. Eulerian network modeling of longitudinal dispersion. *Water Resources Research*, 51(10):8586–8606, October 2015. doi: 10.1002/2015WR017543. URL `https://ui.adsabs.harvard.edu/abs/2015WRR....51.8586M`.

Yashar Mehmani and Hamdi A. Tchelepi. Minimum requirements for predictive pore-network modeling of solute transport in micromodels. *Advances in Water Resources*, 108:83–98, October 2017. doi: 10.1016/j.advwatres.2017.07.014. URL `https://ui.adsabs.harvard.edu/abs/2017AdWR..108...83M`.

Lucas Mejia, Peixi Zhu, Jeffrey D Hyman, Kishore K Mohanty, and Matthew T Balhoff. Coreflood on a chip: Core-scale micromodels for subsurface applications. *Fuel*, 281:118716, 2020.

Xiaoyan Meng and Daoyong Yang. Pore-network modeling of particle dispersion in porous media. *Colloids and Surfaces A*, 580:123768, 2019. ISSN 0927-7757. doi: 10.1016/j.colsurfa.2019.123768.

Zyed Mesticou, Mariem Kacem, and Philippe Dubujet. Coupling effects of flow velocity and ionic strength on the clogging of a saturated porous medium. *Transport in Porous Media*, 112(1): 265–282, 2016.

Hamid Emami Meybodi, Riyaz Kharrat, and Majid Nasehi Araghi. Experimental studying of pore morphology and wettability effects on microscopic and macroscopic displacement efficiency of polymer flooding. *Journal of Petroleum Science and Engineering*, 78(2):347–363, 2011.

Maryam Mirabolghasemi, Maša Prodanović, David A. DiCarlo, and Hongyu Ji. Prediction of empirical properties using direct pore-scale simulation of straining through 3d microtomography images of porous media. *Journal of Hydrology*, 529:768–778, 2015. doi: 10.1016/j.jhydrol.2015.08.016.

S Mohammadi, A Maghzi, MH Ghazanfari, M Masihi, A Mohebbi, and R Kharrat. On the control of glass micro-model characteristics developed by laser technology. *Energy sources, Part A: recovery, utilization, and environmental effects*, 35(3):193–201, 2013.

Somnath Mondal, Chu-Hsiang Wu, and Mukul M. Sharma. Coupled cfd-dem simulation of hydrodynamic bridging at constrictions. *International Journal of Multiphase Flow*, 84:245–263, September 2016. doi: 10.1016/j.ijmultiphaseflow.2016.05.001. URL `https://ui.adsabs.harvard.edu/abs/2016IJMF...84..245M`.

Brian L Morris, Adrian RL Lawrence, PJC Chilton, Brian Adams, Roger C Calow, and Ben A Klinck. Groundwater and its susceptibility to degradation: a global assessment of the problem and options for management. 2003.

Thomas W Muecke. Formation fines and factors controlling their movement in porous media. *Journal of petroleum technology*, 31(02):144–150, 1979.

Rizwan Muneer, M Rehan Hashmet, and Peyman Pourafshary. Fine migration control in sandstones: surface force analysis and application of dlvo theory. *ACS omega*, 5(49):31624–31639, 2020.

Necmettin Mungan. Permeability reduction through changes in ph and salinity. *Journal of Petroleum Technology*, 17(12):1449–1453, 1965.

B Mustin and B Stoeber. Single layer deposition of polystyrene particles onto planar polydimethylsiloxane substrates. *Langmuir*, 32(1):88–101, 2016.

Walid Okaybi, Sophie Roman, and Cyprien Soulaine. Progressive colloidal clogging mechanism by dendritic build-up in porous media. *Soft Matter*, 2025.

Walid Okaybi, Sophie Roman, Laurez Maya, Emmanuel Le Trong, and Cyprien Soulaine. Hydrodynamic pore-bridging and permeability impairement in heterogeneous porous media: microfluidic data-set, 2026a. URL `https://doi.org/10.17612/D1FV-1Z91`. Dataset.

Walid Okaybi, Sophie Roman, and Cyprien Soulaine. From clogging mitigation to clogging acceleration: Particle deposition under oscillatory flow in microfluidic porous media: W. okaybi et al. *Transport in Porous Media*, 153(5):66, 2026b.

Isam I Omran, N Al-Saati, K Hashim, Z Al-Saati, P Kot, RM Al Khaddar, Dhiya Al-Jumeily, Andy Shaw, Felicite Ruddock, and M Aljefery. Assessment of heavy metal pollution in the great al-mussaib irrigation channel. *Desalination and Water Treatment*, 2019.

ME O'neill. A sphere in contact with a plane wall in a slow linear shear flow. *Chemical Engineering Science*, 23(11):1293–1298, 1968.

Edgar Ortega-Roano, Mathieu Souzy, Thomas Weinhart, Devaraj van der Meer, and Alvaro Marin. Clogging of noncohesive suspensions through constrictions using an efficient discrete particle solver with unresolved fluid flow. *PHYSICAL REVIEW E*, 108(064905), 2023. ISSN 2470-0045. doi: 10.1103/physreve.108.064905.

Kofi Osei-Bonsu, Paul Grassia, and Nima Shokri. Investigation of foam flow in a 3d printed porous medium in the presence of oil. *Journal of colloid and interface science*, 490:850–858, 2017.

H Ott, SM Roels, and K De Kloe. Salt precipitation due to supercritical gas injection: I. capillary-driven flow in unimodal sandstone. *International Journal of Greenhouse Gas Control*, 43:247–255, 2015.

Holger Ott, Kees de Kloe, M Van Bakel, F Vos, A Van Pelt, P Legerstee, A Bauer, K Eide, A Van Der Linden, S Berg, et al. Core-flood experiment for transport of reactive fluids in rocks. *Review of Scientific Instruments*, 83(8), 2012.

Daniel S Park, Saade Bou-Mikael, Sean King, Karsten E Thompson, Clinton S Willson, and Dimitris E Nikitopoulos. Design and fabrication of rock-based micromodel. In *ASME International Mechanical Engineering Congress and Exposition*, volume 45257, pages 709–715. American Society of Mechanical Engineers, 2012.

Amin Parvan, Saeed Jafari, Mohammad Rahnama, Saeid Norouzi apourvari, and Amir Raoof. Insight into particle retention and clogging in porous media; a pore scale study using lattice boltzmann method. *Advances in Water Resources*, 138:103530, 2020. doi: 10.1016/j.advwatres.2020.103530.

JAYA KRISHNA PATNAIK, BHABANI SANKAR DAS, SAROJ KANTI MISHRA, SANJIB MOHANTY, SANJAY KUMAR SATPATHY, and DAMODAR MOHANTY. Vascular clogging, mononuclear cell margination, and enhanced vascular permeability in the pathogenesis of human cerebral malaria. *The American journal of tropical medicine and hygiene*, 51(5):642–647, 1994.

Andrew J Pelley and Nathalie Tufenkji. Effect of particle size and natural organic matter on the migration of nano-and microscale latex particles in saturated porous media. *Journal of colloid and interface science*, 321(1):74–83, 2008.

Tanapon Phenrat, Hye-Jin Kim, Fritjof Fagerlund, Tissa Illangasekare, Robert D Tilton, and Gregory V Lowry. Particle size distribution, concentration, and magnetic attraction affect transport of polymer-modified fe0 nanoparticles in sand columns. *Environmental science & technology*, 43(13):5079–5085, 2009.

Marzena Połeć, Urszula Aleksander-Kwaterczak, Katarzyna Wątor, and Ewa Kmiecik. The occurrence of microplastics in freshwater systems–preliminary results from krakow (poland). *Geology, Geophysics and Environment*, 44(4):391–400, 2018.

Stephan Preibisch, Stephan Saalfeld, and Pavel Tomancak. Globally optimal stitching of tiled 3d microscopic image acquisitions. *Bioinformatics*, 25(11):1463–1465, 2009.

Venkatachalam Ramachandran and H Scott Fogler. Multilayer deposition of stable colloidal particles during flow within cylindrical pores. *Langmuir*, 14(16):4435–4444, 1998.

Venkatachalam Ramachandran and H Scott Fogler. Plugging by hydrodynamic bridging during flow of stable colloidal particles within cylindrical pores. *Journal of Fluid Mechanics*, 385: 129–156, 1999.

A. Raoof, H. M. Nick, S. M. Hassanizadeh, and C. J. Spiers. Poreflow: A complex pore-network model for simulation of reactive transport in variably saturated porous media. *Computers and Geosciences*, 61:160–174, December 2013. doi: 10.1016/j.cageo.2013.08.005. URL `https://ui.adsabs.harvard.edu/abs/2013CG.....61..160R`.

Amir Raoof, S. Majid Hassanizadeh, and Anton Leijnse. Upscaling transport of adsorbing solutes in porous media: Pore-network modeling. *Vadose Zone Journal*, 9(3):624–636, August 2010. doi: 10.2136/vzj2010.0026. URL `https://ui.adsabs.harvard.edu/abs/2010VZJ.....9..624R`.

Viviana Re. Shedding light on the invisible: addressing the potential for groundwater contamination by plastic microfibers. *Hydrogeology Journal*, 27(7):2719–2727, 2019.

S. D. Rege and H. S. Fogler. Network model for straining dominated particle entrapment in porous media. *Chemical Engineering Science*, 42(7):1553–1564, January 1987. doi: 10.1016/0009-2509(87)80160-4. URL `https://ui.adsabs.harvard.edu/abs/1987ChEnS..42.1553R`.

S. D. Rege and H. S. Fogler. A network model for deep bed filtration of solid particles and emulsion drops. *AIChE Journal*, 34:1761–1772, 1988. ISSN 0001-1541. doi: 10.1002/aic.690341102.

Sunil D. Rege and H. Scott Fogler. Development of radial models for formation damage in porous media. *Chemical Engineering Communications*, 108:67–83, 1991. ISSN 0098-6445. doi: 10.1080/00986449108910951.

Matthias C Rillig. Microplastic in terrestrial ecosystems and the soil?, 2012.

S. Roman, F. Rembert, A.R. Kovscek, and J. Poonoosamy. Microfluidics for geosciences: metrological developments and future challenges. *Lab on a Chip*, in press, 2025.

Sophie Roman, Cyprien Soulaine, Moataz Abu AlSaud, Anthony Kovscek, and Hamdi Tchelepi. Particle velocimetry analysis of immiscible two-phase flow in micromodels. *Advances in Water Resources*, 95:199–211, 2016.

Esther Rosenbrand, Claus Kjøller, Jacob Fabricius Riis, Frans Kets, and Ida Lykke Fabricius. Different effects of temperature and salinity on permeability reduction by fines migration in berea sandstone. *Geothermics*, 53:225–235, 2015.

Abbas Roustaei and Hadi Bagherzadeh. Experimental investigation of sio 2 nanoparticles on enhanced oil recovery of carbonate reservoirs. *Journal of Petroleum Exploration and Production Technology*, 5:27–33, 2015.

Joseph N Ryan and Menachem Elimelech. Colloid mobilization and transport in groundwater. *Colloids and surfaces A: Physicochemical and engineering aspects*, 107:1–56, 1996.

Niels Ryde, Nikola Kallay, and Egon Matijević. Particle adhesion in model systems. part 14.—experimental evaluation of multilayer deposition. *Journal of the Chemical Society, Faraday Transactions*, 87(9):1377–1381, 1991.

Samuel Peter Ryecroft, Andy Shaw, Paul Fergus, Patryk Kot, Khalid Hashim, Laura Conway, and Adam Moody. A novel gesomin detection method based on microwave spectroscopy. In *2019 12th International Conference on Developments in eSystems Engineering (DeSE)*, pages 429–433. IEEE, 2019.

Behnam Sadri, David Pernitsky, and Mohtada Sadrzadeh. Aggregation and deposition of colloidal particles: Effect of surface properties of collector beads. *Colloids and Surfaces A: Physicochemical and Engineering Aspects*, 530:46–52, 2017.

Adel M Salem Ragab and Ahmed E Hannora. A comparative investigation of nano particle effects for improved oil recovery–experimental work. In *SPE Kuwait oil and gas show and conference*. OnePetro, 2015.

Mandana Samari-Kermani, Saeed Jafari, Mohammad Rahnama, and Amir Raoof. Direct pore scale numerical simulation of colloid transport and retention. part i: Fluid flow velocity, colloid size, and pore structure effects. *Advances in Water Resources*, 144:103694, October 2020. doi: 10.1016/j.advwatres.2020.103694. URL `https://ui.adsabs.harvard.edu/abs/2020AdWR..14403694S`.

Mandana Samari-Kermani, Saeed Jafari, Mohammad Rahnama, and Amir Raoof. Ionic strength and zeta potential effects on colloid transport and retention processes. *Colloid and Interface Science Communications*, 42:100389, 2021. ISSN 2215-0382. doi: 10.1016/j.colcom.2021.100389.

Wenjing Sang, Veronica L Morales, Wei Zhang, Cathelijne R Stoof, Bin Gao, Anna Lottie Schatz, Yalei Zhang, and Tammo S Steenhuis. Quantification of colloid retention and release by straining and energy minima in variably saturated porous media. *Environmental science & technology*, 47(15):8256–8264, 2013.

K Prasad Saripalli, Steven L Bryant, and Mukul M Sharma. Role of fracture face and formation plugging in injection well fracturing and injectivity decline. In *SPE Health, Safety, Security, Environment, & Social Responsibility Conference-North America*, pages SPE–52731. SPE, 1999.

Alban Sauret, Erin C Barney, Adeline Perro, Emmanuel Villermaux, Howard A Stone, and Emilie Dressaire. Clogging by sieving in microchannels: Application to the detection of contaminants in colloidal suspensions. *Applied Physics Letters*, 105(7), 2014.

Alban Sauret, Katarzyna Somszor, Emmanuel Villermaux, and Emilie Dressaire. Growth of clogs in parallel microchannels. *Physical Review Fluids*, 3(10):104301, 2018.

JH Schenkel and JA Kitchener. A test of the derjaguin-verwey-overbeek theory with a colloidal suspension. *Transactions of the Faraday Society*, 56:161–173, 1960.

Joanna Schneider, Rodney D Priestley, and Sujit S Datta. Using colloidal deposition to mobilize immiscible fluids from porous media. *Physical Review Fluids*, 6(1):014001, 2021.

S Schreiber, A Lapanje, P Ramsak, and G Breembroek. Operational issues in geothermal energy in europe: status and overview. *Reykjavik (Iceland): Geothermal ERA NET*, 2016.

Jana Schwarze, Michael Grunze, Markus Karahka, and HJ Kreuzer. Attachment and detachment of particles from a surface under shear flow. *The Journal of Physical Chemistry C*, 123(13): 8153–8159, 2019.

N. Seetha, Amir Raoof, M. S. Mohan Kumar, and S. Majid Hassanizadeh. Upscaling of nanoparticle transport in porous media under unfavorable conditions: Pore scale to darcy scale. *Journal of Contaminant Hydrology*, 200:1–14, 2017. ISSN 0169-7722. doi: 10.1016/j.jconhyd.2017.03.002.

Zenamarkos B Sendekie and Patrice Bacchin. Colloidal jamming dynamics in microchannel bottlenecks. *Langmuir*, 32(6):1478–1488, 2016.

Mukul M Sharma, Habib Chamoun, DSH Sita Rama Sarma, and Robert S Schechter. Factors controlling the hydrodynamic detachment of particles from surfaces. *Journal of colloid and interface science*, 149(1):121–134, 1992.

KV Sharp and RJ Adrian. On flow-blocking particle structures in microtubes. *Microfluidics and Nanofluidics*, 1(4):376–380, 2005.

A. G. Siqueira, E. J. Bonet, and F. S. Shecaira. A 3d network model of rock permeability impairment due to suspended particles in injection water. volume SPE European Formation Damage Conference of *SPE European Formation Damage Conference and Exhibition*, pages SPE–82232–MS, 05 2003. doi: 10.2118/82232-MS. URL `https://doi.org/10.2118/82232-MS`.

Wei Song, Xiaoxiu Liu, Tuanfeng Zheng, and Jiaming Yang. A review of recharge and clogging in sandstone aquifer. *Geothermics*, 87:101857, September 2020. ISSN 03756505. doi: 10.1016/j.geothermics.2020.101857. URL `https://linkinghub.elsevier.com/retrieve/pii/S0375650519300677`.

Alireza Soudmand-asli, S Shahab Ayatollahi, Hassan Mohabatkar, Maryam Zareie, and S Farzad Shariatpanahi. The in situ microbial enhanced oil recovery in fractured porous media. *Journal of Petroleum Science and Engineering*, 58(1-2):161–172, 2007.

Cyprien Soulaine and Hamdi A Tchelepi. Micro-continuum approach for pore-scale simulation of subsurface processes. *Transport in porous media*, 113:431–456, 2016.

Cyprien Soulaine, Julien Maes, and Sophie Roman. Computational microfluidics for geosciences. *Frontiers in Water*, 3:643714, 2021a.

Cyprien Soulaine, Saideep Pavuluri, Francis Claret, and Christophe Tournassat. porousmedia4foam: Multi-scale open-source platform for hydro-geochemical simulations with openfoam®. *Environmental Modelling & Software*, 145:105199, 2021b.

Cyprien Soulaine, Walid Okaybi, Laurez Fogouang Maya, Emmanuel Le Trong, and Sophie Roman. Permeability impairment by hydrodynamic pore bridging: Probabilistic pore-network modeling and microfluidic experiments. *International Journal of Rock Mechanics and Mining Sciences*, 200:106423, 2026.

Youness Soumane. *Etude microfluidique du colmatage d'un milieu poreux modèle par un écoulement de suspension.* PhD thesis, Université Grenoble Alpes [2020-....], 2021.

Mathieu Souzy, Iker Zuriguel, and Alvaro Marin. Transition from clogging to continuous flow in constricted particle suspensions. *Physical Review E*, 101(6):060901, June 2020. ISSN 2470-0053. doi: 10.1103/physreve.101.060901.

W Stumm. Surface chemical theory as an aid to predict the distribution and the fate of trace constituents and pollutants in the aquatic environment. *Water Science and Technology*, 14 (1-2):481–491, 1982.

Dan Sun. Hydrodynamics and effect of velocity on particle filtration due to bridging in water-saturated porous media using cfd–dem simulation. *Environmental Science and Pollution Research*, 30:100124–100136, 2023. ISSN 1614-7499. doi: 10.1007/s11356-023-29398-5.

Fatemeh Tale, Azim Kalantariasl, and Mohammad Reza Malayeri. Estimating transition time from deep filtration of particles to external cake during produced water re-injection and disposal. *Particulate Science and Technology*, 39(3):312–321, 2021.

Qianjing Tang and Amir Raoof. Exploring particle clogging mechanisms through deterministic pore network modeling. *SSRN*, (5047338), 2024. doi: 10.2139/ssrn.5047338.

Taylor. Dispersion of soluble matter in solvent flowing slowly through a tube. *Proc. Roy. Soc. A.*, 219:186–203, 1953.

A. C. Todd, J. E. Somerville, and Graham Scott. The application of depth of formation damage measurements in predicting water injectivity decline. volume SPE Formation Damage Control Symposium of *SPE International Conference and Exhibition on Formation Damage Control*, pages SPE–12498–MS, 02 1984. doi: 10.2118/12498-MS. URL `https://doi.org/10.2118/12498-MS`.

Saeed Torkzaban, Scott A Bradford, and Sharon L Walker. Resolving the coupled effects of hydrodynamics and dlvo forces on colloid attachment in porous media. *Langmuir*, 23(19): 9652–9660, 2007.

Saeed Torkzaban, Scott A Bradford, Martinus Th van Genuchten, and Sharon L Walker. Colloid transport in unsaturated porous media: The role of water content and ionic strength on particle straining. *Journal of contaminant hydrology*, 96(1-4):113–127, 2008.

Tatiana Trantidou, Yuval Elani, Edward Parsons, and Oscar Ces. Hydrophilic surface modification of pdms for droplet microfluidics using a simple, quick, and robust method via pva deposition. *Microsystems & nanoengineering*, 3(1):1–9, 2017.

Todd P Trooien, Mahbub Alam, R Lamm Freddie, and R Freddie. Filtration and maintenance considerations for sdi systems. 1998.

Chuen-Jinn Tsai, David YH Pui, and Benjamin YH Liu. Particle detachment from disk surfaces of computer disk drives. *Journal of aerosol science*, 22(6):737–746, 1991.

Y. Tsuji, T. Kawaguchi, and T. Tanaka. Discrete particle simulation of two-dimensional fluidized bed. 77:79–87, 1993. ISSN 0032-5910. doi: 10.1016/0032-5910(93)85010-7.

E Unsal, ABGM Ten Berge, and DAZ Wever. Low salinity polymer flooding: Lower polymer retention and improved injectivity. *Journal of Petroleum Science and Engineering*, 163:671–682, 2018.

Koohyar Vahidkhah, Peter Balogh, and Prosenjit Bagchi. Flow of red blood cells in stenosed microvessels. *Scientific reports*, 6(1):28194, 2016.

Ravimadhav N Vaidya and H Scott Fogler. Formation damage due to colloidally induced fines migration. *Colloids and surfaces*, 50:215–229, 1990.

Ernest B van der Wee, Brendan C Blackwell, Florencio Balboa Usabiaga, Andrey Sokolov, Isaiah T Katz, Blaise Delmotte, and Michelle M Driscoll. A simple catch: Fluctuations enable hydrodynamic trapping of microrollers by obstacles. *Science Advances*, 9(10):eade0320, 2023.

Nathan Vani, Sacha Escudier, and Alban Sauret. Influence of the solid fraction on the clogging by bridging of suspensions in constricted channels. *Soft Matter*, 18(36):6987–6997, 2022. ISSN 1744-6848. doi: 10.1039/d2sm00962e.

Nathan Vani, Sacha Escudier, Deok-Hoon Jeong, and Alban Sauret. Role of the constriction angle on the clogging by bridging of suspensions of particles. *Physical Review Research*, 6(3): L032060, 2024.

A Verma and K Pruess. Thermohydrological conditions and silica redistribution near high-level nuclear wastes emplaced in saturated geological formations. *Journal of Geophysical Research: Solid Earth*, 93(B2):1159–1173, 1988.

Evert Johannes Willem Verwey. Theory of the stability of lyophobic colloids. *The Journal of Physical Chemistry*, 51(3):631–636, 1947.

Yun-Hong Wang, Yin-Hu Wu, Xin Tong, Tong Yu, Lu Peng, Yuan Bai, Xue-Hao Zhao, Zheng-Yang Huo, Nozomu Ikuno, and Hong-Ying Hu. Chlorine disinfection significantly aggravated the biofouling of reverse osmosis membrane used for municipal wastewater reclamation. *Water Research*, 154:246–257, 2019.

NC Wardlaw and JP Cassan. Oil recovery efficiency and the rock-pore properties of some sandstone reservoirs. *Bulletin of Canadian Petroleum Geology*, 27(2):117–138, 1979.

Majid Ebrahimi Warkiani, Filicia Wicaksana, Anthony Gordon Fane, and Hai-Qing Gong. Investigation of membrane fouling at the microscale using isopore filters. *Microfluidics and Nanofluidics*, 19(2):307–315, 2015.

George M Whitesides. The origins and the future of microfluidics. *nature*, 442(7101):368–373, 2006.

George M Whitesides, Emanuele Ostuni, Shuichi Takayama, Xingyu Jiang, and Donald E Ingber. Soft lithography in biology and biochemistry. *Annual review of biomedical engineering*, 3(1): 335–373, 2001.

Sébastien Wiederseiner, Nicolas Andreini, Gaël Epely-Chauvin, and Christophe Ancey. Refractive-index and density matching in concentrated particle suspensions: a review. *Experiments in fluids*, 50:1183–1206, 2011.

John R Womersley. Method for the calculation of velocity, rate of flow and viscous drag in arteries when the pressure gradient is known. *The Journal of physiology*, 127(3):553, 1955.

Stanley Wu, Alex Nikolov, and Darsh Wasan. Cleansing dynamics of oily soil using nanofluids. *Journal of colloid and interface science*, 396:293–306, 2013.

Hans M Wyss, Daniel L Blair, Jeffrey F Morris, Howard A Stone, and David A Weitz. Mechanism for clogging of microchannels. *Physical review E*, 74(6):061402, 2006a.

Hans M. Wyss, Daniel L. Blair, Jeffrey F. Morris, Howard A. Stone, and David A. Weitz. Mechanism for clogging of microchannels. *Physical Review E*, 74(6):061402, December 2006b. doi: 10.1103/PhysRevE.74.061402. URL `https://link.aps.org/doi/10.1103/PhysRevE.74.061402`. Publisher: American Physical Society.

Younan Xia and George M Whitesides. Soft lithography. *Angewandte Chemie International Edition*, 37(5):550–575, 1998.

Du Xinqiang, Song Yalin, Ye Xueyan, and Luo Ran. Colloid clogging of saturated porous media under varying ionic strength and roughness during managed aquifer recharge. *Journal of Water Reuse and Desalination*, 9(3):225–231, 2019.

Zhibin Yan, Xiaoyang Huang, Lingling Shui, and Chun Yang. Kinetics of colloidal particle deposition in microfluidic systems under temperature gradients: experiment and modelling. *Soft Matter*, 16(15):3649–3656, 2020.

Hongtao Yang and Matthew T Balhoff. Pore-network modeling of particle retention in porous media. *AIChE Journal*, 63(7):3118–3131, 2017.

Kuan-Mu Yao, Mohammad T Habibian, and Charles R O'Melia. Water and waste water filtration. concepts and applications. *Environmental science & technology*, 5(11):1105–1112, 1971.

Yanzhou Yin, Yifei Cui, and Lu Jing. Clogging and unclogging of fine particles in porous media: Micromechanical insights from an analog pore system. *Water Resources Research*, 60 (1):e2023WR034628, 2024. doi: 10.1029/2023WR034628.

Yousang Yoon, Seonil Kim, Jusin Lee, Jaewoong Choi, Rae-Kwon Kim, Su-Jae Lee, Onejae Sul, and Seung-Beck Lee. Clogging-free microfluidics for continuous size-based separation of microparticles. *Scientific reports*, 6(1):1–8, 2016.

Zhenjiang You, Pavel Bedrikovetsky, Alexander Badalyan, and Martin Hand. Particle mobilization in porous media: temperature effects on competing electrostatic and drag forces. *Geophysical Research Letters*, 42(8):2852–2860, 2015.

A Yudin, E Eltaher, A AlYaseen, Z Al-Jalal, and M Faisal. Water wells injectivity enhancement via hydraulic fracturing in open hole completions. In *SPE Annual Caspian Technical Conference*, page D011S002R005. SPE, 2024.

F. Zami-Pierre, R. de Loubens, M. Quintard, and Y. Davit. Effect of disorder in the pore-scale structure on the flow of shear-thinning fluids through porous media. *Journal of Non-Newtonian Fluid Mechanics*, 261:99–110, November 2018. doi: 10.1016/j.jnnfm.2018.08.004. URL `https://ui.adsabs.harvard.edu/abs/2018JNNFM.261...99Z`.

Arno Zang, Günter Zimmermann, Hannes Hofmann, Ove Stephansson, Ki-Bok Min, and Kwang Yeom Kim. How to reduce fluid-injection-induced seismicity. *Rock Mechanics and Rock Engineering*, 52(2):475–493, 2019.

Isidro E Zarraga, Davide A Hill, and David T Leighton Jr. The characterization of the total stress of concentrated suspensions of noncolloidal spheres in newtonian fluids. *Journal of Rheology*, 44(2):185–220, 2000.

Hua Zhang, Alex Nikolov, and Darsh Wasan. Enhanced oil recovery (eor) using nanoparticle dispersions: underlying mechanism and imbibition experiments. *Energy & Fuels*, 28(5):3002–3009, 2014.

Lin Zhang, Pute Wu, Delan Zhu, and Chao Zheng. Effect of pulsating pressure on labyrinth emitter clogging. *Irrigation Science*, 35(4):267–274, 2017.

Min Zhang. *Modeling Particulate Transport to Optimize Hydraulic Fracturing and Refracturing*. PhD thesis, The University of Texas at Austin, 2021.

Min Zhang and Maša Prodanović. Optimizing proppant placement in rough-walled rock fractures. In *Unconventional Resources Technology Conference*, 2019. doi: 10.15530/urtec-2019-1081.

Qiulan Zhang, A Raoof, and SM Hassanizadeh. Pore-scale study of flow rate on colloid attachment and remobilization in a saturated micromodel. *Journal of environmental quality*, 44(5):1376–1383, 2015.

Xiao Zhao, Wen Liu, Zhengqing Cai, Bing Han, Tianwei Qian, and Dongye Zhao. An overview of preparation and applications of stabilized zero-valent iron nanoparticles for soil and groundwater remediation. *Water research*, 100:245–266, 2016.

T Zsirai, P Buzatu, P Aerts, and S Judd. Efficacy of relaxation, backflushing, chemical cleaning and clogging removal for an immersed hollow fibre membrane bioreactor. *Water research*, 46 (14):4499–4507, 2012.

Iker Zuriguel, Angel Garcimartín, Diego Maza, Luis A. Pugnaloni, and J. M. Pastor. Jamming during the discharge of granular matter from a silo. *Physical Review E*, 71(5):051303, May 2005. ISSN 1550-2376. doi: 10.1103/physreve.71.051303.

Walid OKAYBI

Colmatage colloïdal dans les milieux poreux : une étude microfluidique des dynamiques, des mécanismes et du contrôle

Résumé :
Le transport colloïdal dans les milieux poreux joue un rôle central dans les systèmes souterrains, notamment pour les ressources en eau souterraine, l'énergie géothermique et le stockage souterrain d'énergie thermique. Les particules en suspension peuvent provenir de la formation poreuse ou être introduites par les fluides injectés. Leur transport et leur rétention dans l'espace poreux peuvent entraîner un colmatage, réduisant ainsi la perméabilité et l'injectivité. Dans les applications par injection, ces processus peuvent être accentués par les différences physico-chimiques et hydrodynamiques entre les conditions initiales et celles du milieu injecté. Cependant, les mécanismes de colmatage à l'échelle des pores restent mal compris dans les milieux poreux hétérogènes représentatifs des systèmes naturels, en raison de leur opacité qui limite l'observation directe des processus clés. Pour pallier cette limitation, ce travail combine des expériences microfluidiques en milieux poreux hétérogènes avec l'analyse d'images et des simulations d'écoulement à l'échelle des pores afin d'étudier et d'identifier les mécanismes régissant le dépôt de particules, le colmatage, la modification de l'écoulement et l'évolution de la perméabilité selon différents régimes de dépôt et sous diverses conditions physico-chimiques et hydrodynamiques. Les résultats montrent que le colmatage est un processus dépendant du régime et régi par des mécanismes distincts. En conditions adhésives, une nouvelle forme de colmatage progressif a été identifiée : des structures dendritiques se développent à partir d'un site de dépôt préférentiel unique et obstruent progressivement l'espace poreux. Ce mécanisme est contrôlé par les conditions d'écoulement locales, notamment par la taille des zones de stagnation par rapport au diamètre des particules. En conditions répulsives, le colmatage est principalement dû à la formation de ponts hydrodynamiques, où les particules forment des arches stables au niveau des rétrécissements des pores, entraînant une réduction progressive de la perméabilité, principalement contrôlée par la taille et la concentration des particules. L'écoulement oscillatoire n'atténue pas systématiquement le colmatage, mais induit une réponse dépendante du régime : il peut le retarder en conditions d'agrégation dominante, mais l'accélérer aux hautes fréquences en régime hydrodynamique. Globalement, ce travail apporte un nouvel éclairage sur les mécanismes contrôlant le colmatage colloïdal et souligne la nécessité d'une approche adaptée au régime pour prédire et gérer la réduction de la perméabilité dans les systèmes souterrains réalistes.

Mots clés : Milieux poreux, microfluidique, dendrites, colmatage des pores, écoulement oscillatoire, perméabilité.

Colloidal Clogging in Porous Media: A Microfluidic Investigation of Dynamics, Mechanisms, and Control

Abstract:
Colloidal transport in porous media plays a central role in subsurface systems, including groundwater resources, geothermal energy, and underground thermal energy storage. Suspended particles may originate from the porous formation or be introduced with injected fluids. Their transport and retention within the pore space can lead to clogging, thereby reducing permeability and injectivity. In injection-based applications, these processes may be further enhanced by physicochemical and hydrodynamic differences between injected and native conditions. However, pore-scale clogging mechanisms remain poorly understood in heterogeneous porous media representative of natural systems due to their opacity, which limits direct observation of key processes. To address this limitation, this work combines microfluidic experiments in heterogeneous porous media with image analysis and pore-scale flow simulations to investigate and identify the mechanisms governing particle deposition, clogging, flow alteration, and permeability evolution across distinct deposition regimes and under varying physicochemical and hydrodynamic conditions. The results show that clogging is a regime-dependent process governed by distinct mechanisms. Under adhesive conditions, a novel form of progressive clogging is identified, in which dendritic structures grow from a single preferential deposition site and progressively block the pore space. This mechanism is controlled by local flow conditions, particularly the size of stagnation regions relative to particle diameter. Under repulsive conditions, clogging is dominated by hydrodynamic bridging, where particles form stable arches at pore constrictions, leading to stepwise permeability reduction controlled mainly by particle size and concentration. Oscillatory flow does not systematically mitigate clogging, but instead produces a regime-dependent response: it can delay clogging in aggregation-dominated conditions, yet accelerate it at higher frequencies in hydrodynamic regimes. Overall, this work provides new insight into the mechanisms controlling colloidal clogging and highlights the need for a regime-dependent approach to predict and manage permeability reduction in realistic subsurface systems.

Keywords: Porous media, microfluidics, dendrites, pore-clogging, oscillatory flow, permeability.

Institut des Sciences de la Terre d'Orléans (ISTO)
1A rue de la Férollerie, 45071, Orléans, France